SMC Bulletin

A Publication of the Society for Materials Chemistry

Volume 10 No. 2 August 2019

Special Issue on

Materials Chemistry for Nuclear Applications

SOCIETY FOR MATERIALS CHEMISTRY

SMC Bulletin

Vol. 10 **No. 2** **August 2019**

Guest Editor

Dr. Rajesh Ganesan
Materials Chemistry Division
Materials Chemistry and Metal Fuel Cycle Group
Indira Gandhi Centre for Atomic Research
Kalpakkam - 603 102, INDIA

Editorial Board	
Dr. Arvind Kumar Tripathi Chemistry Division Bhabha Atomic Research Centre Trombay, Mumbai, 400 085 e-mail: catal@barc.gov.in	
Dr. Manidipa Basu Chemistry Division Bhabha Atomic Research Centre Trombay, Mumbai, 400 085 e-mail: deepa@barc.gov.in	**Dr. Rajesh Ganesan** Materials Chemistry Division Indira Gandhi Centre for Atomic Research Kalpakkam, 603102 e-mail: rajesh@igcar.gov.in
Dr. G. Kedarnath Chemistry Division Bhabha Atomic Research Centre Trombay, Mumbai, 400 085 e-mail: deepa@barc.gov.in	**Dr. Sandeep Nigam** Chemistry Division Bhabha Atomic Research Centre Trombay, Mumbai, 400 085 e-mail: snigam@barc.gov.in
Dr. Rajesh V. Pai Fuel Chemistry Division Bhabha Atomic Research Centre Trombay, Mumbai, 400 085 e-mail: rajeshvp@barc.gov.in	**Dr. Vivek Polshettiwar** Department of Chemical Sciences, Tata Institute of Fundamental Research, Colaba, Mumbai 400005 e-mail: vivekpol@tifr.res.in

Published by

Society for Materials Chemistry
C/o. Chemistry Division
Bhabha Atomic Research Centre, Trombay, Mumbai, 400 085
E-mail: socmatchem@gmail.com,
Tel: +91-22-25592001

Please note that the authors of the paper are alone responsible for the technical contents of papers and references cited therein.
Front cover shows (a) SEM monograph of (U0.8Nd0.2)O1.95, (b) calibration plot of PbS towards NH3 sensing at 473 K, (c) Ti button prepared via induction melting and (d) polythermal liquidous projection with isothermal contours on LiCl-KCl-NdCl3 system.

Guest Editorial

Dr. Rajesh Ganesan

The current thematic issue is based on materials chemistry research work carried out at Indira Gandhi Centre for Atomic Research, Kalpakkam. The primary mission of this Centre is to conduct a broad based multidisciplinary programme of scientific research and advanced engineering development, directed towards the establishment of the technology of Sodium Cooled Fast Breeder Reactors (FBR) and associated fuel cycle facilities in the Country. The mission includes the development and applications of new and improved materials, techniques, equipment and systems for FBRs, pursue basic research to achieve breakthroughs in Fast Reactor technology.

The focus of this issue of SMC bulletin is on the chemistry of materials for nuclear applications. Some of the recent research work carried out in Materials Chemistry and Metal Fuel Cycle Group of IGCAR are presented. In this issue, articles are covering the topics such as determination of melting transitions and heat capacity measurements of nuclear materials, phase equilibria in molten salt systems and electrochemical methods on de-oxidation of metal oxides Articles based on immobilization of nuclear waste in inorganic materials, pulsed laser deposition of oxide thin films, materials for chemical sensors and synthesis of materials for piezoelectric applications are also featured.

It has been a pleasure to act as guest editor for this special issue on "Materials Chemistry for Nuclear Applications". I thank Prof. V. K. Jain, President, SMC, all the office bearers of executive committee and editorial board of SMC bulletin for this opportunity. I also thank all the authors who have contributed their articles for this issue.

I hope that the readers will find the articles informative and useful.

From the desks of the President and Secretary

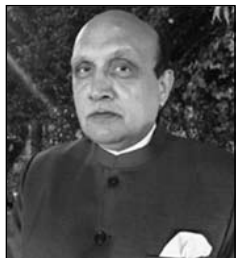

Dr. V. K. Jain
President

Dr. R. K. Vatsa
Hon. Secretary

Dear Esteemed SMC Members and colleagues,

Warm greetings from Executive Council of ***Society for Materials Chemistry*** (SMC),

The SMC and the Editorial Board have been making consistent efforts to bring out thematic issues on contemporary subjects of SMC Bulletin. The present issue is based on the research and developmental work done in the field of materials chemistry for the purpose of nuclear power and applications by the scientists of Indira Gandhi Centre for Atomic Research (IGCAR), Kalpakkam. As you are aware, nuclear reactor operation requires special materials of very high purity, desired neutron cross-sections, high mechanical strength and thermal properties. The behaviour of the nuclear fuel in the reactor under irradiation is itself quite complex as it is continuously exposed to harsh radiation environment and severe thermal gradient for a very long time. Topics covered in this thematic issue include heat capacity measurements of nuclear materials, electrochemical methods on de-oxidation of metal oxides, immobilization of nuclear waste by inorganic materials, synthesis of materials for piezoelectric applications, materials for chemical sensors and pulsed laser deposition of oxide thin films. The first article discusses a variety of methods that could be used for determining the phase transitions. The second article discusses anomalies in temperature dependent heat capacity of uranium-rare earth- mixed oxide system. The third article is about phase equilibria on LiCl-KCl-RECl3(RE: Pr, Nd andGd) pseudo-ternary systems. Molten slat electrolysis can be an efficient and economical method for gaining metals from highly stable metal compounds as reflected in the contents of fourth article. The fifth article is about treatment and disposal of nuclear wastes using inorganic materials. The sixth article is a feasibility study on immobilization of Re (simulant for Tc) in geo-polymer matrix. Next three articles are on synthesis, characterization and applications of thin films dealing with deposition of multi element oxide using pulsed laser deposition, laser ablated PbS films for NH3 sensing and synthesis of highly resistive bismuth titanate ceramics for high temperature piezoelectric applications.

We place on record our sincere appreciation to Dr. Rajesh Ganesan, Guest Editor, who has taken keen interest to bring out this special issue in a timely manner. We also thank all the members of SMC for their continued support and cooperation in the growth of the Society.

CONTENTS

Feature Articles		Page No.
1.	**Methods for the determination of melting transitions in nuclear materials** *K. Ananthasivan*	46
2.	**Anomalies in temperature dependent heat capacity of uranium-rareearth-mixed oxide system** *R. Venkata Krishnan, R. Babu, AbhiramSenapati, G. Jogeswararao and K. Ananthasivan*	60
3.	**Phase equilibria on LiCl-KCl-RECl3 (RE: Pr, Nd and Gd) pseudo-ternary systems** *Sajal Ghosh, P. R. Reshmi, C.V. Vishnu Vardhan, Rajesh Ganesan, R. Sridharan, and T. Gnanasekaran*	68
4.	**Molten salt based direct solid state electrochemical de-oxidation of metal oxides to metal: Our experience at IGCAR** *K.S. Mohandas, N. Sanil, D. Sri Maha Vishnu, T. Biju Joseph, R. Kumaresan, Anwesha Mukherjee and L. Shakila*	75
5.	**Inorganic materials for the treatment and disposal of nuclear wastes** *K. A. Venkatesan and A. S. Suneesh*	93
6.	**Studies on the immobilization of ^{75}Re (simulant for ^{43}Tc) in geo-polymer matrix: a feasibility study** *Vineet Kumar and Hrudananda Jena*	103
7	**Pulsed laser deposition of a few oxide thin films** *P.Manoravi and M.Joseph*	113
8	**Laser Ablated Thin Films of PbS for NH_3 Sensing Under Inert Ambient** *Beatriceveena. T. V., E. Prabhu, V. Jayaraman and K. I. Gnanasekar*	118
9	**Synthesis of highly resistive bismuth titanate ceramics for high temperature piezoelectric applications** *P.M. Aiswarya, A.V. Meera, R. Srinidhi, K.I. Gnanasekar, V. Jayaraman and T. Gnanasekaran*	124

Methods for the determination of melting transitions in nuclear materials

K. Ananthasivan
Reprocessing Group, Indira Gandhi Centre for Atomic Research, HBNI, Kalpakkam 603 102, INDIA
E-mail: asivan@igcar.gov.in

Abstract

Phase diagrams or equilibrium diagrams find extensive application in many industries. These provide vital information about both the phase composition and thermal transitions that take place in multicomponent materials. The determination of phase diagrams essentially comprises determination of the dependence of phase transitions on temperature, pressure and composition. These could be accomplished in a variety of ways by following the discontinuity in the dependence of a chosen physical property. Measurement of the transitions involving liquids are particularly difficult owing to the reactivity of the latter leading to the difficulties encountered in their containment, especially at high temperatures. This article discusses a variety of methods that could be used for determining the phase transition involving liquids.

Keywords: DTA, DSC, Thermal Analysis, spot technique, solidus, liquidus, invariant equilibria involving liquids

1. Introduction

Among the physicochemical properties of technologically important materials the melting point is an important fundamental property. If the material under consideration is a simple metal the term melting point is relevant. For multiphasic materials, the lowest temperature at which liquid appears first when it is heated, is used in place of melting point. It could be the solidus temperature or the temperature pertaining to a phase equilibria in which liquid is formed. Information on the solidus temperature are technologically important, in order to determine the temperature limits of the given practical application involving an alloy. In order to experimentally measure the solidus temperature, often information on the phase diagram is quite useful.

Knowledge on the physicochemical properties of fuel materials is useful for their fabrication as well as for assessing and predicting their behaviour in the reactor. Detailed investigations were made in the past on the physicochemical properties of the fast reactor fuel materials. These physicochemical properties include the thermochemical and thermophysical properties such as melting point, enthalpy, heat capacity, free energy, thermal conductivity, thermal expansion, and vapourisation behaviour of the fuel. Among these the methods available for the determination of the melting point (solidus and liquidus) would be discussed in this article.

2. Relevance of phase diagrams

"Phase diagrams are visual representations of the state of a material as a function of temperature, pressure, and concentrations of the constituent components and are, therefore, frequently hailed as basic blueprints or roadmaps for alloy design, development, processing, and understanding" [1]. The phase equilibria represented in a phase diagram are applicable to materials only under thermodynamic equilibrium conditions. Despite this limitation, the information derived from the phase diagrams can be of great value in many practical applications.

Pelton [2,3] defined a phase diagram as the geometrical representation of the loci of the thermodynamic parameters when equilibrium between different phases under a specified set of conditions is established. This author showed that phase diagrams could be classified based on the parameters used to define the axes of their graphical respresentation, viz., pressure (P), temperature (T), chemical potential (μ_i), and composition. The parameters P and T are also potentials, viz. mechanical potential and thermal potential. The conjugate extensive variables associated with μ_i, P and T (intensive variables) are composition, volume and entropy, respectively [3]. While constructing a phase diagram (in two dimensions) either a potential or its conjugate extensive variable can be represented on each of the two axes. Out of the four "types" of phase diagrams that would result, two are quite identical. Thus, three distinct types of phase diagrams could be constructed. The classification of phase diagrams proposed by Pelton and Schmalzreidis [4] is given in Table 1.

Table 1 Types of phase diagrams [4]

Type	Abscissa	Oridinate	Example
Type 1	Potential	Potential	Unary phase diagrams (P vs. T)
Type 2*	Potential / Conjugate variable	Extensive variable / Potential	Binary phase diagrams (T vs. X or P vs. X) Ellingham diagram
Type 3	Conjugate variable	Conjugate variable	Isothermal sections of ternary diagrams

** doubly degenerate*

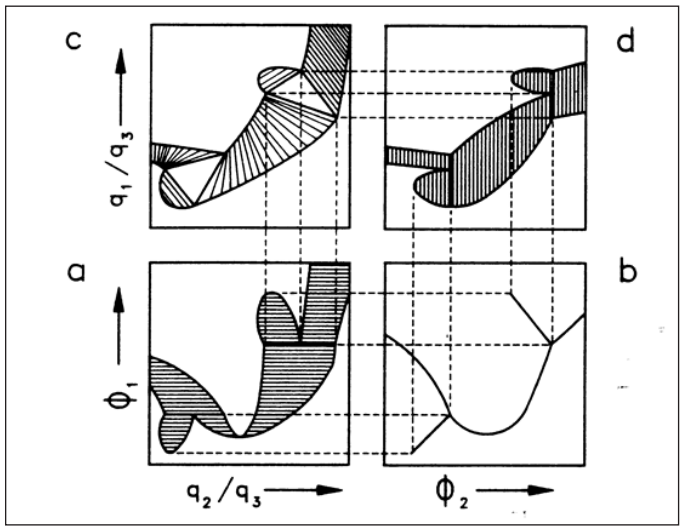

Fig.1: *Schematic representation of the three types of phase diagrams illustrating the topological inter-relationship between them [2]. (a) potential vs. conjugate variable (b) potential vs. potential (c) conjugate variable vs. conjugate variable (d) potential vs. conjugate variable $Ø_1$, and $Ø_2$ are potentials. q_1, q_2 and q_3 represent conjugate variables [2].*

The P vs. T (unary) diagrams for water, sulphur and carbon dioxide are some examples for the type-1 phase diagram. However, type-1 phase diagrams are not restricted only to the unary systems. Similar diagrams could as well be constructed for the binary and higher order systems. Pelton [2,3] showed that for the ternary system Co-Ni-O all the three types of diagrams could be constructed. This author also brought out the inter relationship between the three types of diagrams for a hypothetical system which is given in Fig. 1.

The type-2 phase diagram, in which the ordinate represents the temperature and abscissa the composition (at P = 1 atm), is used more frequently and finds extensive application in metallurgy and materials science. All the binary phase diagrams reported in the compilations of the past belong to this category [5-12]. Even though a given technological problem might very often warrant the use of a multi-component phase diagram, the information on binary phase diagrams forms the basis and is thus very important. The invariant equilibria involving three condensed phases in a binary system (at P=1 bar) are enlisted in Table 2.

Table 2 Solid-liquid equilibria in a binary system involving three phases

Type	Equilibrium reaction upon cooling
Transitions involving solid and liquid phases	
Eutectic	Liquid (L_1) → solid (α) + solid (β)
Monotectic	Liquid (L_3) →liquid (L_2) + solid (ε)
Peritectic	Solid (β) + liquid (L_2) → solid (λ)
Syntectic	Liquid (L_1) + liquid (L_2) →solid (β)
Catatectic (metatectic)	Solid (β)→ solid (α) + liquid (L)
Transition involving only solid phases	
Eutectoid	Solid (β) → solid (α) + solid (λ)
Peritectoid	Solid (α) + solid (λ)→ solid (η)

Construction of a phase diagram requires the experimental determination of the phase equilibria mentioned above. These are determined using alloys with fixed gross composition (along an isopleth) or using measurements on a series of alloys at a given temperature (isothermal) or both. A variety of experimental techniques are available for the determination of phase digrams [13-17]. Some of the methods that are pertinent to identifying the phase transitions involving liquids are described in detail in the following sections.

3. Experimental techniques for the determination of solid to liquid phase transformation temperature

3.1 Methods based on the heat of phase transformation

3.1.1. Thermal analysis (The method of cooling curves)

The latent heat of fusion / freezing for most metals is about $2\times T_m$ (Richards rule) [13] where T_m is the melting point expressed in Kelvin and the specific heat of metals is about 20 J g atom^{-1} K^{-1}. Hence, a perceptible thermal arrest is observed on a cooling curve (temperature vs. time plot) of a molten metal. In the case of alloys the heat is liberated over a range of temperatures and a change in slope rather than a thermal arrest is observed both at the liquidus and the solidus temperatures [2,13]. Eutectic and peritectic transformations are isothermal and exhibit thermal arrests similar to that obtained for pure metals. Idealized cooling and heating curves are illustrated in Fig. 2. Generally for alloys with a narrow range of melting the ingot regains the liquidus temperature on recalescence and an accurate liquidus temperature is measured [13]. Examples of such

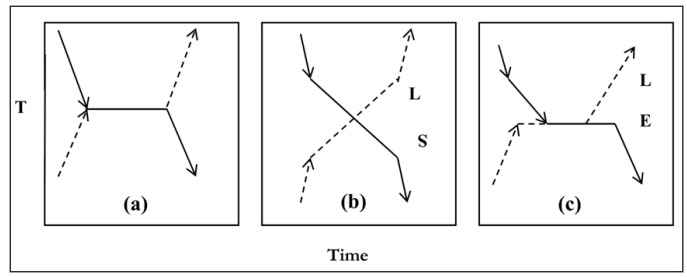

Fig. 2: *Idealized heating and cooling curves for (a) a puremetal, b) an alloy with a range of freezing, and (c) an alloy with with a range of freezing and eutectic transformation. L,S,E are liquidus, solidus and eutectic temeperatures respectively [13].*

alloy systems are Cu-Ni, Bi-Sb and Zr-Ni alloys [18,19]. However, in systems with a considerable freezing range the heat liberated on recalescence of a supercooled melt might be too small to allow accurate measurement of the liquidus temperature. Examples of such alloy systems are Zr-Ni-Al [19]. Errors due to segregation could be eliminated by annealing the alloy below the estimated solidus.

3.1.2 Differential thermal analysis (DTA)

DTA and differential scanning calorimetry (DSC) find extensive application in materials science. Several good treatises are available on these two techniques [20-27]. Both these techniques employ a "differential method", for the measurement of a phase transition temperature. A differential method may be defined as follows [20]:

"A method of measurement in which the measurand is compared with a quantity of the same kind of known value only slightly different from the value of the measurand and in which the difference between the two values is measured".

Differential thermal analysis is defined by the International Confederation for Thermal Analysis and Calorimetry (ICTAC) as follows [20]:

"A technique in which the difference in temperature between the sample and a reference material is monitored against time or temperature while the temperature of the sample, in a specified atmosphere is programmed".

In a typical DTA experiment a test sample and an inert reference are heated or cooled under identical conditions and the temperature difference between the sample and reference, if any, is recorded. This differential temperature is then plotted against time, or against temperature or the heating rate. Changes in the sample such as a phase transition that lead to the absorption or evolution of heat are detected relative to the inert reference. DTA can therefore be used to study phase transitions.

The schematic diagram of a special case of a block type differential thermal analyzer is given in Fig. 3 (a). In general, a DTA apparatus comprises the following components.

a) Sample holder assembly

b) Furnace

c) Temperature programmer

d) Measuring and recording system

The sample holder assembly consists of two thermocouples one each for the sample and reference, and a block to ensure an even heat distribution. The sample is contained in a small crucible designed suitably to house the thermocouples such that the thermocouple bead snug fits into it. These crucibles are made out of either a metal or a ceramic. Alumina, silica, pyrex, platinum and nickel are some of the materials generally used to fabricate these crucibles. In order to contain highly reactive and radioactive alloys often crucibles made out of exotic materials like thoria, beryllia are required. Generally the choice of crucible depends upon the temperature range of investigation and its chemical compatibility with the specimen. In most of the experiments the thermocouples are not placed in direct contact with the sample in order to avoid contamination and degradation.

Strict repeatability of the measuring system over the whole temperature range must be ensured [22]. Depending on the method adopted for measuring the temperature difference, ΔT, the DTA apparatus could be classified into two basic contrasting types, viz. the block-type measuring system and the measuring system with free-standing

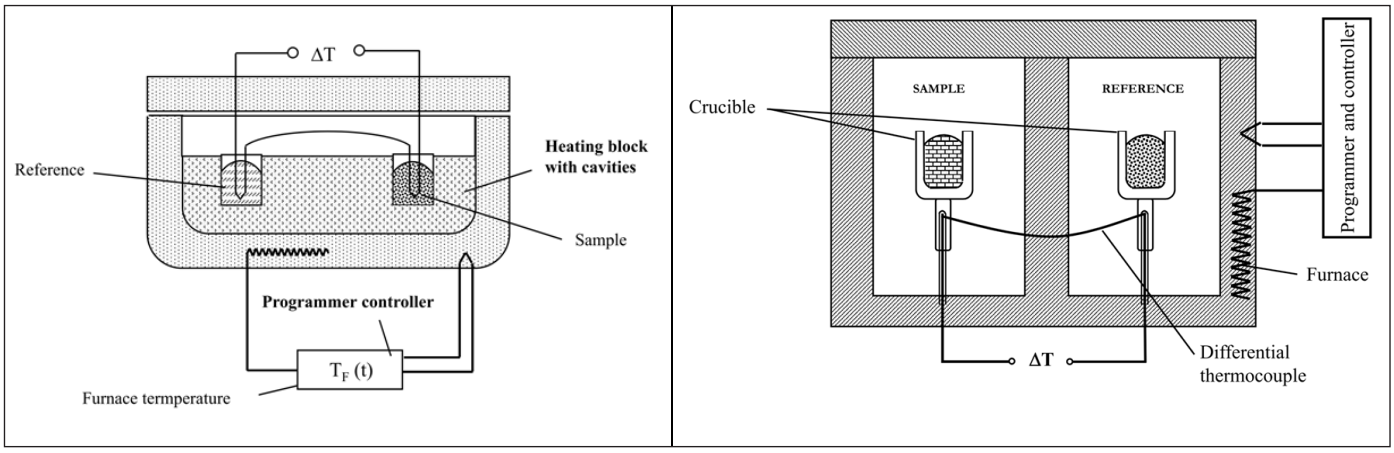

(a) **(b)**

Fig.3: *Schematic diagrams of a DTA apparatus with (a) block type measuring system and (b) free-standing crucibles [25].*

crucibles. These two types are illustrated in Fig. 3 (a) and (b), respectively.

The block type measuring system has a higher sensitivity and has a rapid and almost instantaneous response. However, the duration and height of the signal and its shape depend on the location of the sensor relative to the sample, and on the thermophysical properties of the sample substance. Hence a quantitative evaluation of the heat in question is not possible.

The measuring system with free-standing crucibles is more often used in commercial DTA equipment. In this type of equipment the crucibles are supported over the protective cover of the thermocouples. This design is particularly advantageous since it permits the use of a variety of crucibles and atmospheres and is suitable for "simultaneous thermal analysis" in which thermogravimetry is coupled with DTA.

DTA could be carried out with a single crucible as well. In the technique called single DTA (SDTA), the sample temperature is measured and the reference temperature is calculated using a mathematical model [22]. This method eliminates the use of an inert reference.

Commercial DTA equipments are available in various configurations, which can be used to investigate phase transitions up to 2673 K under different atmospheres including vacuum. Small size of the sample, wide range of measuring conditions (temperature range and atmospheres) and the enhanced sensitivity arising from the differential principle are the major advantages of this technique.

However, the measurement of transitions involving small heat effects (eg. liquidus points in binary systems with steep liquidus boundaries) is often difficult even with the enhanced sensitivity of this technique. Since DTA is a dynamic technique, the attainment of true thermodynamic equilibrium within the specimen during the measurement should be ascertained.

3.1.3 Differential scanning calorimetry (DSC)

In DSC, the difference in heat flow rate (or power) to the sample and to the reference sample is monitored against time while the samples are heated at a predetermined rate. Depending on the method of measurement used, the DSC is classified in to two types, viz. heat-flux DSC and power compensation DSC.

In a heat-flux DSC instrument, the temperature difference between the sample and the reference is recorded after suitable calorimetric calibration, as a direct measure of the difference in heat flow rate or the difference in power [20].

In the power compensation instrument the difference in power supplied to the sample and to the reference, to keep their temperatures nearly the same, is measured directly.

A schematic diagram of the heat flux DSC is given in Fig. 4(a). In this equipment a defined amount of heat that is exchanged through a thermal resistance with the environment is measured. The measured signal is the temperature difference between the sample and the reference (ΔT). It describes the intensity of the exchange and is proportional to the heat flow rate [20]. Modulated DSC, advanced versions with micro electro mechanical systems and Peltier cooling have made this technique more accurate [19].

The power-compensation DSC consists of two furnaces (generally made of platinum iridium alloys) each of which contains a temperature sensor and a heating device (a resistor made of platinum wire). The schematic diagram of a power compensation DSC is given in Fig. 4(b). The

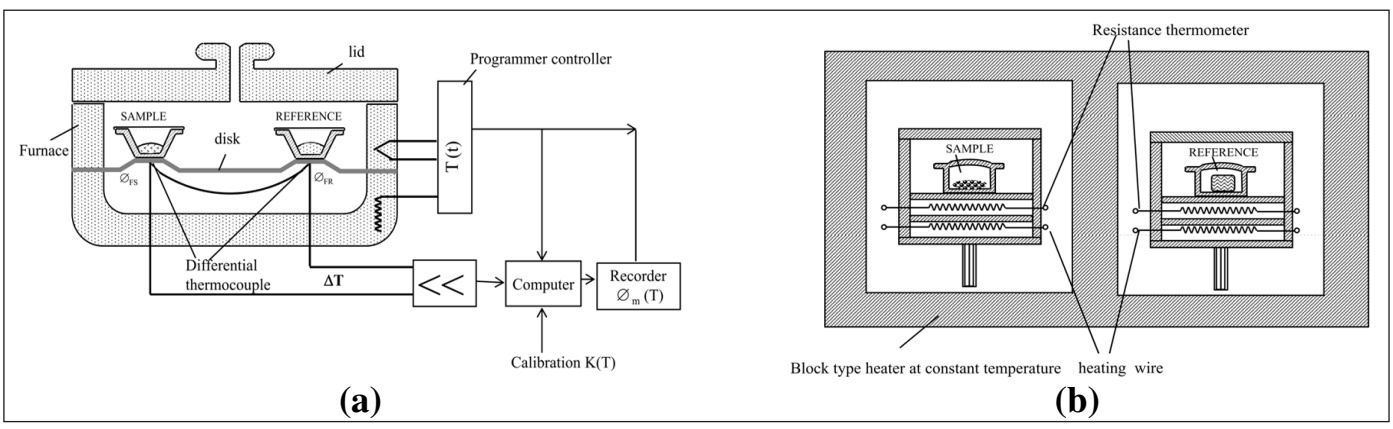

Fig.4: Schematic diagrams of (a) "Heat flux DSC" with disk type sample holders and (b) power compensation DSC apparatus [25]. $\varnothing_{FS,}$ *Heat flow rate from furnace to sample* $\varnothing_{FR}$ *heat flow rate from furnace to sample crucible, K (calibration factor)*

microfurnaces are thermally decoupled from each other and are placed in a metallic block at constant temperature. Compared to the heat flux DSCs, the power compensation DSCs are advantageous because they have an instantaneous response, rapid heat flow (which makes the calibration constant practically independent of the sample reaction), provide a direct measure of the heat of the reaction and requirea simpler caloric calibration.

While using the DTA or DSC for the measurement of phase diagrams, the solidus temperatures are obtained from the extrapolated onset temperatures. The liquidus temperatures are more difficult to determine. Low heating rates (< 2 K min^{-1}) generally help in avoiding "smearing" of the DSC (DTA) curve and in ensuring a better approximation to the true thermodynamic equilibrium. Annealing the alloy sample is particularly important when the temperature of investigation is far lower than the melting points of the constituents of an alloy. The utility of annealing was demonstrated in the investigation of the system Pb-In [28].

3.2 Methods based on microstructural characterization

3.2.1. Solid-liquid equilibration (incipient melting)

Methods based on metallographic techniques involve microstructural examination of the alloy specimen. In the incipient melting technique [13,28,29] a small ingot of the alloy is prepared by melting the constituents in vacuum or inert gas and chill casting the melt. Subsequently small sections of the alloy ingot are annealed at successively higher temperatures for short periods and quenched. Metallographic examination of the specimens which are quenched from just above the solidus temperature reveals signs of melting like spheroidization and loss of shape of the entrapped liquid at the corners and grain boundaries. These features would be absent in the specimens quenched from just below the solidus temperature. Thus the solidus temperatures could be bracketed. This method can be applied for the determination of the liquidus temperature as well. An alloy quenched from just above its liquidus exhibits a fine scale eutectic-like appearance [15], while alloys quenched below the liquidus reveal the presence of large primary crystals in the liquid matrix.

The incipient melting technique is one of the most widely used methods for studying liquid-solid phase equilibria in spite of the following limitations: (i) it is extremely time-consuming, (ii) requires a number of specimens of the same composition and (iii) necessitates fast quenching. These difficulties could be overcome in hot-stage microscopy [13].

3.2.2 Scanning Electron Microscopy (SEM) Electron Probe Micro Analysis (EPMA)

SEM and EPMA are the micro-analytical techniques widely used to image or analyse materials with a resolution that is better than that offered by visible techniques.

Information on approximate composition of different grains could also be obtained in a SEM which has an attachment for carrying out the energy dispersive analysis of the (characterisitic) X-rays (EDX) [30]. Very often presence of intermetallics are identified using EDX [31]. The operating principle and details of construction of SEM are discussed in Ref. [32].

EDX is capable of quantitative analysis on a micro-volume of samples and uses pure elemental and compound standards. This technique is suitable for quantitative elemental mapping with a lateral resolution of 1 μm. This technique is used in conjunction with SEM. The probing electron beam (in SEM) with an energy of 10-20 keV strikes the surface of a conducting sample causing characteristic X-rays to be emitted from that point of the material. These X-rays are generated in a region about 2 μm in depth, and thus EDX is not a surface technique. The low X-ray intensity, necessitates acquisition of images over long periods of time. Elements of low atomic number are difficult to detect by EDX. In windowless systems, elements with as low an atomic number as 4 (beryllium) have been detected, but the problems involved get progressively worse as the atomic number is reduced. Instruments equipped with X-ray microcalorimeter have a much better energy resolution (~3eV) than the traditional Si (Li) detector [33].

Information arising from the entire volume of the specimen can be acquired from the back scattered electrons emanating from within the specimen. The characteristic X-ray signal, which is used to construct the elemental spectra of the specimen arises in a volume within the specimen (0.2 to 2 microns in depth). Both qualitative and quantitative elemental analyses are possible. All elements in the periodic table (beyond lithium for wavelength dispersive spectrometer (WDS), beyond beryllium for energy dispersive spectrometer (EDS)) may be detected. Detection limits for EDS and WDS are about 1000 and 100 ppm, respectively.

This technique can be used in place of metallography for the characterization of the constituent phases present in an annealed and quenched alloy. EDX gives valuable information on the gross composition of the phases present in the specimen and is often useful in identifying new intermetallics [30]. However, the composition and structure of these phases need to be ascertained independently using other methods.

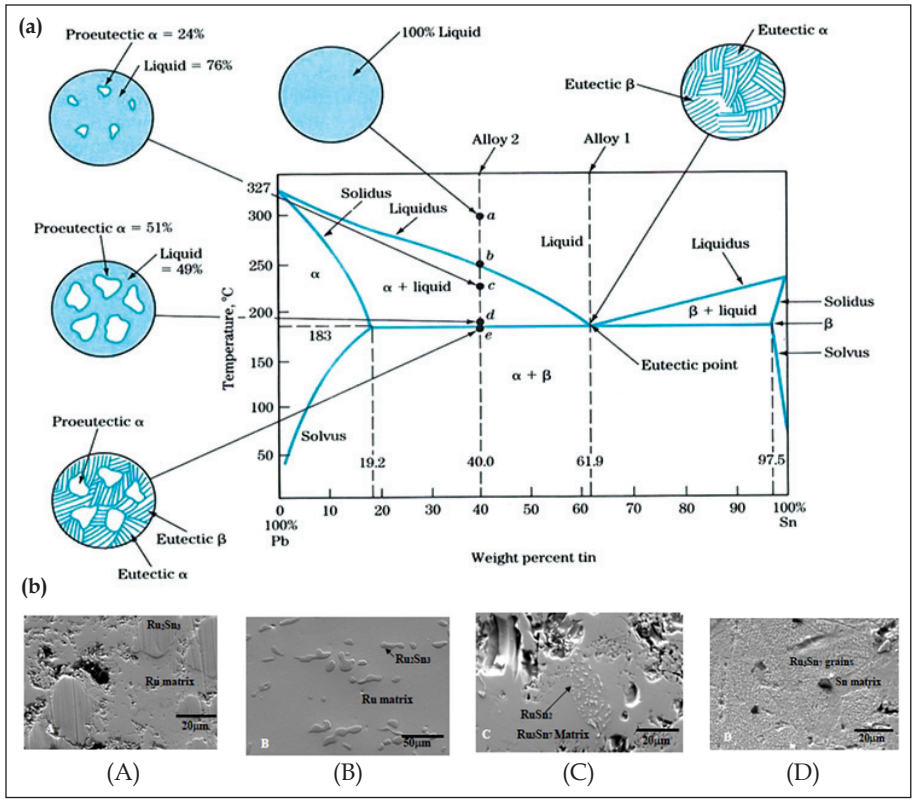

Fig.5: (a) Eutectic phase diagram of Pb and Sn [35] and (b) SEM micrographs of Ru-Sn alloys: (A) $Ru_{0.69}Sn_{0.31}$, (B) $Ru_{0.51}Sn_{0.49}$, (C) $Ru_{0.31}Sn_{0.69}$, (D) $Ru_{0.10}Sn_{0.90}$ [36]

The salient features of an EPMA equipment are as follows [33]. In EPMA, the specimen is bombarded with electrons which have high energies produced by an electron gun. This beam is brought to a fine focus on the surface of the specimen. The beam can be rastered across the surface by means of scan coils in the final lens. Upon bombarding with the primary electrons the specimen emits secondary signals such as backscattered and secondary electrons, characteristic and continuous X-rays, and photons of longer wavelength. The specimen is surrounded by a variety of signal detectors, which make it possible to image the surface as well as derive information on the structure and composition of the surface. The commercial EPMA equipment are so designed as to accommodate three to six wave length dispersive X-ray spectrometers which are inherently large. The spectrometers used in EPMA are much more sensitive to low elemental concentrations than EDX detectors which are usually associated with SEM. Concentrations in the range of 500-1000 ppm can generally be measured, and for some elements within some types of materials, the detection limit can be near 20 ppm. In EPMA all the imaging modes of the SEM are available. Further EPMA is augmented by the analytical capabilities of X-ray microanalysis.

Since the characteristic X-ray emission is used for detecting the elements, EPMA produces highly element-specific signals that can be used for quantitative measurements. In terms of sensitivity (hundreds of ppm) this technique can be placed between EDS and secondary ion mass spectrometry (SIMS). However, EPMA possesses the ability to perform local analysis on a very small region of the surface. The beam current in the EPMA equipment is several orders of magnitude greater than that in the other two techniques, which greatly improves the statistics associated with quantitative X-ray analysis.

Elements lighter than atomic number 8 (oxygen) cannot be measured without reservations, and EPMA is not sensitive to many elements below 100 ppm. Very often by choosing appropriate operational parameters one could circumvent the limitations of this technique. By proper choice and design of the experiment, useful information can be extracted from EPMA. Garg et al. [34] obtained information on solid solubility, and composition of the intermetallics using EPMA. In order to obtain reliable quantitative information by EPMA, a good calibration should be established using known standards and precautions are to be observed in the preparation of samples. Examples of the Pb-Sn and Ru-Sn alloy systems studied by SEM/EDS are given in Fig. 5(a) [35] & Fig. 5(b) [36], respectively.

3.2.3 Methods based on measurement of chemical potential

As dictated by the Gibbs phase rule the variance of thermodynamic activity of a given component in a multi-component system depends upon both the number of components as well as the number of phases in the system, that coexist in equilibrium at a given temperature and pressure. Thus for the equilibria involving condensed phases in a binary system (P =1atm), the thermodynamic activity of either of the components would be univariant in the single phase region while it would remain constant in a two-phase region. Thus plots of activity vs. composition for a two component system would show monotonous variation, constancy and sharp inflexion at the single phase regions, two phase regions and the phase boundaries, respectively. Thus the compositions pertaining to the phase boundaries can be recognized from the measurements on thermodynamic activity.

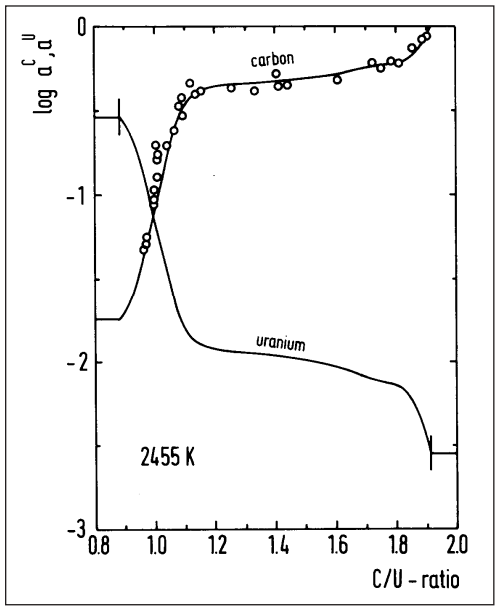

Fig.6: *Variation of the activities of uranium and carbon in the binary system U-C with composition at 2455 K [43]*

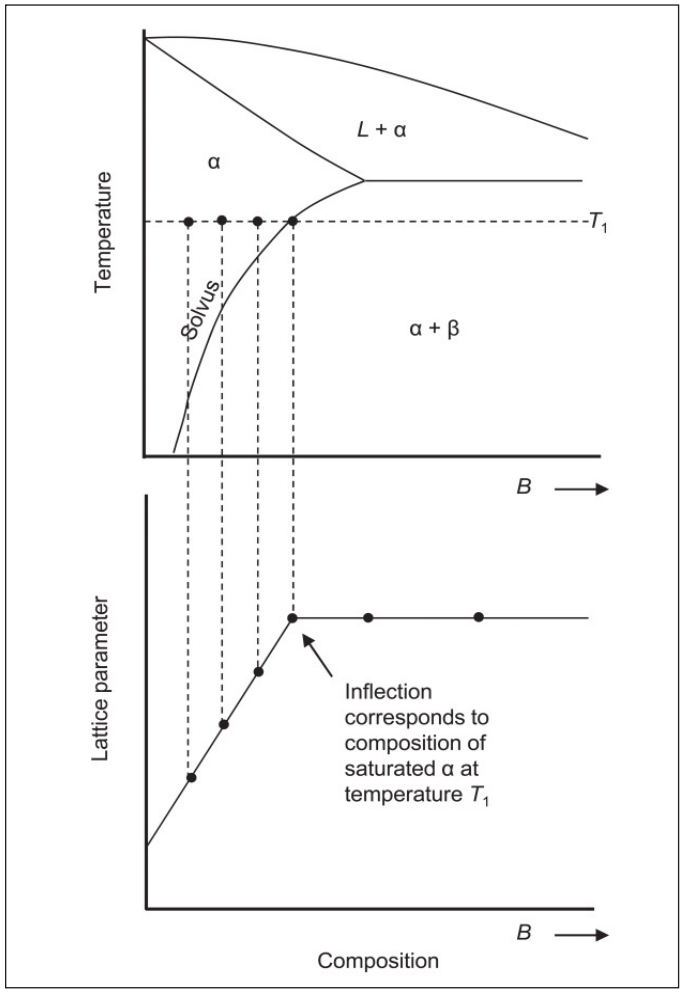

Fig.7: *Method to get the solvus points of a phase diagram through XRD [41]*

The thermodynamic activity of a component can be determined by a variety of techniques, depending on the nature of the constituent components. Measurement of vapour pressure, gas equilibration, thermogravimetric analysis and emf measurements are generally used for the determination of thermodyanamic activity of the constituents of an alloy. The measurement of vapour pressure itself can be accomplished in a variety of ways, for eg. by transpiration techniques, gas equilibration, isopiestic techniques, Knudsen effusion techniques and boiling point method. The basic principles, details of construction of the apparatus, experimental procedure, precautions as well as the merits and demerits of these techniques are discussed in detail in Refs. [37-40]. Thermogravimetry has been used in conjuction with transpiration and Knudsen effusion [40]. Knudsen effusion coupled with mass spectrometry is one of the powerful techniques for the determination of vapour pressures and has the advantage of providing in-situ analysis of the species present in the vapour state [37]. Measurement of thermodyanamic activity using galvanic cells constructed with either a liquid (molten salts / molten metals) or a solid electrolyte are well known [41,42].

Variation of the thermodynamic activity in the system U-C [43] is depicted in Fig.6. These experiments are designed to derive data on the thermodynamic activity as a function of temperature and composition rather than information on phase boundaries. Phase boundaries can also be recognized from calorimetric data obtained for alloys with varying compositions [37].

3.2.4 Methods based on X-ray diffraction

Methods based on X-ray diffraction (XRD) are primarily used for studying solid-solid equilibria. The method of lattice parameters involves synthesizing a series of alloys with different compositions, quenching them after annealing at a desired temperature [31,33,44], and measuring the lattice parameters of these specimens. In a binary alloy (under isothermal isobaric conditions) the lattice spacing would continuously vary with composition in a single phase region while it would remain constant in a two phase region. At the phase boundary a sharp change in the lattice parameter would be observed. Thus when the lattice parameters of the alloys are plotted against composition, the point at which a sharp change in the lattice parameter is observed, would correspond to the phase boundary. By repeating this experiment at other temperatures, the entire phase boundary could be constructed.

In yet another method the lattice parameter measurements are made on samples of an alloy of a known gross composition, annealed at successively

higher temperatures [13,15,29]. A method of determining the solvus points of a phase diagram is highlighted in Fig. 7 [45]. In place of metallography, XRD is used for identifying the constituent phases. This procedure is generally used for finding out the solidus temperature. Alloys quenched from below the solidus would have a constant lattice parameter. However, an alloy with the same composition, but quenched from above the solidus will be biphasic comprising of a chilled liquid and a solid with a composition corresponding to the solidus. The lattice parameter of this solid will vary accordingly. From the knowledge of the variation of the lattice spacing with composition, the solidus composition could be identified. Thus using multiple samples of an alloy with a fixed composition the solidus curve can be constructed. High temperature XRD is an attractive alternative for the above methods [15], provided the molten alloy does not react with the container. This in-situ diffraction at high temperatures could be used for alloys that undergo decomposition during quenching.

3.4 The segregation method

When steep liquidus curves are encountered it is often difficult to determine the same by thermal halts and differential thermal analysis [15]. In such cases the segregation method can be used for the determination of such liquidus. In this method the liquid alloy is heated either in an inert crucible along with the solute or in a crucible made out of the solute metal itself and it could be of great value when (i) the solid-liquid mixture contains relatively large quantities of the liquid and (ii) the solid has a higher density than that of the liquid. Under such conditions the liquid could be extracted and chemically assayed. If the solid settles at the bottom of the crucible that is holding the mixture then the liquid can be sampled easily. When the solid floats on the surface special devices are required for sampling the liquid without contamination [15]. This method is useful only for a simple binary eutectic system with the absence of any intermetallic compound. Careful sampling and accuracy of the chemical analysis are two important prerequisites for this method. Oxidation and contamination of the alloy has to be prevented by making proper choice of the atmosphere and crucible material.

Schram et al. [44] measured the solubilities of tantalum and tungsten in liquid uranium and Dennison et al. [46,47] measured the solubility of uranium in liquid rare-earth metals upto 2423 K by employing this method. Solubility of C, Cr, Mo, V, Nb, Ta, W and Rh in liquid plutonium up to 1273 K was measured by Bowersox and Leary [48,49] using calcium fluoride as a container. Kawabata et al. [50] employed this method for measuring the liquidus in the Ru-Sn system. Grain boundary diffusion and creep can often pose problems in these experiments. The accuracy of the measured values of the solubilities could vary from 5 to 15% [51].

Garg et al. [34] employed a method which was similar to the segregation method for the determination of liquidus. In addition these authors could obtain information on the composition of the intermetallic, and solid solubility using their procedure.

In the solubility measurement method employed by Garg et al. [34], a known amount of sample is charged into a weighed single crystal cup of the solute metal (which has a higher melting point) and placed inside a Knudsen effusion cell. The sample is then heated under vacuum in a suitable furnace to a desired temperature (above the melting point of the sample) and held for sufficient time. This equilibration of the solvent in the solute cup leaves the solute saturated with the former. Subsequently the sample is allowed to cool and the solidified solvent metal saturated with the solute is then selectively dissolved using a suitable reagent (usually HCl or HF) and removed from the cup leaving behind the inert solute as a residue. The single crystal cup is then cleaned, dried and weighed. From the weight loss of the cup and the initial amount of the solvent metal, the saturation solubility corresponding to the liquidus composition at the temperature of measurement is derived. Garg et al. [34] used Th, U, Hf and Zr as the solvents and Mo as the solute to determine the liquidus points.

It is necessary to use a single crystal cup to avoid grain boundary diffusion and creeping of the liquid metal. However, the use of single crystal cup does not preclude the possibility of lattice diffusion. Hence, the applicability of this method is limited to systems which satisfy the following prerequisites: (i) the solid solubility of the solute metal in the solvent should be low and (ii) the diffusion coefficient should be small such that the amount of the solvent metal diffused in the cup is negligible compared to the weight loss of the cup. In such an event, a very thin layer of the solid phase (a solid solution or an intermetallic compund) would be formed at the inner surface of the cup, establishing a pseudo-equilibrium condition. Garg et al. [34] observed the presence of an intermetallic compound at the surface of the single crystal cup. These authors also showed that the solid solubility as well as the composition of the intermetallic compound could be obtained by analyzing the single crystal cup using EPMA.

3.5 Methods based on change in emissivity

3.5.1 Williams method

This method exploits the change in the emissivity at the surface of a metallic specimen brought about by the formation of a liquid during liquefaction. This method was originally suggested by Pirani et al. [51] and was further developed by Williams [52]. In this method the specimen (an alloy of known composition) is shaped in the form of a neck down bar, having a blind hole drilled into its center and normal to its length. This bar is then heated resistively by holding it between two electrodes. The blind hole (which serves as a black-body hole) is observed using an optical pyrometer. The thickness of the specimen is the least at the bottom of the hole, and maximum heating takes place at this portion. The solidus temperature is obtained by determining the temperature at which the black-body condition at the bottom of the hole is disrupted and a black spot appears.

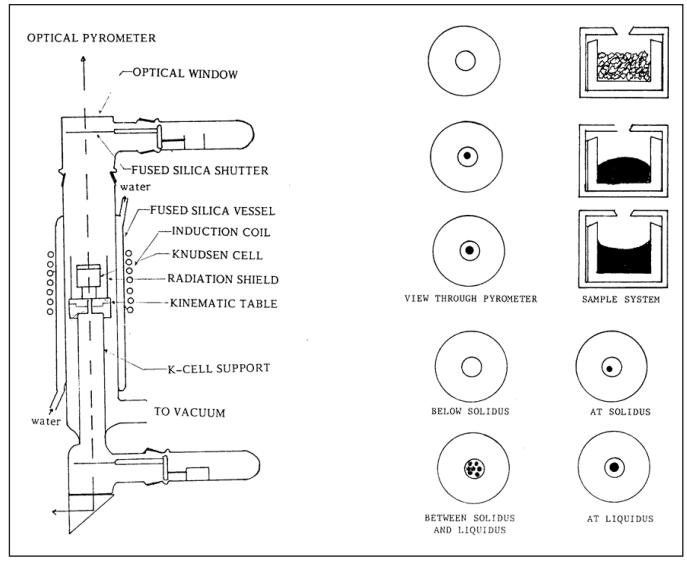

Fig.8: *(a) Apparatus for spot measurements [42, 27], (b) Orifice images observed in the spot method [27]*

Table 3 Some physical properties of selected refractory materials and their stability towards carbon, slags and molten metals [74]

Material		Melting point (K)	Limits of use in oxidizing atmosphere (K)	Thermal shock resistance	Stability				
					Reducing atmosphere	In contact with			
						Carbon	Acid Slags	Basic slags	Molten Metals
Alumina	Al_2O_3	2323	2223	Good	Good	Fair	Good	Good	Good
Beryllia	BeO	2803	2673	Excellent	Excellent	Excellent	--	Fair	Good
Calcia	CaO	2873	2673	Fair	Poor	Poor	Poor	Fair	Fair
Magnesia	MgO	3123	2673	Fair	Poor	Good	Poor	Good	Fair
Silica (crystalline)	SiO_2	2003	1953	Poor upto 593 K Excellent above 593 K	--	--	--	--	--
Silica (vitreous)	SiO_2	--	--	Excellent	Fair	Good	Good	--	--
Thoria	ThO_2	3573	2773	Poor	Good	Fair	Poor	Good	Excellent
Zirconia (CSZ)	ZrO_2	2723 to 2873	2773	Fair	Good	Fair	Good	Poor	Good
Zirconia (YSZ)	ZrO_2	2873	--	--	--	--	--	--	--
Mullite	$3Al_2O_3.2SiO_2$	2103	2073	Fair	Fair	Fair	Good	Fair	Fair
Spinel	$MgO.\ Al_2O_3$	2413	2173	Poor	--	Fair	Fair	Good	--
Zircon	$ZrO_2.SiO_2$	2693	2143	Good	Fair	Fair	Good	Poor	Good
Boron Nitride	BN	3273	--	--	--	--	--	--	--
Aluminium nitride	AlN	2273	--	--	--	--	--	--	--

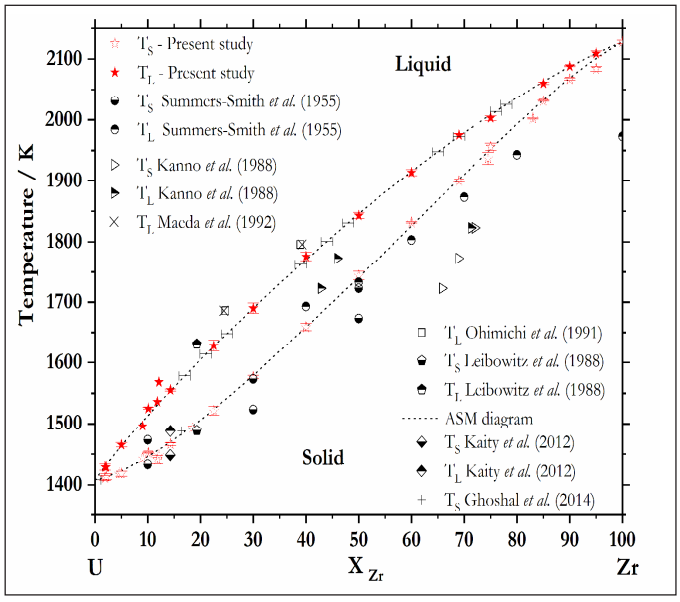

Fig.9: Experimentally measured solidus and liquidus of U-Zr by the spot technique [69]

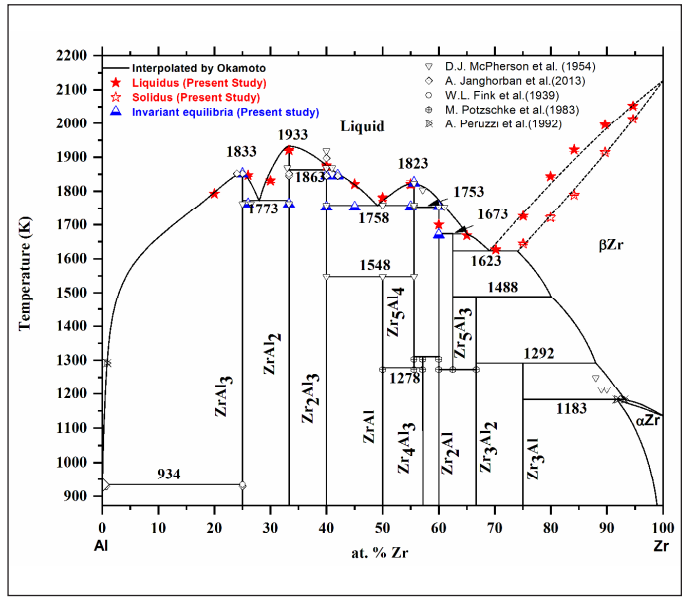

Fig. 11:Experimentally measured solidus and liquidus of Zr-Al by the spot technique [72]

The approximate liquidus temperature can also be determined using this method [28]. To accomplish this, the surface temperature of the specimen is calibrated against the black-body temperature by a series of measurements made below the solidus temperature. Subsequently, the specimen is heated above its solidus. The temperature at which the continuity of the electric circuit is lost due to melting of the central portion is taken to be the liquidus temperature, after making appropriate corrections for the emissivity.

Though this method is simple, it fails to provide an accurate estimate of the liquidus when the alloy sample collapses due to the poor mechanical strength of the solid-liquid mixture even before complete melting had taken place. Fabrication of the specimen into a neck down bar, difficulties encountered in accurate temperature control and the presence of large thermal gradients limit the utility of this method.

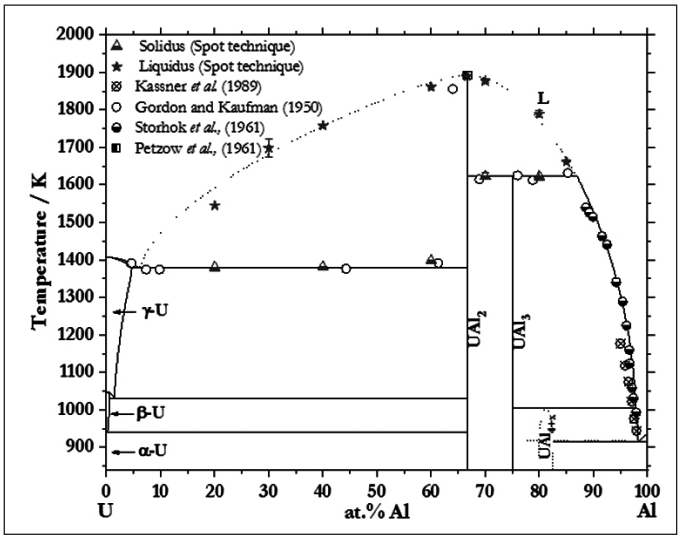

Fig.10: Experimentally measured solidus and liquidus of U-Al by the spot technique [70]

3.5.2 The spot technique

Ackermann and Raugh [53] made some interesting observations during Knudsen-cell experiments, which led to a technique called the "spot technique". Subsequently Ackerman et al. [54-56], Das and Chandrasekaraiah [57] Chandrasekaraiah and Das [58], Das [59], Garg [29], Garg et al. [34,60-64] and Bhatt et al. [65] used this method for the determination of phase diagrams. The spot method makes use of the mirror effect of the molten phase of the sample [66]. A small amount of sample, usually of the order of 1 g of known composition is placed in an inert cup. This cup is centered inside a Knudsen cell and heated under high vacuum. The orifice of the Knudsen cell is viewed through a pyrometer. As long as the sample remains solid, the Knudsen orifice approximates a black body and appears as an uniformly lit bright disc [66] and the temperature measured under such conditions would correspond to its brightness temperature. However, at the solidus temperature when a liquid phase begins to appear, a thin film of the liquid is formed on the surface of the sample. The orifice of the Knudsen cell exhibits a dual behaviour [34] when a reflecting mirror surface is present. It is an incandescent object with respect to the pyrometer as the latter receives maximum radiation from

Table 4 Maximum temperature of compatibility (K) between refractory materials and the volatility of some selected refractories [74]

	C	W	Mo	ThO_2	ZrO_2	MgO	BeO
BeO	2573	2273	2173	2373	2173	2073	--
MgO	2073	2273	1873	2473	2273	--	2073
ZrO_2	1873	1873	2473	2473	-	2273	2173
ThO_2	2273	2473	2173	--	2473	2473	2373

Material	Temperature of vapourization (K)	Material	Temperature of volatility (K) at 3.5×10^{-4} torr
BeO	2673	ThO_2	> 2573
MgO	2173	ZrO_2	> 2573
CeO_2	2148	BeO	2373
SiO_2	2273	MgO	1873
Al_2O_3	2023		
CaO	1973		
SrO	1873		

it. However, for the liquid mirror it is a perfect black object since the surface receives radiation from all directions within the effusion cell except from the orifice. Hence the reflected image of the orifice appears as a black spot when observed through the pyrometer. The temperature at which this dark spot is sighted first, corresponds to the solidus temperature of the alloy under investigation. On further heating several dark spots appear. Garg et al. [34] refer to this as a broken mirror image. When the melting is complete all the dark spots coalesce suddenly into a single large spot. This temperature corresponds to the liquidus. A schematic diagram of the experimental assembly used in a spot experiment is given in Fig. 8. In order to observe the spot effect the cup has to be centrally located in the Knudsen cell and sufficient quantity of the sample should be taken. It is also necessary to use a non-contact mode of heating (electron bombardment or radiofrequency (RF) induction) in order to observe this effect.

Garg et al. [34] showed that the melting points of various metals viz. zirconium, hafnium, thorium and uranium taken in suitable cups could be determined within an accuracy of 5 K. Das and Chadrasekaraiah [57], Chadrasekaraiah et al. [58], and Das [59] examined the accuracy and sensitivity of the spot technique. These authors reported that the melting points of pure copper and platinum could be measured within an accuracy of ±0.2 and ±1.1 K, respectively. Solidus and liquidus boundaries in several binaries have been determined using this technique [54-65].

This technique is convenient for determining the high temperature solid-liquid equilibria in alloys involving refractory metals and is amenable for glove box adaptation. In addition, this method has the additional advantages of in-situ alloying and small sample size. At temperatures below incandescence (< 1073 K), however the spot effect cannot be observed. Yet another disadvantage of this technique is that the spot effect cannot be observed if the sample is heated resistively at high temperatures.

Spot technique can only measure the solidus and liquidus temperatures above 1273 K. This limitation was overcome by a novel idea of illuminating the K-Cell with an appropriate light source and the solidus-liquidus temperatures could be measured below 1273 K till 298 K. This method is called as "illuminated spot technique" [67]. Details of construction and validation of the equipment are given in the ref [67]. By using twin K-Cell cavities, DTA of the sample and reference were measured in addition to the illuminated spot technique. This unique spot-DTA technique can measure the melting of pure metals & alloys by DTA as well as spot method simultaneously [67] at temperatures below incandescence. By using the spot technique, the solidus and liquidus of Cu-Ni [68], U-Zr [69], U-Al [70], U-Sn [71], Ru-Sn [36], Zr-Sn, Fe-Zr and Zr-Al [72] were also measured in the author's laboratory. Data on U-Zr and U-Al are the first of their kind wherein alloys spanning over the entire range of composition were studied by a single technique. Figs. 9-11 show the partial phase diagrams of U-Zr, U-Al and Zr-Al with values measured by the spot technique in corporated. The uncertainty in the measurement is ±3 K (max.). These recent developments [67-72] helped obtain optical images and supported videographic recording of the spot effect for the first time.

3.5.3 The Laser heating method

Recently Manara et al. [73] had developed a container less method for the determination of melting transitions in refractory materials. In this method the specimen itself acts as a container, and it is heated by a high power laser beam. The onset of melting is identified by a laser reflectometer and the temperature is measured with the help of high speed pyrometer. With the help of this set up, these authors re-investigated the system UO_2-PuO_2 and modified the existing solidus liquidusequilibria in this pseudobinary.

3.6 Containment of molten liquid alloys at high temperature

It is evident from the discussions in the previous sections that the chemical compatibility of the molten specimen is a matter of serious concern in thermodynamic measurements made at high temperatures (> 1273 K). Hence the choice of a suitable container is often a crucial factor in such experiments. Refractory metals as well as ceramics (oxides and non-oxides) are often used as containers in such high temperature experiments. Materials that are of relevance to this application are discussed below.

In general, the material to be used as a container in high temperature experiments should possess good thermal shock resistance, good thermal conductivity, good chemical stability in presence of reactive gases (oxygen / halogens), low vapour pressure and should be chemically compatible with the molten specimen to be used. In addition, surface diffusion and creeping of the molten metal should be absent. Among the criteria considered, resistance to grain boundary attack is another important factor when metallic crucibles are considered for containing liquid metals. Interaction with impurities (albeit trace) segregated at thegrain boundaries of the crucible material can lead to liquid metal penetration. Generally elements belonging to groups VA and VIA in the periodic table, are refractory (high melting point) owing to their electronic structure. The low vapour pressures of W, Ta and Re is one of the important factors that make them suitable for high temperature applications [74]. Os, Re, and Mo exhibit high rates of oxidation and form oxides that melt at relatively lower temperatures.Nb, Ta and W form oxide layers that are not protective. Cr is the only refractory metal that forms a tight oxide layer which prevents further oxidation. W, Ta and Mo are best suited for applications where the partial pressure of oxygen in the ambience is insignificantly low. All the three metals are expensive, possess high density and are not resistant to oxidation.

Graphite with high density is suitable for many high temperature applications. Pyrolytic graphite is less reactive and resistant to oxidation. However, most metals pick up carbon from the graphite container in the molten state.

Owing to their thermodynamic stability, the oxides of alkaline earths serve as inert containers for molten metals. Selected physical properties of some of the important oxide ceramics are given in Table 3. Reaction or attack of these ceramics are governed by physical factors as well as thermodynamic properties. The compatibility between some high temperature materials are indicated in Table 4 along with their approximate temperature of volatilization.

Among the binary oxides, thoria, beryllia and zirconia are chemically inert and have low vapour pressure. In comparison with other oxide ceramics beryllia is outstanding in its thermal conductivity, while the lowest level of conductivity is for zirconia and hafnia. Beryllia has excellent thermal stability and is resistant to reduction by carbon and has a high thermal conductivity and uniform thermal expansion. However high cost and chemical toxicity limit the use of this oxide [74]. Thorium oxide has the highest melting point among binary oxides but it has poor thermal shock resistance, expensive and radioactive. Oxide refractories are formed by pressing, tamping and slip casting.

The author has used custom made crucibles out of yttria, thoria and hafnia in the experiments involving highly oxyphyllic uranium bearing alloys.

4. Conclusions

The determination of temperatures of phase transitions that involve liquids is rather tedious. However, the same could be overcome by innovative experiments, viz., the spot method and the laser heating technique. Often the ingenuity of the experimenter has always rendered this area of research very interesting and challenging.

References

1. U.R. Kattner, J. of Metals, 49(12) (1997) 14.
2. A.D. Pelton in: Physical Metallurgy, Part IV Ed. Vol. 1, R.W. Cahn and P. Hassen, 1996, p 525.
3. A.D. Pelton and W.T. Thompson in: Progress in Solid State Chemistry, Vol. 10, Part 3, p. 119.
4. A.D. Pelton and H. Schmalzreid, Met. Trans. 4 (1973) 1395.
5. M. Hansen, Constitution of Binary Alloys, 2nd Ed., McGraw-Hill, New York, 1965.
6. W.G. Moffatt, Handbook of Binary Alloys Phase Diagrams (and supplements), Genium Publishing Corp. Schenectady, New York, 1978-1992.
7. R. Hultgren, R.L. Orr, P.D. Anderson, K.E. Kelly and D.D. Wagman, Selected Values of the Thermodynamic Properties of the Elements and Binary Alloys, Vol. 1, 2 and 3, ASM Metals Park, OH, 1973.

8. N.V. Ageev, Phase Diagrams of Metallic Systems, Vol. 1-22, Academy of Sciences of USSR, Moscow, 1959-1978.
9. O. Kubaschewski, Iron Binray Phase Diagrams, Springer-Verlag, New York, 1982.
10. F.A. Shunk, Constitution of Binary Alloys, Second Supplement, McGraw-Hill, New York, 1969.
11. T.B. Massalski, P.R. Subramanian, H.Okomoto and L. Kacprzak, editors, Binary Alloy Phase Diagrams, American Society for Metals International, Metals Park, OH, 1990.
12. H. Okamato, Desk Handbook: Phase Diagrams for Binary Alloys, ASM, Metals Park, Ohio, 2000.
13. R.A. Buckley, in: Techniques of Metals Research, R.A. Rapp, editor, Interscience, New York, Vol. IV, part I, p. 425.
14. J.B. Mac Chasney and P.E. Rosenberg in : Phase diagrams – Materials Science and Technology, Vol. 1, Ch. 3, A.M. Alper, editor, Academic Press, New York.
15. G.V. Raynor, Physical metallurgy, 2nd Ed., R.W. Cahn, editor, North Holland Publishing Company, Amsterdam, 1970, p. 309.
16. W.J. Hume-Rothery, J.W. Christian and W.B. Pearson, Metallurgical Equilibrium Diagrams, Institute of Physics, London, 1952.
17. A. Prince, Alloy Phase Equilibria, Elsevier Publishing Company, Amsterdam, 1966.
18. J.C. Zhao, editor Methods for phase diagram determination, Elsevier 2011.
19. Yasuda, Y. Tamura, T. Nagira, I. Ohnaka, Y. Yoshihiko, A. Inoue, Nucleation and Growth in Undercooled Melts of Bulk-Metallic Forming $Zr_{60}Ni_{25}Al_{15}$ Alloy, Materials Transactions, 12 (2005) 2762-2767.
20. G. Hohne, W. Hemminger, H.-J. Flammersheim, Differential Scanning Calorimetry, Springer, 1995, Berlin.
21. Recent Advances, Techniques and Applications, Edited by Michael E. Brown, Patrick K. Gallagher, Volume 5, Pages 1-755 (2008)
22. M.E. Brown in: Handbook of Thermal Analysis and Calorimetry, Vol. 1, Principles and Practice, series editor, P.K. Gallagher, Elsevier, 1998, Amsterdam.
23. M.E. Brown, Introduction to Thermal Analysis: Techniques and Applications, Chapman Hall, New York, 1988.
24. J.W. Dodd, K.H. Tonge, Thermal Methods: Analytical Chemistry by Open Learning, Wiley, Chichester, 1987.
25. W. Hemminger, G.Hohne: Calorimetry – Fundamentals and Practice, VerlagChemie, Weinheim, 1984.
26. K.D. Maglic, A. Cezailiyan, V.E. Peletzky editors, Compendium of Thermophysical Property Measurement Methods, Vol. 1, Survey of Measurement Techniques, Plenum, New York, 1984.
27. M.I. Pope and M.D. Judd, Differential Tehrmal Analysis: A Guide to the Technique and its Applications, Heydon, London, 1997.
28. D.S. Evans and A. Prince, Metal Science 12 (1978) 600.
29. S.P. Garg, Ph.D. thesis, Bombay University, Bombay, India (1980).
30. J.I. Goldstein, D.E. Newbury, P. Echlin, D.C. Joy, A.D. Romig Jr., C.E. Lyman, C. Fiori and E. Lifshin, Scanning Electron Microscopy and X-ray Micro Analysis, 2nd Ed., Plenum Press, New York, 1992.
31. C. Sari, F. Vernaza and W. Muller J. Less Common Metals, 92 (1983) 301.
32. V.D. Scott, Quantitative Electron-probe Microanalysis, Ellis Horwood, New York,1995
33. S.J.B. ,Cambridge University Press, UK, 1993, https://doi.org/10.1002/adma.19930051219.
34. S.P. Garg, Y.J. Bhatt and R. Venakatasubramani, Mater. Sci. Forum, Vol. 3, Trans Tech Publications Ltd., Switzerland, 1985, p. 419.
35. http://www.benbest.com/cryonics/lessons.html, accessed on October, 29, 2019
36. K. Ananthasivan, I. Kaliappan, P. R. V. Rao, C. Sudha, and A. L. E. Terrance, A contribution to the Ru - Sn system, J. Nucl. Mater. 305 (2002) 97-105
37. O. Kubaschwski, E.L. Evans and C.B. Alcock, Metallurgical Thermochemistry, Pergamon Press, N.Y., 1967.
38. R.A. Rapp and D.A. Shores, in: Physico-chemical Measurements in Metals Research, Part 2, R.A. Rapp, editors, Interscience Publishers, John Wiley, N.Y., 1970.
39. P. Gordon, Principles of Phase Diagrams in Materials Systems, McGraw-Hill, N.Y. 1968.
40. Y.K. Rao, in Phase Diagrams, Vol. I, A.M. Alper, editor, Academic Press, N.Y. 1970.
41. C.B. Alcock and P. Grieveson, J. Inst. Metals 93 (1961) 304.
42. Z. Moser, in : Calculation of Phase Diagrams and Thermochemistry of Alloy Phases, Y.A. Chang and J.F. Smith, editors, Conf. Proc. Met. Soc., AIME, Warrendale, PA 1979, 242.
43. Hj. Matzke, Science of Advanced LMFBR Fuels, Elsevier Science Publishers B.V., Amsterdam, 1986.
44. C.H. Schram, P. Gordon and A.R. Kaufman, Trans. AIME, 188 (1950) 195.
45. F.C. Campbell, editor, Phase Diagrams – Understanding the Basics, ASM International 2012.
46. D.H. Dennison, M.J. Tschetter and K.A. Gschneidner, Jr., J. Less Common Metals, 10 (1966) 108.
47. D.H. Dennison, M.J. Tschetter and K.A. Gschneidner, Jr., J. Less Common Metals, 11 (1966) 423.
48. D.F. Browersox and J.A. Leary, J. Nucl .Mater. 21 (1967) 219.
49. D.F. Browersox and J.A. Leary, J. Nucl .Mater. 27 (1968) 181.
50. R. Kawabata, M. Myo-Chin and M. Iwase, Met. Trans. B 29 (1998) 577.
51. M. Pirani and H. Alterthurn, Electrochem. 29 (1923) 5 (cited from Ref. 41 p. 4.)
52. J.T. Williams, Trans. AIME 203 (1955) 345. (cited from Ref. 41 p. 4).
53. R.J. Ackermann and E.G. Rauh, J. Phys. Chem. 73 (1969) 769.
54. R.J. Ackermann and E.G. Rauh, High Temp. Sci. 4 (1972) 272.

55. R.J. Ackermann and E.G. Rauh, High Temp. Sci. 4 (1972) 496.
56. R.J. Ackermann, S.P. Garg and E.G. Rauh, J. Am. Ceram. Soc. 60 (1977) 341.
57. D. Das and M.S. Chandrasekaraiah, High Temp. Sci. 161 (1986) 21.
58. M.S. Chandrasekaraiah, D. Das and S.R. Dharwadkar, Z. Metalkde. 509 (1986) 77.
59. D. Das Ph.D. Thesis, Bombay University, Bombay, India, 1985.
60. S.P. Garg and R.J. Ackermann, Met. Trans. 8A (1977) 239.
61. S.P. Garg and R.J. Ackermann, J. Nucl. Mater. 64 (1977) 265.
62. S.P. Garg and R.J. Ackermann, Trans. IIM 32(1979) 62.
63. S.P. Garg and R.J. Ackermann, Scripta Met. 13 (1979) 611.
64. S.P. Garg and R.J. Ackermann, J. Nucl. Mater. 88 (1980) 309.
65. Y.J. Bhatt, R. Venkatramani, Y.S. Sayi and S.P. Garg, Metals Materials and Processes 2 (1) (1990) 49.
66. M.S. Chandrasekharaiah, J.L. Margrave and D. Das, in: J.F. Schooley, editor, Temperature – Its Measurement and Control in Science and Industry, Vol. 6, Part 1, American Institute of Physics, New York, 1992, p. 373.
67. K. Ananthasivan, I. Kaliappan, and P. R. V. Rao, Illuminated spot technique - a novel method for the determination of solid - liquid phase transition temperatures," J. Alloys. Compd. 352 (2003) 148-152 .
68. K. Ananthasivan, S. Balakrishnan, I. Kaliappan, S. Anthonysamy, R. Pankajavalli, and P. R. V. Rao, Determination of solidus and liquidus in the system Cu-Ni by the spot technique, J. Alloys. Compd. 468 (2009) 275-279.
69. S. Balakrishnan, K. Ananthasivan, and K. H. Kumar, Measurement of the solidus and liquidus in the U-Zr system by the spot-technique, J. Alloys. Comp. 689 (2016) 751-758.
70. S. Balakrishnan, K. Ananthasivan, and K. C. H. Kumar, Measurement of liquidus temperatures in the U-Al binary system, page 107-111, XIX Symposium and Workshop on Thermal Analysis (THERMANS - 2013), May 22-May 27, Bhabha Atomic Research Centre, Mumbai, India (2011)
71. K. Ananthasivan, Development of Methods and Materials for the Determination of Solid to Liquid Phase Transformation Temperatures in Alloys, Ph.D. thesis, Department of Chemistry, University of Madras, Tamil Nadu, India (2002)
72. B. Samanta, S. Balakrishnan, R. Pagoti, K. Ananthasivan, K. Joseph, and A. Dasgupta, Measurement of solidus and liquidus in the system Zr-Al (20-95 at.% Zr) by using the spot-technique, Thermochim. Acta 667 (2018) 132-139.
73. Dario Manara, Robert Böhler, Kostantinos Boboridis, Luca Capriotti, Andrea Quaini, Lelio Luzzi , Franck De Bruycker, Christine Guéneau, Nathalie Dupin, Rudy Konings The melting behaviour of oxide nuclear fuels: effects of the oxygen potential studied by laser heating, Procedia Chemistry 7 (2012) 505 – 512.
74. W. D. Kingery, H. K. Bowen and D. R. Uhlman, Introduction to Ceramics, 2nd Ed., Wiley, New York, U.S.A., 1970.

Dr. K. Ananthasivan, *Director, Reprocessing Group, IGCAR is from the 29th batch of BARC training school. He did M Sc (Engg.), Metallurgy from IISc, Bangalore, PhD from Madras University, Postdoctoral fellowship (Chemistry) in Purdue University, IN, USA. He is a senior professor and Chairman – Chemical Sciences Standing Committee of HomiBhabha National Institute. He is the recipient of prestigious HomiBhabha Science and Technology award in the year 2009 and DAE group achievement award in the year 2013. He has guided five numbers of PhD Scholars.*

Anomalies in temperature dependent heat capacity of uranium-rareearth-mixed oxide system

R. Venkata Krishnan[1], R. Babu[1], Abhiram Senapati[1], G. Jogeswararao[1], K. Ananthasivan[2]
1-Materials Chemistry and Metal Fuels Cycle Group, 2-Reprocessing Group, IGCAR, Kalpakkam
**Corresponding author E-mail: venky20005@gmail.com*

Abstract

Uranium-Rare earth mixed oxides $(U_{1-y}RE_y)O_{2-x}$ (RE = La, Gd, Nd) were prepared by citrate gel-combustion. The phase characterization and the determination of solid solubility were carrying out by using X-ray diffractometer. The samples were analyzed for the composition and other impurities. Heat capacity and enthalpy increment measurements were carried out by using DSC and drop calorimetry in the temperature range 298 – 800 K and 800 – 1800 K respectively. Anomalous increase in the heat capacity as a function of temperature is observed in the solid solutions as it was found in the case of pure UO_2. However, the onset temperature of heat capacity anomaly is much lower than that observed for pure UO_2. The phenomenon is attributed to the formation of Frenkel defect of oxygen. The enthalpy / activation energy of defect formation were determined by using the data on excess heat capacity. The relationship between the onset temperature of the heat capacity with the enthalpy of formation of defect and the lattice strain experienced in UO_2 on doping with rare earth cation is established.

Keywords: Heat capacity anomaly, DSC, uranium, rare earth, mixed oxides

1. Introduction

Uranium contributed to 11% of world's production of electricity which is around 2500 billion KWh per year [1]. The majority of the reactors in the world are thermal nuclear reactors which use natural uranium or ^{235}U enriched uranium as fuel. uranium – plutonium mixed oxides or carbides are used in fast reactors. The fission reaction in addition to the emission of large amounts of energy, neutrons, yields various fission products whose mass number range from 60 – 160 [2]. A typical fission product yields for the fission of ^{235}U and ^{239}Pu in fast neutron spectrum is shown in Table. 1

Table 1. Elemental fission product yields in fast neutron spectrum [2]

	Elemental yield (%)	
Chemical Group	**^{235}U**	**^{239}Pu**
Zr+Nb	29.8	20.4
Rare earths + Y	53.4	47.1
Ba+Sr	14.9	9.6
Mo	24.0	20.3
Ru+Tc+Rh+Pd	26.3	51.6
Cs+Rb	22.6	18.9
I + Te	1.2	7.0
Xe+Kr	25.1	24.8

The behaviour of the nuclear fuel in the reactor under irradiation is quite complex as it is exposed to severe thermal gradient and radiation. There are various processes involved in the fuel under irradiation include viz., (i) Physical (ii) Chemical (iii) Mechanical and (iv) Metallurgical [3]. To predict and model the fuel behaviour during irradiation large number of all the processes mentioned above which takes place simultaneously in a complex manner should be taken into account. The software model which incorporates all the contemporary data of the material properties, their mutual interactions and phenomena is a useful tool to design the fuel elements, safety analysis and cross-interpretation of the results obtained by the model with that of the experimental irradiation results. The computer model [3] comprise two categories viz., (i) thermal analysis and mechanical analysis. To model the thermal performance of the fuel the data pertaining to the following is important.

(i) The nature of fission product formed

(ii) Axial and radial redistribution of fission products under thermal gradient and vapour transport mechanism

(iii) Axial and radial redistribution of actinides

(iv) Redistribution of actinides

(v) Information pertaining to solid solution/compound formed due to fuel – fission product, fission product-fission product interactions under high temperature and at certain oxygen potential

(vi) Thermodynamic properties of the products formed due to the above mentioned interactions.

Experiments pertaining to thermophysical properties of UO_2 were carried out and have been thoroughly reviewed by large number of researchers worldwide [4-8]. Hiernaut et al. [8] reported a λ-phase transition at 2670 K in $UO_{2.00}$ and developed a model pertaining to variation of this transition temperature as a function of stoichiometry. Ronchi et al [9] delineated the contribution of various processes to the heat capacity as a function of temperature. Their findings are follows (i) harmonic lattice vibrations contribute majorly from 298 – 1000 K and can be approximated by Debye model (ii) Between 1000 – 1500 K additionally heat capacity increase arises from the anharmonicity of the lattice vibrations (iii) In the temperature region 1500 – 2670 the increase sudden rapid anomalous increase in the heat capacity is attributed to the formation of lattice defects especially from Frenkel defect. The values of heat capacity as a function of temperature reported by Fink et al [4] are reproduced in Fig. 1.

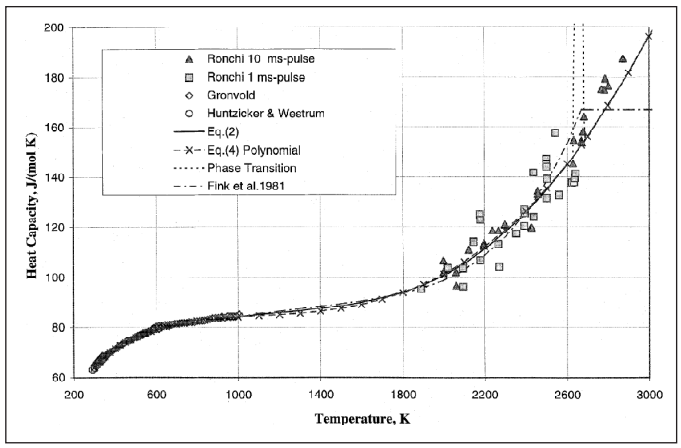

Fig. 1: *Heat capacity data of UO_2 assessment by Fink [4]*

High temperature heat capacity of the fuel under irradiation is one of the important properties for evaluating the fuel temperature profile during normal operation and the evaluation of fuel temperature under accident conditions. Uranium-plutonium mixed oxides are used as fast reactor fuels. Rare earth fission products (La to Gd) have significant fission yields on fast fission of ^{235}U, ^{238}U and ^{239}Pu [10]. These trivalent rare earth oxides form extensive solid solutions with UO_2 [11]. Therefore, the experimental determination of solid solubility of rare earths in UO_2 lattice and the high temperature heat capacity of uranium-rare earth mixed oxides are important to predict the fuel behavior during irradiation. Introduction of aliovalent (+3 oxidation state) cation into the U^{+4} lattice positions in UO_2 is expected to yield point defects and the concentration of these defect is also expected to increase with increase in temperature as seen in the case of UO_2. As in the case of UO_2 these point defects contribute to anomalous increase in the heat capacity with temperature. However, the onset temperature of the anomalous increase in the heat capacity will depend on the nature of cation, its concentration and the activation energy for the formation of defects. In the present article heat capacity data as a function of temperature of $(U_{1-y}, RE_y) O_{2\pm x}$ (RE= La, Gd, Nd) (y = 0.2, 0.4, 0.6, 0.8) is discussed [12 – 14].

2. Experimental

UO_2 of nuclear grade purity supplied by Nuclear Fuel Complex, Hyderabad and RE_2O_3 of 99.9% purity supplied by M/s. Indian Rare Earths were used for preparing the samples. Solid solutions of $(U_{1-y}\ Gd_y)\ O_{2-x}$ were prepared by combustion synthesis using citric acid as fuel. The procedure to obtain the sintered pellets from these combustion derived powders is described in our publication [13]. The characterization for the composition of U and RE in the sample were carried out by using High Pressure Liquid Chromatography (HPLC) technique and the characterization for impurities were carried out by using Inductively coupled plasma – Mass spectrometer (ICPMS, model number ELAN 250 of M/s. Perkn Helmer, Canada). Structural and micro-structural characterizations were carried out by using X-ray Diffractometer (XRD) (Philips-X'pert MPD® system) and Scanning Electron Microscopy (SEM) respectively. The heat capacity measurements were carried out by using Heat flux type Differential Scanning calorimeter (DSC, model: DSC821e of M/s.Mettler Toledo GmbH) in the temperature range 298 – 800 K. The enthalpy increment measurements were carried out by using inverse drop calorimeter (Model: MHTC-96 of M/s. Setaram) in the temperature range 600 – 1873 K. The DSC was calibrated for temperature, heat flow and heat flow rate. The procedure calibration and heat capacity / enthalpy increment measurements by using DSC and drop calorimeter are given in detail in our earlier publications [12, 15].

3. Results and discussions

3.1 Impurity analysis and solid solubility of rare earths in UO_2 lattice

The samples were subjected to analysis for metallic impurities and carbon by using ICP-MS (ELAN 250 of M/s. Sciex , Canada) and carbon analyzer (M/s. Eltra, Germany). The total impurities in all the solid solutions are less than 500 ppm and that of carbon is less than 100 ppm. The XRD patterns of $(U_{1-y}, RE_y) O_{2-x}$ (RE= La, Gd, Nd) (y = 0.2 - 0.8) is shown in Fig. 2 – 4 respectively. The solid

solubility of La, Gd and Nd were found to be at least 80% La, 50% Gd and 80% Nd. The results of solid solubility studies are in good agreement with that reported by Kleykamp [16] for La and Nd who reported it to be 81% and good agreement with that reported by Beals et al [17] who reported it to be 54% for Gd.

A typical SEM monograph of $(U_{1-y}, Nd_y)\ O_{2-x}$ (0.2, 0.4, 0.6, 0.8, 0.82, 0.84) is shown in Fig. 8 – 13 respectively.

As can be seen in these figures the solid solutions with y values up to 0.8 have uniform grain size in the range of 5 – 10 µm with well-defined grain boundaries whereas, the solid solutions having y value >0.8 (0.82 , 0.84 and 0.85) have flaky shaped particles whose grains are not properly formed. This may be attributed to the precipitation of second phase hexagonal Nd_2O_3 (HXN) which are uniformly distributed throughout the matrix of the major phase. The observation is in good agreement with the investigation by XRD, which shows the precipitation of second phase HXN for the solid solution with Nd content greater than 80%.

3.2 Heat capacity as a function of temperature

Heat capacity and the enthalpy increments were measured only for single phase $(U_{1-y}, RE_y)O_{2-x}$ (RE= La, Gd, Nd) solid solutions. Heat capacity values are measured by DSC in the temperature range 298 – 800 K. For higher temperatures data on enthalpy increments were used to compute the heat capacity. The combined data is used for

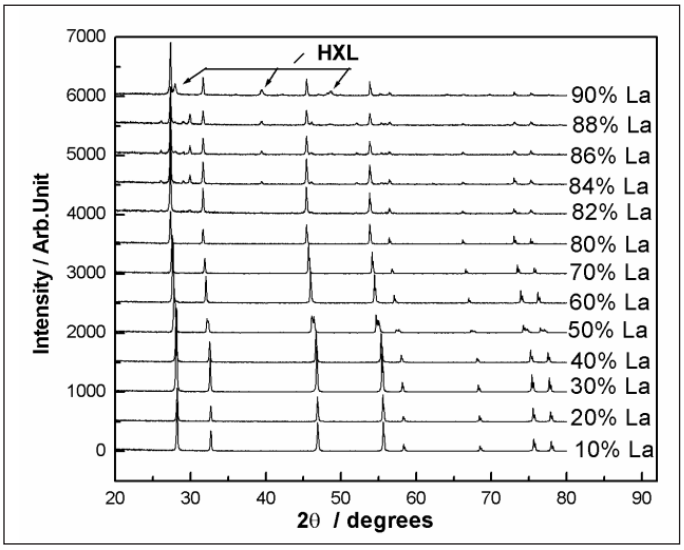

Fig. 2. Room temperature XRD patterns of $(U_{1-y}, La_y)\ O_{2-x}$ (HXL: Hexagonal Lanthana)

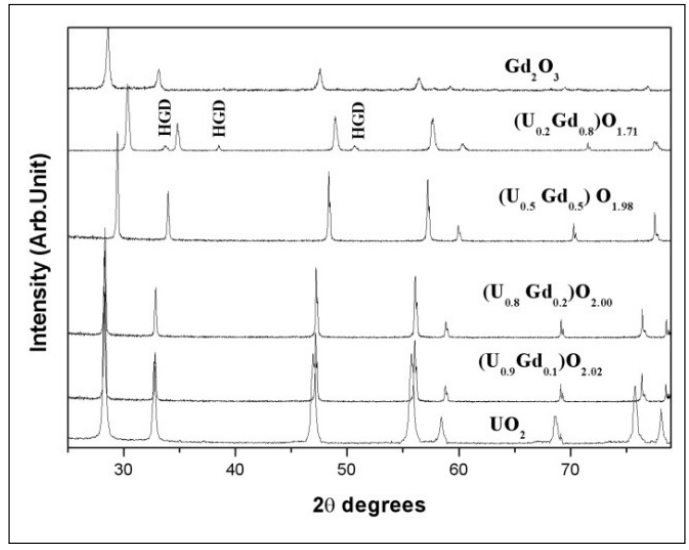

Fig. 3. Room temperature XRD patterns of $(U_{1-y}, Gd_y)\ O_{2-x}$ (HGD: Hexagonal Gadalonia)

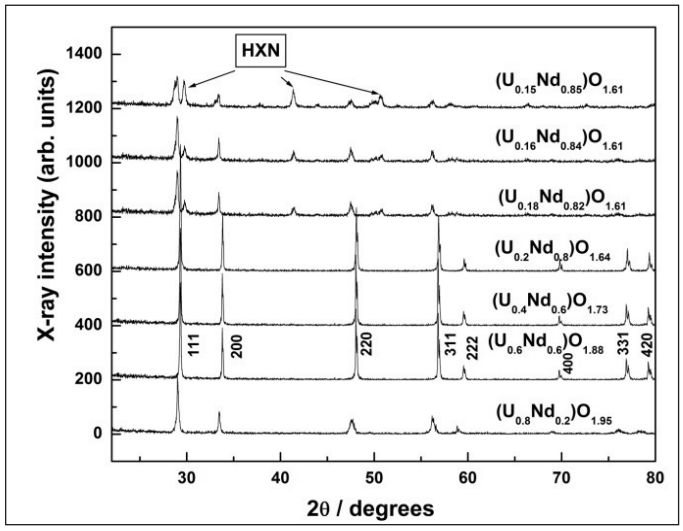

Fig. 4: Room temperature XRD patterns of $(U_{1-y}, Nd_y)\ O_{2-x}$ (HXN: Hexagonal Nd_2O_3)

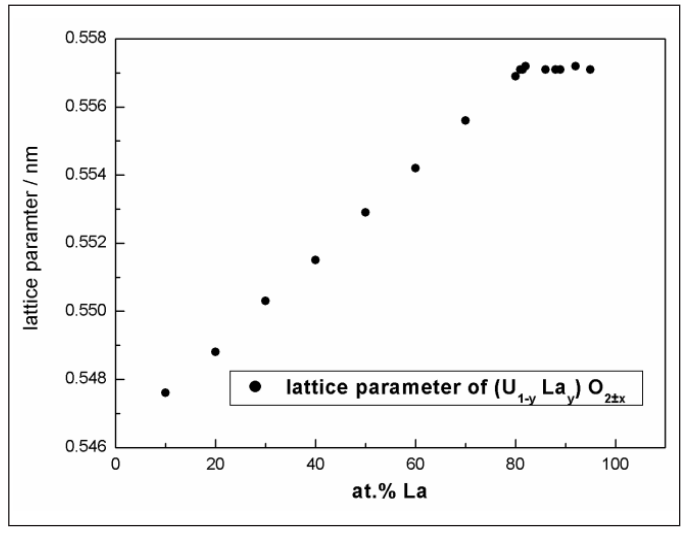

Fig. 5: Lattice parameter of $(U_{1-y}, La_y)\ O_{2-x}$ as a functionof La content

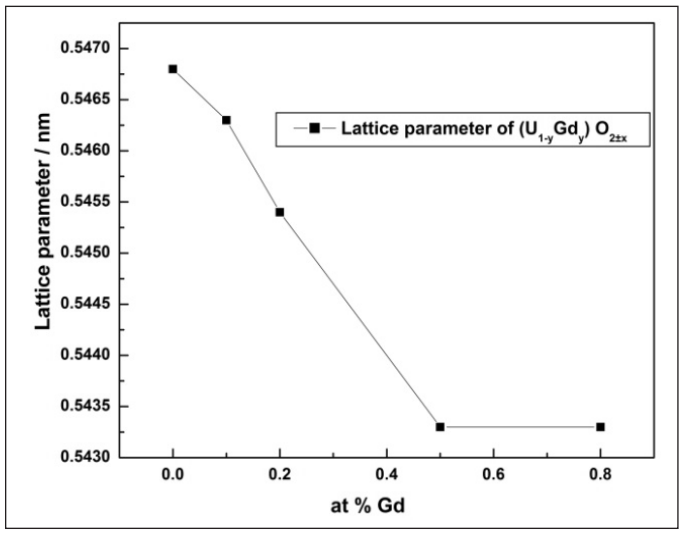

Fig. 6: Lattice parameter of $(U_{1-y}, Gd_y)\ O_{2\pm x}$ as a functionof La content

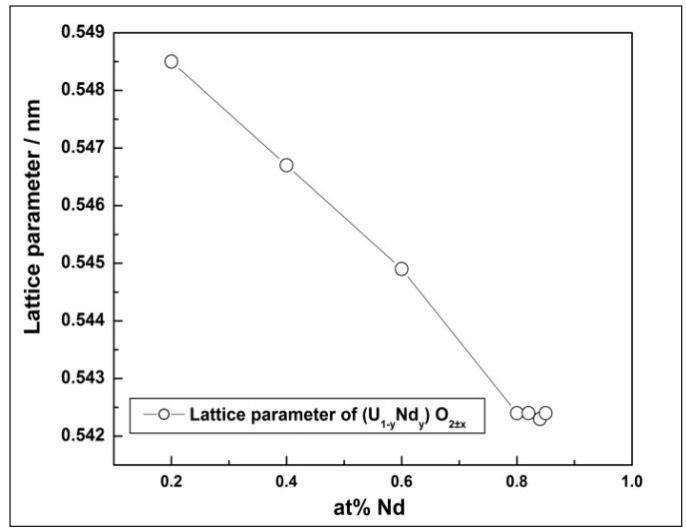

Fig. 7: Lattice parameter of $(U_{1-y}, Nd_y)\ O_{2\pm x}$ as a functionof La content

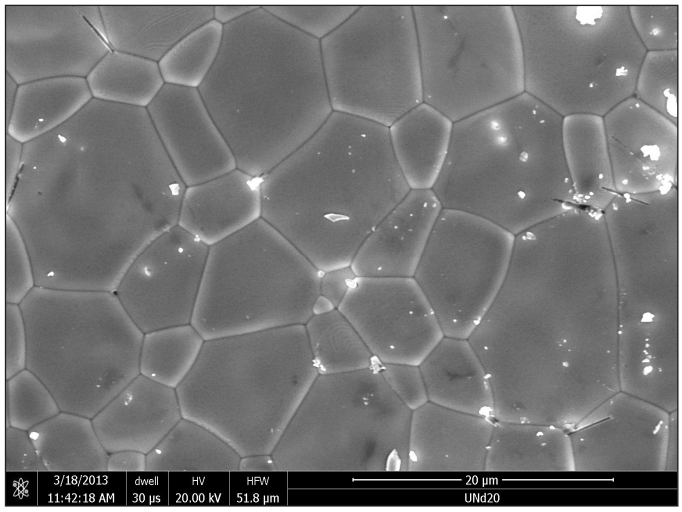

Fig. 8. SEM monograph of $(U_{0.8}, Nd_{0.2})O_{1.95}$

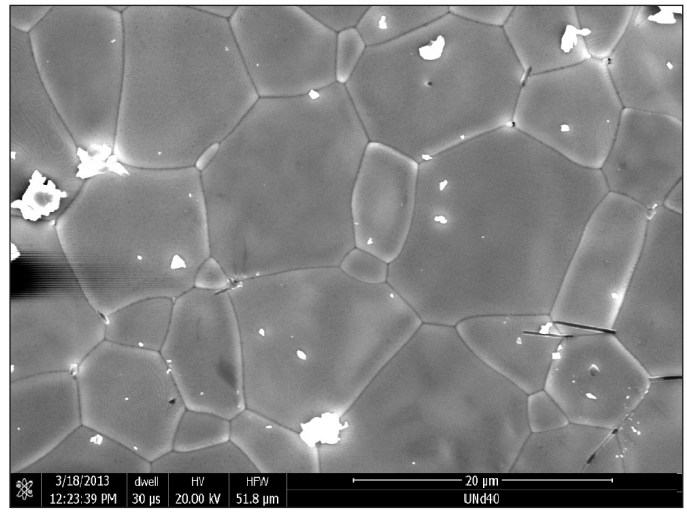

Fig. 9. SEM monograph of $(U_{0.6}, Nd_{0.4})O_{1.88}$

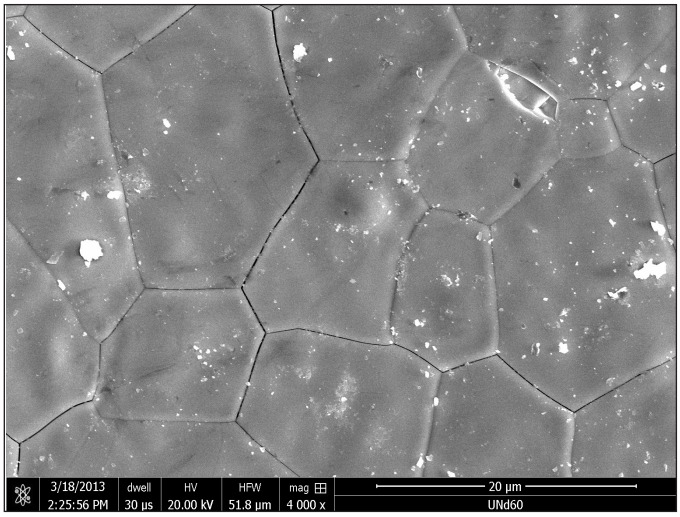

Fig. 10: *SEM monograph of $(U_{0.4}, Nd_{0.6})O_{1.73}$*

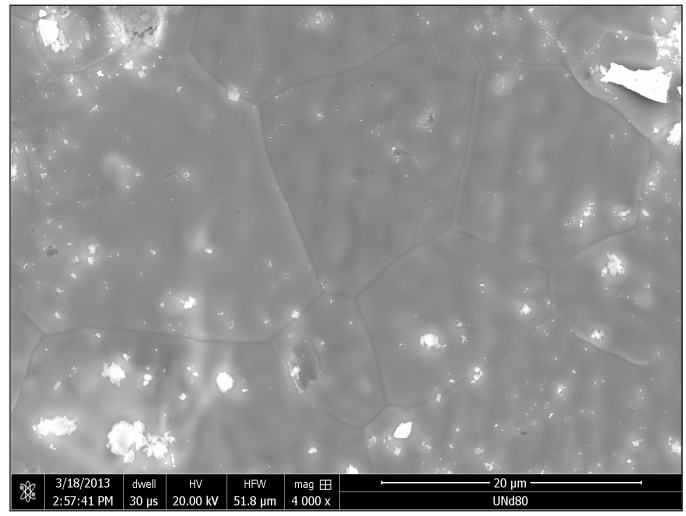

Fig. 11: *SEM monograph of $(U_{0.2}, Nd_{0.8})O_{1.63}$*

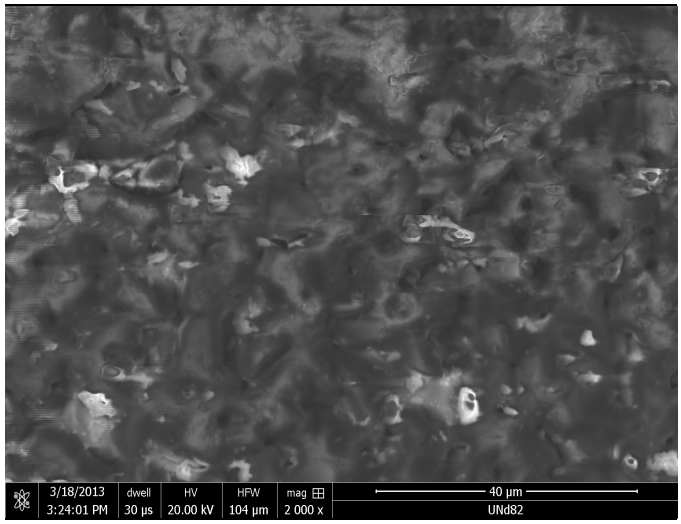

Fig. 12: *SEM monograph of* $(U_{0.18}, Nd_{0.82})O_{1.61}$

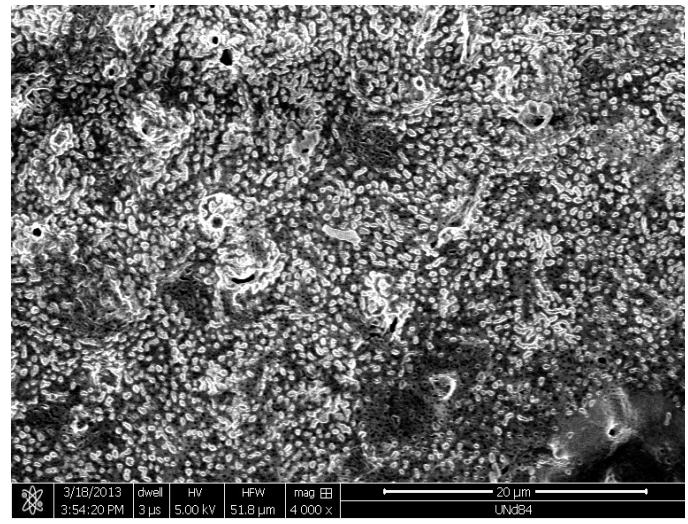

Fig. 13: *SEM monograph of* $(U_{0.16}, Nd_{0.84})O_{1.61}$

fitting the heat capacity as a function of temperature in the temperature range 298 – 1800 K. The heat capacity values as a function of temperature for $(U_{1-y}, RE_y)O_{2-x}$ (RE= La, Gd, Nd) solid solutions is shown in Fig. 14 – 16. As can be seen from the figures considerable anomalous increase in the heat capacity is observed for all the three solid solutions. However, the onset temperature of the anomalous increase in the heat capacity (T_{onset}) varies depending on the rare earth doped and its concentration. For example the T_{onset} of $(U_{0.9}, Gd_{0.1})O_{2-x}$ is in the range of 550 – 600 K whereas that for $(U_{0.8}, Gd_{0.2})O_{2\pm x}$ and $(U_{0.5}, Gd_{0.5})O_{2-x}$ it is in the range of 500 – 550 K. For $(U_{1-y}, RE_y)O_{2-x}$ (RE = La, Nd) T_{onset} is in the range of 1000 – 1200 K and 900 – 1100 K respectively. Also, such anomaly was not found for $(U_{0.8}, Nd_{0.2})O_{2-x}$. This phenomenon could be attributed to the predominant contribution from Frenkel pair oxygen defects as was observed by several other authors [18 – 24]. Matsui et al. [19, 20] measured the electrical conductivity of these $(U_{1-y}, RE_y)O_{2-x}$ (RE = Eu, La)and observed that the temperatures at which the slope of the conductivity curve changes is independent of the dopant and is close to the undoped UO_2. Also, the temperature at which the slope changes in the electrical conductivity curve did not coincide with the onset temperature of heat capacity anomaly. Therefore, the heat capacity anomaly is not due to the electronic contribution to heat capacity (formation of electron-hole pair). Arita et al. [22-23] suggested that doping of trivalent cations to UO_2 produces greater complexity of oxygen arrangements, which in turn induces the formation of oxygen defects resulting in the heat capacity anomaly.

Generally for any solid samples whose contribution to the heat capacity majorly from harmonic and unharmonic vibrations the heat capacity as a function of temperature generally follows the Debye function. In other words the values of the heat capacity will reach plateau over and above the Debye's temperature. For such samples the heat capacity as a function of temperature is fitted using the following polynomial

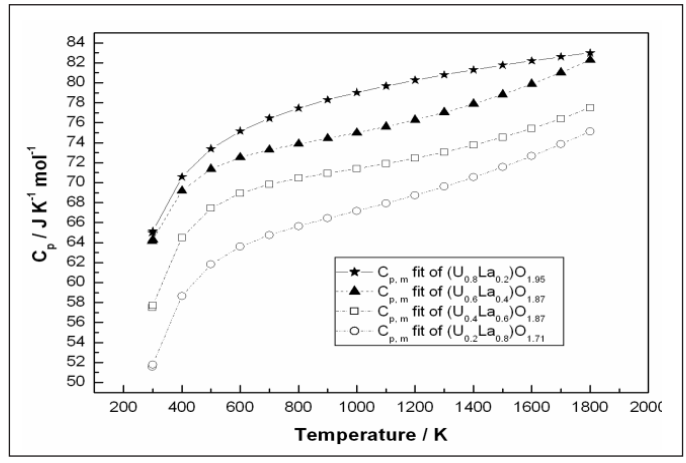

Fig. 14: *Heat capacity data of* $(U_{1-y}, La_y)O_{2-x}$ *as a function of temperature*

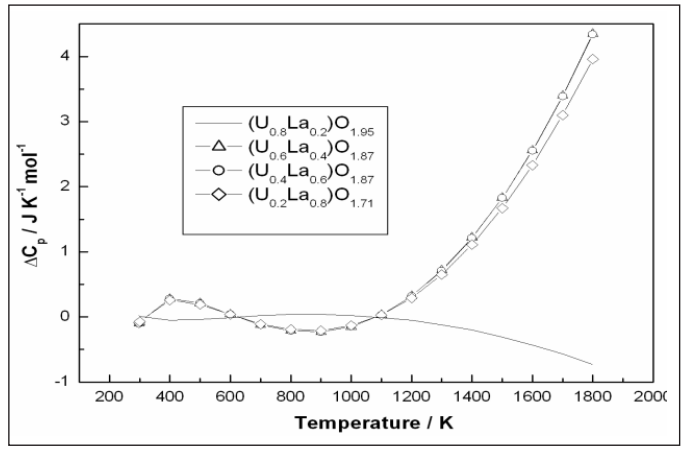

Fig. 15: *Difference between the extrapolated baseline heat capacity and the measured heat capacity of* $(U_{1-y}, La_y)O_{2-x}$

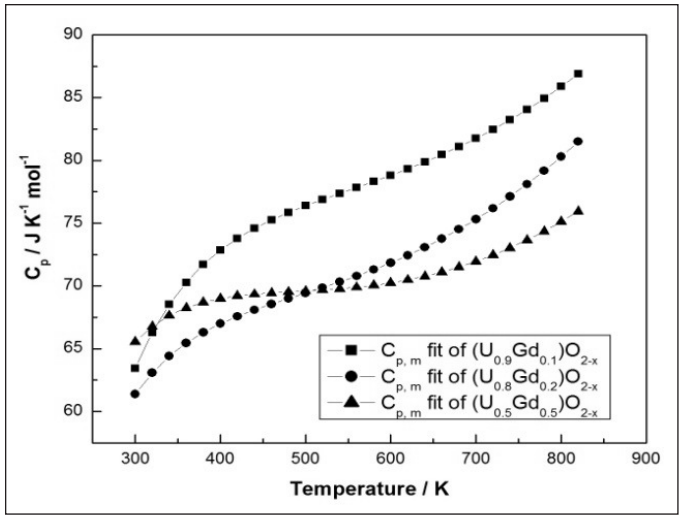

Fig. 16: *Heat capacity data of $(U_{1-y}, Gd_y)O_{2-x}$ as a function of temperature*

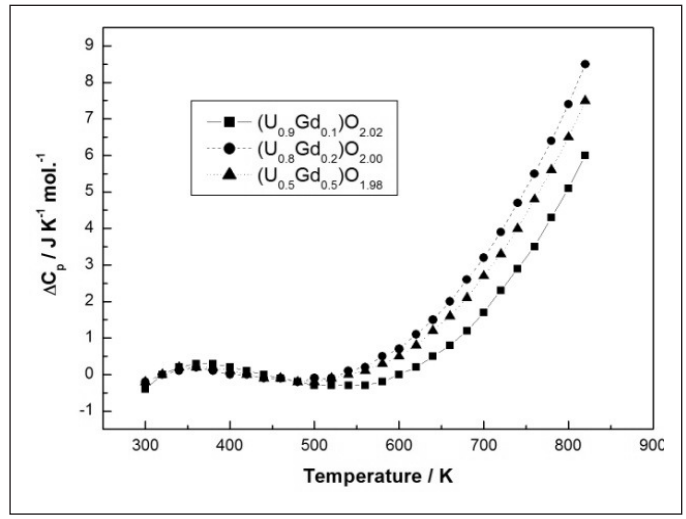

Fig. 17: *Difference between the extrapolated baseline heat capacity and the measured heat capacity of $(U_{1-y}, Gd_y)O_{2-x}$*

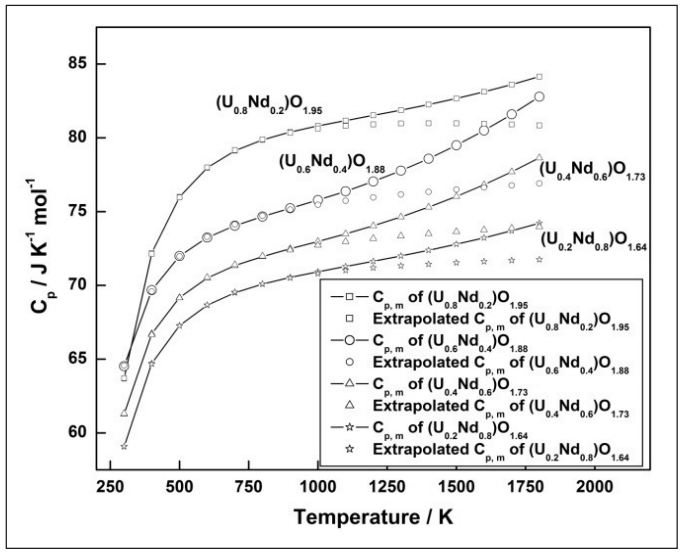

Fig. 18: *Heat capacity data of $(U_{1-y}, Nd_y)O_{2-x}$ as a function of temperature*

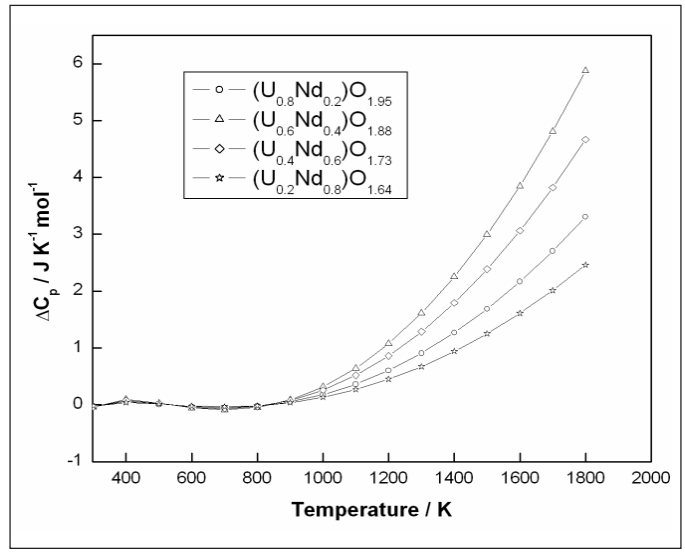

Fig. 19: *Difference between the extrapolated baseline heat capacity and the measured heat capacity of $(U_{1-y}, Nd_y)O_{2-x}$*

$$C_p = a + b\,T + c\,T^{-2} \quad (1)$$

When samples exhibit anomalous increase in the heat capacity at temperatures over and above the Debye's temperature the heat capacity as a function of temperature is fitted using the polynomial given below

$$C_p = a + b\,T + c\,T^{-2} + d\,T^{2} \quad (2)$$

Where a, b, c and d are the coefficient of the least square regression fit and "T" is temperature in Kelvin. To delineate the contribution to the heat capacity from the formation of Frenkel defect from that of the harmonic and unharmonic vibration the base line heat capacity is fit using equation (1) form room temperature to the T_{onset} whereas equation (2) is used to fit the measured heat capacity data for the entire temperature range. The base line heat capacity is then extended from T_{onset} to the final temperature. The heat capacity data fit by using equation (2) is then subtracted from the baseline heat capacity (ΔC_p) and termed as excess heat capacity. The temperature dependence of excess heat capacity of $(U_{1-y}, RE_y)O_{2-x}$ (RE= La, Gd, Nd) is shown in Fig. 17 – 19 respectively. The T_{onset} is the temperature at which there is sudden sharp increase in the values of ΔC_p. The T_{onset} vary depending on the nature of the rare earth dopant. The difference in the onset temperature of heat capacity anomaly was attributed to the difference in the enthalpy or activation energy for the formation of defects. If H_d is the enthalpy of defect formation, the number of defects n_d at any temperature T is given by

Table 2. Relationship between the T_{onset} and enthalpy of formation of defect

Solid solution	Enthalpy of formation of defects (eV)	T_{onset} (K)	Ionic radii of U^{4+} [25] (nm)	Ionic radii of RE^{3+} [25] nm	Difference in ionic radii (nm) $\lvert\Delta a\rvert$
$(U_{1-y}, La_y)O_{2\pm x}$	1.31 – 1.33	1000 - 1200	10.00	11.60	1.60
$(U_{1-y}, Gd_y)O_{2\pm x}$	0.57 – 0.81	500 - 600	10.00	10.53	0.53
$(U_{1-y}, Nd_y)O_{2\pm x}$	1.05 – 1.07	900 - 1100	10.00	11.09	1.09

$$n_d = n_0 \exp(-H_d / kT) \quad (3)$$

And the excess heat capacity (ΔC_p) is given by,

$$\Delta C_p = d/dT\,(n_d H_d) = (n_0 E_d^2 / kT^2) \exp(-H_d / kT) \quad (4)$$

Therefore, the plot of $\ln(T^2\Delta C_p)$ against 1/T is a straight line with a slope of $-H_d/k$. The plot of $\ln(T^2\Delta C_p)$ against 1/T for $(U_{1-y}\,RE_y)O_{2-x}$ (La, Gd, Nd) is shown in Fig. 20 – 22 respectively. The enthalpy of the formation of defects computed from the slopes of the curves in Fig. 20 – 22 is shown in Table. 2.

The difference in enthalpy of the defect formation could be explained in terms of difference in elastic strain experienced by the fluorite lattice of UO_2 due to doping of trivalent lanthanide. The elastic strain $\lvert\Delta a\rvert$ the lattice parameter change per mol% of trivalent dopant doped in UO_2. In other words it is depended on the difference in ionic radii between U^{+4} (8-coordination) and RE^{+3} (8-coordination). The value of $\lvert\Delta a\rvert$ is given in Table. 2. Explanations are available in the literature [26-28] on the differences in the ionic conductivities of the trivalent doped MO_2 fluorite solid-solutions, on the basis of the differences in the elastic strain. The ionic conductivity of the trivalent doped fluorite type oxides, such as UO_2, CeO_2, and ThO_2 where oxygen is the predominant mobile species is higher for solid solutions experiencing lower elastic strain $\lvert\Delta a\rvert$ on doping. The Frenkel defect pair of oxygen is formed more easily under the condition that makes oxygen ions more mobile [20] which in turn could be achieved by doping UO_2 resulting in low elastic strain $\lvert\Delta a\rvert$. In other words, the enthalpy of defect formation increases with increase in $\lvert\Delta a\rvert$ suggesting that the larger elastic strain suppresses the formation of Frenkel pair like defect of oxygen and thus, increases the enthalpy of defect formation. From the Table. 2 it is expected that the elastic strain should vary in the order La > Nd > Gd and therefore the enthalpy of the formation of defect also follows the same order. The onset temperature of heat capacity anomaly follows the reverse trend.

4. Summary

The solid solubility of $REO_{1.5}$ in UO_2 is in determined for RE = La, Gd and Nd. An anomalous increase in the heat capacity is observed in all these solid solutions. This phenomenon is attributed to the formation of Frenkel defect pair of oxygen. From the excess heat capacity data, the enthalpy for the formation of defect was estimated. The relationship between T_{onset}, enthalpy of formation of defect and lattice strain experienced on doping rare earth cation in UO_2 lattice have been established.

References

1. http://www.world-nuclear.org/information-library/nuclear-fuel-cycle/introduction/what-is-uranium-how-does-it-work.aspx
2. D.R. Olander, Fundamental Aspects of Nuclear Reactor Fuel Elements, National Technical Information service, US department of commerce, Springfield, Virginia, 1976
3. P. R. Roy, D.N. Sah, Pramana 24 (1985) 397
4. J. K. Fink, J. Nucl. Mater. 279 (2000) 1
5. J. K. Fink, M.G. Chasanov, L. Leibowitz, J. Nucl. Mater. 102 (1981) 17
6. J. H. Harding, D.G. Martin, P.E. Potter, Thermophysical and thermochemical properties of fast reactor materials, Harwell Laboratory UKAEA Report EUR 12402, 1989
7. T. Hutchings, J. Chem. Soc. Farady Trans. II 83 (1987) 1083
8. J. P. Hiernaut, G.J. Hyland, C.Ronchi, Int. J. Thermophy. 14 (1993) 259
9. C. Ronchi, G.J. Hyland, J. Alloys. Compds 214 (1994) 159
10. E.A.C. Crouch, "Fission –product yields from neutron-induced fission, Atomic data and nuclear data tables, 19 (5) (1977) Academic Press, New York and London, pp501
11. R.J. Beals, J.H. Handwerk, B.J. Wrona, J. Am. Ceram. Soc. 52(11) (1969) 578 – 581
12. R. Venkata Krishnan, V.K. Mittal, R. Babu, A. Senapati, S. Bera, K. Nagarajaj, J. Alloys and Compds. 509 (2011) 3229
13. R. Venkata Krishnan, G. Panneerselvam, P. Manikandan, M.P. Antony, K. Nagarajan, J. Nucl. Radiochem. Sci. 10 (2009) 19
14. R. Venkata Krishnan, R. Babu, G. Panneerselvam, B.M. Singh, A. Senapati, K. Ananthasivan, M.P. Antony, K. Nagarajan, Ceram. Int. 40 (2014) 4395
15. R.Venkata Krishnan, K. Nagarajan, Thermochim. Acta 440 (2006) 141 -145
16. H. Kleykamp, J. Nucl. Mater. 206 (1993) 82
17. R.J. Beals, J.H. Handwerk, and B.J. Wrona, J. Am. Ceram. Soc. **52**, (1969) 578.

18. H. Inaba, K. Naito, M. Oguma, J. Nucl. Mater. 149 (1987) 341 – 348
19. T. Matsui, Y. Arita, K. Naito, J. Radioanal. Nucl. Chem. 143 (1) (1990) 149 – 156
20. T. Matsui, T. Kawase, K. Naito, J. Nucl. Mater. 186 (1992) 254 – 258
21. K.C. Mills, F.H. Ponsford, M.J. Richardson, Thermochim. Acta 139 (1989) 107 – 120
22. Y. Arita, T. Matsui, S. Hamada, Thermochim. Acta 253 (1995) 1 – 9
23. Y. Arita, H. Hamada, T. Matsui, Thermochim. Acta 247 (1994) 225 – 236
24. H. Inaba, K. Naito, M. Oguma, H. Masuda, J. Nucl. Mater. 137 (1986) 176 – 178
25. R. D. Shannon, Acta Cryst. A32 (1976) 751 – 767
26. D.J. Kim, J. Am. Ceram. Soc. 72(8) (1989) 1415
27. J.A. Kilner, R. J. Brook, Solid state ionics 6(3) (1982) 237
28. J.A. Kilner, Solid state chemistry, Proceedings of the second European Conference, Ed. R. Metselaar, H.J.M. Heijligers, J. Schoonman, Elsevier, Amsterdam, 1983, pp189.

Dr. R. Venkata Krishnan, *Head, Advanced Fuels Studies Section, Fuel Chemistry Division, Materials Chemistry and Metallic Fuel Cycle Group, IGCAR, Kalpakkam joined IGCAR in the year 1998 after successfully completing and ranking first (Homi Babha Awardee) from 41st Batch of BARC training School. His research area of interest includes development of advanced nuclear fuels by sol-gel process, measurement of thermophysical and thermochemical properties, design and development of advanced equipments and instruments and its validation, synthesis of nano-materials by using citrate gel-combustion synthesis etc. He has co-authored 65 peer-reviewed international journal publications and more than 50 publications in national and international conferences.*

Dr. Rajagopal Babu *graduated from the University of Madras in 1980 and obtained Ph.D from Mumbai University in 2001. He joined as SA/B in IGCAR, Kalpakkam. Since then he was working in Radio-Chemistry Laboratory till his superannuation in April 2019. He has vast experience in the field high temperature thermodynamics mainly calorimetric techniques for the determination of thermodynamic properties of materials of interest in nuclear technology. He has co-authored around 100 research papers published in peer-reviewed international journals and conferences*

Shri Abhiram Senapati*obtained his M.Sc. in Chemistry from Madras University, Chennai. He joined in IGCAR in the year 2007. His current area of research include preparation, characterization and measurement of thermo-physical properties of* $(U_{1-y}RE_y)O_{\pm x}$, *(RE = Rareearth) by using differential scanning calorimeter. Internal gelation studies for the preparation of* UO_2 *and* CeO_2 *microspheres. He is also life member of Indian Thermal Analysis Society (ITAS).*

Shri. G. Jogeswara Rao*joined IGCAR in the year 2008. He has done M.Sc.in Chemistry from Madurai Kamaraj University, Tamilnadu. His research interest include synthesis of sol gel based nuclear fuel materials, determination of thermochemical and thermophysical properties of samples pertaining to nuclear industry by using solution calorimeter and inverse drop calorimeter.*

Dr. K. Ananthasivan, *Director, Reprocessing Group, IGCAR is from the 29th batch of BARC training school. He did M Sc (Engg.), Metallurgy from IISc, Bangalore, PhD from Madras University, Postdoctoral fellowship (Chemistry) in Purdue University, IN, USA. He is a senior professor and Chairman – Chemical Sciences Standing Committee of Homi Babha National Institute. He is the recipient of prestigious Homi Babha Science and Technology award in the year 2009 and DAE group achievement award in the year 2013. He has guided five numbers of PhD Scholars.*

Phase equilibria on LiCl-KCl-$RECl_3$ (RE: Pr, Nd and Gd) pseudo-ternary systems

Sajal Ghosh*, P.R. Reshmi, C.V. Vishnu Vardhan, Rajesh Ganesan, R. Sridharan, T. Gnanasekaran
Materials Chemistry and Metal Fuel Cycle Group
Indira Gandhi Centre for Atomic Research, Homi Bhabha National Institute
Kalpakkam-603102
**Corresponding author Email: sajal@igcar.gov.in*

Abstract

The pseudo-ternary phase diagrams of LiCl-KCl-$RECl_3$ are investigated to understand the interaction of $RECl_3$ (RE: Pr, Nd and Gd) with LiCl-KCl molten salt medium by differential thermal analysis (DTA) and characterization of the coexisting phases in the solid-state using X-ray diffraction (XRD). The primary and secondary crystallization temperatures for the samples are deduced from the heating runs of DTA traces, and the phases responsible for the various thermal events are ascertained. The coexisting phases at selected temperatures after long term equilibrations were identified by XRD. The results of these experiments showed that the LiCl-KCl-$RECl_3$ system consists of several pseudo-binary and quasi-ternary sections. Isothermal sections at selected temperatures and the liquidus projection with isothermal contours were deduced.

Keywords: Metallic fuel reprocessing, LiCl-KCl-$RECl_3$, Ternary phase diagram, Differential thermal analysis, Isothermal section, Liquidus projection.

1. Introduction

Reprocessing of spent nuclear fuels is being adopted for the utilization of nuclear fuels. Conventionally, reprocessing is practiced by the solvent extraction of actinides using tributyl phosphate (TBP) solvent along with diluents and is known as aqueous reprocessing. However, it has several issues, such as radiation damage, temperature instability of solvents, generation of huge liquid waste volume, etc. These issues are overcome by pyrochemical reprocessing involving molten salts and are the most promising options in the nuclear fuel cycle for advanced fuels [1,2]. It has several advantages, such as the ability to process fuel after high burn up with high Pu content, short cooling time, fewer criticality problems, actinide recycle potential, etc. with minimization of nuclear waste [3].

Molten LiCl-KCl eutectic is used as a liquid electrolyte medium in the high temperature pyrochemical reprocessing of spent fuel. Spent fuel primarily includes actinides, rare earth elements, noble metals, alkali and alkaline earth elements, etc. In this pyrochemical process [4], the spent fuel is loaded into the anode basket of an electrorefining cell containing molten salt as the electrolyte. The actinides are selectively deposited at the cathode (steel/cadmium) due to the difference in the redox potentials of the elements. The fission products remain in the anode basket and in the electrolyte. As reprocessing of the spent fuel is carried out in batches, the buildup of anodically dissolved fission products in the molten salt medium with time could lead to the formation of high melting ternary or higher-order compounds and in progressive increase of the liquidus temperature of the salt medium [5] which in turn would influence the pyrochemical process parameters. Rare earth elements constitute 25% of the total fission products formed. Praseodymium, neodymium and gadolinium are some of the rare earth fission-product elements [6] and it is necessary to understand the interaction of $RECl_3$ in the LiCl-KCl medium. This paper summarizes the investigations of phase equilibria in the LiCl-KCl-$RECl_3$ (RE: Pr, Nd and Gd) ternary systems.

2. Literature survey

Several authors have reported the LiCl-KCl binary phase diagram as a simple eutectic system. This system is also optimised using the CALPHAD technique by several authors. A brief summary of the literature on this system is given in Ref. [7]. Basin et al. [8] studied the phase diagram using an experimental setup combining oscillation phase analysis and thermal analysis techniques. Since their data are in close agreement with those reported by previous investigators, the phase diagram reported by them is used for the construction of the ternary phase diagrams in the present work.

Based on analysis of literature on LiCl-$RECl_3$ (RE: Pr, Nd) binary systems [7,9], the LiCl-$PrCl_3$ and LiCl-$NdCl_3$ phase diagrams reported by Kim and Okamoto [10] are considered and the only experimental phase diagram reported on LiCl-$GdCl_3$ system is considered [11]. These LiCl-$RECl_3$ (RE: Pr, Nd, Gd) binary data are used for the construction of the respective ternary phase diagrams.

A literature survey on KCl-$RECl_3$ (RE: Pr, Nd) binary systems [7,9] revealed that the KCl-$PrCl_3$ and KCl-$NdCl_3$ phase diagrams reported by Seifert et al. [12,13] are consistent. Among the experimental phase diagram of KCl-$GdCl_3$ reported in the literature, more recent and consistent data reported again by Seifert et al. [14] is considered. These KCl-$RECl_3$ (RE: Pr, Nd, Gd) binary data are used as the basis for the construction of the respective ternary phase diagrams.

Literature data on the LiCl-KCl-$RECl_3$ (RE: Pr, Nd and Gd) ternary systems are limited. Nakamura and Kurata [15] reported the partial phase diagram of the isopleth connecting $(LiCl\text{-}KCl)_{eutectic}$ and $RECl_3$ (up to 25 mol% $RECl_3$) by investigations involving thermal analysis, visual observation, electromotive force measurement and powder X-ray diffraction methods. For the samples containing <17 mol% $RECl_3$ (RE: Pr, Nd), they identified LiCl, KCl and K_2RECl_5 as coexisting phases below the solidus temperatures. Zhang et al. [16] studied the ternary LiCl-KCl-$NdCl_3$ system by differential thermal analysis (DTA). They determined the secondary and tertiary crystallization temperatures from the heating DTA traces by applying the onset extrapolation method, whereas the liquidus projection was derived from the cooling curves of DTA experiments. It is to be noted that alkali and rare earth halide molten salts are known for supercooling behaviour and hence the primary crystallization temperatures reported by them might be associated with significant uncertainties. No experimental data have been reported in the literature on the LiCl-KCl-$GdCl_3$ ternary system. This system was assessed by Zhou et al. [17] by the CALPHAD method using the two-sublattice model. The solubility of $GdCl_3$ in LiCl-KCl melt was determined from the phase diagram developed.

3. Experimental

3.1. Materials

Anhydrous LiCl (99.995%, M/s. Alfa Aesar, Germany), $PrCl_3$, $NdCl_3$, $GdCl_3$ (all 99.99%, M/s. Aldrich, Germany) were used in this work. Anhydrous potassium chloride (99.995%, M/s. Alfa Aesar, Germany) was further purified and used. Details of salt purification are described elsewhere [18]. All the samples are air and moisture sensitive in nature and hence were handled inside the inert atmosphere glove box. The purity of these starting materials was confirmed by determining their melting points by DTA and characterisation by XRD.

3.2. Preparation of samples and DTA studies

Calculated amounts of LiCl, KCl and $RECl_3$ (RE: Pr, Nd and Gd) were mixed to prepare samples of preselected compositions (~500 mg each). The compositions of the samples chosen for DTA are shown in Fig. 1. Weighing and mixing of these samples were carried out inside the argon atmosphere glove box. Sufficient amount of these samples (~35 mg) were loaded inside decarburized iron tubes (2.5 mm I.D., 3.2 mm O.D., 15 mm long), hermetically sealed by pulsed arc tungsten inert gas (TIG) welding and heated to 780°C under flowing hydrogen and cooled slowly for pre-equilibration and leak-checking. The pre-equilibrated samples analysed by DTA with heating rates of 2°C, 3°C and 5°C min^{-1} while the cooling rate in all the runs was maintained at 3°C min^{-1}. Argon - 4 % hydrogen gas mixture was used as carrier gas at a flow rate of 20 ml min^{-1} to prevent the oxidation of iron tubes during the experiments [7,9].

3.3. Equilibration studies and XRD analysis

To identify the coexisting phases in the LiCl-KCl-$RECl_3$ (RE: Pr, Nd and Gd) ternary system, appropriate amounts of LiCl, KCl and $RECl_3$ were mixed to prepare samples inside the inert atmosphere glove box. They were loaded in decarburised iron tubes (4 mm I.D., 5 mm O.D., 25 mm long) and hermetically sealed by pulsed arc TIG welding. The iron tubes were in turn sealed in quartz tubes under high vacuum, heated above the liquidus temperatures of the samples and maintained at that temperature for 1 h for homogenization which was determined from the DTA studies. The samples were then cooled slowly to 280°C and equilibrated at that temperature for 300 h duration, followed by quenching in liquid nitrogen. Samples with compositions close to that of K_3RECl_6 were also equilibrated at 490°C and 525°C for 24 h and quenched in liquid nitrogen. The compositions of the samples chosen for XRD analysis are also shown in Fig.1. The samples were

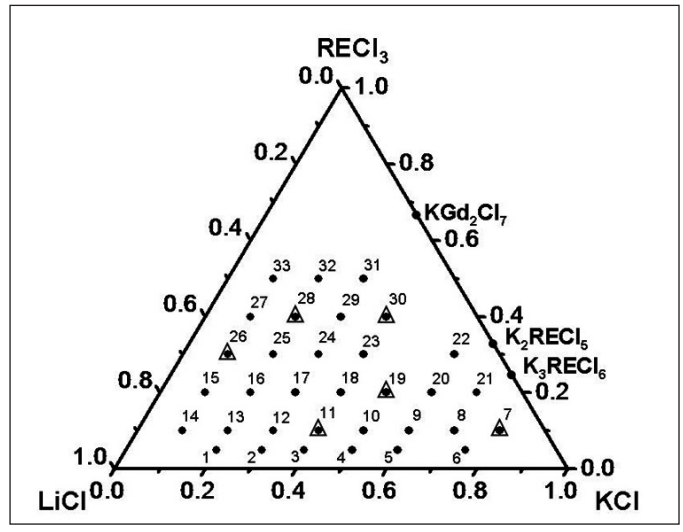

Fig.1: Compositions of XRD [Δ] and DTA [●]samples studied.

retrieved by cut opening the iron tubes and analysed by XRD using CuKα radiation. Details of samples preparation for XRD analysis are described elsewhere [7,9].

4. Results and Discussion

4.1 DTA studies

Representative DTA patterns of samples of LiCl-KCl-$RECl_3$ (RE: Pr, Nd and Gd) are shown in Figs.2 to 4. Solidus temperatures were obtained from the DTA traces by the onset extrapolation method [19]. The liquidus temperatures were obtained from the analysis of the DTA traces obtained during heating runs only, because appreciable super cooling occurred during the cooling runs. The liquidus temperature was determined by differentiating the DTA trace and noting the maximum in the differential curve, near the tail end of the DTA trace. The liquidus temperatures thus determined were found to be independent of the heating rate. The first endotherm occurring at the lowest temperature is attributed to the ternary eutectic involving the melting of the three solids. As the sample is heated above the ternary eutectic temperature, the melting of the second and the third solid phases continues. DTA pattern would show a change in the slope of the curve at the secondary crystallization temperature when the melting of the second solid phase is complete. The melting of the third solid is completed at the liquidus temperature.

Representative DTA of LiCl-KCl-K_2PrCl_5 section is shown in Fig.2. The first endothermic thermal event is assigned to the solidus temperature. The average solidus temperature of all the samples whose compositions lie in this section is 318 ± 4°C and this is attributed to the ternary eutectic temperature. The eutectic temperature was reported as 352°C by Nakamura and Kurata [15]. It is expected that the addition of a third component to the LiCl-KCl binary eutectic system with eutectic temperature of 352°C would decrease the solidus temperature below 352°C. Hence, the observed solidus temperature of 318 ± 4°C determined from the 15 different samples lying in this section is considered to be more reliable. The ternary eutectic composition of this section found to lie closer to the

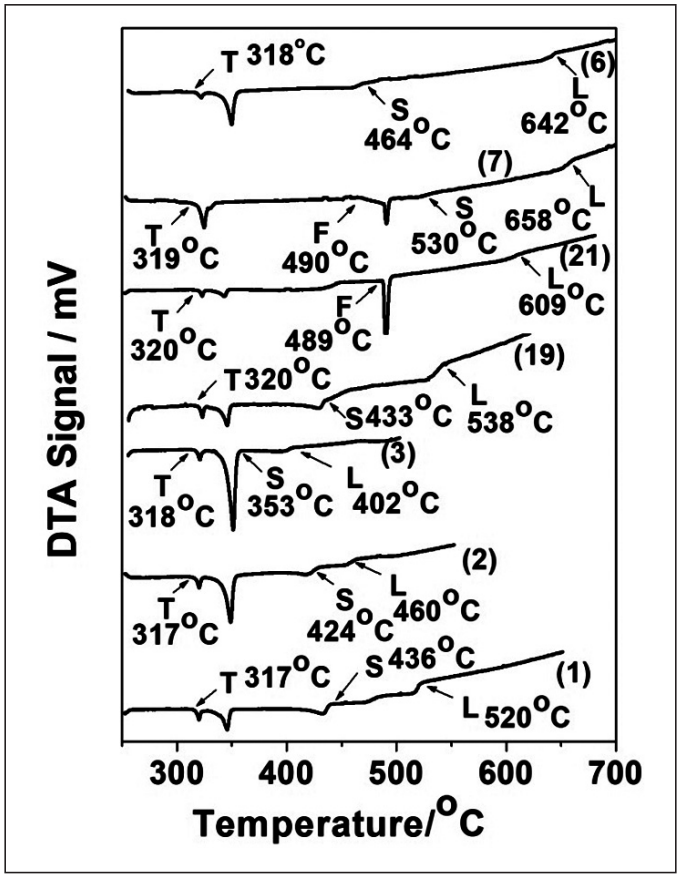

Fig.2: Representative DTA traces of samples lying in the LiCl-KCl-K_2PrCl_5 section.T→ Ternary eutectic temperature, F→ Compound formation temperature, S→ Secondary crystallization temperature, L→ Liquidus temperature. Numbers in parenthesis correspond to sample numbers.

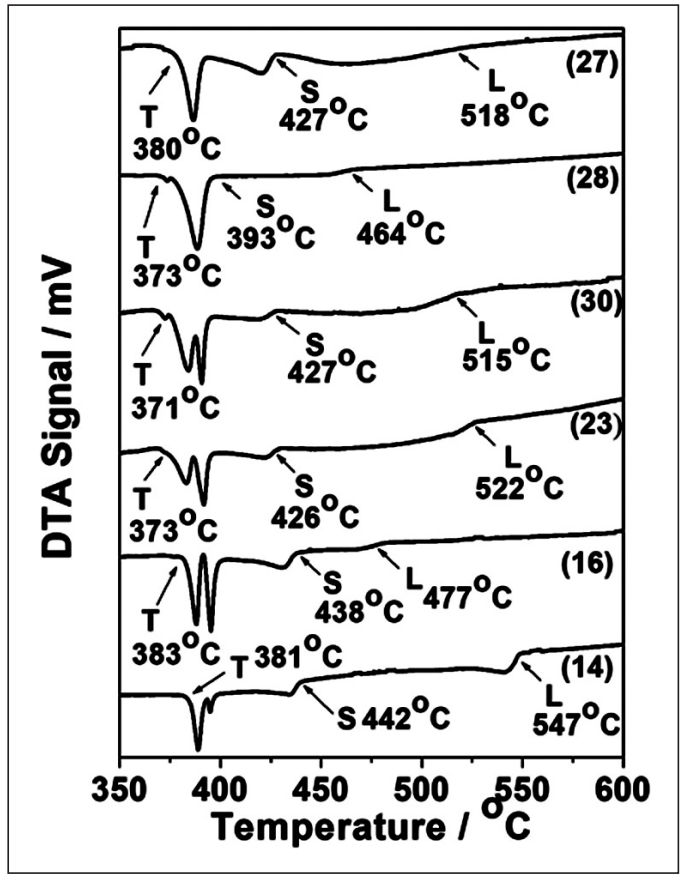

Fig.3: Representative DTA traces of samples lying in the LiCl-K_2NdCl_5-$NdCl_3$ section. T→ Ternary eutectic temperature, S→ Secondary crystallization temperature, L→ Liquidus temperature. Numbers in parenthesis correspond to sample numbers.

composition of sample no. 3 i.e, 55.6 mol% LiCl-39.4 mol% KCl-5 mol% $PrCl_3$. Thermal events such as compound formation, secondary crystallization temperatures and liquidus temperatures were also determined. In a similar fashion, thermal events in the LiCl-K_2PrCl_5-$PrCl_3$ section were also deciphered.

Representative DTA of LiCl-K_2NdCl_5-$NdCl_3$ section is shown in Fig.3. The first endothermic thermal event is assigned to the solidus temperature. The ternary eutectic temperature is deduced to 376 ± 9°C. It is to be pointed out that pure LiCl, K_2NdCl_5 and $NdCl_3$ do not show any thermal event up to 376°C. The DTA traces of samples having composition around the ternary eutectic point should exhibit primary and secondary crystallization temperatures closer to the ternary eutectic temperature. Based on the analysis of DTA traces of samples in this section, the ternary eutectic composition is delineated as 46.2 mol.% LiCl-32.5 mol.% K_2NdCl_5-21.3 mol.% $NdCl_3$. Nakamura and Kurata [15] observed the ternary eutectic temperature as 383°C, while Zhang et al. [16] reported it as 360°C in this phase field. Other thermal events such as secondary crystallization temperatures and liquidus temperatures were also derived from the DTA traces. In a similar fashion, thermal events in the LiCl-KCl-K_2NdCl_5 section were also deciphered.

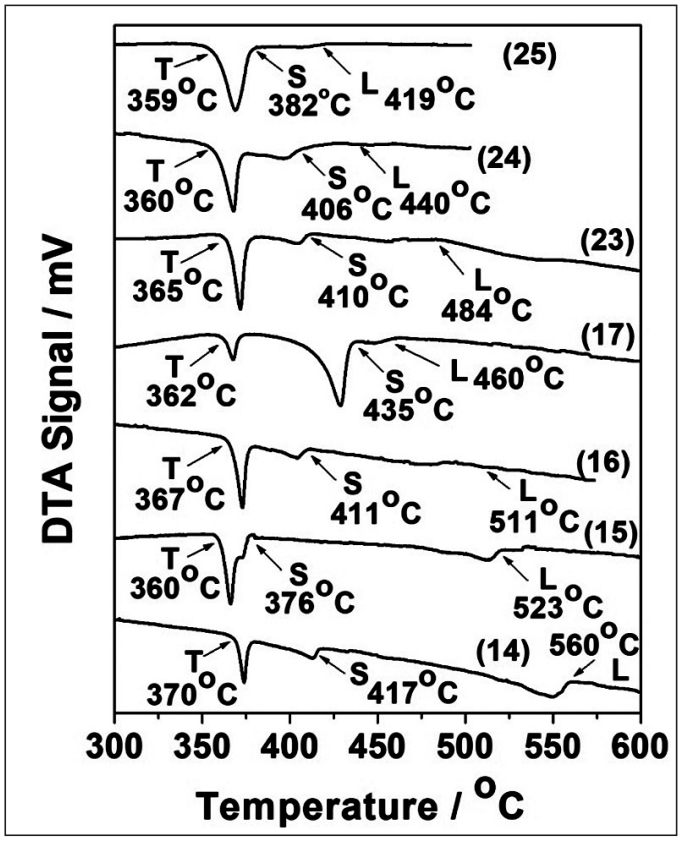

Fig.4: Representative DTA traces of samples lying in the LiCl-K_2GdCl_5-KGd_2Cl_7 section. T→ Ternary eutectic temperature, S→ Secondary crystallization temperature,L→ Liquidus temperature. Numbers in parenthesis correspond to sample numbers.

Representative DTA of LiCl-K_2GdCl_5-KGd_2Cl_7 section is shown in Fig.4. The first endothermic thermal event is assigned to the solidus temperature. The ternary eutectic temperature is deduced as 365 ± 6°C. The DTA traces of samples having composition around the ternary eutectic point should exhibit primary and secondary crystallization temperatures closer to the ternary eutectic temperature. Other thermal events such as secondary crystallization temperatures and liquidus temperatures were also derived from the DTA traces. In a similar fashion, thermal events in the LiCl-KCl-K_3GdCl_6, LiCl-K_3GdCl_6-K_2GdCl_5 and LiCl-KGd_2Cl_7-$GdCl_3$ sections were also deciphered.

From the DTA, invariant reactions such as ternary eutectic and peritectic, their corresponding temperatures and compositions were determined for all the three ternary systems.

4.2. XRD characterization of samples after equilibrations

XRD patterns of the samples after their equilibration at 280°C were analyzed to deduce the coexisting phases. Samples of each of the ternary systems were also equilibrated at 525°C and 490°C, respectively. Analysis of XRD results of all the samples showed the absence of any quaternary compound. At 280°C, the results indicated

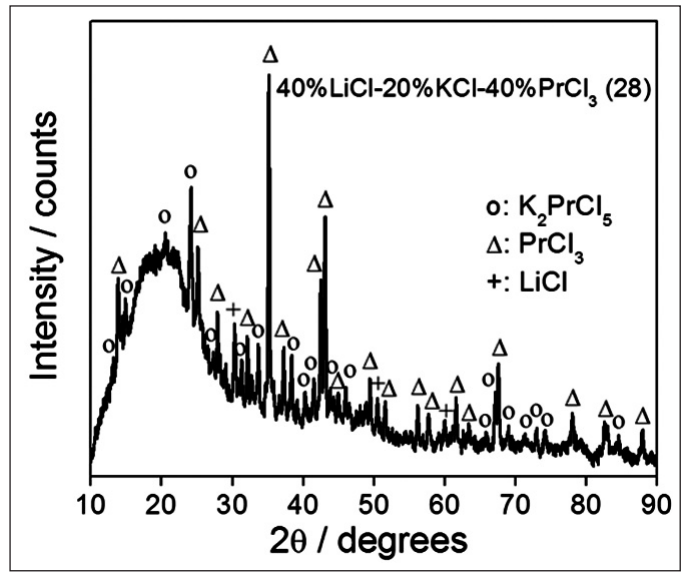

Fig.5: XRD pattern of samples equilibrated at 280°C. Coexisting phases identified: K_2PrCl_5, $PrCl_3$ and LiCl. Number in parenthesis corresponds to sample number

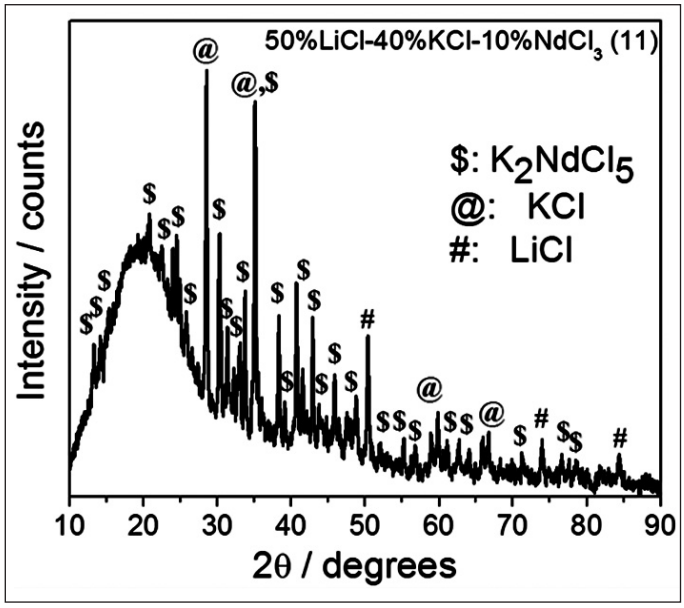

Fig.6: XRD pattern of samples equilibrated at 280°C. Coexisting phases identified: K_2NdCl_5, LiCl and KCl. Number in parenthesis corresponds to sample number.

the coexistence of LiCl-KCl-K_2RECl_5 and LiCl-K_2RECl_5-$RECl_3$ (RE: Pr, Nd) phase fields. Figs.5 and 6 shows the representative XRD patterns of these samples. The coexistences of LiCl-K_2PrCl_5-$PrCl_3$ and LiCl-KCl-K_2NdCl_5 are shown in Fig.5 and Fig.6, respectively. In the case of LiCl-KCl-$GdCl_3$ system, the following phase fields were identified at 280°C: LiCl-KCl-K_3GdCl_6, LiCl-K_3GdCl_6-K_2GdCl_5, LiCl-K_2GdCl_5-KGd_2Cl_7 and LiCl-KGd_2Cl_7-$GdCl_3$. Representative XRD patterns of coexistence of LiCl-K_2GdCl_5-KGd_2Cl_7 is shown in Fig.7.

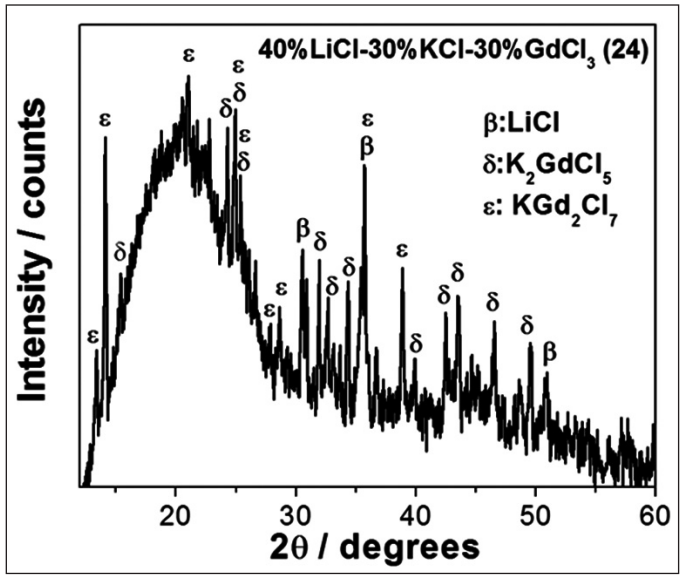

Fig.7: XRD pattern of samples equilibrated at 280°C. Coexisting phases identified: LiCl, K_2GdCl_5, KGd_2Cl_7. Number in parenthesis corresponds to sample number.

5. Construction of isothermal cross-sections

Based on various thermal events identified from the DTA traces of samples and coexistence of the phases in the solid-state identified by XRD analysis along with the consistent application of Gibbs phase rule, isothermal sections at chosen temperatures were constructed for the temperature range 400°C to 600°C. A representative isothermal section of LiCl-KCl-$PrCl_3$ system at 400°C is shown in Fig.8. The phase boundaries were deduced based on the ascertained thermal events in the DTA traces and interpolation of the temperatures of various thermal events (like secondary crystallization and liquidus temperatures) of the adjacent samples.

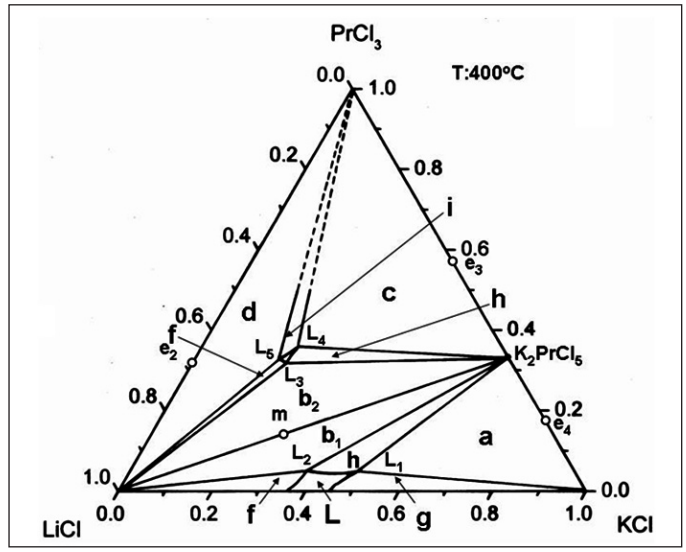

Fig.8: Tentative pseudo ternary LiCl-KCl-$PrCl_3$isothermal section at 400°C. L: liquid, a: KCl + K_2PrCl_5+L_1(liquid in equilibrium with KCl and K_2PrCl_5, b_1: LiCl + K_2PrCl_5+L_2(liquid in equilibrium with LiCl and K_2PrCl_5 in the LiCl-KCl-K_2PrCl_5 section), b_2: LiCl + K_2PrCl_5+L_3(liquid in equilibrium with LiCl and K_2PrCl_5 in the LiCl-K_2PrCl_5-$PrCl_3$ section), c: K_2PrCl_5+ $PrCl_3$+L_4(liquid in equilibrium with K_2PrCl_5 and $PrCl_3$, d: LiCl + PrCl3 + L_5 (liquid in equilibrium with LiCl and $PrCl_3$), f: L + LiCl, g: L + KCl, h: L + K_2PrCl_5, i: L + $PrCl_3$.

6. Liquidus projection

Liquidus projection of LiCl-KCl-$RECl_3$ systems were constructed using (i) the liquidus temperatures obtained from the traces of heating DTA experiments, (ii) the reported liquidus temperatures of the binary systems that form the edges of the ternary system and (iii) following the guidelines given in reference [20]. A representative liquidus projection is shown in Fig. 9 for the LiCl-KCl-$NdCl_3$ system. It consists of isothermal contours at the interval of 50°C between 400°C to 650°C. In the liquidus projection, contours from the corner of pure LiCl indicate the temperatures at which solid LiCl in equilibrium with the

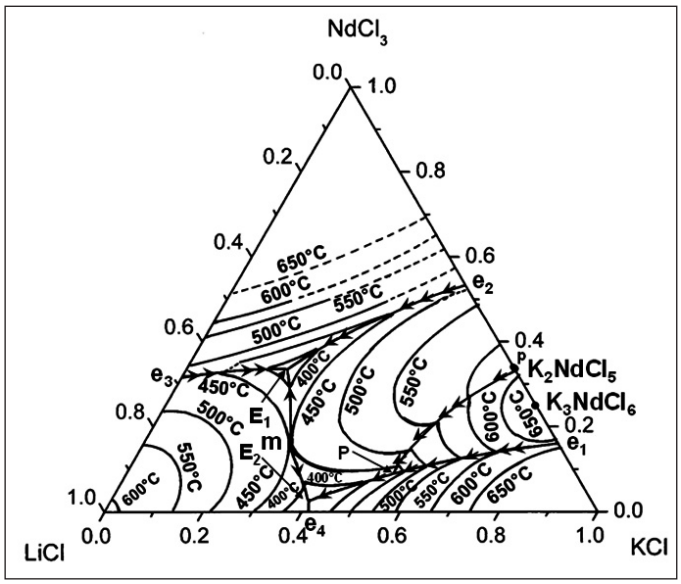

Fig.9: Polythermal liquidus projection with isothermal contours on LiCl-KCl-$NdCl_3$ system, Dashed lines indicate the extrapolated liquidus temperatures

liquid dissolve completely at those compositions. Similar contours are shown from the corners of KCl, K_2RECl_5 and $RECl_3$. The error associated with the composition in the drawn isothermal contours is estimated to be within 2 mol %.

7. Conclusion

The LiCl-KCl-$RECl_3$ ternary phase diagrams are investigated by DTA and XRD. There is no evidence of quarternary compound formation in the LiCl-KCl-$RECl_3$ ternary phase diagrams. The ternary phase diagram consists of two quasi-ternary phase diagrams, namely, LiCl-KCl-K_2RECl_5 and LiCl-K_2RECl_5-$RECl_3$. The ternary eutectic temperature is observed at ~315°C in the LiCl-KCl-K_2RECl_5 pseudo-ternary section. The pseudo-ternary peritectic reaction temperatures were also determined. The eutectic temperature was observed at ~380°C in the LiCl-K_2RECl_5-$RECl_3$ section. The isothermal cross-sections of this ternary system have been constructed at selected temperatures based on the coexisting phases deciphered. Polythermal liquidus projections with isothermal contours have been constructed for the LiCl-KCl-$RECl_3$ systems.

References

1. D. Olander, J. Nucl. Mater. 389 (2009) 1-22.
2. J.P. Ackerman, Ind. Eng. Chem. Res. 30 (1991) 141-145.
3. K. Nagarajan, B. Prabhakara Reddy, Suddhasattwa Ghosh, G. Ravisankar, K.S. Mohandas, U. Kamachi Mudali, K.V.G. Kutty, K.V. Kasi Viswanathan, C. Anand Babu, P. Kalyanasundaram P.R. Vasudeva Rao, Baldev Raj, Energy Proceedia 7 (2011) 431-436.
4. J. J. Laidler, J.E. Battles, W.E. Miller, J.P. Ackerman, and E.L. Carls, Prog. Nucl. Energ. 31 (1997) 131-140.
5. T.Y. Gutknecht, G.L. Fredrickson, Thermal characterization of molten salt systems, INL/EXT-11 23511. Idaho National Laboratory, 2011.
6. E.A.C. Crouch, Atom. Data. Nucl. Data 19 (1977) 417-532.
7. S. Ghosh, R. Ganesan, R. Sridharan, T. Gnanasekaran, J. Phase Equilib. Diffus. 39 (2018) 916-932.
8. A.S. Basin, A.B. Kaplun, A.B. Meshalkin, N.F. Uvarov, Russ. J. Inorg. Chem. 53 (2008) 1509-1511.
9. S. Ghosh, R. Ganesan, R. Sridharan, T. Gnanasekaran, Thermochim. Acta, 653 (2017) 16-26.
10. I.-S. Kim, Y. Okamoto, Phase Diagram for Binary Systems, NdCl3–LiCl and PrCl3–LiCl, JAERI-Research 99-033, 1999.
11. C. Zheng, Z. Zhao, Rare Earth. 14 (1993) 65-66.
12. H.J. Seifert, J. Sandrock, J. Uebach, Z. Anorg. Allg. Chem. 555 (1987) 143-153.
13. H.J. Seifert, H. Fink, J. Uebach, J. Therm. Anal. 33 (1988) 625-632.
14. H. J. Seifert, J. Sandrock, G. Thiel, Z. Anorg. Allg. Chem. 598-599 (1991) 307-318.
15. K. Nakamura, M. Kurata, J. Nucl. Mater. 247 (1997) 309-314.
16. Y. Zhang, C. Zheng, Y. Yupu, Acta. Metall. Sin. B 2 (1989) 13-17.
17. W. Zhou, Y. Wang, J. Zhang, M. Khafizof, J. Nucl. Mater. 508 (2018) 40-50.
18. S. Ghosh, R. Ganesan, R. Sridharan, T. Gnanasekaran, J. Nucl. Mater. 467 (2015) 280-285.
19. G.W.H. Hohne, W.F. Hemminger, H.-J. Flammersheim, Differential Scanning Calorimetry, Berlin Heidelberg, Springer-Verlag, 2003.
20. F.N. Rhines, Phase Diagrams in Metallurgy: Their Development and Application, McGraw-Hill Book Company, New York, 1956.

	Dr. Sajal Ghosh *obtained his M.Sc degree from The University of Burdwan. After graduating from the 49th batch of BARC training school, he started his research career in Chemistry Group, IGCAR in 2006. He obtained Ph.D degree from the Homi Bhabha National Institute (HBNI - Kalpakkam Campus), Bombay. His research interests include development of chemical sensors for liquid metals, high temperature thermodynamics and phase equilibria investigation on molten salt systems.*
	Mrs. P. R. Reshmi *obtained her B.Sc degree from Mahatma Gandhi University, Kottayam, Kerala and M.Sc from Annamalai University. She joined IGCAR in 2001. Currently she is working in development of online electrochemical carbon and hydrogen sensors for liquid sodium, carbon activity measurement of D9 and IFAC-1SS alloys by foil equilibration method.*
	Mr. C. V. Vishnu Varadhan *obtained his M. Sc from IIT Madras. After graduating from 50th batch of BARC training school, he started his research career in IGCAR. His research interests include high temperature thermodynamics and phase transformations, electrolytic domain boundary measurements of various solid electrolytes.*
	Dr. Rajesh Ganesan *obtained his M.Sc from Hyderabad Central University. After graduating from the 37th batch of BARC training school, he started his research career in IGCAR in 1994. He obtained his Ph.D from Indian Institute of Technology Bombay and pursued his post-doctoral research in Univeristy of Vienna, Austria. His research interests include development of sensors for liquid metals, high temperature thermodynamics and phase diagrams.*
	Dr. R. Sridharan *obtained his M.Sc from Indian Institute of Technolog, Madras (IITM), Chennai in the year 1979. He then graduated from the 23rd batch of the BARC Training School and joined Indira Gandhi Centre for Atomic Research (IGCAR) in 1980. He obtained his Ph.D from IITM,Chennai in the year 1996. His research area involved investigation of phase diagrams of materials and systems for use in sodium coolant circuits of Fast Breeder Reactor. He has been awarded the Scientific & Technical Excellence Award (2007) in recognition of his contribution in the development of electrochemical hydrogen meter (ECHM) that enables detecting steam leaks at its inception in sodium circuits of fast reactors.*
	Dr. T. Gnanasekaran *obtained his M.Sc and Ph.D from University of Madras. After graduating from the 17th batch of BARC Training School, he joined IGCAR in 1974. He was a postdoctoral fellow at the University of Vienna, Austria and was a visiting scientist at the Nuclear Research Centre, Karlsruhe in Germany. His main themes of studies are high temperature thermodynamics, electrochemistry and development of chemical sensors for use in liquid metals and gaseous ambients. He is recipient of HomiBhabha Award for Science and Technology for his work in sodium chemistry and former Associate Director of Chemistry Group, IGCAR.*

Molten salt based direct solid state electrochemical de-oxidation of metal oxides to metal: Our experience at IGCAR

K.S. Mohandas, N. Sanil, D. Sri Maha Vishnu, T. Biju Joseph, R. Kumaresan, Anwesha Mukherjee, L. Shakila
Pyrochemical and Materials Processing Division, Materials Chemistry and Metal Fuel Cycle Group,
Indira Gandhi Centre for Atomic Research, Kalpakkam- 603102, India.
**Corresponding author E-mail: ksmd59@yahoo.com*

Abstract

Electrochemical de-oxidation of solid metal oxides to metals in high temperature molten salt medium, by electrons (FFC Cambridge process) and by in-situ generated electro-positive metals like lithium and calcium (electro-metallothermic reduction process) has been a recent development in electrometallurgy for production of metals and alloys. Since discovery of the process in late 1990's, preparation of many metals and alloys has been reported in the FFC Cambridge process from around the world. In the context of development of pyroprocessing of spent oxide nuclear fuels, electro-deoxidation of UO_2 and simulated spent oxide fuels has been studied extensively in the electro-lithiothermic reduction method by atomic energy institutes of South Korea, USA and Japan. We, at the Pyrochemical and Materials Processing Division of IGCAR, have been closely following the developments in this area of work and also studying the electro-reduction behaviour of many metal oxides in the different processes. A brief introduction of the solid state electro-deoxidation processes and a bird's eye view of our research work in this area, especially with regard to the electro-deoxidation of solid UO_2 (electro-lithiothemic process), ThO_2 (FFC Cambridge and electro-calciothermic processes) and TiO_2 (FFC Cambridge process) has been presented.

Keywords: FFC process, electro-deoxidation, molten salt electrolysis, uranium oxide

1. Introduction

Production of metals from metal compounds has been a major activity of human kind from time immemorial. Most of the metals existed on earth's crust as metal compounds and they are chemically reduced with strong reducing agents like calcium, magnesium and lithium or carbon to gain the metals. Discovery of electrochemical processes for metal production enabled production of many metals that were difficult to be produced by the conventional chemical reduction method due to the high stability of the metal compounds. Many reactive metals like sodium, potassium, lithium, magnesium and calcium have been produced by electrolysis of the respective fused chlorides. Molten salt electrolysis has evolved as an efficient and economical method for gaining metals from highly stable metal compounds.

In the recent past, two high temperature molten salt electrolytic processes for direct conversion of metal oxides to metals/alloys, both coming under the category of direct electro-deoxidation (also called electro-reduction), have been reported [1]. In one of the processes, namely FFC Cambridge process [2,3], electrons served as the reductant where as in the other called electro-metallothermic method, a strong reductant like lithium [1,4] or calcium [5,6], generated in-situ from the molten electrolyte medium by electrolysis, served as the reductant. In both the cases, the solid metal oxide, which is in contact with current conducting metal part, forms the cathode in the electrolytic cell and the oxygen present in it is removed as O^{2-} ions to obtain the metal. In course of time, the solid metal oxide electrode transforms to the corresponding metal. The cell reactions and salient features of the solid-state electrochemical processes are briefly explained below.

1.1 FFC Cambridge process

The process is generally conducted in calcium chloride melt at 900-950 °C or in calcium chloride containing melts at lower temperatures (for example $CaCl_2$-NaCl melt at 650°C). Graphite serves as the anode. Generally the cell is operated by applying a constant voltage, 3.0 or 3.1 V (at 900 °C). Under the influence of the applied potential, the oxygen present in the oxide is ionized as O^{2-} ions, which upon leaving the electrode is transported to the graphite anode, where it is oxidized and discharged as CO_2 or CO. As the process is continued, the oxide electrode is converted to the corresponding metal.

The cell is represented as

Cell: C(s) / $CaCl_2$ (l) / MO_x (s)

Cell reactions:

$$MO_x + 2ne^- \rightarrow MO_{(x-n)} + nO^{2-} \text{ at cathode} \quad (1)$$

$$nO^{2-} + n/2\ C \rightarrow n/2\ CO2 + 2ne\text{-} \text{ at anode} \quad (2)$$

Net reaction:

$$MO_x + n/2\ C \rightarrow MO_{(x-n)} + n/2\ CO_2 \quad (3)$$

For anodic evolution of CO, the equation can be written as

$$nO^{2-} + nC \rightarrow nCO + 2ne^- \quad (4)$$

Net reaction:

$$MO_x + nC \rightarrow MO_{(x-n)} + nCO \quad (5)$$

The significant aspect of the electro-deoxidation in the FFC Cambridge process is that the de-oxidation occurs at an applied potential, which is lower than that required for producing calcium metal from the calcium chloride melt by electrolysis (decomposition potential of $CaCl_2$ at 900 °C is 3.21 V).The reduction is considered to occur by the 'oxygen ionisation mechanism' [7] as shown in the equation (1). Several metal oxides have been deoxidised, in laboratory experiments, to corresponding metals in

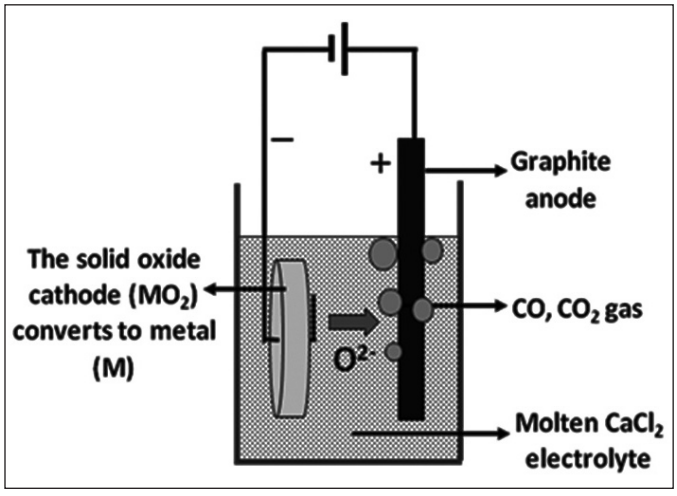

Fig. 1: Schematic diagram of FFC Cambridge process

this process [1,8]. The process also enables production of alloys, when the oxide electrode is prepared from a mixture of metal oxides. The schematic of the process is given in Fig.1.

1.2 Electro-metallothermic reduction process

In this process, a reductant metal is in-situ electro-generated on the solid oxide electrode which is configured as the cathode in the cell and the metal chemically reduces the oxide to metal. In order to reduce stable metal oxides to metal, reductant metal needs to be highly electropositive in nature and hence lithium and calcium metals are often the reductant metals of choice. Generally, in the electro-lithiothermic reduction process, LiCl melt containing 0.5-3 wt.% Li_2O have been used used as the electrolyte and in the electro-calciothermic process, molten calcium chloride containing 0.5-1 wt.% CaO is used as the electrolyte. Electrolysis of the dissolved oxide (Li_2O and CaO), generates metals (Li, Ca) necessary for reduction of the solid oxide. Platinum is generally used as the anode in electro-lithiothermic reduction process. Graphite or platinum can be used as anode in the electro-calciothermic process. Electro-calciothermic process for reduction of solid TiO_2 to Ti is also known as Ono-Suzuki process (OS process) [5]. The chemical and/or electrochemical processes governing the solid-state reduction process are given below. The schematic diagram the electro-metallothermic reduction process, with platinum or graphite anode, is depicted in Fig. 2.

Electro-lithiothermic process	**Electro-calciothermic process**
Cell: Pt (s) / LiCl, Li_2O(l) / MOx (s)	**Cell: C(s) / $CaCl_2$, CaO(l) / MO_x (s)**
At cathode: $Li^+ + e^- \rightarrow Li$ (6) $MO_x + 2n\ Li \leftrightarrow MO_{(x-n)} + 2n\ Li^+ + nO^{-2}$ (7)	At cathode: $Ca^{2+} + 2\ e^- \rightarrow Ca$ (10) $MO_x + n\ Ca \rightarrow MO_{(x-n)} + nCa^{2+} + n\ O^{2-}$ (11)
At platinum anode: $nO^{2-} \rightarrow n/2\ O_2\ (g) + 2n\ e^-$ (8)	At graphite anode: $nO^{2-} + n/2\ C \leftrightarrow n/2\ CO_2 + 2ne^-$ (12)
Net reaction: $MO_x + 2n\ Li \rightarrow MO_{(x-n)} + 2n\ Li^+ + n/2O_2$ (9)	Net reaction: $MO_x + n\ Ca + n/2\ C \rightarrow MO_{(x-n)} + n\ Ca^{2+} + n/2\ CO_2$ (13)

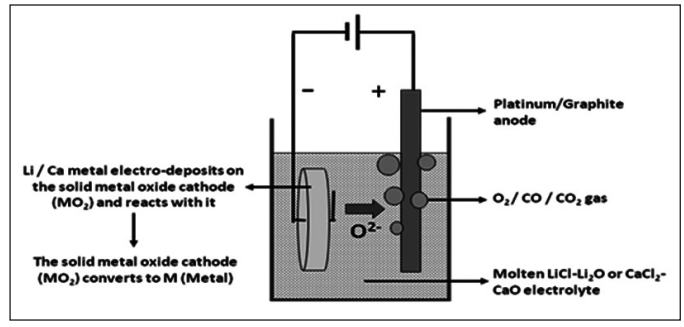

Fig. 2: Schematic of the electro-metallothermic reduction process

Solubility of lithium metal in LiCl melt is very low (0.4 mol.% at 650 °C [9]) and therefore the metal deposited on the oxide electrode remain there for sufficient period of time for the reduction reaction to take place. However, in the case of calciothermic reduction, solubility of calcium metal in calcium chloride melt is high (4 mol.% at 900 °C [10]) and this makes the electro-deposited calcium to dissolve quite fast into the melt. Obviously, the poor availability of calcium metal on the oxide electrode makes the reduction inefficient. However, calcium is a stronger reductant than lithium and its availability in the melt can favour the reduction process. This apart, calcium chloride melt under cathodic polarizing condition, is known to generate Ca^+ ions ($Ca^{2+}+e^- \rightarrow Ca^+$) and the presence of the monovalent calcium ion provides a strong reducing atmosphere to the melt which could further help in the reduction of the oxide. However, the difference in the melt characteristics between lithium chloride and calcium chloride needs to be taken into account during the design and operation of electro-reduction cells for optimum performance.

1.3. Special features of solid state electro-reduction process

1.3.1. Conventional reduction vs solid-state electrochemical reduction

The direct solid-state electro-reduction processes are unique when compared to the conventional chemical as well as electrochemical metal production processes. In conventional electrolytic process for metal production, the metal compound is directly electrolyzed from an electrolyte medium in which it is dissolved as ions. But in the new processes, the metal oxide is not dissolved in the electrolyte melt, but exists as solid (preform or powder) in contact with the molten electrolyte. In these processes, the de-oxidation of the metal oxide takes place in one step, where as in the conventional chemical reduction, the metal oxide is first converted to a metal halide and the halide is subsequently reduced to the metal with the help of a reductant metal. The two step process becomes necessary to avoid contamination of the freshly reduced metal with oxygen. Obviously, the metal production in a single step in the new electro-deoxidation processes offer significant advantages over the two-step conventional reduction processes. As the electrolyzed metal product remains as solid at the cathode, its recovery from the cell becomes relatively easy when compared to that from conventional chemical and electrochemical reactors.

1.3.2. The oxide cathode and cathodic process

The unique solid-state reduction of the metal oxides, in both the processes, necessitates special operation conditions for the successful operation of electrolytic cells. Firstly, the oxide as well as the reduced metal should not dissolve in the electrolyte melt and the solid preform should not disintegrate during its transformation from oxide to metal. For this, generally, the oxide preforms are prepared by powder compaction followed by high temperature sintering. Oxygen should be transported from the bulk parts of the solid oxide preform to the reaction interface by diffusion under the applied potential gradient of the cell. Diffusion of oxygen in the solid oxide is a slow process and hence the distance of diffusion of oxygen in the solid oxide should be made as minimum as possible. In other words, the oxide preform should be made as porous and thin as possible, but at the same time mechanically robust to prevent disintegration during the oxide to metal conversion steps.

The oxide electrode is always in contact with a metal part, through which electrons are supplied to it. The design of the oxide preform and cathode assembly is of critical importance in the solid-state reduction process. In laboratory studies, in the simplest construction, the oxide preform is generally tied to a metal wire and the latter serves as the current lead to the former. Photographs of some of the cathode assemblies used in our work are shown in Fig. 3.

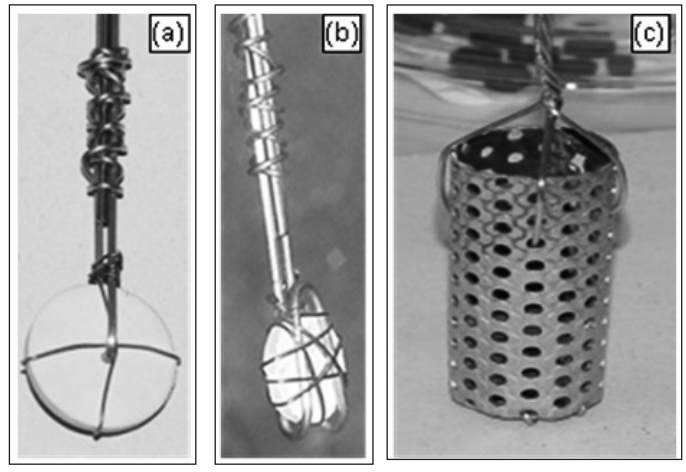

Fig.3: *Photographs of different cathode assembly designs used in our studies, (a) oxide pellet tied with metal wire, (b) oxide pellet wrapped around with metal wire and (c) oxide pellets in metal basket*

1.3.3. The selection of electrolyte medium

Oxygen, removed as O^{2-} ion, from the metal oxide needs to be discharged at the anode and hence the electrolyte medium should have good solubility for its oxides. Both calcium chloride and lithium chloride have high solubility for corresponding oxides [9,10]. Lithium chloride melts at 605 °C and hence electro-lithiothermic reduction cells are operated at about 650 °C. Calcium chloride melts at 772 °C

and hence the cells with pure $CaCl_2$ or $CaCl_2$-CaO melts are operated above 850 °C. Uranium is low melting (m.p. 1132 °C) and hence it forms an impermeable metal layer on the surface of the oxide preform during electro-reduction in $CaCl_2$ or $CaCl_2$-CaO melts [11,12]. This could prevent contact of calcium to the bulk parts of the oxide preform and thereby prevent reduction of the inner parts of the oxide electrode. The electro-deoxidised U metal, processed in low-melting LiCl-Li_2O melt, is porous in nature and hence the electrolyte medium is found more suitable for reduction of UO_2 to U.

1.3.4. The anodes

The electrolyte melt invariably contains O^{2-} ions; those added to the melt as well as generated from the oxide cathode by the electro-reduction process. When graphite is used as anode in such melts, the anodically generated CO_2 gas dissolves in the melt to produce carbonate ions ($CO_2 + O^{2-} \rightarrow CO_3^{2-}$), which subsequently undergo reduction at the cathode and oxidation at the anode [13,14] as,

$$CO_3^{2-} + 4e^- \rightarrow C + 3O^{2-} \quad (14)$$

$$C + 2CO_3^{2-} \rightarrow 3CO_2 + 4e^- \quad (15)$$

The redox cycling consumes electricity unproductively. Significant quantity of carbon particulate matter is also generated in-situ during oxidation of O^{2-} ions, which contaminates the electrolysed metal product [15]. This also complicates the cell operation. The problems become severe when the oxide content of the electrolyte melts is high. Hence, the amount of CaO added to calcium chloride is often restricted to an optimum level of ~0.5 wt. % when graphite is used as anode. A too low oxide concentration is not desirable as it could impose transport limitation of oxide ions across the electrolyte [16]. In the case of cells with platinum anode too, the oxide content of the melt should be kept low (1-2 wt.%) to prevent high temperature oxidation of the reactor assembly by anodically generated oxygen gas. Stability of carbonate ions and the associated problems becomes severe at lower temperatures and hence graphite is not used as anode in electro-lithiothermic reduction cells, which operate at relatively lower temperatures (650 °C). Platinum is the anode of choice in such cells; for example, electro-lithiothermic reduction of UO_2 to U in LiCl-Li_2O melts.

Platinum is considered as an inert electrode in chloride melts containing dissolved oxides, but actually it is not so. Platinum anodically reacts in LiCl-Li_2O melt to form lithium platinate (Li_2PtO_3) [17], which eventually degrades the electrode and necessitates replacement after few reduction runs. Graphite rods are usually connected to a sturdy ss rod, which serve as the current lead. In experiments were

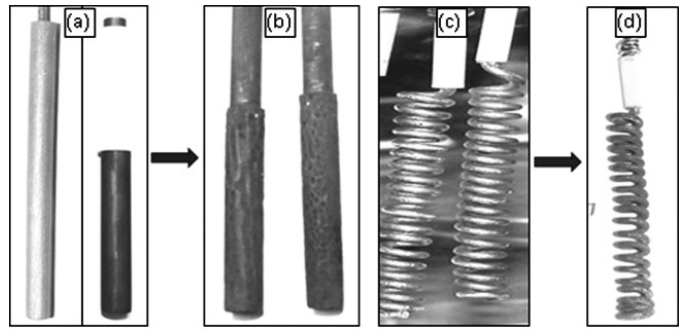

Fig.4: Photograph of graphite anode (a) before and (b) after use in the cell. Similarly, platinum anode before and after use in the cell are shown in (c) and (d).

platinum is used as anode, platinum wires made as coil, is connected to ss rod to serve as the current lead.The photographs of different graphite and platinum anodes used in our studies are given in Fig. 4.

1.3.5. Factors affecting solid-state electro-reduction

The solid-state electro-reduction behavior of oxides varies depending on the thermodynamic stability of the oxide and physico-chemical characteristics of the oxide preforms. Other factors which affect the electro-reduction reaction are applied voltage, temperature of operation, duration of electrolysis, electrolyte melt and its composition etc..These aspects need to be considered while selecting the electro-reduction process suitable for each metal compound. For example, lithiothermic reduction of UO_2 is thermodynamically feasible, but not feasible with ThO_2. Electro-calciothermic reduction is therefore necessary for reduction of ThO_2 to Th. While higher melting metals like Ti, Th, Nb etc. can be processed in $CaCl_2$ melts, the higher temperature melt is not suitable for processing of low-melting uranium in the solid state process. While FFC Cambridge process suits better for electro-reduction of metal oxides, that are reactive in calcium chloride melt (for eg. TiO_2), the process is not found suitable for oxides that are not reactive in the electrolyte medium (for eg. UO_2 and ThO_2).

Current efficiency of the molten salt electro-reduction process is low, often less than 50%. This will vary depending on the preparation of the solid oxide preform, electrolyte medium used, temperature, applied voltage, design of the cathode assembly etc.. A relatively high potential for electro-reduction in the case of FFC Cambridge process could lead to significant reduction in current efficiency due to the electronic conduction imparted to the melt under the experimental condition. Charge, in excess of that required theoretically for reduction of the mass of the oxide, need to be passed through the cell to achieve complete reduction of the oxide. Diffusion of oxygen through the solid oxide is a

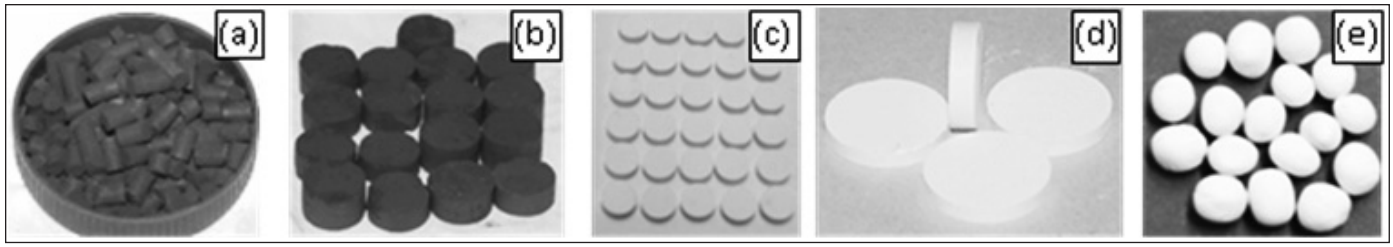

Fig.5: *Powder compacted and sintered pellets of UO_2 (a and b) and TiO_2 (c and d). Hand–shaped TiO_2 granules are shown in (e).*

slow process and hence reduction of the oxide too will be a slow process. But the speed of reduction can be increased by proper design of the oxide electrode. The reduction can takes place only at 3-phase interlines, i.e. the points where the electron, oxide and electrolyte are in contact and hence the efficiency of the process is decided to a great extent by the design of the electrode to provide it with maximum number of 3-phase interlines. The electrode design which enables easy escape routes for the oxygen ions from the bulk of the solid preform to the bulk electrolyte melt and dissolution in it will make the reduction of oxide faster.

We have carried out extensive studies on the electrochemical reduction behavior of different metal oxides with different electro-deoxidation characteristics like, UO_2, ZrO_2 (electro-lithiothermic reduction), ThO_2 (electro-calciothermic reduction, FFC Cambridge process), TiO_2, Nb_2O_5 and CeO_2 (FFC Cambridge process). The salient features of these studies and some typical results are briefly presented in this article.

2. Experimental aspects

2.1 Preparation of oxide preforms

Often the starting material is the oxide powder and different methods can be used to prepare the preforms. The oxide pellets were prepared from its powders. The oxide powder was mixed with a binder (polyvinyl alcohol) and plasticiser (polyethylene glycol) and made slurry in isopropyl alcohol medium. The powder obtained after drying off the alcohol, was thoroughly ground and pressed to pellets of sizes in the range of 6-25 mm dia. and 2-5 mm thick. The green pellets were subsequently sintered at ~ 1200 °C for 3 h in air for most of the oxides referred to in this paper, but with an exception to UO_2. UO_2 green pellets were sintered at ~1600 °C in Ar+4% H_2 mixture to avoid its oxidation to U_3O_8. In some studies where highly porous pellets were required, the oxide powder was mixed with pore formers like graphite powder, which upon sintering was burnt off as carbon dioxide, thus leaving behind highly porous oxide preforms. The open porosity of the pellets were determined by Archimedes Method (water impregnation method) and found to be on an average 30-40% porosity, which was good enough for our laboratory scale studies. The photographs of powder compacted and sintered pellets of UO_2, TiO_2 and hand-shaped granules of TiO_2 are shown in Fig. 5. The cathode assembly, which consists of the solid oxide and the current conducting metal part (Fig.3), is designed and used depending on the requirement of the experiment.

2.2. Preparation of electrolyte and characterization using Cyclic Voltammetry technique

LiCl, Li_2O, $CaCl_2$ and CaO are moisture sensitive chemicals and hence need to be handled in inert atmosphere (argon) glove box.

Preparation of moisture-free electrolyte is of paramount importance in molten salt electro-deoxidation work. Good quality $CaCl_2.2H_2O$ was dried under vacuum for about 72 h and slowly heated to ~750 °C, below the melting point. It was allowed to remain at the temperature for few hours and thereafter heated to temperatures above the melting point and pre-electrolysed at 2.5 V to remove any trace of moisture still left in the melt. The pre-electrolysed salt was used in all the experiments. LiCl is more hygroscopic than $CaCl_2$ and hence it should be handled and dried more carefully. The salt was heated, under vacuum, at 500 °C for 3 days and weighed mass of Li_2O powder, was added to the melt to make the required electrolyte melt composition, eg. LiCl-1wt% Li_2O melt.

Prior to the reduction experiments, Cyclic voltammetry (CV) of inert electrodes (tungsten WE for probing the cathodic reactions and graphite or platinum WE for probing anodic reactions), was carried out in all the melts. A Ni/NiO system was generally used as the reference electrode in the CV measurements [17]. The CV traces also served as sign boards on the purity of the melt; the absence of any irregular currents between the cathodic and anodic limits of the melt indicated the absence of redox active impurities of the melt and hence good purity of the melt. Typical cyclic voltammograms obtained with tungsten, graphite and platinum working electrodes in LiCl, LiCl-1wt% Li_2O, $CaCl_2$ and $CaCl_2$-0.5wt% CaO melts are shown in Fig. 6.

From the CV traces, the potential for the reactions ($2Cl^- \rightarrow Cl_2 + 2e^-$), ($Ca^{2+} + 2e^- \rightarrow Ca$, $Li^+ + e^- \rightarrow Li$,

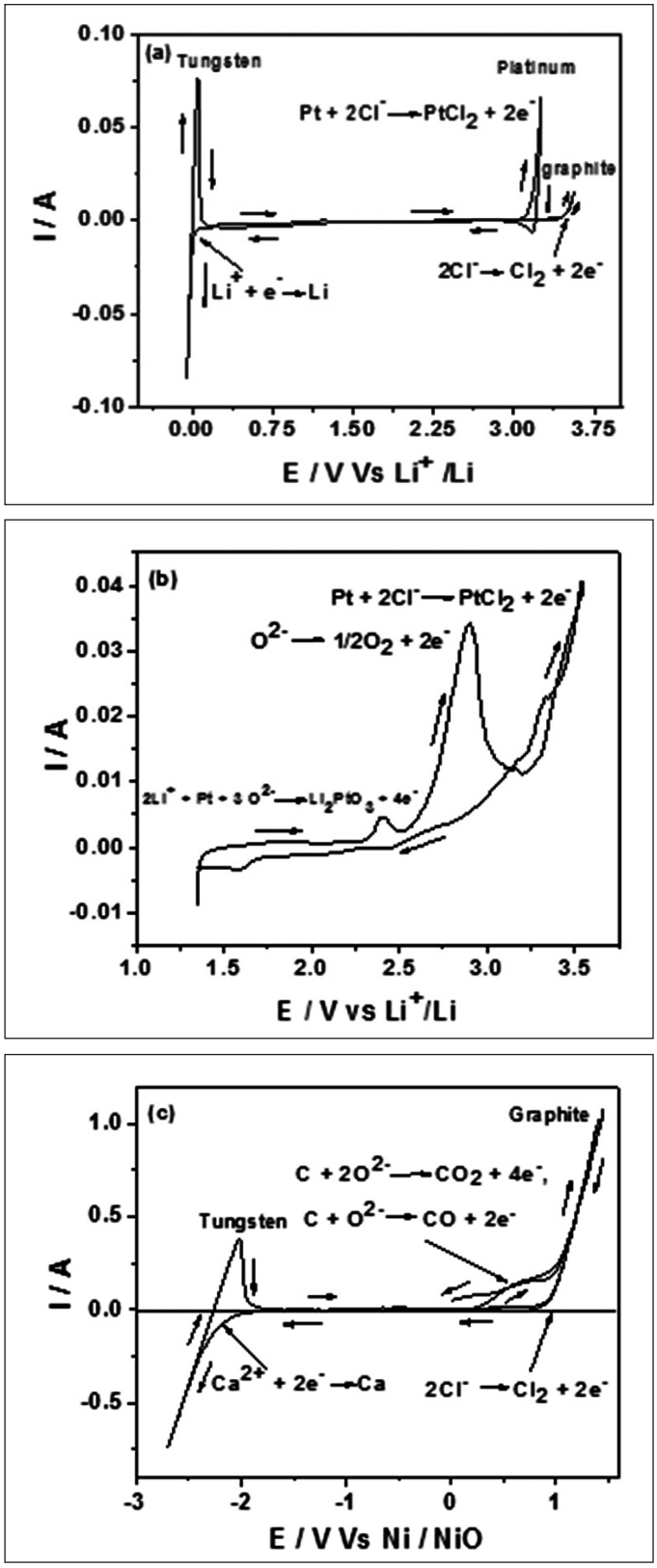

Fig.6: Cyclic voltammograms of tungsten (cathodic), platinum and graphite (anodic) working electrodes in pure LiCl (a) and platinum working electrode in LiCl-1wt% Li_2O (b) melts at 650 °C. The CV traces of tungsten and graphite working electrodes in pure $CaCl_2$ melt and $CaCl_2$-0.5wt% CaO melt at 900 °C are shown in (C)

$C + 2O^{2-} \rightarrow CO_2 + 4e^-$, $C + O^{2-} \rightarrow CO + 2e^-$, $Pt + 2Cl^- \rightarrow PtCl_2 + 2e^-$ (platinum dissolution) and $O^{2-} \rightarrow O_2 + 2e^-$ (oxygen evolution) can be obtained. Knowledge of all these potentials is necessary for operation of the different electro-reduction cells successfully.

2.3. The electrochemical reactor, assembly and operation

The reactor used for lab-scale studies is of simple construction. For studies with LiCl-Li_2O melt at 650 °C, the reactor is made of SS 304, where as the one with calcium chloride electrolyte and operating above 850 °C needs to be made of Inconel to prevent high temperature oxidation/corrosion. The reactor vessel body is welded to a thick flange and the reactor is closed leak-tight with the help of a mating flange and O-ring seal in between the flanges. Fins are welded to the outside upper part of the reactor, below the flange, to remove heat by conduction and thus to protect the O-ring seal from damage by heat. The upper flange of the vessel is provided with many ports, through which different electrodes could be inserted to the reactor in leak tight condition. The reactor also has provisions for argon gas inlet/outlet so that the molten salt experiments can be carried out under dynamic inert gas atmosphere. The electrolyte is taken inside an alumina or ss crucible. Metal reflectors are provided towards the relatively colder, top inside area of the reactor to prevent vapours produced from the hot electrolyte at the bottom, from reaching those areas of the vessel and depositing over there. Schematic diagram of the reactor assembly is shown in Fig.7. Photograph of an electro-reduction experimental set up is given in Fig. 8.

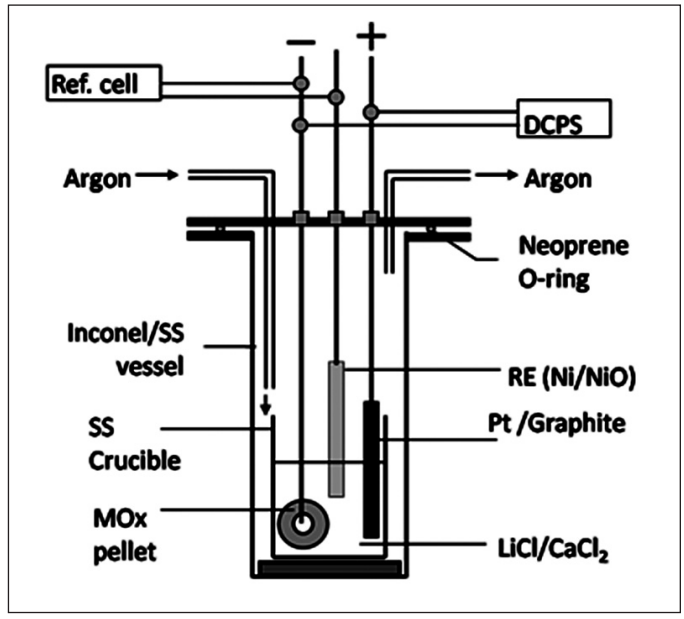

Fig.7: Schematic diagram of electro-reduction cell

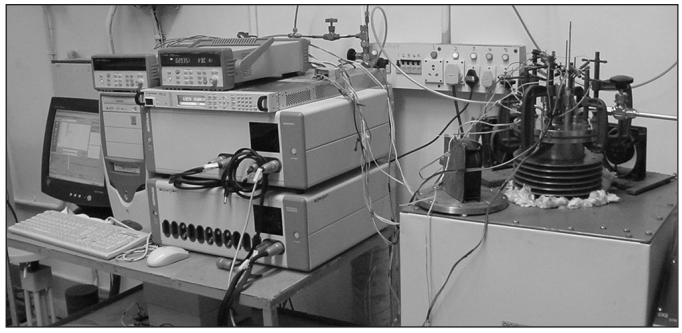

Fig.8: *The experimental set up for cyclic voltammetry and electro-deoxidation studies.*

As mentioned previously, both LiCl and $CaCl_2$ are air and moisture sensitive chemicals and hence it needs to be handled in inert atmosphere glove box as shown in Fig.9. Also, the electro-deoxidation experiments need to be carried out under the cover of purified argon gas flowing through the cell.

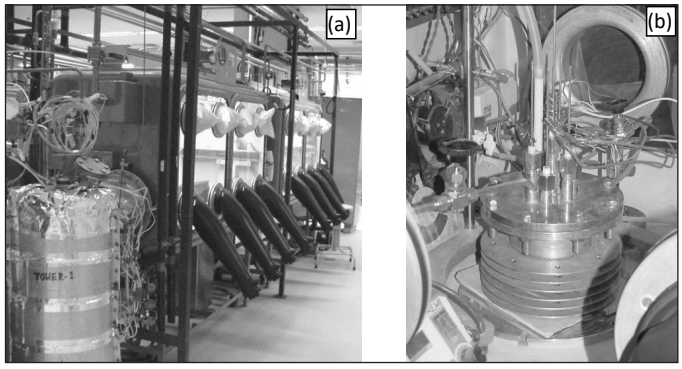

Fig.9: *Photograph of the argon gas atmosphere glove box (a) and a cell assembled inside the box (b).*

The required amount of the electrolyte salt powder is loaded in alumina/ss crucible and placed at the bottom of the reactor. All the electrodes are then introduced through the veco-seal arrangement provided at the top-mating flange of the reactor. The reactor vessel is taken out of the glove box after ensuring its leak tightness and placed vertically on the electric furnace kept outside. The reactor is heated to the desired temperature, even as purified argon gas is flushed through it. Upon melting of the salt, CV measurements are carried out with the help of a potentiostat to obtain the electrochemical window of the electrolyte. Thereafter the electrodes are dipped into the melt and electrical connections are made to the DC power supply, with the oxide as the cathode and graphite or platinum as the anode.

Typical electrolysis curve obtained during constant voltage (3.0 V) electro-deoxidation of TiO_2 in the FFC method is given in Fig. 10. As can be seen from the reaction scheme of the process discussed previously in section 1.1, the oxygen present in the oxide, changed as O^{2-} ions upon ionisation, leaves the cathode and discharges at the graphite anode as gaseous CO or CO_2. The flux of oxygen ions emanating from the oxide electrode is decreased with time, which is represented by the cell current. The experiment is stopped when the current becomes stable. Thereafter the cell is allowed to cool to room temperature and taken back to the glove box, where it is opened to recover the electrolysed product.

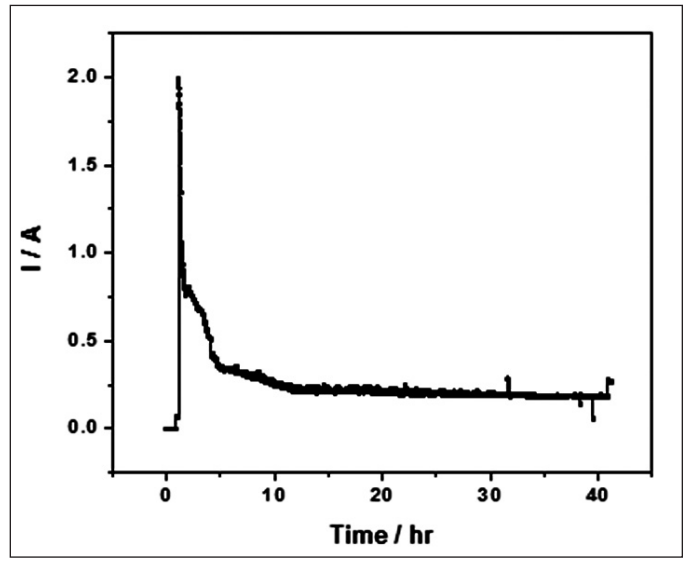

Fig.10: *Variation of cell current during electrolysis of a TiO_2 pellet in $CaCl_2$ melt at 3.0 V*

In the electro-lithiothermic reduction, ss crucible is loaded with required amount of LiCl and it is slowly heated to 650 °C. After the CV measurements, the cell is allowed to cool to room temperature and appropriate amount of Li_2O is added to make the required composition upon melting of the salt. Again CV measurements are carried out. The oxide pellets (often UO_2) placed in a perforated metal cup is used in the cell as cathode against a platinum coil anode. In the electro-calciothermic reduction of ThO_2 to Th, $CaCl_2$-CaO melt is used as electrolyte and graphite as the anode. Calcium has high solubility in the melt and hence effective deposition and retention of calcium metal on the ThO_2 pellets are difficult. Therefore, current efficiency of the electro-calciothermic process is lower than that of electro-lithiothermic process.

Unlike the FFC cells, the electro-metallothermic reduction cells using platinum as anode need better potential control to avoid dissolution of platinum in the melt. Hence, such cells are generally operated in the constant current mode. During electrolysis, lithium/calcium metal is electrochemically generated and deposited

on the MO_x pellets (cathode) and it is allowed to chemically react with the oxide pellets by interrupting the current applied to cell for a pre-determined period of time. When the current on the electrolytic cell is interrupted, the electrolytic cell reverts to a galvanic cell and the difference in the potential between the two cells, the IR drop, is shown up as vertical lines in the v-t curves (Fig. 11). In the beginning, the cathodic voltage, upon current interruption, shows high positive values indicating the presence of oxide in the pellet electrode. As electrolysis is continued, more and more area of the oxide electrode is reduced and finally when all of the oxide is reduced to metal, lithium metal deposits on it, as indicated by the Li/Li^+ potential of the electrode. Electrolysis is continued further for a little while, so as to allow deposition of sufficient lithium metal on the electrode and thus to maximize the extent of reduction of the oxide pellet. After completion of the experiment, the pellet is lifted and positioned above the melt and allowed to cool to room temperature under argon gas flow through the cell.

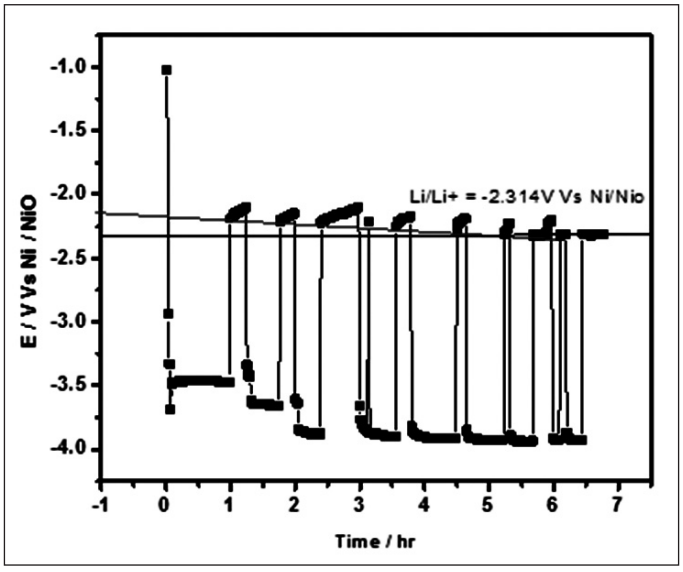

Fig. 11: Typical potential response of a UO_2 cathode during constant current electrolysis in LiCl-Li_2O melt (the vertical lines indicate IR drop during current interruption).

The electrolyzed pellet after recovery from the cell was thoroughly washed with distilled water to remove the adhered salt, vacuum-dried and then used for analysis. Phase identification of the product was carried out using XRD (PHILIPS xPERT diffractometer with Cu-Kα radiation) and microstructure using SEM (PHILIPS, XL 30 with EDX). Electro-reduction experiments were carried out using a DC power supply (Agilent Technologies, N6700B) and the potential and current data from these experiments were recorded using a data acquisition system (AGILENT, 34970A). The amount of oxygen present in the electrolyzed samples was determined by the inert gas fusion technique. In some experiments, the elemental composition of the electrolyzed samples was determined by ICP-OES method. From all these data, the nature and extent of reduction of the oxide to metal was ascertained. The reduced metal is highly porous in form and therefore amenable for re-oxidation and hence it is a good practice to consolidate it by vacuum induction melting to an ingot.

3. Our work at a glance

Results of some representative experiments carried out with different metal oxides in our laboratory and salient features of the reduction process are briefly discussed in this section.

3.1 Electro-lithiothermic reduction of UO_2

Uranium dioxide is the major constituent of spent oxide nuclear fuel and hence in the context of pyroprocessing, electro-reduction of it has been investigated in detail by a few groups [1,18-20]. We have carried out basic studies to understand the fundamentals of electro-reduction behavior of UO_2 with pellets weighing about a gram [21] and gradually developed the process for reduction of 200 g batches of UO_2, with a reduction efficiency of ~98%. The reduced pellets were distilled under vacuum at 900 °C to get rid of the adhering frozen salt and subsequently electro-refined in LiCl-KCl melt at 500 °C to gain the pure U metal from the electrolysed product containing about 2 wt% of UO_2. Apart from the LiCl-Li_2O melts, electro-reduction experiments were also carried out in $CaCl_2$-NaCl melt [22] and $CaCl_2$ deficient LiCl-KCl-$CaCl_2$ melt [23] to test the suitability of the melts for UO_2 reduction and also with an aim to study the mechanistic aspects of UO_2 reduction. It was concluded in this study that electrochemical reduction of UO_2 occurs by a one step, four electron transfer ($U^{4+} \rightarrow U$), without formation of any ternary intermediate compounds. Similarly, we have studied for the first time, the feasibility of use of graphite as anode in place of platinum in LiCl-Li_2O melt in UO_2 electro-reduction cells [24]. The studies showed that electro-reduction of UO_2 is possible with graphite anode, but buildup of carbon particulate matter in the melt affects the smooth operation of the cell and also the efficiency of electro-reduction in a significant manner. However, in the backdrop of the prohibitive cost of platinum, studies on the use of carbon anodes have picked up of late [25-28].

Details of a typical electro-reduction experiment carried out with 100g UO_2 pellets of dimension 6 mm dia. x 6 mm long in LiCl-1wt.% Li_2O melt with platinum anode at 650 °C, have been discussed below.

CV measurements gave the potentials for lithium deposition on W electrode, oxygen evolution on platinum electrode and platinum dissolution as -2.3 V, +0.5 V to +1.4 V, and +1.4 V respectively against Ni/NiO reference electrode. From this data, it was obvious that the platinum anode potential should be above +0.5 V and below +1.4 V for the electro-reduction to occur without anodic dissolution of platinum in the melt. The reduction of UO_2 to U in the electro-lithiothermic process, is assumed to take place as per the following two reactions, one electrochemical and the other chemical.

$$Li + e^- \rightarrow Li \text{ (at cathode – electrochemical)} \quad (16)$$

$$UO_2 + 4\,Li \rightarrow U + 2Li_2O \text{ (at cathode – chemical)} \quad (17)$$

The UO_2 pellets were taken in a crucible made of SS as shown in Fig.3. (section 1.3.2). Four platinum electrodes (2 mm diameter) shaped as coil were used as the anodes. The arrangement of electrodes above the electrolyte melt inside the cell is shown in Fig. 12.

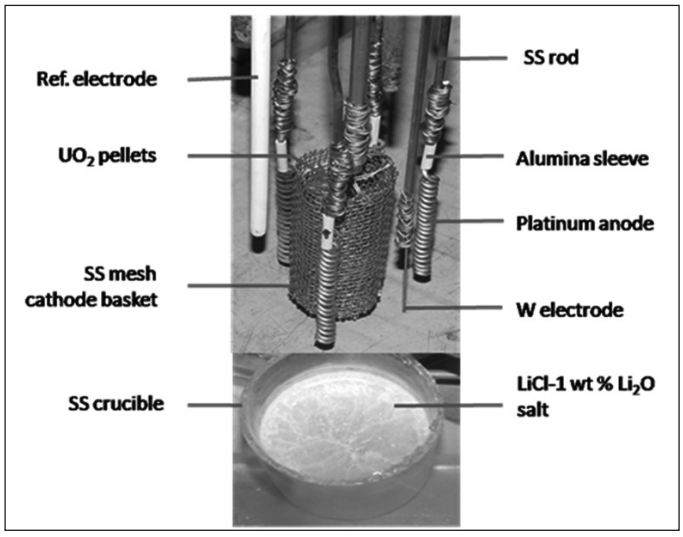

Fig.12: *The electrode arrangement inside the electro-deoxidation cell. Four platinum anodes are placed radially around the cathode basket containing UO_2 pellets. The crucible containing electrolyte can be seen below the electrode assembly.*

The electrolysis was carried out as per the procedure given towards the end of section 2.3. A constant current of 10 A was impressed on the cell, which made Li metal to deposit on the UO_2 cathode at -2.3 V. The electro-deposited lithium metal reacted with the UO_2 pellets as per the reaction (17). The alternate steps of deposition of lithium on the UO_2 pellets and allowing time for its reaction with the UO_2 pellets by interruption of the cell current were continued until the pellets were converted to U metal and lithium metal deposited on it. The experiment was discontinued after observing stable Li potential of the electrode for about 30 minutes. The electrolysis curve of the experiment resembled to that given in Fig. 11. Due to low current efficiency of molten salt electro-deoxidation processes, usually 150-200 % charge than that theoretically required for reduction of the given mass of UO_2 needs to be passed through the cell to obtain ~98% reduction of the oxide mass [29,30]. Therefore, 200% charge was passed through the cell in the present experiment.

The cell was allowed to cool to room temperature and the cathode basket containing electro-reduced U metal was removed from the cell. The cathode basket was cut through the middle to remove the electrolyzed U metal with significant amount of the frozen salt adhering to it. The cathode was taken in a ss distillation vessel and heated to 900 °C under vacuum to distill off all the LiCl salt adhering to it. The salt-free electrolysis product was analyzed for U metal content by quantitatively measuring the volume of hydrogen gas produced by reacting it with 48% HBr acid, $(U + 4HBr \leftrightarrow UBr_4 + 2H_2)$ in a gas burette. The hydrogen was also estimated using an in-house developed polymer hydrogen sensor [31]. It was found to contain ~98% U metal and the rest unreduced UO_2. The impure product is then electro-refined in a bath of LiCl-KCl-5 wt% UCl_3 to collect pure U metal. The impure metal was taken as the anode in the electro-refiner against a steel rod cathode. On application of a small potential difference between the electrodes, U metal was deposited on the steel cathode in the form of dendrites. The U dendrites were then vacuum-distilled at 900 °C to remove occluded salts and the salt-free metal was induction-melted to get a pure U metal ingot. All the unit process steps of electro-conversion, of UO_2 pellets to U metal, its purification and consolidation are depicted in Fig.13 below. The SEM images of the fractured surface of original UO_2 pellet and that of the electrolyzed product are given in Fig. 14a and 14b respectively.

Having studied the reduction process in 200g scale, a molten salt experimental facility is being buit up at present to carry out electrochemical reduction of UO_2 and other oxides in kilogram scale.

3.2 Electro-lithiothermic reduction of ZrO_2

Zirconium is an important element in the preparation of many metal alloys. In nuclear technology, reduction of ZrO_2 to Zr assumes importance in the context of pyroprocessing of spent oxide nuclear fuels [18], which contains ZrO_2. For reprocessing of the spent oxide fuel, all the oxides present in the spent fuel needs to be reduced to metal form first and then the mixture subjected to molten salt electro-refining to recover the actinides of interest. The reduction of ZrO_2 to Zr in LiCl-Li_2O melt is reported as very difficult due to the formation of intermediate compound,

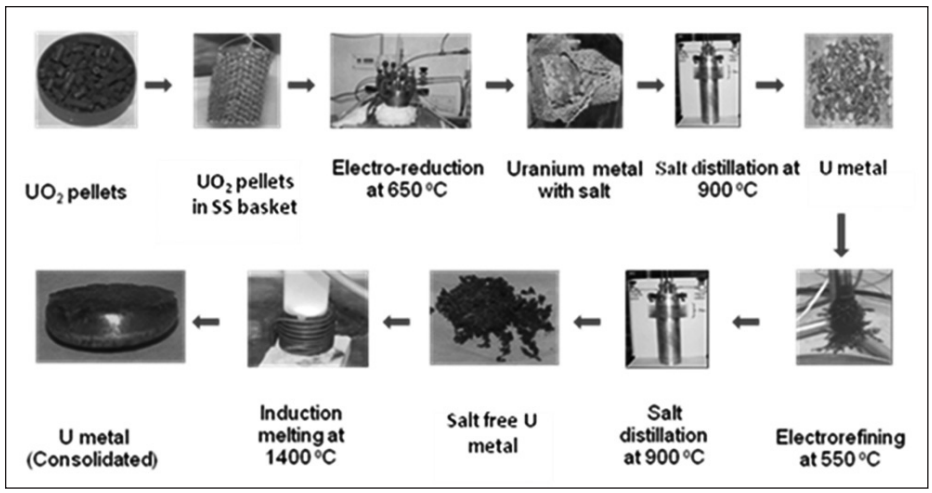

Fig.13: *Unit steps of electrochemical conversion of UO_2 pellets to U metal, its purification by electro-refining in LiCl-KCl-UCl_3 bath at 550 °C and consolidation by induction melting*

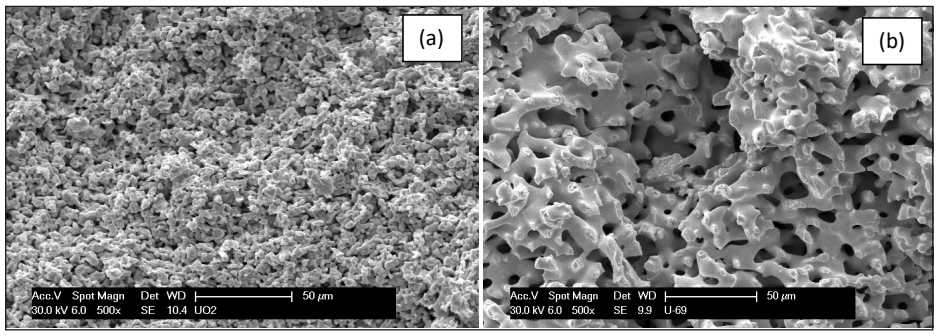

Fig. 14: SEM images of fractured surface of (a) original UO2 pellet and (b) the electro-reduced U metal.

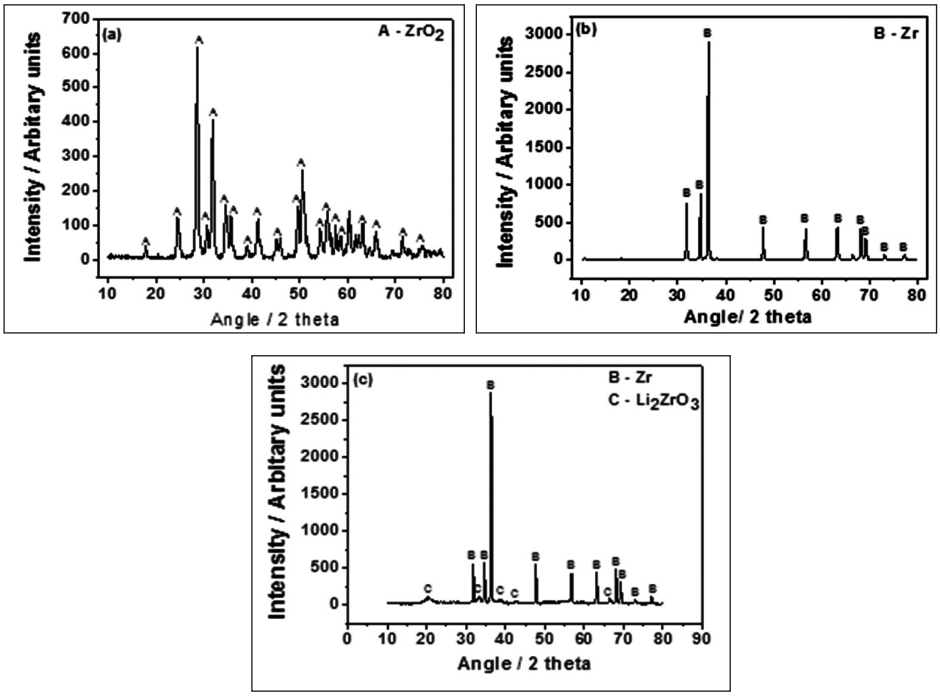

Fig.15: XRD spectra of the original ZrO2 pellet (a) the pellet after electrolysis in pure LiCl (b) and in LiCl-0.5wt.% Li2O melt (c) with graphite anode.

Li_2ZrO_3, which is considered to resist the reduction [32,33]. We have taken up the study on electro-reduction of ZrO_2 in this backdrop. We have studied the electrochemical reduction behavior of both ZrO_2 and Li_2ZrO_3 [34].

Powder compacted and sintered ZrO_2 pellet, (i) wound around with SS wire (which also served as the current lead to the oxide pellet) and (ii) placed in SS crucible were the two kinds of cathode assemblies used in the study. Pure LiCl and LiCl containing varying quantities, up to 1wt.%, of Li_2O were used in the different experiments. Graphite was used as anode for the melt compositions, LiCl (0-0.5) wt.% Li_2O and platinum for the compositions, LiCl-(0.5,1) wt.% Li_2O. Li_2ZrO_3 pellets were also prepared and subjected to electrolysis. 200 to 300% of charge, compared to that theoretically required for reduction of the mass of the ZrO_2/Li_2ZrO_3 electrode, was passed through the cell in most of these experiments. The electrolysis was carried out in a similar way, as explained above for the reduction of UO_2.

XRD pattern of the original ZrO_2 pellet and the pellet after electrolysis in pure LiCl and in LiCl-0.5wt.% Li_2O melt with graphite anode are given in Fig.15 a, b and c. The pellet was electro-reduced to Zr metal in both the melts, but very small amounts of Li_2ZrO_3 was also present in the samples reduced in the Li_2O containing melt, indicating thereby that the formation of the ternary compound is possible in Li_2O containing melts. The results of experiments carried out with 0.5 wt.% and 1 wt.% Li_2O melts, with platinum anode and given in Table 1, too showed that the oxide was reduced to Zr and small quantities of Li_2ZrO_3 was also present in the reduced sample.

Table 1. Details of experiments and results of analysis of the reduction products of ZrO_2 electrolysis in LiCl-Li_2O melt using platinum anode.

Melt	Mode of electrolysis	Charge passed (%)	Phases identified in XRD analysis
LiCl-0.5 wt.% Li_2O	CC at 0.5-0.75 A	200	Zr
LiCl-1 wt.% Li_2O	CC at 1 A (ZrO_2 pellets in SS cup)	200	ZrO_2, Li_2ZrO_3
LiCl-1 wt.% Li_2O	CC at 0.5 A	200	Zr (M), Li_2ZrO_3 (m)

CC= Constant Current, M=Major, m= minor

The electro- reduction experiments carried out with Li_2ZrO_3 pellets, in similar way as done for ZrO_2 pellets, showed that it could also be reduced to zirconium metal, contrary to the reports available in the literature [32,33]. It was concluded in this study [34] that the configuration of the ZrO_2 electrode used, viz. powder compacted and sintered solid preform connected directly to the current lead wire, probably made the difference in the results. Mohandas and Fray [35,36] studied electrochemical reduction of ZrO_2 pellets in $CaCl_2$ melt at 900 °C and reported that electro-reduction of ZrO_2 pellets was difficult when those were sintered at temperatures lower than 1100 °C, but reduced when the sintering temperature was raised above 1200 °C. It is assumed that the electrical resistance of the ZrO_2 pellet was decreased by higher temperature sintering and the better electron transport in the pellet thus became possible, helped in its electro-reduction to Zr. This, probably, was not possible with pellets sintered at lower temperature and also with powder electrodes. The previous studies were carried out with small quantities of ZrO_2 powders and, it appears, that this electrode configuration was not appropriate for lithium metal deposition on the poor conducting oxide particles and hence its reduction.

3.3 Electro-reduction of TiO_2 (FFC Cambridge process)

Titanium is the most sought after metal of our times due to its many excellent properties as structural, corrosion-resistant and bio-compatible material. It is also a metal of strategic importance. Titanium is produced by the conventional Kroll process, where TiO_2 is carbochlorinated at 900 °C to $TiCl_4$, which is subsequently chemically reduced to titanium by magnesium [37]. The batch process is labour-intensive and cumbersome and hence titanium cost is prohibitively high. Efforts were continuing internationally, to develop an alternative electrochemical reduction process for titanium production. FFC Cambridge process has many a good features for reduction of TiO_2 to Ti and hence it is being studied for production of titanium all over the world [7, 38-41]. We have carried out extensive studies to understand the fundamental aspects of electro-reduction of TiO_2 with powder compacted and sintered pellets [42] as well as sintered powders [43]. As reported previously by many groups in this area [44, 45], we also observed that the reduction of the oxide proceeded via. formation and decomposition of Ca-Ti-O intermediate compounds. Schwandt et al [44] have reported the reduction pathway of TiO_2 to Ti in the FFC process as given below:

$$5TiO_2 + Ca^{2+} + 2e^- = Ti_4O_7 + CaTiO_3 \quad (18)$$

$$4Ti_4O_7 + Ca^{2+} + 2e^- = 5Ti_3O_5 + CaTiO_3 \quad (19)$$

$$3Ti_3O_5 + Ca^{2+} + 2e^- = 4Ti_2O_3 + CaTiO_3 \quad (20)$$

$$2Ti_2O_3 + Ca^{2+} + 2e^- = 3TiO + CaTiO_3 \quad (21)$$

$$CaTiO_3 + TiO = CaTi_2O_4 \quad (22)$$

$$CaTi_2O_4 + 2e^- = 2TiO + Ca^{2+} + 2O^{2-} \quad (23)$$

$$TiO + 2e^- = Ti + O^{2-} \quad (24)$$

A schematic representation of the progress of reduction of titanium dioxide powder particles to titanium, given in Ref. 43, has been reproduced below (Fig.16).

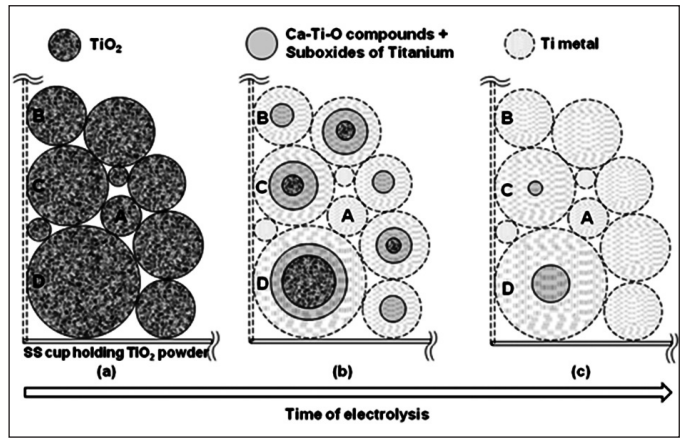

Fig.16: *A schematic showing the progress of electro-reduction of a TiO_2 powder electrode in $CaCl_2$ melt with time [43].*

Results of a typical electro-reduction experiment, carried out with 10g of hand-shaped and sintered TiO_2 granules are given below. The potential vs time graph during the electro-reduction run and the corresponding current trace are given in Fig.17 a and 17 b respectively. During this experiment, potential was applied in steps of 0.3 V from 2.5 V to 3.1 V with hold at 2.5 V for 10h, then at 2.8 V for 24 h and finally maintained at 3.1 V for rest of the electrolysis duration. The electrode was held at each voltage until the electrolytic current was decreased to the

lowest stable value (Fig.17 b). This indicated the end of reactions taking place in the cathode in that particular voltage regime. The outlet gas from the cell during the period was tested for the presence of CO_2 by bubbling it through baryta ($Ba(OH)_2$) solution and absence of white precipitate confirmed the absence of CO_2 evolution on the anode and hence the end of the de-oxidation reactions at the applied potential. These two data were used to monitor and control the electrolysis. The granules after the run were washed by ultrasonicating them with dilute HCl followed by distilled water to remove the adhered salt.

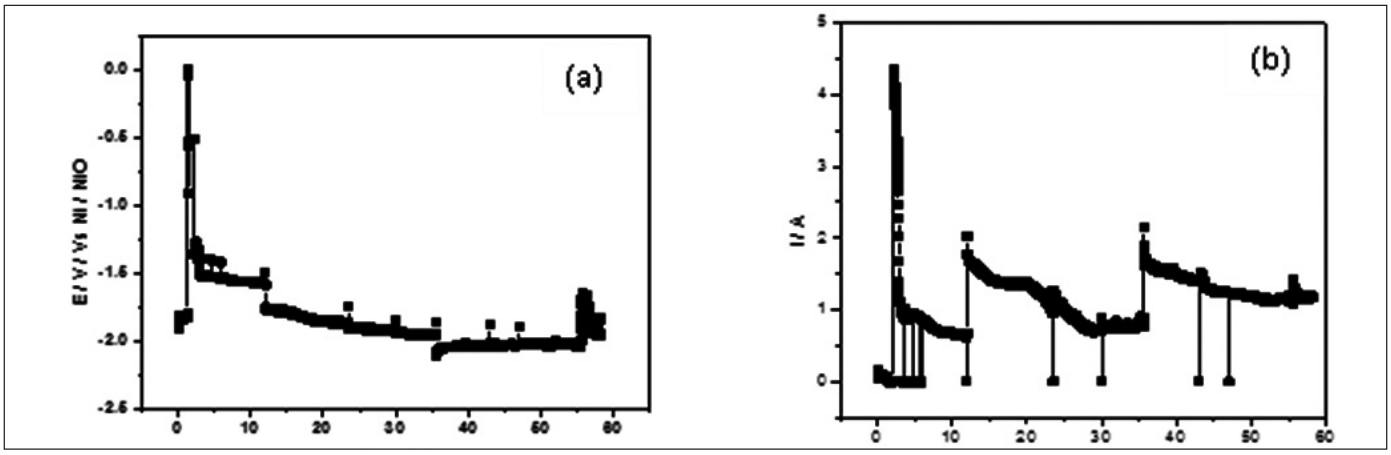

Fig.17: *(a) Variation of the potential of TiO_2 cathode with time and (b) the corresponding current trace during its electrolysis in $CaCl_2$ melt at 900 °C.*

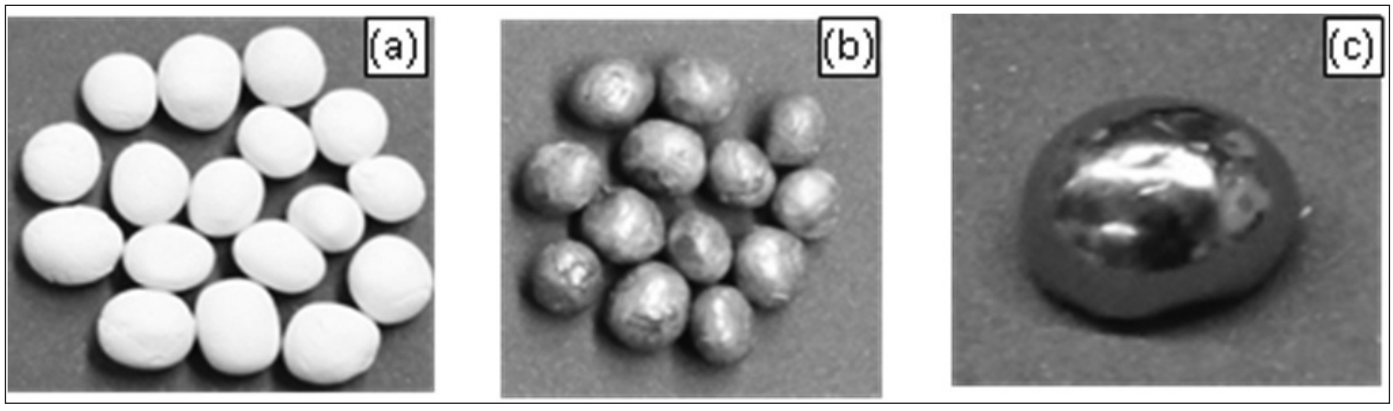

Fig.18: *Photograph of TiO_2 granule (a) before electrolysis (b) cleaned after electrolysis and (c) consolidated Ti button obtained by induction melting.*

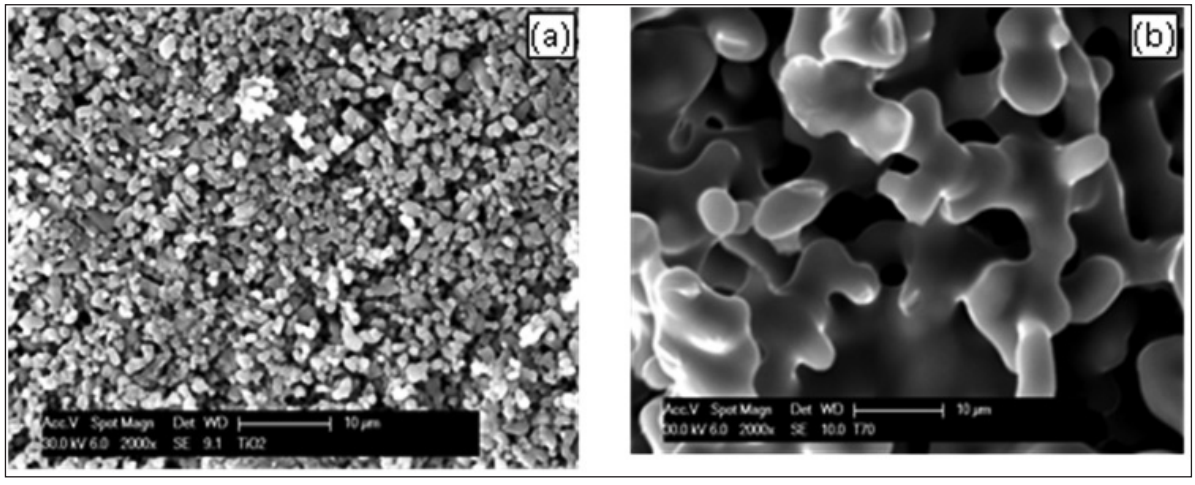

Fig.19: *SEM image of granule (a) before and (b) after electrolysis*

The dried granules were then manually polished to remove the adhering black coating on those. The photographs of the original granules and the product obtained after electrolysis are given in Fig.18a and 18b respectively. About 1 g of the Ti metal product was arc melted to obtain a fine Ti button (Fig.18c). The oxygen content of the Ti metal button was estimated as 150 ppm by inert gas fusion technique. The SEM of the fractured surface of original TiO_2 granule and the Ti metal produced from it are shown given in Fig.19a and 19b respectively. The nodular microstructure of the product clearly shows that the granule was converted to Ti metal.

3.4 Electro-reduction of solid ThO_2 to Th (electro-calciothermic and FFC process)

Thorium based metallic alloys are being considered as fuel for future metal fuelled fast nuclear reactors and hence conversion of ThO_2 to Th is of importance to nuclear technology.

ThO_2 powder was prepared in-house by gel-combustion method, where thorium nitrate pentahydrate $[Th(NO_3)_4.5H_2O]$ was allowed to react with citric acid $[C_6H_8O_7]$ at 200-240 °C in air as per the equation.

$$(4\ Th(NO_3)4.\ 5H_2O + 2C_6H_8O_7 + 5O_2 \longleftrightarrow 4\ ThO_2 + 16\ NO_2 + 12\ CO_2 + 28\ H_2O) \quad (25)$$

Electro-deoxidation studies were carried out in both electro-calciothermic and FFC methods in $CaCl_2$-0.5wt.%CaO melts and in pure $CaCl_2$ melt respectively. The CV measurements gave calcium metal deposition (-2.27 V), chlorine gas evolution (+0.97 V) and CO_2 gas evolution (+0.33 V) potentials. CV measurements were also carried out with the sintered ThO_2 pellet as the working electrode against graphite rod as the counter electrode. The CV trace obtained is shown in Fig.20. On the forward (cathodic) scan, one current wave starting at -1.12 V and and peaking at – 1.84 V was seen. This current wave corresponded to the electro-reduction of ThO_2 to Th ($Th^{4+} \rightarrow Th$). As the scan was extended to higher cathodic potentials, calcium metal was deposited on the ThO_2 electrode ($Ca^{2+} + 2e = Ca$). On the anodic side, two current waves, the first one peaking at -1.37 V and second one peaking at - 0.58 V were seen. The first wave was attributed to the oxidation of the cathodically generated Ca metal ($Ca \rightarrow Ca^{2+} + 2e$) and the second wave to the oxidation of the Th metal to ThO_2 ($Th \rightarrow Th^{4+}$).It was inferred from these data that electro-deoxidation of ThO_2 to Th, in both $CaCl_2$ and $CaCl_2$-0.5 wt.%CaO melts, will occur at - 1.84 V and beyond [46].

In order to understand the mechanism of electro-deoxidation of ThO_2 to Th in both FFC process and electro-calciothermic process, few pellets were subjected

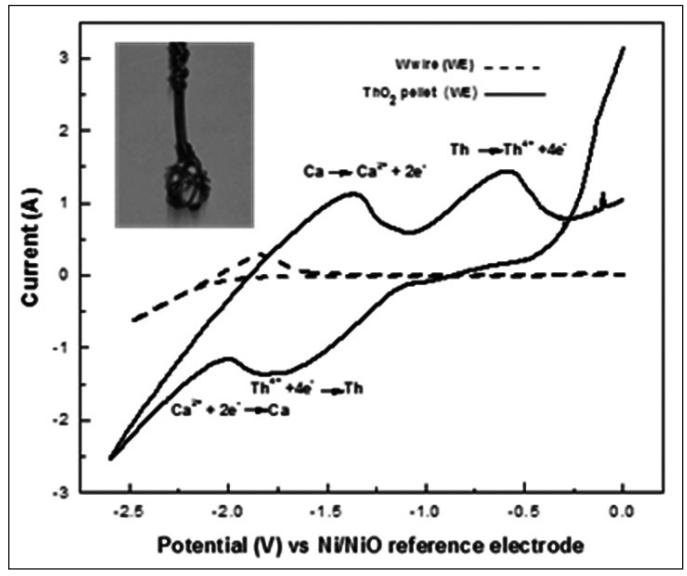

Fig. 20: Cyclic voltammograms of tungsten and ThO_2 pellet working electrodes in $CaCl_2$-0.5 wt.% CaO melt at 900 °C, Scan rate 50 mV/s. Inset: Photograph of the tantalum wire wound ThO_2 working electrode.

to electrolysis for different durations of time. The crystallographic phases identified in those pellets by XRD analysis are given in Table 2. From the results it was discerned that thorium dioxide was converted to thorium in a single step of four electron transfer similar to the conversion of UO_2 to U and no intermediate compounds were formed in the reduction process [47]. The reduction occurred much faster in the electro-calciothermic process than in the FFC process. The XRD of original ThO_2 pellet and that of the reduced product are shown in Fig.21a and 21b. The corresponding SEM images are shown in Fig. 21c and 21d respectively.

Table 2: The results of electro-reduction of ThO_2 pellet electrodes in the FFC and electro-calciothermic processes

Electro-lysis run no.	FFC Cambridge process		Electro-calciothermic reduction process	
	Time (h)	Phases	Time (h)	Phases
(1)	2	ThO_2	2	ThO_2 (major), Th (minor)
(2)	6	ThO_2 (major), Th (minor)	4	ThO_2 (minor), Th (major)
(3)	12	ThO_2 (minor), Th (major)	8	Th
(4)	24	Th	12	Th
(5)	48	Th	--	

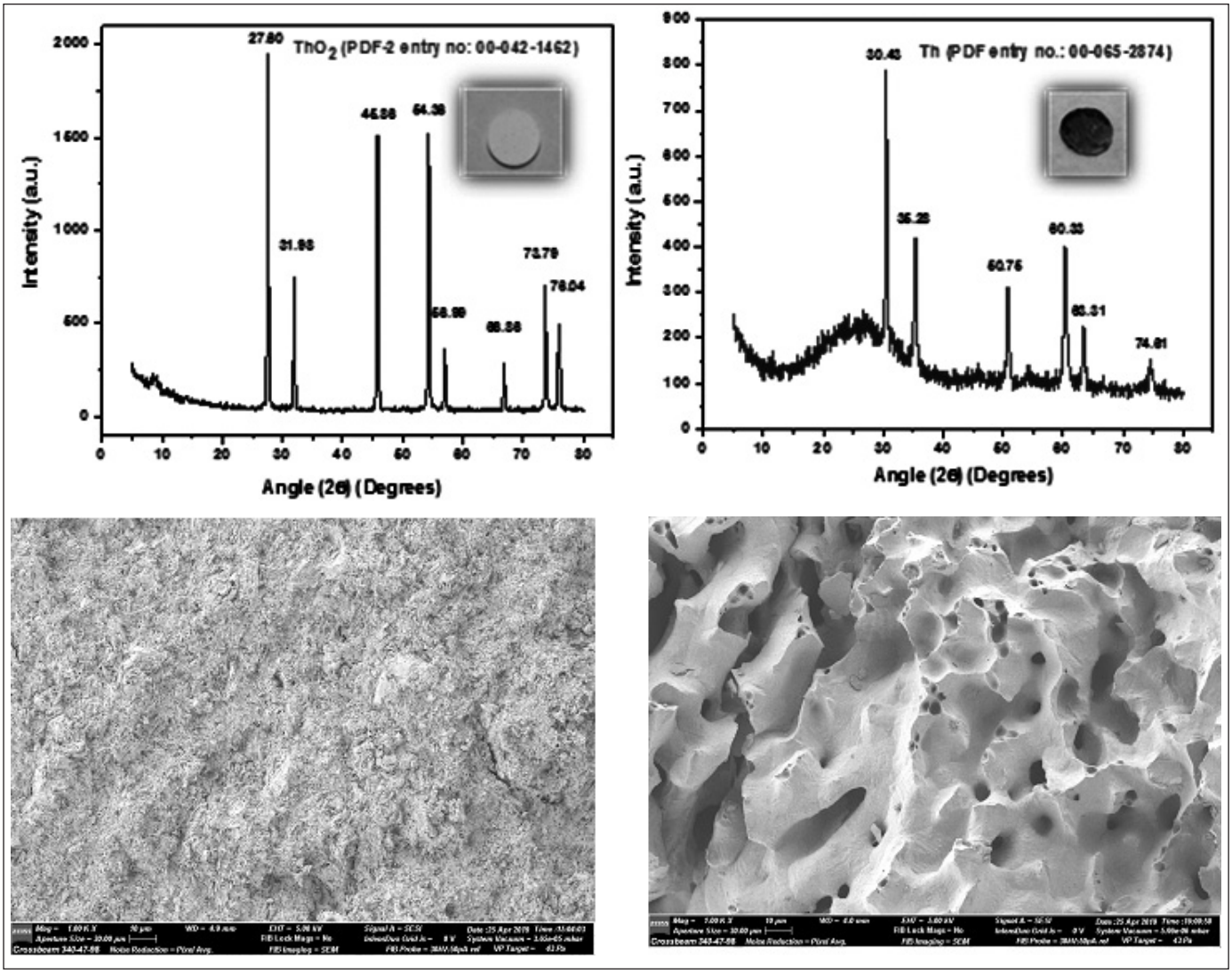

Fig. 21: The XRD patterns and SEM images (cross-section) of sintered ThO_2 pellet before and after electro-reduction are shown in [(a) and (b)] and [(c) and (d)] respectively.

3.5. Electro-reduction of Nb_2O_5 (FFC Cambridge process & electro-calciothermic process)

Niobium is a very important metal ingredient in the making of various types of stainless steel, alloys for aerospace applications, super alloys of importance like those used in heat exchangers of nuclear reactors and also for making superconductive magnets. Basic studies on the electro-reduction behavior of Nb_2O_5 were carried out on sintered Nb_2O_5 pellets in various melts to investigate the reaction mechanism. The investigations revealed that the electro-reduction of solid Nb_2O_5 to Nb occurs in three stages; i) cathodic insertion of calcium ion into the oxide electrode to form calcium niobates ii) formation and decomposition of the higher calcium niobates and suboxides of Nb (iii) calciothermic reduction of oxide by Ca metal produced during electrolysis and the three steps may be occurring together or individually [48]. The mechanism was arrived at by sampling of the reaction products at different intervals of time during the course of electro-reduction of dense Nb_2O_5 pellets and by analysis and characterization of the pellets by different techniques including XRD, SEM/EDS, wet chemical analysis, oxygen determination by inert gas fusion etc. The half-cell potentials of the cathode measured throughout the course of reduction of the pellet were also used in the analysis of the chemical phases present in the partially-reduced samples. The influence of various parameters on the reduction process, viz. temperature of operation, porosity, melt composition, applied voltage and anode material were also investigated. High temperature, high open porosity and high applied voltage were found to enhance the extent of reduction of the original preform [49].

3.6 Electro-reduction of CeO_2 (FFC Cambridge process)

Many chemical and physical properties of CeO_2 are similar to that of PuO_2 and hence the former is used as a surrogate to the latter in nuclear research to avoid handling of radiotoxic PuO_2. Electro-deoxidation experiments were carried out, in the FFC mode, with powder compacted and sintered CeO_2 pellets in molten $CaCl_2$ (900 °C) and molten $CaCl_2$-32 wt% NaCl (650 °C) electrolytes. Unlike the results obtained with all other oxides discussed this far, in most of the experiments, CeO_2 was converted to CeOCl only and not to Ce [50]. Similar results were reported by Claux et al [51]. However, Ce metal was formed when a preform made of a mixture of CeO_2 and NiO_2, was electro-deoxidised [52]. This showed that formation of Ce metal is favoured in the presence of an alloying element like Ni (forming Ni-Ce alloy), but in the absence of it, formation of CeOCl is thermodynamically more favoured.

$$CeO_2 + 3\,Ca + 2CaCl_2 \rightarrow 4\,CeOCl + 2\,CaO \quad (26)$$

$$2CeO_2 + 2\,e^- + CaCl_2 \rightarrow 2CeOCl + 2\,CaO \quad (27)$$

Claux et al [51] proposed the above two reactions for formation of the thermodynamically favoured CeOCl. CeOCl probably prevents reduction of the oxide to Ce. The result may be extendable to the electrochemical reduction of plutonium too in the FFC Cambridge process.

3.7 General studies

Some unique experiments were carried out as part of this study to probe into the very fundamental nature of solid-state electrochemical conversion of metal oxide to metal in the FFC Cambridge process.

There was a strong feeling in a section of investigators that the oxide reduction in the FFC Cambridge process was effected by calcium metal and not electrons. In order to gain clarity on this fundamental problem, we have carried out electrochemical reduction of Nb_2O_5 in molten sodium chloride medium. Unlike CaO, Na_2O is less stable than that of Nb_2O_5 and hence reduction of Nb_2O_5 to Nb by sodium metal is thermodynamically not feasible. However, Nb_2O_5 was found reduced to Nb in our study [53]. In the absence of any other reductant available in the molten salt medium, it was inferred that the reduction was effected by electrons as follows.

$$Na_xNb_yO_z + (2z\text{-}x)e^- \rightarrow yNb + xNa^+ + zO^{2-} \quad (28)$$

The 'oxygen ionization mechanism' must, therefore, be applicable to reduction of oxides in molten calcium chloride in the FFC Cambridge process too. However, our study proved that unlike other melts, calcium chloride or calcium chloride containing melts provided a strong reducing environment under cathodic polarizing conditions due to the presence of electro-generated Ca^+ ions and this favorable condition was aiding the reduction of the oxides in the FFC Cambridge process, in addition to the oxygen ionization by electrons [23, 54].

As mentioned previously, three phases, viz. the oxide, electron and electrolyte should coexist for electro-reduction to occur in a solid oxide and as a consequence of this condition (3-PI mechanism), the electro-reduction will preferably occur on the outer surface of the oxide preform and the reaction front will move inward with time. However, if the oxide is electrically conducting, electrons will be available throughout the preform so that the 3-PI condition can be reduced to 2-PI, which in turn could alter the physical progress of reduction of the oxide through the preform. Through a comparison of the electro-reduction behavior of electrically conducting TiO_2 and non-conducting SiO_2, we have proved that this in fact is the case [55]. Similarly, influence of electrical conductivity of the solid oxide electrode and the intermediate compounds formed during electro-reduction on the electro-reduction process was demonstrated by a comparative study of the electroreduction behavior of good conducting TiO_2 and poor conducting ZrO_2 electrodes [56].

In cyclic voltammetric measurements, the potential-current data of the working electrode are only measured and used to gain information on the electrode reactions. However, we have observed that simultaneous measurement of the counter electrode potentials can be useful in gaining a comprehensive understanding of the cell reaction, especially in the case of electro-reduction cells where multiple electrode reactions take place during conversion of the oxide to metal [57]. Understanding of the net cell reactions, prior to operation of an electro-reduction cell, can be of help in the better planning and operation of the electro-reduction cell.

4. Conclusion

Direct conversion of solid metal oxides to metal in a single step by high temperature molten salt electrolysis offers a huge advantage over the conventional chemical and electrochemical reduction methods of production of metal from oxides. The generic processes can be used to produce many metals in the periodic table, but as the chemical and electrical characteristics are unique to each metal oxide and metal, the process may require some modifications to achieve the necessary conditions for electro-reduction of such a variety of metal oxides. Though R&D work on the metal production processes have been going on for the past two decades, none is developed to a scale for commercial exploitation as of today, though significant strides have

been made in the electrochemical reduction of UO_2 and spent oxide fuels. Most of the high temperature molten salt processes for metal production, be it the Hall Heroult process for aluminium production or the other processes for alkali and alkaline metal production, took a long time since its discovery to shape those as full-fledged processes for commercial exploitation as we see today. The direct solid state electro-reduction processes are of recent origin only and persistent efforts over a long period of time might develop these processes too for commercial exploitation in the years to come. Our limited experience in this area of work, a gist of which is given in this article, makes us believe that the processes have the potential to emerge as successful alternative metal production technologies for production of at least a few metals in the periodic table. The simplicity and the environment-friendly nature of the direct solid-state electro-deoxidation processes when compared to the cumbersome, labour-intensive and unsafe nature of conventional metal production processes, make a strong case for development of the former processes for metal production for the modern world.

Acknowledgement

The authors wish to express thanks to Shri. V. Arunkumar for his excellent support in carrying out the electro-reduction experiments and also in the preparation of several samples for analysis and characterization by different techniques.

References

1. K. S. Mohandas, *Mineral Processing and Extractive Metallurgy (Trans. Inst. Min. Metall. C)*, 2013,*122*, 195-212.
2. K. S. Mohandas, D. J. Fray, *Trans. Indian. Inst. Met.*, 2004, *57*, 579-592.
3. D. J. Fray, T. W. Farthing, G. Z. Chen, *International Patent WO 99/64638, PCT/GB99/01781*, 1999.
4. K. V. Gourishankar, L. Redey, M. A. Williamson, *Light Metals (ed:W. Schneider), The Minerals, Metals and Materials Society (TMS), Warrendale, PA*, 2002, 1075-1082.
5. K. Ono, R. O. Suzuki, *The Journal of The Minerals, Metals & Materials Society*, 2002, *54*, 59-61.
6. A. H. Jones, R. Watson, T. Paget, R. Campbell-Kelly, T. Caldwell, D. J. Fray, *Journal of Nuclear Fuel Cycle and Waste Technology*, 2015, *13*, 1-5.
7. G. Z. Chen, D. J. Fray, T. W. Farthing, *Nature*, 2000, *407*, 361-364.
8. A. M. Abdelkader , K. T. Kilby , A. Cox, D. J. Fray, *Chem. Rev.*, 2013, *113*, 2863-2886.
9. A. Merwin, M. A. Williamson, J. L. Willit, D. Chidambaram, *J. Electrochem. Soc.*, 2017, *164*, H5236-H5246.
10. R. O. Suzuki, S. Fukui, *Materials Transactions*, 2004, *45*, 1665-1671.
11. Y. Sakamura, M. Kurata, T. Inoue, *J. Electrochem. Soc.*, 2006, *153*, D31-D39.
12. K. S. Mohandas, L. Shakila, N. Sanil, D. S. M. Vishnu, K. Nagarajan, *Proceedings of the FRAY International symposium on Metals and Materials Processing in a Clean Environment, Cancun, Mexico, Molten Salts & Ionic Liquids*, 2011, *3*, 239-252.
13. C. Schwandt, D.J. Fray, *Z. Naturforsch.*, 2007, 62a, 655-670.
14. C. Schwandt, D.T.L. Alexander, D.J. Fray, *Electrochimica Acta*, 2009, 54, 3819-3829.
15. D. S. M. Vishnu, J. Sure, K. S. Mohandas, *Carbon*, 2015, *93*, 782-792.
16. C. Schwandt, *Electrochimica Acta*, 2018, 280, 114-120.
17. T. B. Joseph, N. Sanil, L. Shakila, K. S. Mohandas, K. Nagarajan, *Electrochimica Acta*, 2014, *139*, 394-400.
18. E.Y. Choi, S. M. Jeong, *Progress in Natural Science: Materials International*, 2015, *25*, 572-582
19. C. S. Seo, S. B. Park, B. H. Park, K. J. Jung, S. W. Park, S. H. Kim, *J. Nucl. Sci. and Technol.*, 2006, *43*, 587-595.
20. E. Y. Choi, J. M. Hur, I. K. Choi, S. G. Kwon, D. S. Kang, S. S. Hong, H. S. Shin, M. A. Yoo, S. M. Jeong, *J.Nucl. Mater.*, 2011, *418*, 87-92.
21. T. Biju Joseph, N. Sanil, K.S. Mohandas, K. Nagarajan, *Proceedings of the Conference on Molten Salts in nuclear Technology (CMSNT 2013)*, BARC, Mumbai, January 9-11, 2013, 226-229.
22. D.S. Vishnu, N. Sanil, G. Panneerselvam, R. Sudha, K. S. Mohandas, K. Nagarajan, *J. Electrochem. Soc.*,2013, *160*, D394-D402.
23. D. Sri Maha Vishnu, N. Sanil, K.S. Mohandas, K. Nagarajan, *Journal of Nuclear Materials*, 2016, *470*, 179-186.
24. T. Biju Joseph, N. Sanil, K. S. Mohandas, K. Nagarajan, *J. Electrochem. Soc.*, 2015, *162*, E51-E58.
25. H. Y. Ryu, S. M. Jeong, Y. C. Kang, J. G. Kim, *Asian Journal of Chemistry*, 2013, *25*, 7019-7022.
26. S. W. Kim, D. H. Heo, S. K. Lee, M. K. Jeon, W. Park, J. M. Hur, S. S. Hong, S. C. Oh, E. Y. Choi, *Nuclear Engineering and Technology*, 2017, *49*, 1451-1456.
27. J.M. Hur, J.S. Cha, E.Y. Choi, *ECS Electrochem. Lett.*, **2014,** *3*, E5-E7.
28. S. W. Kim, M. K. Jeon, H. W. Kang, S. K. Lee, E. Y. Choi, W. Park, S. S. Hong, S. C. Oh, J. M. Hur, *J. Radioanal. Nucl. Chem.*, 2016, *310*, 463–467.
29. E. Y. Choi, J. W. Lee, J. J. Park, J. M. Hur, J. K. Kim, K. Y. Jung, S. M. Jeong, *Chemical Engineering Journal*, 2012, *207-208*, 514-520.
30. W. Park, E. Y. Choi, S. W. Kim, S. C. Jeon, Y. H. Cho, J. M. Hur, *J Nucl Mater*. 2016, *477*, 59-66.
31. D. S. M. Vishnu, N. Sanil, N. Murugesan, L. Shakila, C. Ramesh, K. S. Mohandas, K. Nagarajan, *J. Nucl. Mater.*, 2012, *427*, 200-208.
32. Y. Sakamura, M. Lizuka, S. Kitawaki, A. Nakayoshi, H. Kofuji, *J Nucl Mater.*, 2015, *466*, 269-279.
33. S. D. Herrmann, L. A. Wurth, N. J. Gese, *International Pyroprocessing Research Conference, Fontana, Wisconsin*, August 27, 2012.
34. K. S. Mohandas, N. Sanil, L. Shakila, *J. Nucl.Mater.*, 2019, *521*, 109-119.

35. K. S. Mohandas, D. J. Fray, *Metall. Mater. Trans. B*, 2009, *40*, 685-699
36. K. S. Mohandas, D. J. Fray, *Proceedings of the FRAY International symposium on Metals and Materials Processing in a Clean Environment, Molten Salts & Ionic Liquids., Cancun, Mexico*, 2011, *3*, 219-238.
37. W. J. Kroll, *Trans. Electrochem. Soc.*, 1940, *78*, 35-47.
38. C. Schwandt, G. R. Doughty, D. J. Fray, *Key Engineering Materials*, 2010, *436*, 13-25.
39. M. Ma, D. Wang, W. Wang, X. Hu, X. Jin, G. Z. Chen, *Journal of Alloys and Compounds*, 2006, *420*, 37-45.
40. Ch. R. V. S. Nagesh, *Titanium extraction technologies, DRDO Technology Spectrum*, May 2012, 139-145.
41. Ch. R. V. S. Nagesh, C. S. Ramachandran, *Transactions of Nonferrous Metals Society of China*, 2007, *17*, 429-433.
42. K. S. Mohandas, L. Shakila, N. Sanil, D. S. M. Vishnu, K. Nagarajan, *Proceedings of the FRAY International symposium on Metals and Materials Processing in a Clean Environment, Molten Salts & Ionic Liquids Cancun, Mexico*, 2011, *3*, 253-268.
43. D. Sri Maha Vishnu, N. Sanil, L. Shakila, R. Sudha, K.S. Mohandas, K. Nagarajan, *Electrochimica Acta*, 2015, *159*, 124–130.
44. C. Schwandt, D. J. Fray, *Electrochimica Acta*, 2005, 51, 66-76.
45. D. T. L. Alexander, C. Schwandt, D. J. Fray, *Electrochimica Acta*, 2011, *56*, 3286-3295.
46. A. Mukherjee, K.S. Mohandas, M. Joseph, Proceedings of the *DAE-BRNS 13th National Symposium on Nuclear and Radiochemistry (NUCAR-2017), KIIT University, Bhubaneswar,* ***6th-10th February,*** 2017.
47. A. Mukherjee, R. Kumaresan, K. S. Mohandas, B. P. Reddy; *Proceedings of the Symposium on 'Critical Non-Ferrous Metals: Establishing the value chain' (CNFM – 2019), IIT Bombay, Mumbai*, 15th – 16th April, 2019.
48. D. S. M. Vishnu, N. Sanil, L. Shakila, G. Pannerselvam, R. Sudha, K. S. Mohandas, K. Nagarajan, *Electrochimica Acta*, 2013, *100*, 51-62.
49. D. S. M. Vishnu, N. Sanil, K.S. Mohandas, K. Nagarajan, *Acta Metall. Sin. (Engl. Lett.)*, 2017, *30*, 218-227.
50. N. Sanil, L. Shakila, D.S. Vishnu, K.S. Mohandas, K. Nagarajan, *Abstracts of the Second International Conference on Advances in Nuclear Materials (ANM-2011), Mumbai*, 2011, 151.
51. B. Claux, J. Serp, J. Fouletier, *Electrochimica Acta*, 2011, *56*, 2771-2780.
52. B. Zhao, L. Wang, L. Dei, G. Cui, H. Zhou, R. Vasanthakumar, *Journal of Alloys and Compounds*, 2009, *468*, 379-385.
53. D. S. M. Vishnu, N. Sanil, K.S. Mohandas, *Journal of Alloys and Compounds*, 2016, *677*, 258-265.
54. A. Mukherjee, K.S. Mohandas, *Proceedings of the Second International Conference on Electrochemical Science and Technology (ICONEST-2107), J N Tata Auditorium, IISc, Bengaluru*, 10th-12th August, 2017.
55. D. S. M. Vishnu, N. Sanil, K. S. Mohandas, *Research Reviews: Journal of Material Science*, 2017, *5*, 55-65.
56. K. S. Mohandas, D. J. Fray, *Journal of Applied Electrochemistry*, 2011, *41*, 321-336.
57. D. S. M. Vishnu, N.Sanil, K.S. Mohandas, *International Research Journal of Pure and Applied Chemistry*, 2017, *15*, 1-13.

Dr. K.S. Mohandas *obtained his masters' degree in Chemistry from Banaras Hindu University in 1983 and the same year joined the 27th batch of BARC training school. On successful completion of the course, he joined the then Radiochemistry Laboratory at IGCAR, Kalpakkam and since then working in the area of metal production by molten salt electrolysis. He was awarded Ph.D. degree by University of Madras for his doctoral thesis on a novel low temperature molten salt electrochemical process (300 °C) for production of sodium metal from sodium chloride. During 2004-2005, he was a Research Associate at the Materials Science and Metallurgy department of University of Cambridge, UK under Prof. Derek Fray, FRS, FREng. and there he worked on the FFC (Fray-Farthing-Chen) Cambridge process; a novel molten salt electrochemical process for direct conversion of solid metal oxides to metal , discovered and patented around the time by Prof. Derek Fray and his co-workers at the University. Since then Dr. Mohandas has made extensive studies on the solid state electrochemical reduction behaviour of many different metal oxides like* TiO_2, ZrO_2, Nb_2O_5, CeO_2, SiO_2 *and* UO_2 *in both molten* $CaCl_2$ *and* $LiCl$-Li_2O *medium. The reduction mechanisms of some of these oxides were elucidated for the first time and the original results published in journals of international repute. Two doctoral theses were produced from the work. Dr. Mohandas has published the first review on the subject of direct electrochemical reduction of metal oxides to metal and delivered a keynote lecture on the topic at the 'Fray International Symposium held at Mexico in December 2011. More recently, Dr. Mohandas and his team have been engaged in studies pertaining to direct electrochemical conversion of solid* UO_2 *to U and demonstrated the process in 200g UO2/batch size. He has been busy establishing a molten salt laboratory for electro-conversion of kilogram scale of UO2 and other metal oxides to metal.*

	Shri. N.Sanil *received his B.Sc. degree in Chemistry from University of Calicut, Kerala. He joined Indira Gandhi Centre for Atomic Research, Kalpakkam in 1995 and is presently working in the Materials Chemistry & Metal Fuel Cycle Group, His research areas include high temperature molten salt electrolysis, molten salt electrochemistry and direct oxide reduction of metal oxides to metal in high temperature molten salt medium.*
	Dr. D. Sri Maha Vishnu *completed his M.Sc. Chemistry from Pondicherry University. He obtained his Ph.D from Homi Bahabha National Institute, Mumbai (IGCAR Campus). Since 2015, he is doing his Post Doctoral Research in University of Nizwa, Sulatanate of Oman and working from University of Cambridge. His research areas are molten salt based de-oxidation of metal oxides by FFC Cambridge process, high temperature electrochemistry, electrolysis, synthesis of alloys by molten salt electrolysis etc.*
	Dr. T. Biju Joseph *received his M.Sc. degree in Chemistry from Cochin University of Science and Technology (CUSAT), Kochi, Kerala. He obtained his Ph.D from Madras University by working in Indira Gandhi Centre for Atomic Research, Kalpakkam. He is presently working as Assistant Professor in CMS College, Kottayam, Kerala. His research areas of interest are molten salt electrochemistry, electrolysis and direct oxide reduction of metal oxides to metal in high temperature molten salt medium.*
	Dr. R. Kumaresan, *Scientific Officer/ E joined IGCAR in the year 2009. He completed his M.Sc. degree from Madurai Kamaraj University and PhD from University of Madras. At present he is the Programme Leader, Metal Processing Studies Programme, MC&MFCG, IGCAR. He has published more than 30 papers in various peer-reviewed international journals and his field of interest includes direct oxide reduction, molten salt electrochemistry, solvent extraction and ion exchange.*
	Miss. Anwesha Mukherjee *obtained her B.Sc. degree in Chemistry from the University of Burdwan, Bardhaman in the year of 2012 and received her M.Sc. degree in Chemistry from the Indian Institute of Technology Guwahati, Assam, India in the year of 2014. She joined Indira Gandhi Center for Atomic Research (IGCAR), as Scientific Officer/C in 2015 after successfully completing one year (2014-2015) orientation course in Nuclear Science & Engineering (OCES – 2014, Nuclear Fuel Cycle Chemistry discipline) from BARC Training School at IGCAR campus. Currently she is working at Pyrochemical and Materials Processing Division, Materials Chemistry & Metal Fuel Cycle Group, IGCAR as Scientific Officer/D. She is also pursuing Ph.D. (August 2017 onwards) from Homi Bhaba National Institute (HBNI), Mumbai, Maharashtra, India and her research interest includes high temperature molten salt electrochemistry and solid state electrochemical reduction of metal oxides to metals in molten salt medium.*
	Smt. L. Shakila *has obtained her B.Sc degree in Chemistry from Madras University, Chennai and M.Sc. degree in Chemistry from Madurai Kamaraj University, Madurai. She has joined Indira Gandhi Centre for Atomic Research, Tamilnadu, in 2008, in Pyro-chemical Processing Studies Section. She is involved in the electro-chemical reduction of many metal oxides like* TiO_2, UO_2, ZrO_2 *and* CeO_2 *to metal by molten salt electrolysis.*

Inorganic materials for the treatment and disposal of nuclear wastes

K. A. Venkatesan* and A. S. Suneesh
Fuel Chemistry Division, Materials Chemistry and Metal Fuel Cycle Group
Indira Gandhi Centre for Atomic Research, Kalpakkam 603 102.
Corresponding Author Email: kavenkat@igcar.gov.in

Abstract

Inorganic sorbents are proven candidates for the selective separation of toxic and radiotoxic metal ions from aqueous medium. Extensive research in this area has been carried out over few decades and the research fetched few potential sorbents for separating long lived fission products such as ^{90}Sr and ^{137}Cs from aqueous wastes. They are also commercially available now. Various synthetic methods have been reported for finely tuning the cavity size of the sorbent to enhance the selectivity of metal ion of interest. The attraction over this material is further augmented by the organomodification on the surface of the inorganic matrix. The driving force for such organofunctionalized sorbents (OFS) originate from the fact that they can be tuned to task-specific form by proper selection of complexing moieties. The aim of this article is to summarize the applications of inorganic sorbents for the separation of fission products (^{137}Cs and ^{90}Sr) and surface modified adsorbents for lanthanide-actinide separations.

Keywords: Ion exchange, Inorganic ion exchanger, Cesium, Strontium, Hybrid Materials.

1. Introduction

Today, nuclear power is contributing about 17% of the global electricity generation [1, 2]. The demand for energy is steadily increasing with ever increasing population and rapid industrialization all over the world and nuclear option for the generation of power appears to be inevitable for future [2]. The technology for reprocessing of spent nuclear fuels was established over few decades and its operation results in the generation of the radioactive wastes [1]. Various classification systems were used to categorize radioactive wastes depending upon the content of radionuclides, origin of the waste, type of radiation, half-life of nuclides, hazardous lifetime of the waste, radiotoxicity, specific activity and dose rate [4].

All radioactive wastes emit ionizing radiation characteristic to the radionuclides present in it. These ionizing radiations are known to set a complex sequence of physical, chemical and biological changes along the path of its travel [5]. The critical targets are the DNA macromolecules that carry the genetic information and control the development and division of the cells. Exposure of ionizing radiation generates free radicals and charged particles in the cells that can translate and change the structure of DNA [6, 7]. The effects of this exposure can cause either acute damage in which the cells are killed immediately or it can result in delayed effect in which the cell transformation appears only in the subsequent generations. Due to these deleterious effects of radioactive materials, the International Commission of Radiological Protection (ICRP) provides guidelines and regulation of radiation standards to public and workers at nuclear facilities [8].

Nuclear waste is normally composed of major quantity of innocuous component contaminated with minor amounts of hazardous radionuclides. The technology required for the management of nuclear waste should focus on separating/concentrating the hazardous components from the large volume of innocuous waste [9]. Separation of radionuclides minimizes the volume of the active component that is to be safeguarded for long time and lowers the risk of contaminating the environment. Moreover, the concentration of active components dramatically reduces the cost of disposal. The other larger fraction of innocuous component, obtained after the treatment, can be either disposed or handled without many hazards. Various techniques [10-12] that are currently available for waste treatment include (1) solvent extraction (2) solid phase adsorption (3) membrane process (4) precipitation etc., They can be employed independently or in-combination with other techniques.

Solid phase extraction is a promising technique for the separation of radionuclides from nuclear wastes owing to its simplicity, robustness, regenerating ability, engineering capability and technologically demonstrated [12]. This method has been extensively applied in various stages of nuclear fuel cycle operations and other activities involving radioactive materials [13, 14]. Among the various solid phase extraction methods, the methods based on inorganic materials are popular for the separation of cesium and strontium from nuclear wastes. The attractive features

Table 1. Recently reported inorganic sorbents that are promising for fission products and actinides

Sorbent	Metal ion studied	Reference
Titanium silicate/ silicotitanates	UO_2^{2+}, Cs^+, Sr^{2+}	33-35
Potassium zirconium-titanium silicate	Cs^+,Sr^{2+}	36,37
Amorphous zirconium phosphate	Cs^+, Sr^{2+}	38
Copper and zinc ferrocyanides	Cs^+	39,40
Ammonium tungstophosphate (AWP)–calcium alginate	Cs^+	41
Poly antimonic acid	Sr^{2+}	42
Hydrous zirconium oxide	Sr^{2+}	43
Zirconium molybdate – zirconium tungstate	Cs^+, Sr^{2+}	44
Hydrous mixed oxides of Sb, Nb, Si, Ti, and W	Cs^+, Sr^{2+}	45
Tin antimonate	Co^{2+}	46
Ammonium molybdophosphate	Th^{4+}, Cs^+	47, 48
Thorium phosphate hydrogen phosphate	Cs^+, Sr^{2+}, Am^{3+}	49
Layered Manganese oxide	Cs^+, Sr^{2+}, Co^{2+}	50
Sodium titanate	Sr^{2+}	51
Zeolites	Cs^+, Sr^{2+}	52
Clays	Cs^+	53
Hydroxyl magnesium silicates	Cs^+	54
Alumino silicates	Cs^+	55
Calcium silicates	Cs^+	56

of the inorganic materials are high selectivity, chemical and radiation stability for treating radioactive wastes. Moreover, the spent inorganic sorbents can be converted to glass or ceramic for final disposal [15]. However, the main limitation of any inorganic sorbent is to obtain them in granulated form with high ion exchange capacity. Nevertheless, inorganic sorbents are proven candidates for the separation of radioactive metal ions from a complex mixture [16-29] and the success and development of inorganic sorbents seen over the years could be attributed only to their application in the field of radioactive waste treatment.

Pioneering work in this area was carried out by Amphlett [21] and later on, the development prospects of this area of research was elevated by Clearfield [18], Abe [19], Lehto [23], Qureshi [22] and others [24-30]. Several research articles, monographs, IAEA reports and books on this topic were available since its introduction that makes one to choose a particular type material for a kind of treatment required [20, 31, 32]. Table 1 lists some of the inorganic sorbents reported over the past five years that are promising for the removal of long lived fission products especially cesium – 137, strontium – 90 and actinides.

Most of the inorganic sorbents studied for removing cesium and strontium have three dimensional frameworks. The tunnels and cavities present in these micro porous materials offers a suitable location for the exchanging ion and these cavities can the finely tuned or tailor-made for a specific cation by adopting appropriate synthetic method. Further, it is possible to manipulate the cavity size by substituting various metal atoms into the framework structure for enhancing the selectivity of the sorbent. Thus the interests over these types of materials are ever increasing even though the subject was introduced few decades ago. In the following few pages, discussion is restricted to only few well-studied and demonstrated inorganic sorbents that exhibit strong affinity for cesium and strontium.

2. Inorganic Sorbents

2.1 Crystalline silicotitanates

Crystalline silicotitanates (CST) developed [57] at Sandia National Laboratory in collaboration Texas A& M university, was originally comprised of seven to eight phases. Among these, TAM-5 was identified to have very high selectivity for cesium and strontium from a wide range

of pH (0 – alkaline) even in the presence high concentrations of sodium ion [57]. The synthetic formulations for the preparation CST enriched with TAM-5 phase was carried out by the researchers at Sandia and Texas, which has resulted in a commercially available sorbent called UOP IONSIV IE –910 (IE-911 granular form). The performance of this sorbent for the sorption of various radioactive metal ions is well documented [34, 35]. Another engineered form of crystalline silicotitanate, IONSIVTM IE-911, developed by Tranter *et al.* also studied for cesium from simulated Idaho National Engineering and Environmental Laboratory acidic tank waste feed solution [58]. The authors performed a large scale laboratory scale demonstration for the separation of cesium from a simulated waste solution [59, 60]. Celestian *et al.* [34] synthesized few crystalline silicotitanates and investigated the atomistic mechanisms responsible for the extra ordinary selectivity of cesium by crystalline silicotitanates with the help of DFT calculations. Similarly, a group of researchers from Pacific Northwest National Laboratory employed crystalline silicotitanate for the removal of cesium (^{137}Cs) from the aqueous phases of the tank wastes. Su and coworkers from Pacific Northwest National Laboratory investigated the thermal conversion of silicotitanates to the durable waste form for disposal [61]. Similarly, Anderws *et al.* also studied and demonstrated the feasibility of vitrification with the cesium bearing crystalline silicotitate [62]. In this work, the authors separated cesium from Hanford tank waste using crystalline silicotitanate and immobilized the waste into glass form. Silicotitanates have also been explored for the separation of cesium and strontium in India [63-65]. Chitra *et al.* reported synthesis of crystalline silicotitantate and studies on the sorption behavior of cesium and strontium [63, 64]. Kamble *et al.* investigated the feasibility of using crystalline silicotitante for the separation of cesium and strontium from low-level radioactive aqueous waste solutions [65].

2.2 Microporoustitano silicates

Several micro porous titano silicates are also reported for the separation of cesium and strontium [66, 67]. Sitinakites [68] and pharmacosiderites [69] are the major titanium silicates reported in this category. Titanium silicate is an analogue of mineral, pharmocosiderite, with a molecular formula $K_3H(TiO)_4(SiO_4)$. $4H_2O$ was studied for the separation of cesium and strontium from ground water and alkaline waste solution [69, 70]. The structure of this compound is made up of a framework of TiO_6 octahedra and SiO_4 tetrahedra linked together in such a way it creates a 3-dimensional tunnel structures. The charge neutralizing exchangeable cation K^+/H^+ reside close to the face centers of the unit cell. The alkali metal ion selectivity for $K_3H(TiO)_4(SiO_4).4H_2O$ was reported to be $Cs^+>K^+>Na^+>Li^+$. The channel openings present in pharmocosiderite type titanium silicate are not large enough to allow hydrated cesium ion to diffuse freely into the pores. Partial dehydration was the pre-requisite for the entry of Cs^+ ion into titanium silicate. However, the channel opening can be increased by partial substitution of germanium into the lattice of titanium silicate, which has resulted in the increase in the distribution coefficient of cesium from ~5000 mL/g to 50,000mL/g.

Another sorbent structurally similar pharmocosiderate is sodium titanosilicate which was reported to be extremely selective for ^{137}Cs and ^{90}Sr [71, 72]. The reason for high selectivity of cesium was found to be resulting from the coordination environment provided by the tunnel structure in which the Cs^+ ions are encapsulated by the sphere of eight oxygen atoms of the framework like crown ether. The Cs^+ ion present in this environment is so tightly held that the reversible ion exchange reaction could not be taken to completion under mild eluting conditions. Microporoussilicotitanates are suitable for ion exchange of cesium from the aqueous feed solution in the pH range 1-10.

2.3 Hydrous oxides

Many insoluble metal oxides have the ability to sorb various metal ions from aqueous solution. Several hydrous metal oxides are shown to have high selectivity for chemically toxic metals [43, 45] and radioactive

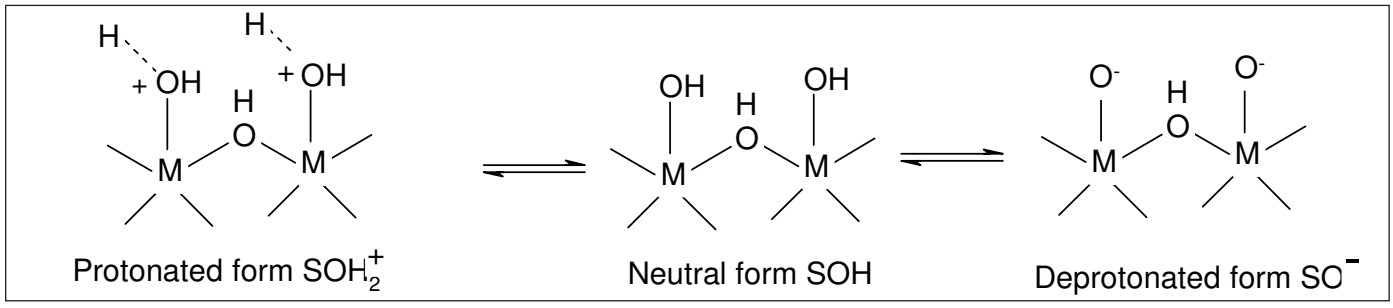

Fig. 1: *The amphoteric nature of hydrous oxides. The surface hydroxyl groups (-SOH) can associate or dissociate to give protonted (SOH2+) or deprotonated (SO-) forms*

metal ions [43]. Hydrous titanium oxide (HTO) [73] and hydrous antimony oxide (HSbO) [74] are very effective in removing strontium from alkaline solution and acid solution respectively. Among hydrous oxides, sodium titanate developed by Lehto *et al* was most promising and commercially available as "Sr Treat" for the removing of strontium from alkaline solutions [72]. It was reported that "Sr Treat" was very selective for strontium from strongly alkaline solution containing 3 M Na^+ ion. The utility of this sorbent was demonstrated in engineering scale also.

The sorption of metal ions on hydrous oxides depend on the characteristic properties of surface hydroxyl (SOH) groups (see figure 1). The surface hydroxyl groups (-SOH) present on the sorbent can associate with $H^+$from aqueous phase and converted to protonated SOH_2^+ form or dissociate to give deprotonated SO^-form depending upon the pH of the solution in contact with the sorbent as shown above. The point of zero charge (PZC) is the pH at which the $[SO^-] = [SOH_2^+]$, i.e. the net charge on the surface of oxide is zero. PZC is a convenient reference value for characterizing hydrous oxides and its magnitude depends on the history, purity, crystallinity, temperature, degree of hydration etc. of the sample [75]. When pH < PZC, the net charge on the oxide surface is positive with exchangeable anionic groups and when pH > PZC the oxide acts as cation exchanger. The following Table 2 provides the PZC values reported in literature for some metal oxides [75]. It is seen that for most of the hydrous oxides the value falls in the pH range 3-10, which indicates that these sorbents are best suited for the removal of metal ions from ground water and alkaline conditions.

Table 2. Point of zero charge (PZC) of various hydrous oxides [75]

Inorganic sorbent	PZC
α-SiO_2	2.9
α-TiO_2	5.8
Fe_3O_4	6.6
α-Fe_2O_3	8.5
α-Al_2O_3	9.1
α-$Al(OH)_3$	10.0
β-MnO_2	4.6 – 7.3
SnO_2	7.3
ZrO_2	2.88
ThO_2	9.2
Silica titania gel (Si/Ti =1)	4.88

Similarly, iron hydroxides also have been reported for sorption of toxic and radiotoxic metal ions from aqueous waste [76-78]. Daus *et al.* reviewed literature reports on several iron hydroxides and iron oxy hydroxides for arsenic removal from water [77]. Ajouyeda *et. al* reported the sorption of chromium on to natural iron hydroxides and aluminum hydroxides [78]. Organo modified iron oxides are also used for the magnetic assisted separation of radioactive metals from aqueous streams (to be discussed below).

2.4 Isopoly and heteropolyacids

The elements such as Mo, W and V have the astonishing property of polymerization to form poly oxometallates under acidic conditions. Among the poly oxometallates, one of the very old system is ammonium 12-molybdophosphate ($(NH_4)_3[PO_4Mo_{12}O_{36}]$) which is also well studied for the selective removal of cesium from acidic solution [47, 48]. $[PO_4Mo_{12}O_{36}]^{3-}$ has the well known Keggin structure, in which the phosphate PO_4 present in the center of the cage surrounded by twelve MoO_6 octahedra [79] asshown in the Figure 2. Though the anion has the charge of –3, it is distributed over 36 oxygen atoms on theouter periphery of the Keggin ion.

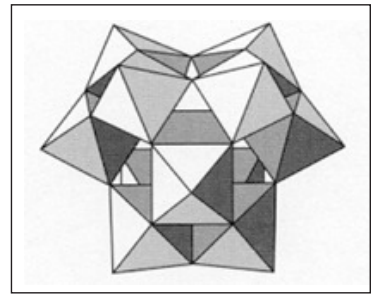

Fig.2: *Stereoscopic view of $[PO_4Mo_{12}O_{36}]^{3-}$anionic unit*

The selectivity sequence decreases in the order Cs^+>Rb^+> K^+> Na^+>Li^+. Ammonium phosphomolybdate(AMP) is well recognized for its superior selectivity of Cs and the theoretical capacity of AMP is 1.57 meq/g. However, complete ion exchange of ammonium ions by cesium is not favorable due to the structural rearrangement of Kegginunit while undergoing exchange [74] thus leading to an apparent capacity of 1.0 meq/g. Further, the characteristic property of AMP and other hetero poly acid are that they are precipitated as fine crystals, and therefore it is difficult to obtain workable flow rates if they are employed as sorbent. AMP has microcrystalline structure with particle size of ~3-5 μm and in view of this AMP is either impregnated in inorganic porous materials or embedded in organic solid supports [47, 48]. Several researchers have reported the preparation of ammonium molybdophosphate

immobilized on a polyacrylonitrile support (AMP-PAN) for cesium separation from acidic waste solutions. Todd *et al*. employed AMP-PAN for the treatment of cesium containing acidic tank wastes stored at Idaho National Laboratory, USA [80]. Similarly, the researchers from Bhabha Atomic Research Centre investigated the feasibility of separating cesium from concentrated high level liquid waste by using AMP impregnated on a special Advanced Lyophilic Ion-eXchanger (ALIX) [81]. Several reports on AMP-silica composites are also available for the separation of cesium separation from acidic media [47]. AMP based sorbents are highly suitable for the cesium sorption from the aqueous feed solution in fairly concentrated nitric acid medium (0.1 M to 3 M).

2.5 Natural Clay Materials

Zeolites are a large group of natural and synthetic hydrated aluminum silicates [82]. They are characterized by a three-dimensional structures with large cage-like cavities for accommodating sodium, calcium, or other cations (positively charged atoms or atomic clusters); water molecules; and even small organic molecules [82]. The ions and molecules in the cages can be undergoing ion exchange with other metal ions without any destruction in the aluminosilicate framework. In view of this, zeolites find wide use as ion-exchange agents, catalysts, and molecular filters in a range of industrial processes. The structure of zeolite is based on the three-dimensional frameworks of silica and alumina tetrahedra, that is, silicon or aluminum ions surrounded by four oxygen ions in a tetrahedral configuration. Each oxygen is bonded to two adjacent silicon or aluminum ions, linking them together. Clusters of tetrahedra form box-like polyhedral units that are further linked to build up the entire framework. The aluminosilicate framework of a zeolite has a negative charge, which is balanced by the cations housed in the cage-like cavities. Zeolites have much more open, less dense structures than other silicates; between 20 and 50 percent of the volume of a zeolite structure is voids.

Naturally occurring inorganic clay minerals have been suggested as a backfill material for the retardation of cesium and strontium in the engineered repositories [83]. Clay minerals refer to a group of hydrous aluminosilicates [84]. In contrast to zeolites, these types of clay materials have a layer structure [84]. The clay minerals consist of two basic units, an octahedral unit and a tetrahedral unit. The octahedral unit is comprised of closely packed oxygen and hydroxyls group of aluminium and other ions such as magnesium, iron etc. and the tetrahedral unit is constituted predominantly by silicate network. Each tetrahedral (or octahedral) units are linked with other tetrahedral unit form a sheet like structure. Aluminosilicate condensates in 2:1 ratio of tetrahedral Si sheets with an octahedral Al sheet are called 2:1 phyllosilicates. Coupling of only one Si sheet to one Al sheet gives rise to 1:1 phyllosilicates. In many phyllosilicates either Al^{3+}or Si^{4+}ions are isomorphically substituted partially by lower valence metal cations of similar sizes like Mg^{2+} and Fe^{2+}. The isomorphic substitution gives rise to a deficiency of positive charge. This deficiency is balanced by cations such as alkaline earth ions (e.g., Ca^{2+}) or alkali metal ions (e.g., Na^{+}). These ions are exchangeable, giving raise to the ion exchange capacity up to 1 mmol/g depending upon the degree of deficiency. Zeolites and naturally occurring aluminosilicates are highly suitable for the cesium exchange in the pH range 1-10, depending up on the structure of zeolite and aqueous feed conditions.

2.6 Hexacyanoferrates

Some hexacyanoferrates are reported to exhibit a good selectivity for cesium [17, 28, 29]. These hexacyanoferrates have been prepared with various compositions and structures using transition metal ions. In fact, ferrocyanides act as cation exchangers with high affinity for heavy alkali metal ions, especially for Cs^{+}. The affinity series Cs^{+}>Rb^{+}> NH_4^{+}> K^{+}> Na^{+} was found for Cu, Ni, Fe(III) and Zirconium ferrocyanides. The disadvantage of the insoluble hexacyanoferrates is the low mechanical strength of the materials obtained by classical precipitation method, which does not permit the sorbents for fixed bed operation. They require a solid support such as silica and silica gel when they are used in columns. Potassium nickel hexacyanoferrate complex have been widely studied for the separation for cesium. Similarly, several other complexes of hexacyanoferrates such as copper (II) hexacyanoferrate (II) [85], Nickel hexacyanoferrate [86] etc. have been reported for the separation of cesium. Hexacynaoferrates are highly suitable for cesium separation from the aqueous phase feed solution having pH varies from 2 to 12.

2.7 Limitations of inorganic sorbents

Even though the inorganic sorbents for the treatment of nuclear waste is very promising, industrially demonstrated and have greater advantage over organic resins, they have some limitations. First of all, the yield of the required product is a function of synthetic methodology adopted for the preparation. Parameters such as concentration of metal ion, pH, temperature, stirring rate etc strongly influence the quality of the sorbent to a large extent and all the more it is difficult maintain the identical conditions at every instant of preparation. Secondly, even if the correct method is adopted the product usually ends up in fine amorphous or crystalline powder. In such cases

it is not possible to obtain workable flow rates if they are employed for column operation. These powders need to be granulated or impregnated in to some solid supports for achieving considerable flow rates during waste treatment. The impregnated sorbents have lower capacity than the original and therefore the throughput becomes low. Thirdly, the sorbents have slow rate of uptake and low ion-exchange capacity when compared to organic resins on most occasions. Finally, the important "limitation" from the nuclear waste point of view is that most of the inorganic sorbents exhibit selectivity for group I and II metal ions and they can separate from ground water and alkaline conditions. But, only a few inorganic sorbents are reported till date for the removal of fission products (even for cesium and strontium) and actinides from acid solution. It is difficult to tailor make the inorganic sorbent for selectivity removing actinides, platinum group metals (Ru, Rh, Pd) from acid solution because the aqueous phase chemistry of these metal ions is very complex and these metal ions are normally exist as a coordinate complex with various anions. These limitations indicate that the sorbents developed so far are inadequate for separating them from acid solution and do indicate that there is a need for further development of sorbents.

3. Organic-inorganic hybrid materials

Inorganic oxides such as silica gel can be tuned to task specific adsorbent by modifying the surface of silica gel with the specific organic compounds that can form a strong complex with metal ion of interest [82, 83]. These organic-inorganic hybrid materials also known as organofunctionalized inorganic materials (OFIM) form a strong co-ordinate complex with target metal ions. Thus the selectivity and extractability are higher for OFIMs. The concept of surface modification of the co-polymer existed since the very early development of ion exchange resins [87, 88]. The advantage of linking the metal ion specific ligands on to the polymer matrix generally prevents the loss of extractant encountered in solvent extraction and extraction chromatography procedures. Grafting the metal ion specific ligands on to the inorganic solid supports involves carrying out organomodification on the surface of the silica gel to covalently link the task-specific moieties on silica gel. The adsorbent prepared in this method contains 5-10% of organics on the inorganic matrix. One way is to begin with silylation reaction on silica followed by linking the task specific ligands (target molecule) in the subsequent steps. Another way is to prepare the precursor containing the ligand (target molecule) in liquid phase followed by silylation reaction at the end. Figure 3 shows the grafting of glycolamic acid on silica gel, which was used for the mutual separation of lanthanides and actinides from the aqueous raffinate obtained after minor actinide partitioning. The pH of the aqueous feed depends on the functional groups present on the silica gel. For mutual separation of lanthanides and actinides usually pH 1-3 is preferred.

4. Magnetic adsorbents

Magnetic solid phase separation methods (MSPS) is emerging as a promising technique for the separation of toxic and radiotoxic metal ions from various aqueous streams [89-91]. In MSPS technique, the magnetic particles (MPs) are added to the waste solution to extract the target metal ion. The MPs are then separated from the solution by means of an external magnetic force. The separated MPs are then immersed in a stripping solution for recovery of metal ions from the adsorbed surface. A typical magnetic adsorbent consists of Fe_3O_4 or Fe_2O_3 as inorganic moiety on which the organic (ligand) is grafted by using a silylating reagent such as tetraethoxylsilane, tetramethoxysilan etc. The use of MSPS offers several advantages especially for the treatment of nuclear wastes as compared to conventional solid phase extraction. Since this method uses the application of external magnetic field, the particle size of the adsorbent can be lowered to as low as nano-size for efficient and rapid extraction of metal ions from waste solution. In addition, there is no need for packing of MPs in column

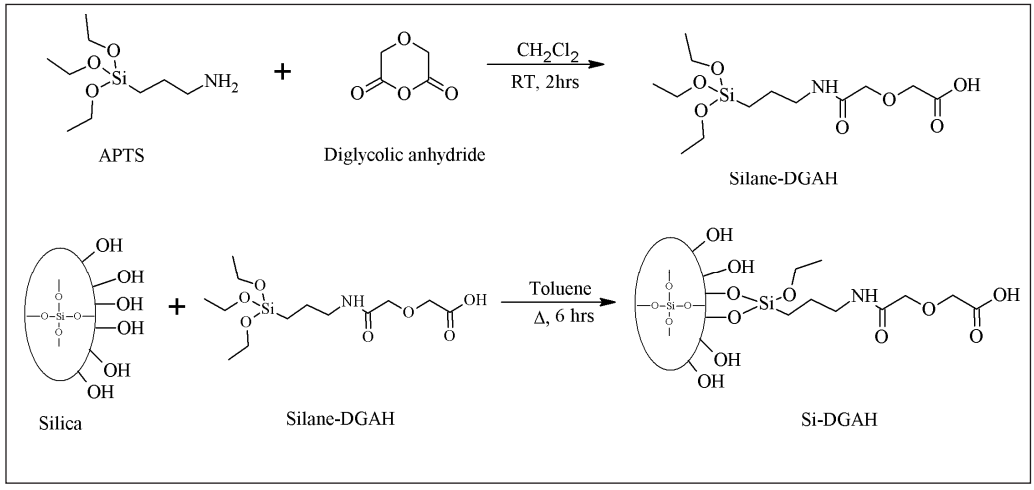

Fig. 3:*Scheme for the synthesis of diglycolamic acid functionalized silica gel*

as it is usually operated in batch mode and the phase separation is quickly achieved by external magnetic field [89-91]. The adsorbents are synthesized by chemical modification of iron oxide. Among the various oxides, Fe_3O_4 has been popularly used as magnetic adsorbent because of its enhanced ferromagnetic behavior. Fe_3O_4 is prepared by co-precipitation of Fe^{3+} and Fe^{2+} salt. As prepared Fe_3O_4 surface contains several Fe-OH groups. The surface of Fe_3O_4 is later modified by a process involving hydrolysis and condensation process between Fe_3O_4 and an alkoxysilane. The third step involved for the synthesis is the organo modification of the surface-Si-OH with the organic attachment. The ligand of interest is initially attached to an organosilane and was anchored on to the Fe-Si by esterification process. A typical magnetic separation is illustrated in figure 4. Several research papers are available for the use of magnetic adsorbents for the separation of metal ions from various feed solutions [92-95]. pH of the aqueous feed solution usually varies from pH 1-8.

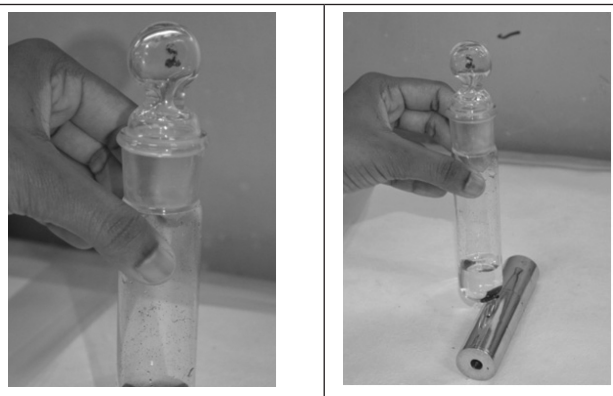

Magnetic particles present in the aqueous phase after sorption of metal ions	Magnetic particles were separated by using magnet Permanent magnet

Fig. 4: *Demonstration of magnetic separation of target metal ion by using a permanent magnet.*

5. Scope of inorganic materials and conclusions

In conclusion, purely inorganic based sorbents are the best choice for isolating ^{137}Cs and ^{90}Sr, if the feed solution is neutral or alkaline. The summary of the review concludes that crystalline silicotitanates, various metal hydrous oxides, isopolyacids such as ammonium phosphomolybdates, aluminosilicates, hexacyanoferrates etc are the well-studied inorganic sorbents suitable for the separation of radioactive cesium and strontium. These inorganic sorbents requires adjustment of pH of the feed solution. Except some fission products, most of the other metal ions and actinides present in the nuclear waste exist in the form of co-ordinate type complex species with anions present in the waste. Naturally occurring clay materials can be employed for sorption or retardation of radionuclides wherever they are applicable. Inorganic exchangers which take up metal ions by simple ion exchange at cavity site present in the three dimensional net work, may not be find its utility for separating these complex species, in such cases, organo functionalized inorganic materials may turn out to be a best choice. The studies on organofunctionalized inorganic materials containing complexing moieties is very limited and therefore, there is a need to develop organo functionalized materials for the specific extraction of fission products and actinides from aqueous waste generated during reprocessing. The survey also indicates that it is possible to prepare magnetic adsorbents with wide variety of functionalities that are specific to metal ions of nuclear interest and there is lot of scope for utilizing them, not only for the treatment of non-radioactive wastes but also to meet the current and future challenges of nuclear wastes.

References

1. Energy, Electricity and Nuclear Power Estimates for the Period up to 2050, IAEA REFERENCE DATA SERIES No. 1, 2017, IAEA-RDS-1/37
2. I. Dincer, C. Acar, A review on clean energy solutions for better sustainability. *Inter. J. Energy Res.*, **2015**, *39(5)*, 585-606.
3. Standardization of radioactive waste categories, IAEA-Technical report series No 101, IAEA, Vienna, 1970
4. Classification of Radioactive Waste, General Safety Guide, *IAEA SAFETY STANDARDS SERIES* No. GSG-1
5. W.F. Morgan, M.B. Sowa, Non-targeted effects induced by ionizing radiation: mechanisms and potential impact on radiation induced health effects, *Cancer lett.*,**2015**,*356(1)*,17-21.
6. E. Alizadeh, T.M. Orlando, L. Sanche, Biomolecular damage induced by ionizing radiation: the direct and indirect effects of low-energy electrons on DNA, *Annual Rev. Phys. Chem.*, **2015**, *66*, 379-98.
7. S. Behjati, G. Gundem, D.C.Wedge,N.D. Roberts, P.S. Tarpey, S.L. Cooke, P. Van Loo, L.B. Alexandrov, M. Ramakrishna, H. Davies, S. Nik-Zainal, Mutational signatures of ionizing radiation in second malignancies, *Nature Commun.*, **2016**,*7*,12605.
8. Protecting People Against Radiation Exposure in the Event of a Radiological Attack (International Commission on Radiological Protection, ICRP Publication 96, 2005, pp-51
9. Principles of Radioactive Waste Management Safety Fundamentals, IAEA, Safety Series No. 111-F, IAEA, Vienna (1995).
10. M. Aguilar, J.L. Cortina (Eds), Solvent extraction and liquid membranes: *Fundamentals and applications in new materials*. CRC Press; 2008.
11. A.K. Pabby, S.S. Rizvi, A.M. Requena, *Handbook of membrane separations: chemical, pharmaceutical, food, and biotechnological applications.* CRC press; 2008.
12. F. Helfferich, *Ion Exchange*, McGraw-Hill Book Company, New York, 1962.

13. M.Streat, D.Naden, Ion exchange in uranium extraction, In: Ion exchange and sorption processes in hydrometallurgy, Critical Reports on Applied Chemistry, Vol 19, John Wiley & sons, Britain, (1987) p 1 – 55
14. Advances in Technologies for the treatment of low and intermediate level radioactive liquid wastes, *IAEA, Technical report series* No 370, Vienna, 1994
15. W.K. Kot, I.L. Pegg, M. Brandys, M. Penafiel, Vitrification of Inorganic Ion-Exchange Media, VSL-16R3710-1 (No. ORP-61830). Hanford Site (HNF), Richland, WA (United States), 2018.
16. B.R. Figueiredo, S.P. Cardoso, I. Portugal, J. Rocha, C.M. Silva, Inorganic ion exchangers for cesium removal from radioactive wastewater. *Sep. Purif. Rev.*, **2018**, *47(4)*, 306-36.
17. M.S. Gasser, M.I. Aly, H.F. Aly, Selective removal of cesium ions from aqueous solutions using different inorganic metal hexacyanoferrate-prepared sorbents, *Particulate Sci. Technol.*, **2018**, *7*, 1-0.
18. A. Clearfield, Inorganic Ion Exchangers, Past, Present, and Future, *Solvent Extr. Ion Exch.*,**2000**, *18*, 655 –678
19. M.Abe, Ion-Exchange Selectivities of Ionorganic Ion Exchangers, In: Ion exchange and solvent extraction, J.A. Marinsky and Y. Marcus (Eds.)., M.Dekker, Inc., New York, 1995, Vol. 12, p-381 – 440
20. A. Clearfield, Inorganic Ion Exchange Materials, CRC Press, Boca, Raton, FL, 1982.
21. C.B. Amphlett, Inorganic Ion Exangers, Elsevier, Amsterdam, 1964.
22. M. Qureshi, K. G. Varshney, Inorganic Ion Exchngers, in Chemical Analysis, CRC Press, Boca Raton, FL, 1991.
23. J.Lehto, R.Harjula, Selective Separation of radionuclides from nuclear waste solutions with inorganic ion exchangers, *Radiochim. Acta*, **1999**, *86*, 65 - 70
24. D. Alby, C. Charnay, M. Heran, B. Prelot, J. Zajac, Recent developments in nanostructured inorganic materials for sorption of cesium and strontium: synthesis and shaping, sorption capacity, mechanisms, and selectivity-a review, *J. Hazard. Mater.*,**2018**, *344*, 511-30.
25. B.R. Figueiredo, S.P. Cardoso, I. Portugal, J. Rocha, C.M. Silva, Inorganic ion exchangers for cesium removal from radioactive wastewater, *Sep. Purif. Rev.*, **2018**,*47(4)*, 306-36.
26. V.V. Yurchenko, A.V. Sviridov, A.F. Nikiforov, V.S. Semenishchev, A.F. Nizamova, Separation of cesium and strontium from aqueous solutions by sorbents based on bentonite clays, In: *AIP Conference Proceedings*, 2018, AIP Publishing.
27. O.A. Moamen, H.A. Ibrahim, N. Abdelmonem, I.M. Ismail, Thermodynamic analysis for the sorptive removal of cesium and strontium ions onto synthesized magnetic nano zeolite, *Microporous and Mesoporous Materials*, **2016**,*223*,187-95.
28. G.N. Pshinko, L.N. Puzyrnaya, V.S. Shunkov, A.A. Kosorukov, V.Y. Demchenko, Removal of cesium and strontium radionuclides from aqueous media by sorption onto magnetic potassium zinc hexacyanoferrate (II),*Radioch emistry*,**2016**,*58(5)*,491-7.
29. M.S. Gasser, M.I.Aly, H.F. Aly, Selective removal of cesium ions from aqueous solutions using different inorganic metal hexacyanoferrate-prepared sorbents, *Particulate Sci. Technol.*, **2018**, *7*, 1-0.
30. V.V. Milyutin, N.A. Nekrasova, N.Y. Yanicheva, G.O. Kalashnikova, Y.Y. Ganicheva, Sorption of cesium and strontium radionuclides onto crystalline alkali metal titanosilicates, *Radiochemistry*, **2017**,*59(1)*, 65-9.
31. Inorganic ion exchangers and adsorbents for chemical processing in the nuclear fuel cycleiaea, Vienna, 1985, IAEA-TECDOC-337
32. Application of ion exchange processes for the treatment of radioactive waste and management of spention exchangers, Vienna, 2002, IAEA-TECDOC-408
33. A. Clearfield, Structure and ion exchange properties of tunnel type titanium silicates, *Solid State Sciences*, **2001**, *3*, 103 – 112
34. A.J. Celestian, J.D. Kubicki, J. Hanson, A. Clearfield, J.B. Parise. The mechanism responsible for extraordinary Cs ion selectivity in crystalline silicotitanate, *J. Am. Chem. Soc.*,**2008**,*130(35)*, 11689-94.
35. A.M. Rovira, S.K. Fiskum, H.A. Colburn, J.R. Allred, M.R. Smoot, R.A. Peterson, K.M. Colisi, Cesium ion exchange testing using crystalline silicotitanate with Hanford tank waste 241-AP-107, *Sep. Sci. Technol.*, **2019**, *23*, 1-0.
36. A. Clearfield, A.I. Burton, L.N. Burton, D.M. Poojary, S.A. Khainakow, On the selectivity regulation of K2ZrSi3O9. H2O - type ion exchangers, *J. Molecular Structure*, **1998**,*470*, 207 - 213
37. N. Döbelin, T. Armbruster, N. Dobelin, T. Armbruster, Microporous titanosilicate AM-2: RB-exchange and thermal behavior, *Mater. Res. Bull.*,**2007**, *42*, 113–125.
38. A.Dyer, T.Shaheen, M.Zamin, Ion exchange of strontium and cesium in to amorphous zirconium phosphate, *J. Mater. Chem.*, **1997**, *7*, 1895 - 1988
39. H.K.Lee, D.S.Yang, W.Oh, S.J.Choi, Copper ferrocyanide functionalized core-shell magnetic silica composites for the selective removal of cesium ions from radioactive liquid Waste. *J. Nanoscience Nanotechnol.*,**2016**, *16(6)*, 6223-30.
40. G.N. Pshinko, L.N. Puzyrnaya, V.S. Shunkov, A.A. Kosorukov, V.Y. Demchenko, Removal of cesium and strontium radionuclides from aqueous media by sorption onto magnetic potassium zinc hexacyanoferrate (II),*Radiochemistry*, **2016**, *58*, 491-7.
41. H. Mimura, M.Saito, K. Akiba, Y. Onodera, Selective uptake of cesium by ammonium tungstophosphate (AWP) - calcium alginate composites, *Solvent Extr. Ion Exch.*, **2000**, *18*, 1015 – 1027.
42. A. Bilewicz and J. Narbutt, Crystalline polyantimonic acid - an adsorbent for radiostrontium and a potential primary barrier in waste repositories, *Radiochim. Acta*,**2001**, *89*, 783 - 784
43. K.A. Venkatesan, G. PanneerSelvam, P.R. VasudevaRao, Sorption of strontium on hydrous zirconium oxide, *Separation Sci. and Tech.*, **2000**,*35*, 2343 – 2357.
44. S. Kumar, M. Sivaiah, K.A. Venkatesan, R. Krishna, G. Murthy, P. Sasidhar, Removal of cesium and strontium from acid solution using a composite of zirconium molybdate and zirconium tungstate. *J. Radioanal. Nucl. Chem.*,**2003**,*258*, 321-7.
45. T.Moller, A. Clearfield, R. Harjula, Preparation of hydrous mixed metal oxides of Sb, Nb, Si, Ti and W with a pyrochlore structure and exchange of radioactive cesium and strontium

ions into the materials, *Microporous and Mesoporous Materials*, **2002**, *54*, 187 – 199.

46. R. Koivula, R. Harjula, J. Lehto, Structure and ion exchange properties of tin antimonates with various Sn and Sb contents, *Microporous and Mesoporous Materials*,**2002**, *55*, 231 – 238.
47. S.V. Ingale, R. Ram, P.U. Sastry, P.B. Wagh, R. Kumar, R. Niranjan, S.B. Phapale, R. Tewari, A. Dash, S.C. Gupta, Synthesis and characterization of ammonium molybdophosphate-silica nano-composite (AMP-SiO_2) as a prospective sorbent for the separation of ^{137}Cs from nuclear waste,*J. of Radioanal. Nucl. Chem.*, **2014**, *301*, 409-15.
48. M. I. Ali, H.G. Nowier, Separation and purification of Th from U by ammonium molybdophosphate from nitric acid, *Radiochim. Acta*, **2002**, *90*, 285 – 288.
49. E. Pichot, N. Dacheux, V. Brandel, M. Genet, Investigation of $^{137}Cs^{+}$, $^{85}Sr^{2+}$ and $^{241}Am^{3+}$ ion exchange on thorium phosphate hydrogenphosphate and their immobilization in the thorium phosphate diphosphate,*New J. Chem.*,**2000**, *24*, 1017-23.
50. A. Dyer, M. Pillinger, R. Harjula, S. Amin, Sorption characteristics of radionuclides on synthetic birnessite-type layered manganese oxides,*J. Mater. Chem.*, **2000**, *10*, 1867-74.
51. D. Yang, S. Sarina, H. Zhu, H. Liu, Z. Zheng, M. Xie, S.V. Smith, S. Komarneni, Capture of radioactive cesium and iodide ions from water by using titanatenanofibers and nanotubes. *Angew. Chem.*, **2011**, *50*, 10594-8.
52. E.H. Borai, R. Harjula, A. Paajanen, Efficient removal of cesium from low-level radioactive liquid waste using natural and impregnated zeolite minerals,*J. Hazard. Mater.*,**2009**, *172*, 416-22.
53. V.V. Yurchenko, A.V. Sviridov, A.F. Nikiforov, V.S. Semenishchev, A.F. Nizamova, Separation of cesium and strontium from aqueous solutions by sorbents based on bentonite clays, In: AIP Conference Proceedings, 2018, Vol. 2015, No. 1, p. 020115), AIP Publishing.
54. M.M. Hamed, M. Holiel, I.M. Ahmed, Sorption behavior of cesium, cobalt and europium radionuclides onto hydroxyl magnesium silicate, *Radiochim. Acta*,**2016**,*104*, 873-90.
55. M.D. Kaminski, C.J. Mertz, M. Ferrandon, N.L. Dietz, G. Sandi, Physical properties of an alumino-silicate waste form for cesium and strontium. *J. Nucl. Mater.*,**2009**, *392*, 510-8.
56. S.A. El-Korashy, Synthetic crystalline calcium silicate hydrate (I): Cation exchange and caesium selectivity. *Monatshefte für Chemie*, **2002**, *133*, 333-43.
57. R. G. Dosch, The use of titanates in decontamination of defense waste, SAND 78 – 0710, Sandia National Laboratories, June 1978
58. T. J. Tranter, R.D. Tillotson, T.A. Todd, Evaluation of IONSIV™ IE–911 as a cesium removal option for INEEL acidic tank waste. *Sep. Sci. Technol.*,**2005**, *40*, 157-70.
59. T. J. Tranter, R.D. Tillotson, T.A. Todd, Laboratory-Scale Column Testing Using Crystalline Silicotitanate (IONSIV™ IE-911) for Removing Cesium from Acidic Tank Waste Simulant. 1: Cesium Exchange Capacity of a 15 cm^3 Column and Dynamic Stability of the Exchange Media. *Solv. Extr. Ion Exch.*,**2005**, *23*, 583-93.
60. T. J. Tranter, R.D. Tillotson, T.A. Todd, M.D. Argyle, Laboratory-Scale Column Testing Using Crystalline Silicotitanate (IONSIV™ IE-911) for Removing Cesium from Acidic Tank Waste Simulant. 2: Determination of Cesium Exchange Capacity and Effective Mass Transfer Coefficient from a 500 cm^3 Column Experiment. *Solv. Extr. Ion Exch.*, **2005**, *23*, 595-609.
61. Y. Su, M.L. Balmer, B.C. Wang, B.C. Bunker, M. Nyman, T. Nenoff, A. Navrotsky, Evaluation of thermally converted silicotitanate waste forms. *Mat. Res. Soc. Symp. Proc.*, **1999**, *556*, 77-84.
62. M.K. Andrews, J.R. Harbour, Glass formulation requirements for Hanford coupled operations using crystalline silicotitanates (CST) (1997), OSTI Report, No. WSRC-RP-97-0265
63. S. Chitra, S. Viswanathan, S.V. Rao, P.K. Sinha, Uptake of cesium and strontium by crystalline silicotitanates from radioactive wastes. *J. Radioanal. Nucl. Chem.*, **2011**, *287*, 955-60.
64. S. Chitra, A.G. Shanmugamani, R. Sudha, S. Kalavathi, B. Paul, Selective removal of cesium and strontium by crystalline silicotitanates. *J. Radioanal. Nucl. Chem.*,**2017**, *312*, 507-15.
65. P. Kamble, P. Sinha Roy, D. Banerjee, A. Ananthanarayanan, J.G. Shah, G. Sugilal, K. Agarwal, A new composite of crystalline silicotitanate for sequestration of ^{137}Cs and ^{90}Sr from low-level aqueous waste solution. *Sep. Sci. Technol.*, **2019**, *23*, 1-8.
66. J. Rocha, M.W.Anderson, MicroporousTitanosilicates and other Novel Mixed Octahedral, Tetrahedral Framework Oxides, *European J. Inorg. Chem.*, **2000**, *2000*, 801-18.
67. A.I. Bortun, L.N. Bortun, D.M. Poojary, O Xiang, A. Clearfield. Synthesis, Characterization, and Ion Exchange Behavior of a Framework Potassium Titanium Trisilicate $K_2TiSi_3O_9$ H_2O and Its Protonated Phases, *Chem. Mater.*, **2000**, *12*, 294-305.
68. C.V.Philip, S.H.Kim, M.Philip, R.G.Anthony, The effect of hydrogen peroxide on a CST under cesium ion exchange conditions,*Sep. Sci. Technol.*, **2003**, *38*, 3009-29.
69. A. Dyer, M. Pillinger, S. Amin, Ion exchange of caesium and strontium on a titanosilicate analogue of the mineral pharmacosiderite, *J. Mater. Chem.*, **1999**, *9*, 2481-7.
70. E.A. Behrens, P. Sylvester, A. Clearfield, Assessment of a sodium nonatitanate and pharmacosiderite-type ion exchangers for strontium and cesium removal from DOE waste simulants, *Environ. Sci. Technol.*, **1998**, 32, 101-7.
71. R. Saberi, A. Nilchi, R.S. Garmarodi, R. Zarghami, Adsorption characteristic of 137Cs from aqueous solution using PAN-based sodium titanosilicate composite, *J. Radioanal. Nucl. Chem.*, **2010**, *284*, 461-9.
72. T. Möller, R. Harjula, J. Lehto, Ion exchange of ^{85}Sr, ^{134}Cs and ^{57}Co in sodium titanosilicate and the effect of crystallinity on selectivity, *Sep. Purif. Technol.***2002**, *28*, 13-23.
73. M.Kubota, I.Yamaguchi, Y.Morita, K.Okada, Immobilizations of strontium and cesium using hydrous titanium oxide and zeolite, Radioact. Waste Manage. *Nucl. Fuel Cycle*,**1986**, *7(3)*, 303-16.
74. P. Cakir, S. Inan, Y. Altas, Investigation of strontium and uranium sorption onto zirconium-antimony oxide/polyacrylonitrile (Zr-Sb oxide/PAN) composite using experimental design. *J. Hazard. Mater.*,**2014**, *271*, 108-19.

75. K.A. Venkatesan, N. Sati Sasidharan, P.K. Wattal, Specific adsorption of cesium on silica – titania, *J. Radioanal. Nucl. Chem.*, **1997**, 222, 223 – 226.
76. B. Daus, R. Wennrich, H. Weiss, Sorption materials for arsenic removal from water: a comparative study. *Water Res.***2004**, *38*, 2948-54.
77. K.P. Raven, A. Jain, R.H. Loeppert,. Arsenite andarsenate adsorption on ferrihydrite: kinetics, equilibrium, and adsorption envelopes. *Environ. Sci. Technol.*, **1998**, *32*, 344–9.
78. O. Ajouyed, C. Hurel, M. Ammari, L.B. Allal, N. Marmier, Sorption of Cr (VI) onto natural iron and aluminum (oxy) hydroxides: effects of pH, ionic strength and initial concentration, *J. Hazard. Mater.***2010**, *174*, 616-22.
79. D. Ding, Z. Zhang, R. Chen, T. Cai, Selective removal of cesium by ammonium molybdophosphate–polyacrylonitrile bead and membrane. *J. Hazard. Mater.***2017**, *324*, 753-61.
80. T.A. Todd, N.R. Mann, T.J. Tranter, F. Šebesta, J. John, A. Motl, Cesium sorption from concentrated acidic tank wastes using ammonium molybdophosphate-polyacrylonitrile composite sorbents. *J. Radioanal. Nucl. Chem.*, **2002**, *254*, 47-52.
81. L. Varshney, V. Venugopal, A. Kumar, V. Tessy, S.D. Mishra, Recovery of cesium from high level liquid nuclear waste by an advanced polymer composite. BARC Newsletter. 2012 Jul 15;327.
82. W.M. Meier, Zeolites and zeolite-like materials,*Pure Applied Chem.*, **1986**, *58*, 1323-8.
83. S. Norris Multiple Roles of Clays in Radioactive Waste Confinement–Introduction. Geological Society, London, Special Publications. **2019**, SP482-2019.
84. R.A. Schoonheydt, C.T. Johnston, Clay minerals and their surface, In: Surface and interface chemistry of clay minerals. 2018, Vol. 9, pp. 1-21, Elsevier, Amsterdam.
85. C.L. Neskovic, C.V. Madjar, B. Jimenez, A. Pantazaki, V. Federici, A. Tamburini, M. Fedoroff, E. Persidou, A copper hexacyanoferrate/polymer/silica composite as selective sorbent for the decontamination of radioactive cesium, *Radiochim. Acta*, **1999**,*85*, 143 – 148.
86. I.M. Ismail, M.R. El-Sourougy, N.A. Moneim, H.F. Aly, Preparation, characterization, and utilization of potassium nickel hexacyanoferrate for the separation of cesium and cobalt from contaminated waste water, *J. Radioanal. Nucl. Chem.*,**1998**, *237*, 97-103.
87. A.T. Hubbard, , 2002. Encyclopedia of surface and colloid science (Vol. 1). CRC press., pp-191-203
88. E.F. Vansant, P. Van Der Voort, K.C. Vrancken, Chemical modification of the silica surface, In: Characterization and chemical modification of the silica surface. Vol. 93, Amsterdam, Elsevier; 1995 Apr 25.pp-194-292
89. M. Šafaříková, I.Šafařík, Magnetic solid-phase extraction. *J. Mag. Mag. Mater.***1999**, 194, *108*-12.
90. AR. Türker, Separation, preconcentration and speciation of metal ions by solid phase extraction. *Sep. Purif. Rev.***2012**, 41, 169-206.
91. G. Giakisikli, A.N. Anthemidis, Magnetic materials as sorbents for metal/metalloid preconcentration and/or separation. A review, *Analytica Chim. Acta*, **2013**, *789*, 1-6.
92. H. Zhang, X. Zhao, J. Wei, F. Li, Removal of cesium from low-level radioactive wastewaters using magnetic potassium titanium hexacyanoferrate, *Chem. Eng. J.*, **2015**, *275*, 262-70.
93. A.S. Suneesh, R. Kumaresan, R. Jain, K.A. Venkatesan, M.P. Antony, B.M. Bhanage, A magnetic adsorbent for the mutual separation of Am (III) and Eu (III) from dilute nitric acid medium, *Colloid Inter. Sci. Commun.***2016**, 12, 13-6.
94. A.S. Suneesh, R. Jain, K.A. Venkatesan, M.P. Antony, B.M. Bhanage, P. R. VasudevaRao, Novel Diglycolamic Acid Functionalized Iron Oxide Particles for the Mutual Separation of Eu (III) and Am (III), *Solvent Extr. Ion Exch.*, **2015**, *33*, 656-70.
95. R. Yi, G. Ye, F. Wu, D. Lv, J.Chen, Magnetic solid-phase extraction of strontium using core–shell structured magnetic microspheres impregnated with crown ether receptors: a response surface optimization, *J. Radioanal. Nucl. Chem.*, **2016**, *308(2)*,599-608.

Dr K A Venkatesan *obtained MSc Degree from University of Madras in the year 1991. He is from 35th Batch of BARC-TS, Trombay. After completion of training, he joined Process Engineering and Systems Development Division, BARC in the year 1992. He moved to Indira Gandhi Centre for Atomic Research in the year 1998. Currently Dr K A Venkatesan is serving as Head, Actinide Partitioning Studies Section (APSS) in the Fuel Chemistry Division of IGCAR, Kalpakkam, India. At IGCAR, he has published over 175 peer –reviewed international journal publications that include three reviews also. He has filed four patents. He has been guiding several PhD students. Dr K A Venkatesan is the recipient of Department of Atomic Energy (DAE) Group Achievement Award in 2012 and the prestigious DAE-Scientific Research Council's "Outstanding Investigator Award" in the year 2014. In 2018 he received PN Pathak Memorial award for his outstanding and sustained contributions in research and development area associated with fast reactor fuel reprocessing and waste management.*

Dr. A.S. Suneesh *joined Fuel Chemistry Division, IGCAR in 2008 after graduating from BARC Training School, IGCAR Campus (51th Batch, Nuclear Fuel Cycle Chemistry discipline). He obtained his Ph.D. degree from the Homi Bhabha National Institute in 2017. He is the recipient of "DAE Group achievement award". His current research interest includes novel hybrid ion exchange materials for trivalent actinide separation and fission product separation, magnetic materials, development of extractant for lanthanide-actinide separation.*

Studies on the immobilization of ^{75}Re (simulant for ^{43}Tc) in geo-polymer matrix: a feasibility study

Vineet Kumar[1,3], Hrudananda Jena[*, 1, 2]

[1]*Homi Bhabha National Institute, IGCAR Campus,* [2]*Materials Chemistry Division, Materials Chemistry and Metal Fuel Cycle Group,* [3]*Health Physics Unit, BARC Facilities, Kalpakkam-603102, India*

**Corresponding author E-mail:hnje@igcar.gov.in*

Abstract

Geopolymers are inorganic ceramic materials that form long range, covalently bonded, SiO_4-AlO_4 tetrahedral frameworks leading to the formation of amorphous solid. These materials were prepared at low temperatures (60-80^{0}C) by mixing silica and alumina gels in alkaline medium. The low temperature treatment of the process minimizes the loss of volatile fission products such as TcO_4^- from the LLW. Silico-aluminate based (-Si-O-Al-) geo-polymers were synthesized at 60^{0}C by varying Si/Al ratio from 1.2 to 1.5. Re (surrogate for Tc) was loaded to the geopolymer matrix to explore its immobilization. The geopolymers and Re–loaded geopolymer were characterized by XRD, FTIR, TG-DTA and SEM-EDAX. Further, geopolymers were also synthesized under hydrothermal conditions. The products synthesized by various techniques were dried and characterized by XRD, FTIR, TG-DTA and SEM-EDAX. Chemical Durability studies were carried out on the Re loaded (2.56 wt%) matrices and found to show a normalized leach rate of ~ 13.3 x 10^{-3} g/cm^2.day.

Keywords: Geopolymer, X-ray diffraction, Rhenium, Low level liquid waste

1. Introduction

Radioactive waste is generated by various activities, such as reprocessing of nuclear fuel, use of radio-isotopes by hospitals and industries. Safe immobilization of radioactive waste is essential and need of the hour for the safe operation of power plants, long term sustainability of nuclear energy and public acceptability [1]. The close fuel cycle systems need reprocessing of spent fuel and the immobilization of waste for the environmental safety of the nuclear installations. The waste generated in nuclear plants are categorized as high level waste (HLW), intermediate level (ILW) and low level waste (LLW). Low level waste contains significant quantities of Tc–radio isotopes in addition to various other radio-nuclides. Since ^{99}Tc isotope has significant fission yield (6.06%), high mobility, with a long half life (2x10^5 years) and moreover it gets oxidized to volatile technetium pertechenetate (TcO_4^-)[2,3] a highly volatile species; therefore it needs to be separated and immobilized [4]. Further, ^{99m}Tc has applications in the nuclear medicine, so separation and immobilization into a suitable matrix of such radio-nuclides can have societal applications. If ^{99}Tc is released to air, it will get attached to the dust particles present in air and finally get settled on the plant or on soil and would enter into the food chain. If released to aquatic environment, it gets accumulated in marine organism and plant and subsequently enters into the food chain. If it is disposed off in terrestrial environment, some fraction of it comes to soil and ground water and eventually enters into the food chain. To circumvent all the above mentioned problems, a suitable matrix should be selected so that ^{99}Tc can be immobilized at relatively low temperatures, avoiding the volatilization loss. Since Tc is a synthetic element and radioactive, a simulant such as rhenium (Re, non radioactive) is used in place of Tc. Further, the chemical and physical properties of the elements are very much similar [5]. The ionic radii of Tc and Re in different oxidation states and different co-ordination type are also almost similar [6]. Xu etal has studied the incorporation of Re (surrogate for Tc) into iron phosphate glass, with 1.1 mass % loading by melting process at 1000^{0}C; however, they reported that Re escaped from the melt when temperature increased [7]. Invetigations were carried out to explore the suitability of geopolymer [8] as a candidate matrix for the immobilization of Re. Geo-polymers are inorganic ceramic materials that form long –range, covalently bonded non crystalline networks [9] as shown below.

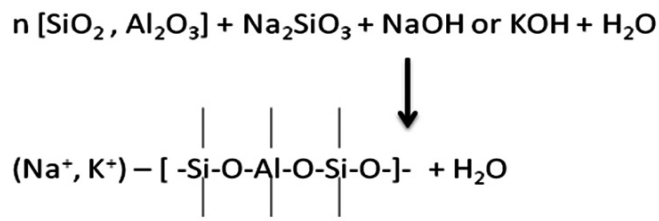

These materials are a new generation of environment friendly cement and are made of silica and alumina as their major constituents [10]. In this study, geopolymer was synthesized and rhenium was incorporated into the

geopolymer matrix. The geopolymers so prepared with and without Re loading was characterized by XRD and various other techniques. The leaching studies on the Re loaded samples were also carried out by static leaching conditions. The results obtained in this study are described in this paper.

2. Materials and methods

Geopolymers were synthesized by using silica (SiO_2), alumina (Al_2O_3), sodium silicate (Na_2SiO_3), sodium hydroxide (NaOH) and water. The activator solution was composed of sodium hydroxide, sodium silicate and water. The water and sodium silicate were weighed and mixed in a beaker. The sodium hydroxide was weighed and placed into another beaker. The weighed sodium hydroxide pellets were poured into beaker containing sodium silicate solution. The solution was stirred until the solution became clear. During this process, a significant amount of heat is released. The solution was covered and kept at least 3 hrs for cooling at room temperature. The silica and aluminum hydroxide were weighed and put in a bowl. Silica and aluminum hydroxide were grinded thoroughly. After that the activator solution was added to the mixture of silica and aluminum hydroxide and mixed thoroughly by grinding. During grinding cohesive mass was formed. Then the mix was placed in an oven at 60 ^{0}C for complete drying. Table 1 shows the variation of NaOH concentration, Na_2O/SiO_2, $Na_2O/Al(OH)_3$ and water/solid ratio for the preparation of geopolymers. Further the geopolymers are named for identification purpose as geo-polymer1 (abbreviated as Geop1) for the ratio of Na_2O/SiO_2 = 0.220; similarly for Na_2O/SiO_2 ratio = 0.320 as Geop2, and geopolymer synthesized by hydrothermal process abbreviated as Hy-Geop. Similarly, Table-2 shows the weight % of precursors and activators for different Si/Al ratio. Table-3 represents the mole % of precursor,activator for different Si/Al ratio. The concentration of precursors and activators in weight and mole percent for the rhenium loaded geopolymer having Si/Al ratio of 1.36 is shown in Table-4.

Table 1: Experimental conditionsused for synthesis of Geopolymer.

Name of Geopolymer	Na_2O/SiO_2	$Na_2O/Al(OH)_3$	Water/Solid	NaOH concentration (M)
Geop1	0.220	0.230	0.770	4-5
Geop2	0.320	0.370	1.190	2-3
Hy-Geop	0.109	0.097	1.004	3-4

Table 2: Weight % of precursors and activators for different Si/Al ratio

Name of Geopolymer	Si/Al	SiO_2 [wt%]	$Al(OH)_3$ [wt%]	Na_2SiO_3 [wt%]	NaOH [wt%]	H_2O [wt%]
Geop1	1.36	18.01	22.56	10.18	5.40	43.78
Geop2	1.54	13.04	16.49	11.99	4.08	54.38
HyGeop	1.19	17.74	22.33	4.27	5.53	50.10

After preparation of Re-loaded geo-polymer, it was examined by XRD and observed to form nitratine ($NaNO_3$) phase [11]. The nitratine phase did not decompose even on further heat treatment at 200^{0}C, 300^{0}C and 500^{0}C in air ambience. Therefore, reduction of nitratine was carried out by adding glucose and heat-treating the mixture at 700^{0}C for 4h in air.

Table 3: Precursors and activators expressed in mole % for different Si/Al ratio

Name of Geopolymer	Si/Al	SiO_2 [mole%]	$Al(OH)_3$ [mole%]	Na_2SiO_3 [mole%]	NaOH [mole%]	H_2O [mole%]
Geop 1	1.36	9.25	8.92	2.62	4.2	75.01
Geop 2	1.54	5.93	5.78	2.68	2.78	82.81
Hy-Geop	1.19	8.43	8.16	1.00	3.95	78.66

Preparation of Re-loaded geo-polymer: Rhenium (Re) loaded in Geopolymer1 (Si/Al : 1.36)

Table 4: Concentration of precursors, activators and Re in Geopolymer1 shown in Mole, Mole%, Wt., Wt% for the geopolymer having Si/Al =1.36.

Name of Geopolymer	Type	Si/Al	SiO_2	$Al(OH)_3$	Na_2SiO_3	NaOH	H_2O	Re
Geop 1	Wt.(g)	1.36	0.140	0.1761	0.079	0.0425	0.35	0.0207
Geop 1	% Wt.	1.36	17.32	21.78	9.77	5.25	43.30	2.56
Geop 1	Mole	1.36	$2.33*10^{-3}$	$2.28*10^{-3}$	$0.65*10^{-3}$	$1.06*10^{-3}$	0.019	$0.11*10^{-3}$
Geop 1	% Mole	1.36	9.16	8.96	2.55	4.17	74.71	0.434

Characterization methods

Powder X-ray diffraction was used to examine the formation of geopolymer and/or absence/presence of any un-reacted phases. M/s.Panalytical X'Pert powder diffractometer with Cu-K_α radiation, mono-chromatized by a curved graphite crystal placed in front of the NaI (Tl) scintillation detector was used to characterize the powders. Scans were made in the 2θ range of 5-80 deg.with a scan rate of 0.05 deg. per second and a counting time of six seconds per step.

The geo-polymer materials are mainly composed of aluminosilicate network and alkali cations. The aluminosilicate network having possible number of linkages (Si-O-Si, Si-O-Al, Si-O, Si-O-M where M=Na), each having different vibrational modes. The measurements by infrared spectroscopy were carried out by using Bomem, MB-100 FTIR, resolution 4 cm^{-1} in mid IR range (4000-400 cm^{-1}).

The morphology of the sample surface was characterized by scanning electron microscopy (SEM XL 30, Philips, LaB_6 filament and resolution 2 nm) and the composition of the surface was further analyzed by SEM-EDS.

3. Results and Discussion

3.1 XRD analysis of geopolymer

The powders so prepared were characterized by X-ray diffraction technique and the typical XRD pattern showed the formation of geopolymer having a broad amorphous peak centered around two theta value of 25-30 degree as shown in Fig.1. Depending on the reaction conditions some crystalline peaks corresponding to crystalline

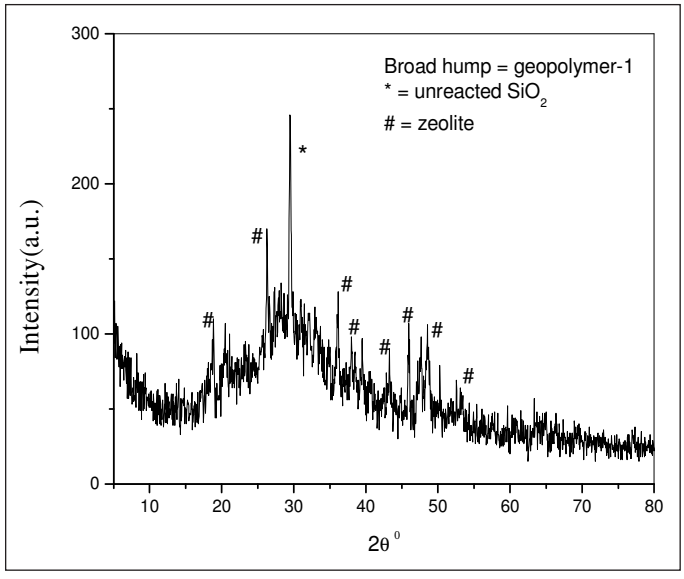

Fig.1: *XRD pattern of geopolymer1 (Si/Al=1.36)*

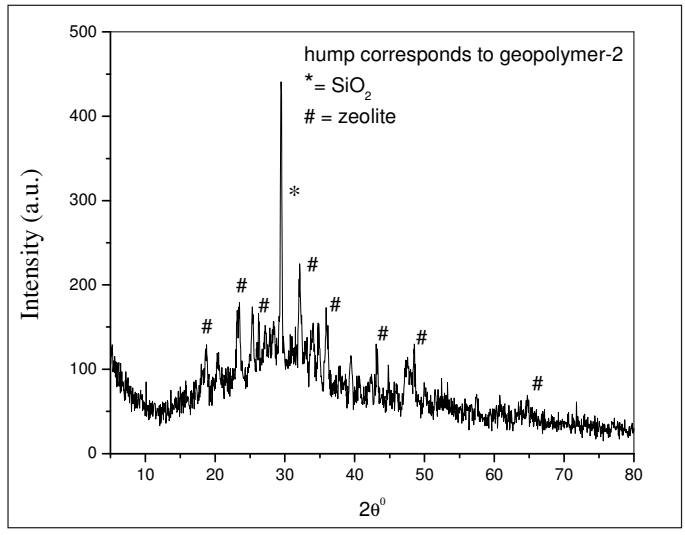

Fig.2: *XRD Pattern of geopolymer2 (Si/Al=1.54)*

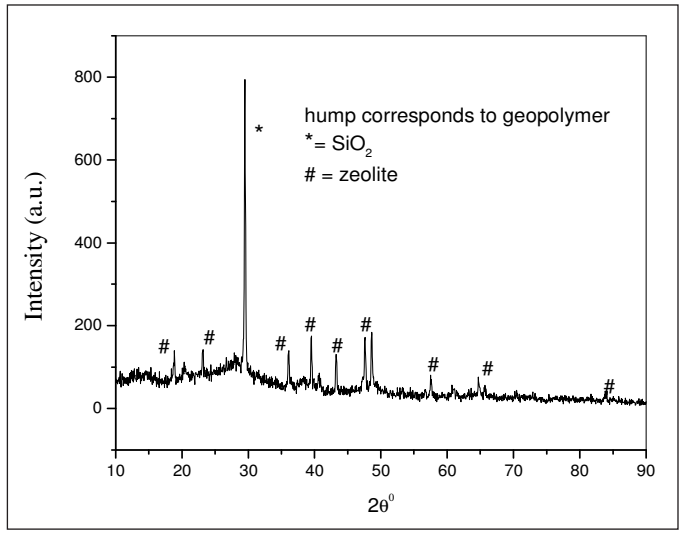

Fig. 3: *XRD pattern of geopolymer prepared in hydrothermal condition (Si/Al=1.19)*

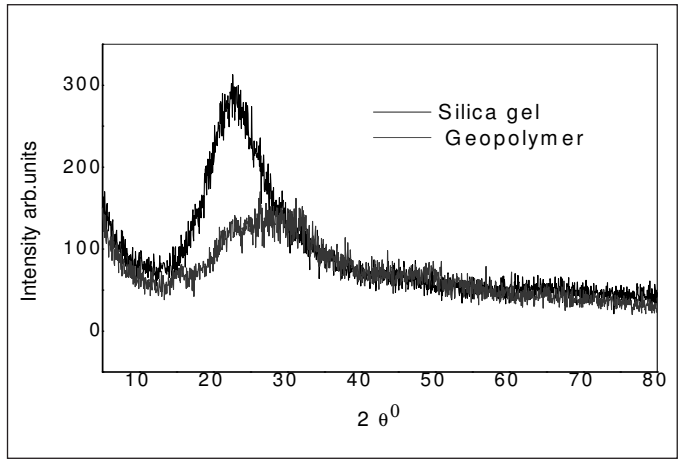

Fig.4: *XRD pattern of and Silica gel and geopolymer (Si/Al=1.36)*

SiO_2 are also observed in the XRD patterns (Fig.2). The geopolymer prepared under hydrothermal condition showed more intense peaks in the XRD pattern indicating the enhancement of crystallization (Fig.3). Geopolymer was also synthesized by using nano-crystalline silica gel; a broad hump is only observed in the XRD pattern as shown in Fig.4. However, on loading (incorporating) rhenium into the geopolymer matrix the position of the broad hump is shifted towards higher 2θ value in the XRD pattern. This may be an indication of the substitution of Re into the geopolymer matrix.

3.2 FTIR Spectra of geopolymers

In Fig. 5 the FTIR spectra of the geopolymers (geopolymer1 (Ge1), geopolymer2 (Ge2) and (Hyge 2)) are shown. All the geopolymers found to contain hydroxyl groups in their framework structure as evident from the FTIR spectra. Geopolymer framework contains large amount of adsorbed water and hydroxyl groups as part of the structure. The band at 3450 cm^{-1} is ascribed to (OH) hydroxyl stretching. The band at 1650 cm^{-1} is attributed to the OH bending vibrations. The band at 600 cm^{-1} is due to Al-O-Si stretching vibration and the band at 450 cm^{-1} is due to Si-O-Si bending vibration. The band at ~710 cm^{-1} is ascribed to the bending vibration of tetra co-ordinated Al(IV)-O-Si in a cyclic structure observed in the FTIR spectra of geopolymer indicates the formation of aluminosilicate networks [12-15]. The most characteristics band is located between 900 and 1100 cm^{-1}, it is attributed to the asymmetric stretching "X-O" (where X represents Si or Al).

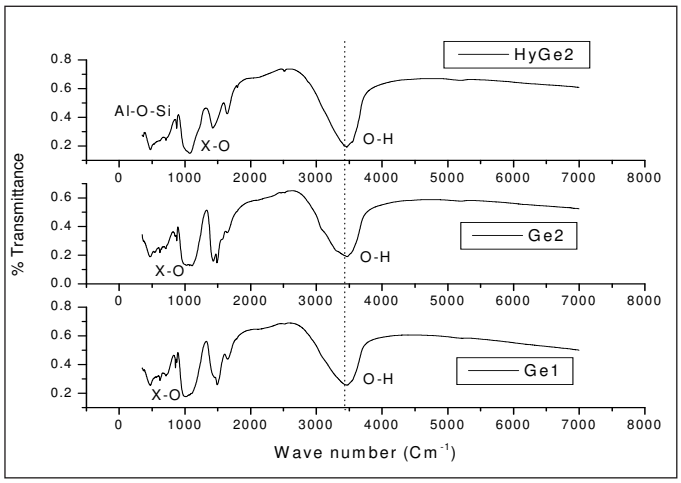

Fig.5: FTIR spectra of geopolymer1 (Ge1), geopolymer2 (Ge2) and (Hyge 2) geopolymer

3.3 Thermogravimetric analysis of Geopolymer

The thermogravimetry (TGA) and differential thermal analysis (DTA) studies show the thermal characteristics of the material at 25-900^{0}C temperature range under Ar ambience. In Figs. (6-8), the first major decline in weight is associated with the dehydration of water from pores (dehydration), which shows 10% weight loss in the temperature range from 25 to 120^{0}C. The second significant weight loss occurs between 120 ^{0}C to 300 ^{0}C and this weight loss is specifically associated with the loss of inter layer and structure bound water in Sodium Alumino Silicate Hydrated gel (N-A-S-H Gel).This mass loss corresponds to the dehydration process of amorphous gel phases (N-A-S-H Gel). Nedelijkovic et.al [16] and Carlos et.al [17] has also observed similar weight loss in their study. The third weight loss in the temperature range between 500 ^{0}C to 800 ^{0}C is due to decomposition of carbonates present in the geopolymer matrix. Formation of carbonate is most probably due to the absorption of atmospheric CO_2 by Na_2SiO_3 as shown in eqn.1 to produce mono silicic acid and enhancing the gel formation as suggested by M.D.Garba et.al. [18]. The broad exotherm in all the three thermograms around 240-650^{0}C is due to recrystallization of the geopolymer.

$$2Na_2SiO_3 + 2CO_2 + 4\,H_2O \rightarrow 2\,Si(OH)_4 + 2Na_2CO_3 \qquad (1)$$

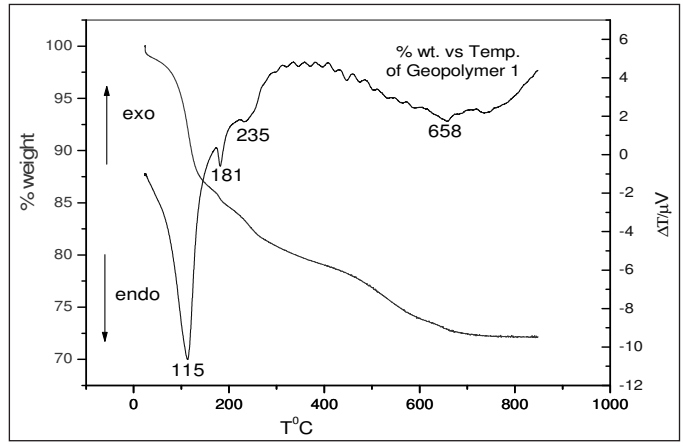

Fig.6: TG-DTA thermogram of geopolymer1, Si/Al ratio =1.36

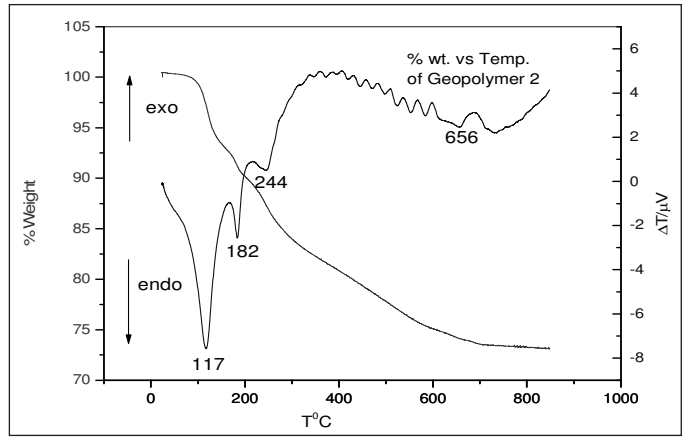

Fig.7:TG-DTA plot of geopolymer2, Si/Al ratio= 1.54

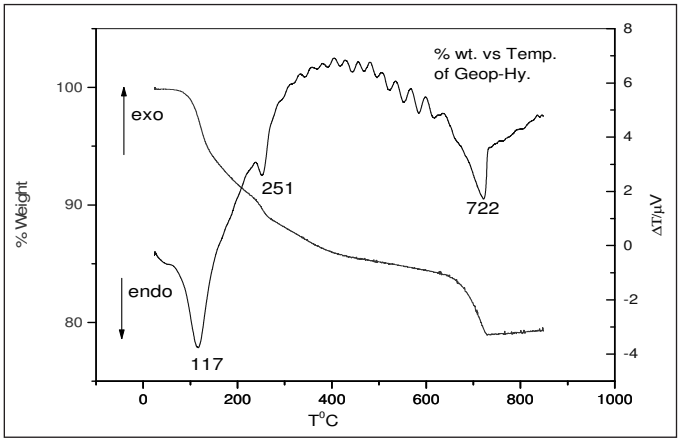

Fig.8: TG-DTA plot of geopolymer prepared under hydrothermal condition , Si/Al ratio =1.19

3.4 Surface morphology and elemental analysis of Geopolymers prepared by normal condition (at 60^{0}C and atmospheric pressure)

3.4.1 Microstructure of geopolymer1

The surface morphology and microstructure of the powders are shown in Fig.9 (a) and 9 (b). The black and white portion of the image corresponds to the existence of geopolymer. The dark continuous patch consists of gel-like material with microcracks and micropores which can be clearly observed on the surface. The corresponding EDX (Fig. 9 (c) of the images show the presence of Na,Si and Al in the material geopolymer-1. The SEM micrograph of geopolymer-2 shown in Fig. 10 (a-b) and the corresponding EDX shown in Fig.10 (c) shows the presence of Na, Si, Al in geopolymer -2 as the constituent elements. The micocracks observed in SEM images as shown in Fig. 9(a) and (Fig. 10 (a) were caused because of loss of water from the pores during poly condensation in the gel matrix [19] on drying the powders.

3.4.2 Surface morphology and elemental analysis of Geopolymer2

3.4.3 Characterization of rhenium-Loaded Geopolymer

The XRD pattern of the 2.56 wt.% Re loaded geopolymer is shown in Fig. 12. The XRD pattern shows the formation of nitratine. Since rhenium nitrate solution was used as the source of Re; nitrate anions (NO_3^{-1}) react with Na present in the matrix leading to the formation of crystalline nitratine

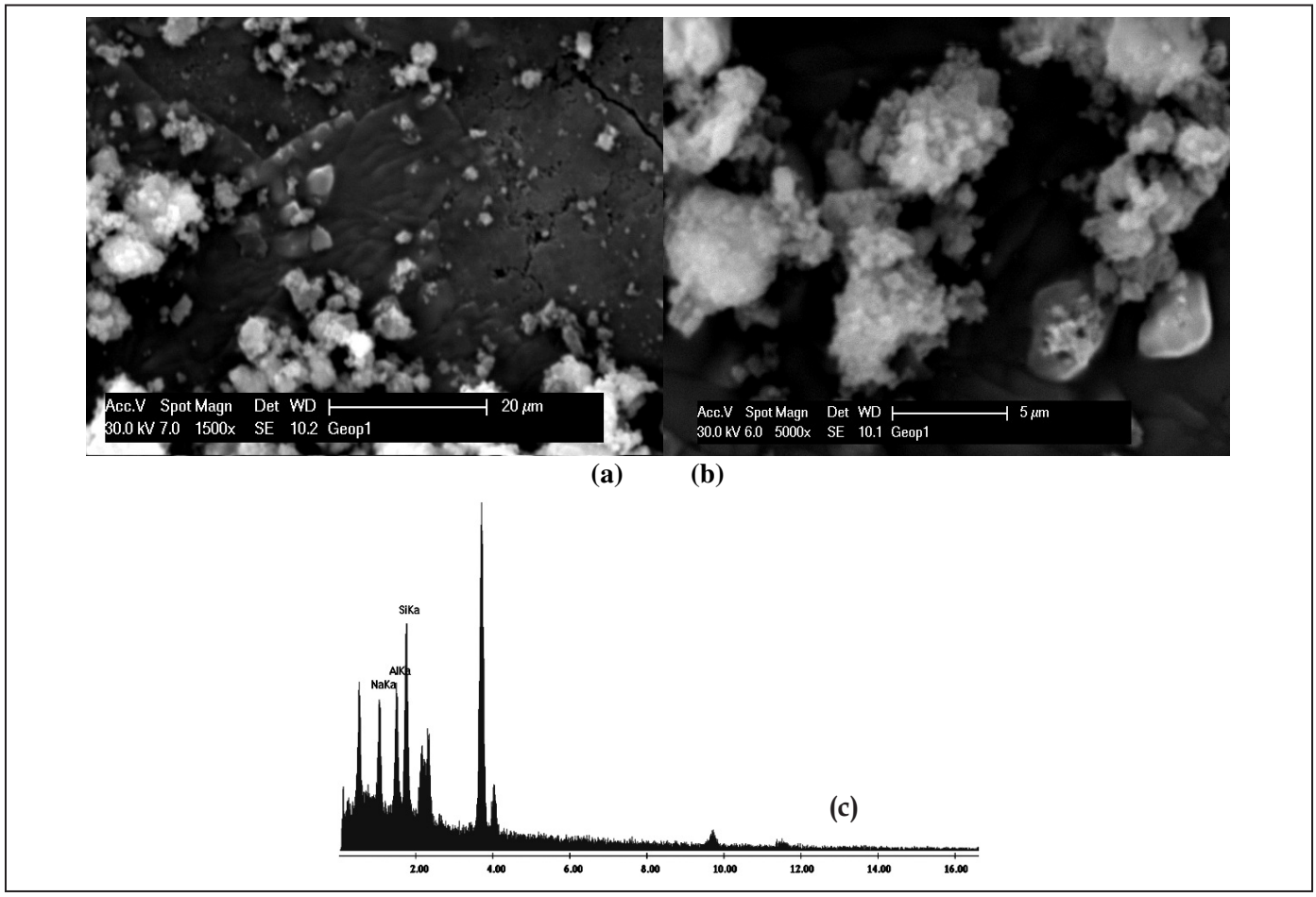

Fig.9: Surface morphology of geopolymer1 (a) at 1500x and (b) at 5000x magnification (c) Energy dispersive X-ray spectroscopy of geopolymer1

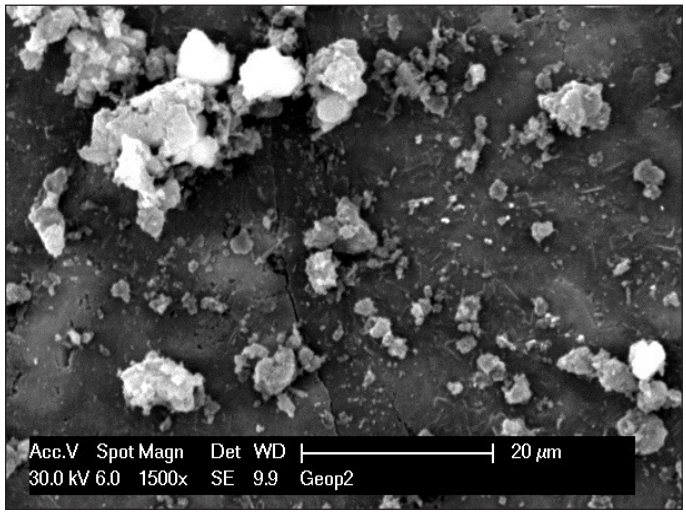

(a)

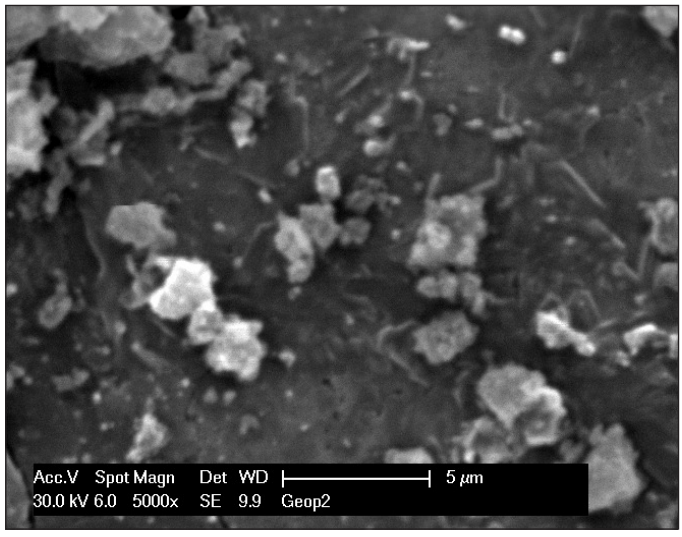

(b)

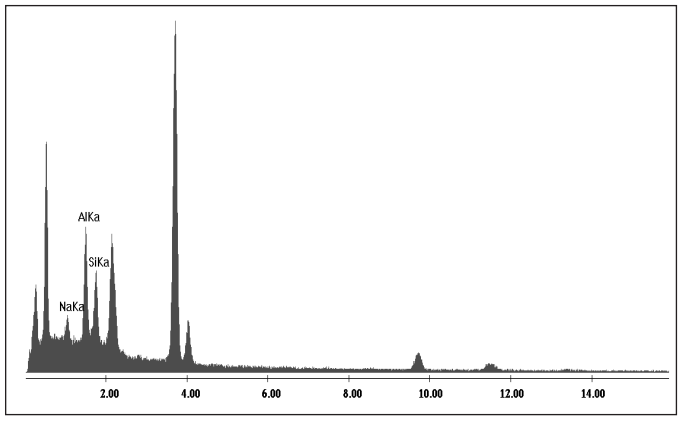

(c)

Fig.10: *Surface morphology of geopolymer2 (a) at 1500x and (b) at 5000x magnification and (c) Energy dispersive X-ray spectra of geopolymer 2*

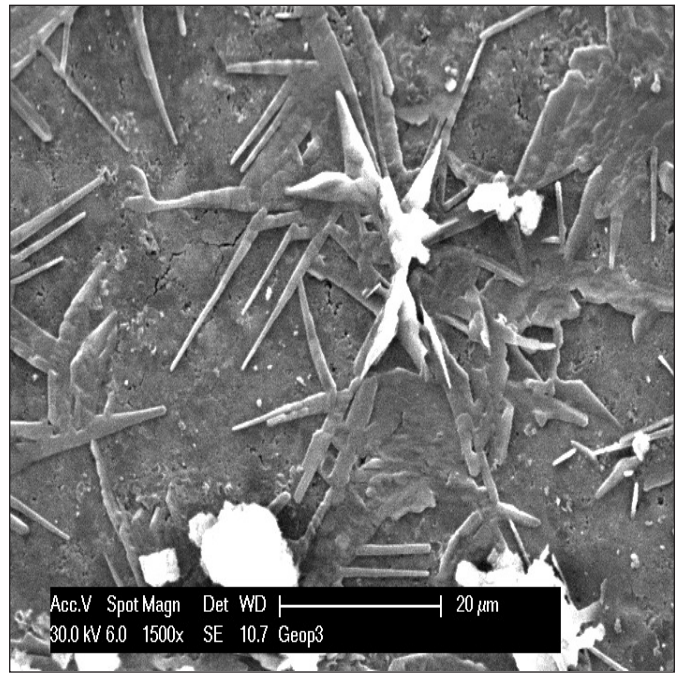

(a)

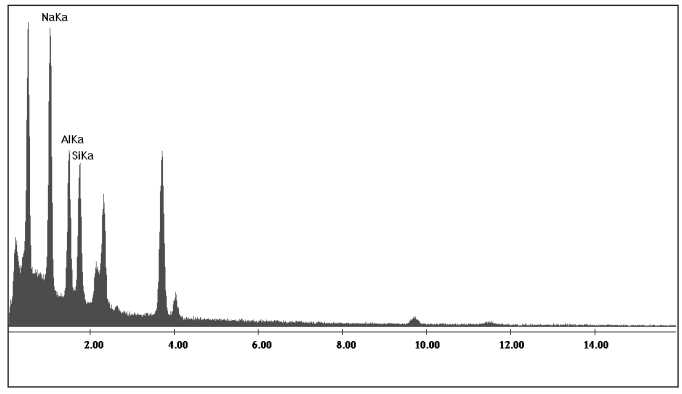

(b)

Fig. 11: *(a) SEM micrograph of the geopolymer prepared under hydrothermal condition and (b) corresponding EDS of the sample.*

($NaNO_3$) at 60^0C. However, on heating the powders at 200^0C/5h, 300^0C/5h, 500^0C/5h under air ambience in three different steps and subsequent examination of the powders by XRD, revealed that the nitratine does not decompose at and below 500^0C. The XRD pattern of Re-loaded geopolymer that was heated at 500^0C/5h was showing only nitratine phase. Attempts were made to reduce the nitratine by adding glucose and subsequent heating of the sample at 700^0C/5h in air. A change of colour of the powders from slight yellowish to white was observed. The powder was analyzed by XRD. Some of the most intense peaks of the XRD pattern as shown in Fig.13 was found to match with the XRD pattern of sodium aluminium rhenium oxide silicate [$Na_8Al_6(ReO_4)_2(SiO_4)_6$] as reported in the ICDD-PDF

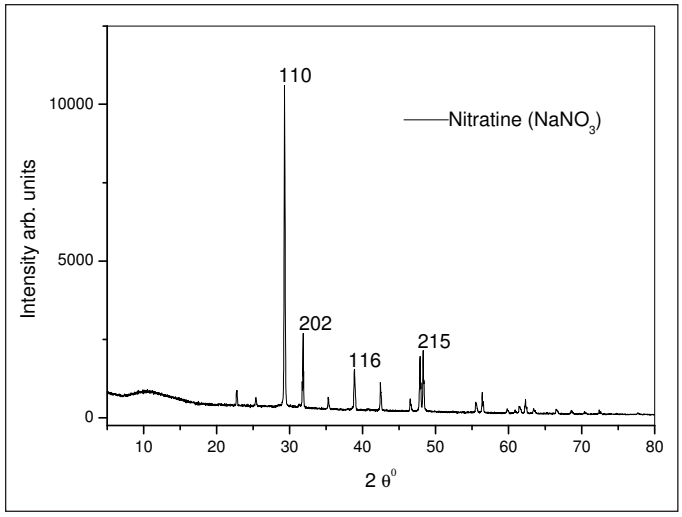

Fig.12:*XRD pattern of Re-loaded geopolymer before reduction*

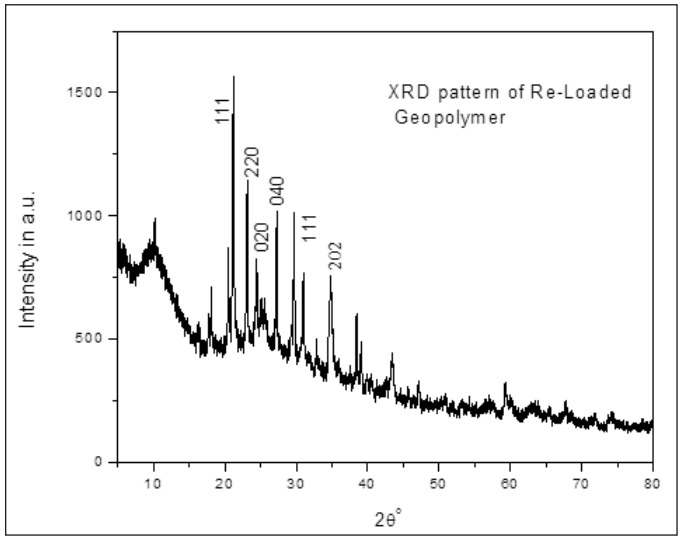

Fig. 13: *XRD pattern of Re-loaded Geopolymer after reduction*

data base [20] indicating the incorporation of Re into the geopolymer matrix.

3.4.4 FTIR-spectra of Re-loaded Geopolymer :

In pristine geopolymer a band is observed at 710 cm^{-1} in FTIR spectra (Fig. 5) indicating the formation of Al(IV)-O-Si bonds. However, after loading rhenium in geopolymer this band shifts towards the lower wave number (697 cm-1).The shift is approximately 13cm^{-1} demonstrates an obvious change in the network linkage (bonding character) resulting in the formation of new product with different structural arrangement. The band observed at 1451cm^{-1} is due to the asymmetric stretching of carbonate (O-C-O stretching), which suggests the presence of sodium carbonate as a result of the reaction between excess sodium/ sodium hydroxide and atmospheric CO_2. A shift in band position from 1451cm^{-1} to 1388 cm^{-1} was also observed for this functional group in Re-loaded geopolymer. All these observations support the incorporation of Re into geopolymer framework.

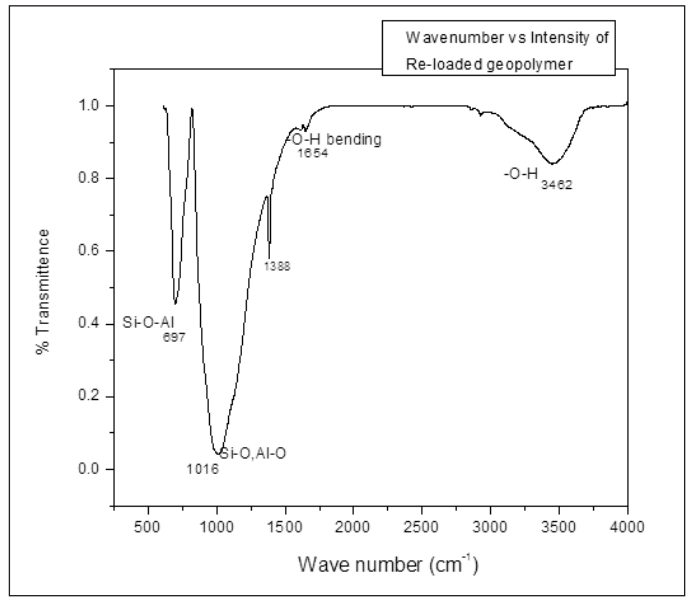

Fig.14: *FTIR spectra of Re-loaded Geopolymer after reduction.*

3.4.5 TGA-DTA of Re-loaded geopolymer:

The TGA-DTA plot in Fig. 15 of Re-loaded geopolymer shows the absence of endotherm around (115-117^{0}C) as observed in Fig 6-8 (geopolymer without Re loading). In Fig. 6-8 the TGA-DTA plots corresponds to the samples which were heat-treated at 60^{0}C only and were not loaded with Re. Whereas, the plots in Fig. 15 corresponds to the powders that are loaded with Re and were heat-treated at 700^{0}C/5h. Therefore, the endotherm at ~115^{0}C is not observed in Re –loaded sample (Fig. 15); this is attributed to the loss of interlayer water from Re-loaded sample at elevated temperatures. However, the observed endotherm at 182^{0}C and 316^{0}C are due to the loss of structure bound water of the Si-O-Al network. Further, the broad exotherm is not very prominent as was observed in case of pristine geopolymers (without Re loading). This may be attributed to the absence of recrystallization in case of Re- loaded sample, which has already been heat-treated at 700^{0}C/5h.

3.4.6 Surface morphology of Re-loaded Geo-polymer after reduction with Glucose

The surface morphology and microstructure of Re-loaded geopolymer as shown in Fig. 16 is different compared to the unloaded geopolymers (Fig. 9(a,b) , Fig.10 (a,b), Fig.11(a). In Re –loaded geopolymer the surface is having cracks and micro-pores. This might have been created by the evolution of NO_x gas, water, CO_2 etc. during

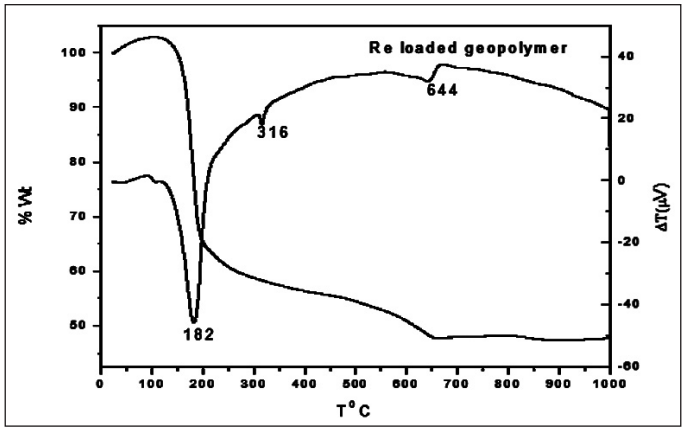

Fig.15: TG-DTA plot of rhenium loaded geopolymer

heat-treatment at 700^{0}C/5h. The corresponding EDX of the surface is shown in Fig. 16(a) that indicates the presence of Na,Si,Al and Re in the synthesized matrix. Further, elemental mapping of the constituent elements were carried out by SEM (shown in Fig. 16). The images of the elemental maps are shown in Fig. 17 (a,b,c,d). Fig. 17(a) shows the distribution of rhenium in the matrix, similarly distribution of Al is shown in Fig. 17(b), Na in Fig. 17(c) and Si in Fig. 17(d) respectively. This confirms that Re is retained in the geopolymer matrix.

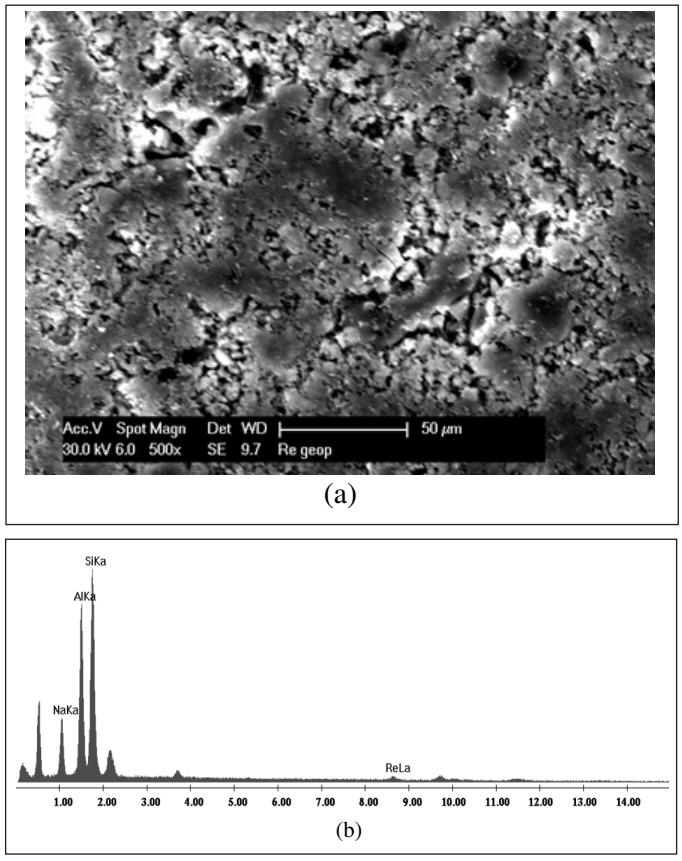

Fig. 16: (a). Surface morphology and (b)Energy dispersive X-ray spectroscopy of rhenium loaded geopolymer

3.4.7 Elemental mapping

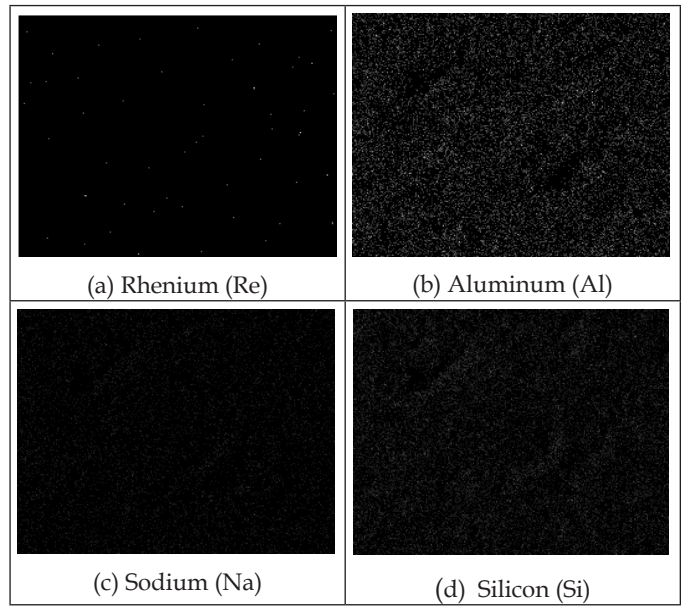

Fig.17: (a-d). Elemental mapping of rhenium loaded geopolymer

3.4.8 EDXRF of rhenium loaded Geopolymer (elemental analysis)

The retention of rhenium in geopolymer matrix is confirmed by ED-XRF analysis. The analysis of rhenium was carried out by using (Re-L_α) peak in EDXRF spectra at energy 8.652 keV as shown in Fig. 18. The presence of Re in the matrix further confirms the fixation of rhenium (simulant for technetium) in geopolymer matrix.

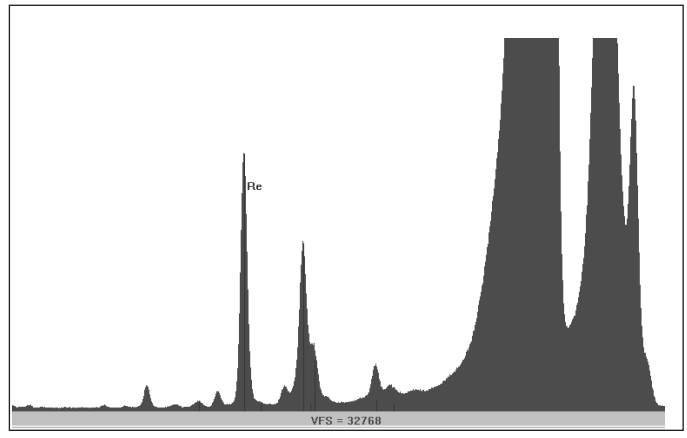

Fig.18: EDXRF of rhenium loaded geopolymer

3.4.9 Leaching study of the Re-loaded geopolymer

Normalized elemental leach rate =

[Weight of element in solution*weight of the solid]/ [Weight of element in solid*surface area of the solid* leaching time]

Or **Normalized leach rate = $[C_{Re} * V]/[F_{Re} * S_A * L_t]$ (eq. 2)**

C_{Re} : concentration of the leachate (Re) in solution (g/mL)

V : volume of leachant solution (mL)

F_{Re} : mass fraction of the Re present in Geopolymer matrix in unleached condition

S_A : Surface area of the pellet put in millipore water for leaching study (cm^2)

L_t : leaching duration in days

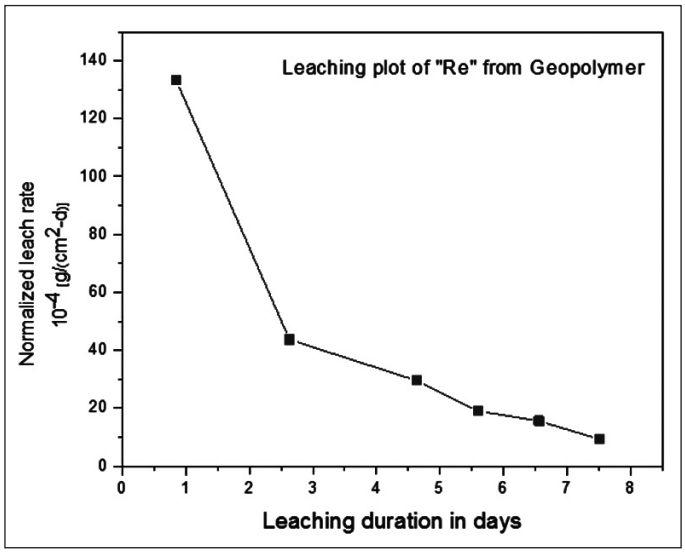

Fig. 19: *Leaching plot of rhenium from rhenium loaded geopolymer*

The normalized leach rate of rhenium was calculated by using the formula [21,22] given in eq.2. The leach rate was found to be high for the first day as shown in Fig. 19; subsequently it is reduced and attains a constant value. This is ascribed to the saturation of the lechant in due course of time. However, the normalized leach rate is found to be 13.3×10^{-3} g/cm^2.day. The leach rate is slightly higher than the acceptable limit.

4. Summary

Geopolymers were synthesized at 60^0C by varying Si/Al ratio from 1.20 to 1.50. Re (2.56 wt%) surrogate for Technetium (Tc) was loaded to the geopolymer matrix. The geo-polymers and Re –loaded geopolymer were characterized by XRD, FTIR, TG-DTA and SEM-EDX. XRD patterns of geopolymers show a broad hump (amorphous peak) centered around 2 theta value of 25-30 degree. The geopolymer reaction leads to the formation of some crystalline zeolite phases as observed by XRD. The bonding of geopolymer and Re (surrogate for Tc) loaded geo-polymer were checked by FTIR analysis. A new peak at approximately 710 cm^{-1} from the bending vibration of tetra co-ordinate Al(IV)-O-Si in a cyclic structure emerged on the FTIR spectra of geopolymers indicates the formation of aluminosilicate networks. The most characteristics band is located between 900 and 1100 cm^{-1}, it is attributed to the asymmetric stretching of "X-O" (where X represents Si or Al). Further, geopolymers were also synthesized under hydrothermal conditions. The products so formed were dried and characterized by XRD, FTIR, TG-DTA and SEM-EDAX. The thermal characterization of geopolymers was checked by thermo gravimetric analysis (TGA) and found to show weight loss up to 650^0C, and no weight loss beyond 650^0C up to 1000^0C as determined in this study. Chemical durability studies of Re (surrogate for Tc) loaded geopolymer matrix was carried out and found to show a normalized leach rate of Re ~ 13.3×10^{-3} g/cm^2.day. The present study shows that geopolymers can be a candidate matrix for retaining Re (surrogate for Tc) by adopting low temperature processes.

Acknowledgements

The authors are very much thankful to Dr. B.K.Panigrahi, Director, MC & MFCG, Dr. K. Ananthasivan, former Associate Director, M & FCG, Dr. N.Sivaraman, Associate Director, M & FCG, Dr. V.Jayaraman, Head, Materials Chemistry Division (MCD) and Dr. C. Remash, former Head, Materials Processing Chemistry Section for their support and constant encouragement. Authors gratefully acknowledge Mr. M.R.Shankaran, former Head,HP unit, BARC-facilities at Kalpakkam for support and encouragement. The authors duly acknowledge Dr. R.Sudha , SO/F, MPCS for recording the SEM micrographs of the samples.

References:

1. Radioactive Waste Management Status and Trends #4 , International Atomic Energy Agency, IAEA/WMDB/ST/4, Feb. **2005**.
2. M. Langowski, J. Darab, P. Smith, Volatility literature of chlorine, iodine, cesium, strontium, technetium and rhenium;technetium and rhenium volatility testing. PNNL-11052, Pacific Northwest National Laboratory, **1996**.
3. H.Lamer. Lammertz, E. Merz and S. Halaszovich, *Mat. Res. Soc. Symp. Proc.*, **1985**, *44*, 823- 829.
4. N.W. Golchert, J. Sedlet, radioanalytical determination of Tc-99 in environmental water samples, *Anal. Chem.*, **1969**, *41*, 669-671.
5. W.M.Haynes ,*CRC Handbook of Chemistry and Physics*, CRC Press/Taylor and Francis, Boca raton,FL, 95th ed. .**2014**.
6. R.D Shannon, Revised effective ionic radii and systematic studies of interatomic distances in halides and chalcogenides, *Acta Cryst.*, **1976**, *A32*, 751-767.
7. Kai Xu, PavelHrma, Wooyong Um, Jong Heo, Iron phosphate glass for immobilization of ^{99}Tc , *J of Nuc Mater.* **2013**, *441*, 262-266.

8. A.D.Cozzi, C.J.Bannochie, P.R.burket, C.L.Crawford and C.M.Jantzen,Immobilization of Radioactive waste in Flyash based geopolymers, *World of Coal Ash (WOCA) conference*, **2011**, May 9-12, Denver, CO, USA.
9. P. Duxson, A. F-Jiménez, J. L. Provis, G. C. Lukey , A. Palomo, J. S. J. van Deventer, geopolymer Technology: The current state of the art, *J Mater Sci* , **2007**, *42*, 2917–2933.
10. H. Akbari, R. Mensah- Biney,J. Simms, Production of geopolymer binder from coal flyash to make cement-less concrete, **2015** world of coalash (WOCA) conference in Nasvhille, May 5-7, TN, USA.
11. C. Palache, H. Berman, and C. Frondel, **195**1, Dana's system of mineralogy, soda-niter (7th edition), *II*, 300–302.
12. V.F.F Barbosa,.; K.J.D MacKenzie,.; C. Thaumaturgo, Synthesis and characterisation of materials based on inorganic polymers of alumina and silica: Sodium polysialate polymers. *Int. J. Inorg. Mater.* **2000**, *2*, 309–317.
13. A. Aronne,.; S. Esposito,C. Ferone,.; M. Pansini,.; P. Pernice,. FTIR study of the thermal transformation of barium-exchanged zeolite A to celsian.*J. Mater. Chem.* **2002**, *12*, 3039–3045.
14. J.D Ortego, Y. Barroeta, Leaching effects on silicate polymerization, A FTIR and 29Si NMR study of lead and zinc in Portland cement. *Environ. Sci. Technol.* **1991**, *25*, 1171–1174.
15. N.J Clayden , S. Esposito, A. Aronne, P. Pernice,. Solid state ^{27}Al NMR and FTIR study of lanthanum aluminosilicate glasses.*J. Non-Cryst. Solids* **1999**, *258*, 11–19.
16. Nedelijkovic, Marija, arbiGhanmi, Microstructural and mineralogical analysis of alkali activated Fly ash slag pastes,Guang 3rd International RILEM conference on microstructure related durability of cementitiouscomposites **2016**.
17. A Carlos. Rosas-Casarez, P Susana., M Arredondo-rea, Jose. Gomez-soberon, L Jorge. Alamaral-sanchez, Ramon Corral Higuera, Experimental study of XRD, FTIR and TGA techniques in geopolymeric materials.**2014**,*4*, 221-226.
18. M.D.Garba, Sodiumsilicate cement squeeze in massive salt formations, *Elixir Appl. Chem.*, **2012,***51,* 10923-10931.
19. S.Alehyen, M.EL Achouri, M.Taibi, Characterization, microstructure and properties of flyash based Geopolymer,**2017**,*8*,1783-1796
20. International Centre for Diffraction Data (ICDD)- Powder Diffraction File, PDF # 04-013-6684, **2018**.
21. J. M. Juoi, M. I. Ojovan, Characterization and durability of glass composite waste from immobilising spent clinoptilolite, *WM'07 conference, Tucson*, AZ, 2007.
22. N. V. Ojovan, I. V. Startceva, A. S. Barinov, M. I. Ojovan, D. H. Bacon, B. P. McGrail, J. D. Vienna, Product consistency test of fully radioactive high-sodium content borosilicate glass K-26, *Mat. Res. Soc. Sym. Proc.*, **2004**, *824*.

ShriVineet Kumar *joined BARC Training School, Mumbai in the year 2015 (59th batch) after completing his M.Sc (Chemistry) degree from Banaras Hindu University (BHU), Varanasi, Utter Pradesh, India in 2015. He joined BARC Facilities (KARP) at Kalpakkam in 2016. Subsequently he obtained his M.Tech degree in the discipline of "Radiological Safety Engineering with specialization in Nuclear Engineering" from HBNI in 2018. Currently he is working in Environmental Survey Laboratory, NAPS, Narora.*

Dr. Hrudananda Jena *joined BARC Training School, Mumbai in the year 1990 (34th batch) after completing his M.Sc (Chemistry) degree from Utkal University, Bhubaneswar, Odisha, India. Subsequently joined IGCAR in the year 1991. He obtained his Ph.D (Materials Science) degree from Indian Institute of Science (IISc.) Balgalore, in 2005. He worked as visiting scientist in the Department of Physics, Southern University, USA on DOE (USA) sponsored project on SOFC materials from 2005- 2006. Currently, he is working on synthesis and processing of nuclear materials in Materials Chemistry Division, IGCAR. His research interest includes synthesis and characterization of novel radwaste matrices (ceramic, glass and glass bonded composites) and their characterization by various techniques. He is a faculty in Chemical Sciences in HBNI and heading Materials Processing Chemistry Section. He is a recipient of National Rural Talent Scholarship in the year 1978-82. He has published nearly 100 papers in journals, book chapters and symposia proceedings.*

Pulsed laser deposition of a few oxide thin films

P. Manoravi[1], M.Joseph[1,2]
[1]*Materials Chemistry and Metal Fuel Cycle Group,*
[2]*Raja Ramanna Fellow & HBNI, Indira Gandhi Center for Atomic Research, Kalpakkam-603 102*
Corresponding author E-mail: mj@igcar.gov.in

Abstract

Oxide thin films find many technological applications in different areas such as sensors, fuel cells, batteries, optoelectronics, memory devices, etc. Brief discussion on the preparation of a few oxide thin films such as $La_{0.9}Sr_{0.1}Ga_{0.8}Mg_{0.2}O_{2.85}$, $CaZrO_3$, VO_x, doped ZnO, $LiCo_{0.85}Cr_{0.15}O_2$ and poly- ethyleneoxide (PEO) by pulsed laser deposition (PLD) will be presented in this article.

Keywords: PLD, Oxide thin films, LSGMO, CaZrO3, LIV-MS

1. Introduction

Thin films of novel materials are being used extensively in devices for diverse applications. Ever since the successful deposition of thin films of high temperature super conductors in 1986, preparation of thin films using pulsed laser deposition (PLD) has become one of the technologically important applications of lasers in materials science. PLD is surprisingly very simple to do and yet very versatile. However, the fundamental processes involved in this deposition can be complex and are not yet well understood. Therefore, the realization of the potential of this technique for production of optimum quality thin films has been slow.

In the thin film deposition of oxides, it is important to have precise control of the cation/oxygen stoichiometry and phase purity. For oxides comprising many cations, it is extremely difficult to fabricate thin films using techniques other than PLD. PLD process enables one to transfer materials from the target stoichiometrically to the substrate and also provides excellent structural properties for most grown films. Hence, PLD is unique in such applications [1]. In this article we summarize results on the preparation of a few such oxide thin films.

2. Experimental

Pulsed laser depositions were carried out using either a Nd-YAG laser (second harmonic, 532 nm beam) or an ArF excimer laser (193 nm). In some of the PLD studies using the Nd-YAG laser, plume characterization was done by using a quadrupole mass spectrometer and the experimental assembly is shown in Fig.1. The details of this experimental facility have been presented elsewhere [2]. Briefly, we use a differential pumping system containing the PLD chamber maintained at a vacuum of ~ $1x10^{-6}$ Torr (2000 l/s, diffusion pump) and the mass spectrometer chamber at ~ $1x10^{-7}$ Torr (cryo pump, 1500 l/s). Mass resolved time-of-arrival spectra were obtained for each of the species. The details of the facility using ArF laser have been presented elsewhere [3]. In studies using the ArF laser the plume was not characterized.

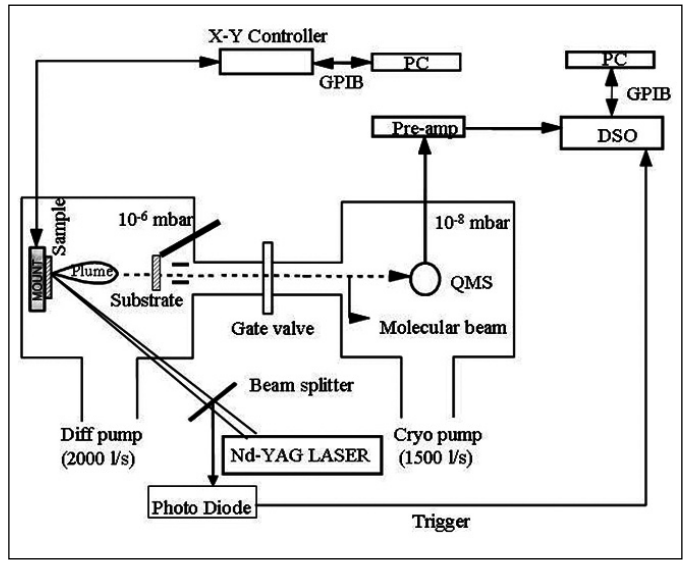

Fig.1: *Schematic of in-house developed pulsed laser deposition facility [2]*

3. Results and Discussions

$CaZrO_3$ thin films

Oxygen sensors find potential application in nuclear industry and particularly in Liquid Metal cooled Fast Breeder nuclear Reactors (LMFBRs). Oxygen present as an impurity in liquid sodium, the coolant in LMFBR, can react with the stainless steel clad components and form compounds (e.g. Na_2CrO_3), which will lead to enhanced corrosion of the clad. Hence, the oxygen present as an impurity in coolant is to be monitored on-line [4]. The presently used yttria stabilized thoria (YDT) based electrochemical oxygen sensors have problems, such

as, poor thermal shock resistance, unsatisfactory sensor performance when exposed to high concentration of oxygen, high cost, etc. The alternative to YDT is calcia-stabilized zircoina (CSZ). However, CSZ is susceptible to sodium attack forming Na_2ZrO_3, which is not an ionic conductor. This problem can be over come by providing a coating of chemically stable oxygen ion conductor on CSZ [5]. One of the suggested materials for this purpose is $CaZrO_3$ [5]. Hence, it is of interest to prepare thin films of $CaZrO_3$. However, one would expect non-congurant evaporation reactions such as $CaZrO_3$ -> <ZrO2>+CaO(g) on heating. Hence, conventional physical vapor deposition may not be feasible. We have prepared thin films of $CaZrO_3$ at room temperature using PLD and then post- annealed the film to get a crystalline $CaZrO_3$ thin film, as confirmed by XRD[6]. In order to get some insight into the deposition process, the plume analysis was performed using a mass spectrometer.

$La_{0.9}Sr_{0.1}Ga_{0.8}Mg_{0.2}O_{2.85}$ thin films

There is a disadvantage in the use of a $CaZrO_3$ thin film in the above application as the oxygen ion conductivity of $CaZrO_3$ is poor compared to CSZ. The recently reported $La_{0.9}Sr_{0.1}Ga_{0.8}Mg_{0.2}O_{2.85}$ (LSGMO) is a much better oxygen ion conductor [7], and hence, can be considered as a better material to be coated over CZS tubes for the sensor development. Also, thin films of LSGMO, have potential application in development of solid oxide fuel cells. It is difficult to prepare a thin film of an oxide of many component elements by methods other than PLD. Therefore, PLD was used to prepare thin films at room temperature and these films were post annealed at 730 °C.

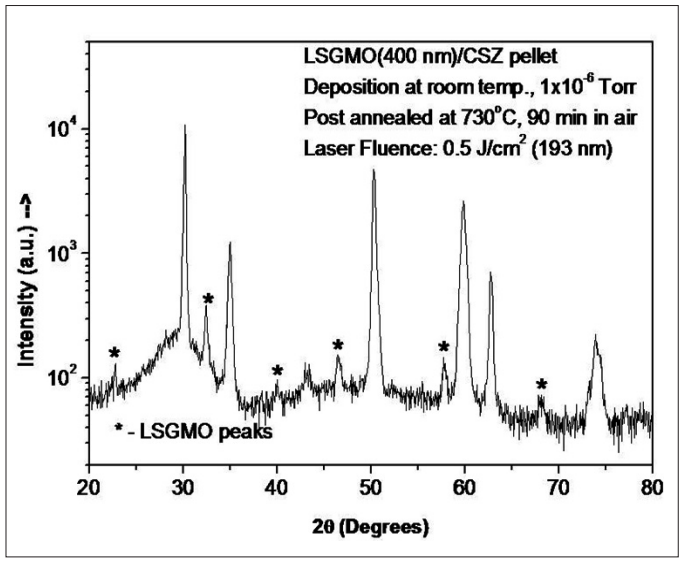

Fig.2: X-ray diffraction pattern of $La_{0.9}Sr_{0.1}Ga_{0.8}Mg_{0.2}O_{2.85}$ thin film on calcia-stabilized zirconia pellet [8].

This mode of preparation at room temperature followed by post annealing is convenient when actual deposition is done on CSZ tubes. The typical XRD pattern of the thin film coated on a CSZ pellet is shown in Fig. 2. LSGMO films were prepared on various substrates and their conductivity was also measured [8].

Similar to the case of $CaZrO_3$, the mass analysis of the plume was performed for the LSGMO system and the species intensity obtained is shown in Fig. 3(a&b). In the case of $CaZrO_3$, stoichiometric film was obtained when the deposition is done in an ambient pressure of 150 mtorr of O , whereas under vacuum (1x10-6 torr) the film obtained was only CSZ. On the other hand, in the case of LSGMO, the film obtained was stoichiometric only when the deposition was done under vacuum and even at an O_2 pressure of 5-10 mtorr, only film of mixed oxides resulted.

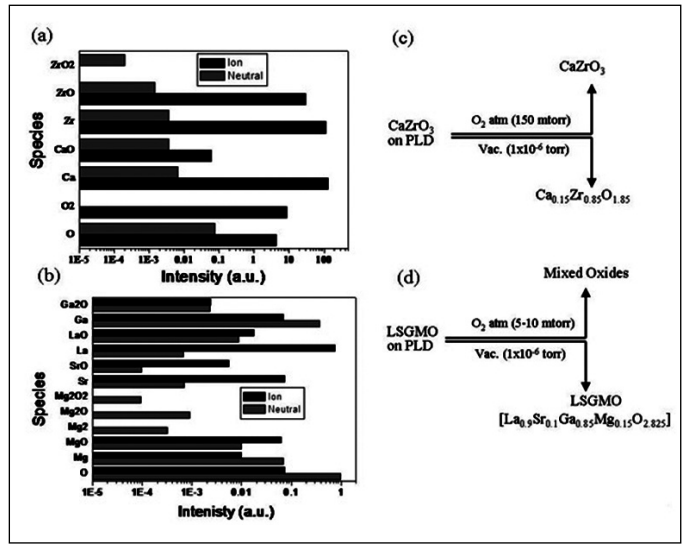

***Fig.3:** Typical mass spectrum of species observed on laser vaporization of (a) $CaZrO_3$; (b) LSGMO; (c) & (d) indicates the stoichiometry of the film obtained for the above two targets in presence of oxygen atmosphere or under vacuum[9].*

This is shown schematically Fig. 3(c&d) and the reason for such observation is explained in ref. [9].

$La_{0.5}Sr_{0.5}CoO_y$ (LSCO) thin films

Oxygen sensors of limiting current type are needed for use under ambient conditions in fast reactor operating area. The conventional oxygen sensors used for this purpose are of galvanic cell type using solid electrolytes and these sensors respond logarithmically to oxygen concentration; i.e. for a change of 1% in oxygen concentration, the typical emf change is only about 1 mV. In an industrial environment where electromagnetic interference prevails, it is better to have a sensor having a linear response based on the limiting current type. Pt is commonly used as the electrode material. The limitation

with the Pt electrode is that due to high electrode-electrolyte interfacial impedance, these sensors have to be operated at high temperatures. To address this problem, Zouyan et al [10] used a mixed ionic-electronic conductor. Unlike LSGMO, $La_{0.5}Sr_{0.5}CoO_{3-\delta}$ (LSCO) is a mixed ionic - electronic conductor [11]. Further more, in SOFC application, LSCO is a potential cathode material for electrolytes such as LSGMO. Hence, it is of interest to prepare thin films LSCO. We obtained highly oriented and smooth films of LSCO on STO(001) substrate[8]. For instance the average roughness obtained for this film

VO_x thin films

Considerable effort is being made towards the development of infrared (IR) thermal imaging devices due to their numerous applications in night vision cameras, remote sensing, etc. In a microbolometer based imaging device, a thin layer of a thermally sensitive material is used whose electrical resistance varies rapidly due to the change in temperature caused by the absorption of IR radiation. Hence, the temperature coefficient of resistance (TCR) around room temperature is one of the important parameters influences the performance of such uncooled microbolometers. Of various semiconducting materials, vanadium oxide is a preferred candidate to be used in uncooled IR imaging systems due to its excellent resistance properties. Eventhough deposition of vanadium oxide thin films by different methods have been reported in the literature, we prepared thin films of this material using PLD and characterized them with regard to their possible application to develop night vision cameras for defense uses [12]. A typical pattern of the 2D 10-element microbolomter array was prepared by PLD. In order to get a uniform film, the substrate along with the mask, positioned slightly off-axis (at room temperature) was rotated at rate of about 8 rpm at an optimized laser fluence of 1.4 J/cm^2 under vacuum. The films obtained were amorphous and the XPS results indicated that vanadium present as a mixture of V^{5+} and V^{4+}. TCR was evaluated by measuring the change of bolometer resistance with temperature in the range 298-373K. This study clearly indicated that the conduction was thermally activated process, with Ea =0.532 eV. The dR/dt around room temperature was 9.3 x 10^3 Ω/°C and TCR was 5%K^{-1}[13]. The obtained TCR value is higher than those measured for most of the vanadium oxide bolometers prepared by sputtering methods making this technique more attractive for device applications.

ZnO thin films

ZnO is another interesting material studied extensively because of its potential applications in various fields, such as UV resistive coatings, gas sensors, solar cells, etc. due to its unique characteristics of piezoelectric, electron conductance and optical transmittance. The range of application of this cost effective material could be widened to a greater extent if one could prepare p-type thin films of ZnO. Efforts were made towards this end and we had earlier prepared such films by Ga, N co-doping method [14,15]. In this method both Ga (donor) and N (acceptor) dopants are doped at the same time and the substitution of N at the appropriate sites in the ZnO lattice is stabilized by the formation of N-Ga-N type bond, there by the repulsive interaction between N acceptors is reduced, leading to an enhancement of acceptor doping. i.e., if a N-Ga-N type of bond is formed in the ZnO lattice, then its bonding orbital will be at the shallow levels to the valance band, thereby can induce p-type conductivity. For this, we need to have N:Ga ratio in the film as 2:1. On the other hand if the ratio is close to 1:1, then the resultant film showed an excellent n-type behavior. Controlling this required ratio of Ga to N in the gas phase seems to be a very difficult task. In our study, the required Ga is taken in the form of Ga doped ZnO target, which is then subjected to laser ablation using an ArF excimer laser. The required N is provided by passing N_2O through an ECR (electron cyclotron resonance) plasma source. High resistivity p-type ZnO films ($\rho=5\times10^5$ Ω.cm; $n=2\times10^{10}$ cm^{-3}) were obtained through simple N doping using N_2O gas. Low resistivity p-type films ($\rho=0.5$Ω.cm; $n=5.5\times10^{19}$ cm^{-3}) were obtained through a codoping approach, using Ga as the donor and N as the acceptor dopant in N_2O atmosphere and very low resistance n-type films ($\rho=5\times10^{-4}$ Ω.cm; $n=2\times10^{22}$ cm^{-3}) were obtained again through co-doping using Ga and N, but under N_2 atmosphere. The optical transmissions for these p- & n-type films are more than 85% in the wavelength range of 300 to 800 nm. It was noted that the window for obtaining different electrical behavior seems to be extremely narrow and very sensitive to experimental parameters – particularly, to the plume-ECR beam interaction region. Also, it was observed that in Li-doped ZnO prepared by PLD method shown Ferroelectric behavior with a memory window of 1.2 V [16].

$LiCo_{0.85}Cr_{0.15}O_2$ thin films

Research to develop all solid thin film power cells or micro-batteries is receiving wide interest, in view of their potential applications in further miniaturization of microelectronics. We have prepared thin films of chromium substituted lithium cobalt oxide ($LiCo_{0.85}Cr_{0.15}O_2$), which is one of the potential electrode

materials in the development of micro Li-batteries. Good quality film was obtained through PLD as was confirmed by detailed IR & Raman spectral studies of film and that of the target [17].

Polyethylene oxide thin films

Polymer electrolytes play an important role in the development of solid-state ionic devices such as batteries, sensors, etc. Of the various polymer electrolyte systems, polyethylene oxide (PEO) based electrolyte systems are very stable and show promise for several device applications. PEO, as such, is an insulator and it becomes ionically conducting after doping with suitable metal salts, e.g., lithium and sodium salts. PEO based electrolytes are used in batteries in the form of thick films prepared by conventional methods. But for the fabrication of micro batteries, PEO is required in the form of thin films and preparation technique must be very clean to match the needs of modern microelectronics industries. While conventional physical evaporation is not feasible because polymers decompose on heating, the feasibility of other deposition techniques is yet to be optimized. PEO when pelletized becomes translucent and hence poorly absorbs laser energy. We have demonstrated, for the first time, the thin film deposition of pure PEO and zirconium oxide dispersed PEO of different molecular weights using PLD [18]. IR studies confirmed the formation of a PEO thin film and XRD studies indicated a crystalline structure similar to that of the target PEO pellet. Films deposited with a laser fluence of less than 1.6 J/cm^2 were found to be smoother than films obtained with higher laser fluences. The dependence of the nature of the thin film on the molecular weight of the target PEO was studied. Low molecular weight (app 1000-5000 amu) targets gave more particulate ejection compared to high molecular weight (5,000,000 amu) targets. Dispersion of fine ZrO_2 powder in the target PEO matrix resulted in lowering the ablation threshold and increasing the film deposition rate. The best film obtained in this work corresponds to a target of PEO (molecular weight 5 x10^6 amu.) + 10 mol% ZrO_2, at a laser fluence of 720 mJ/cm^2 under high vacuum conditions.

4. Conclusion

Thin films of oxides (both inorganic and organic) have immense potential towards the development of sensors and new micro devices in various applications. In this article results obtained on the pulsed laser deposition of thin films of a few technologically important oxides is summarized.

Acknowledgements

The authors are grateful to Prof. D. Mangalraj, Prof. Sa.K. Narayandass of Bharathiar University and Prof. T. Kawai, Prof. H.Tabata of Osaka University, for their support in part of the above studies.

References

1. *Pulsed laser deposition of thin films*, Eds. D.B. Chrisey and G.K. Hubler, (John Wiley & sons, Inc., NY 1994).
2. M. Joseph, N.Sivakumar, *Instrumentation Sci. & Tech.* ***26*** *(1998) 81-94*
3. M.Joseph, H.Lee, H.Tabata , T.Kawai, *J. Appl. Phy.* ***88*** *(2000) 1193-95.*
4. H. U. Borgstedt, C. K. Mathews, *Applied Chemistry of Alkali Metals*, Plenum Press, New York (1987)
5. G. Periaswami, *Electrochemical studies related to the development of on-line meters for use in liquid sodium* (Ph.D. Thesis, University of Madras, Madras 1988)
6. M.Joseph, N.Sivakumar, P.Manoravi, S.Vana Varamban, *Solid State Ionics* ***144*** *(2001) 339-346.*
7. K. Huang, J. B. Goodenough, J. Alloys and Compounds **303-304**, 454 (2000) and references there in.
8. M.Joseph, P.Manoravi, H. Tabata, T. Kawai, *J. Appl. Phys.* **92** (2002) 997-1001
9. M. Joseph, N. Sivakumar, P. Manoravi, "Laser Induced Vaporization Mass-spectrometry Studies on Refractory Materials at Ultra High Temperatures", Chapter - 15 in a book titled "***Materials Under Extreme Conditions: Recent Trends and Future Prospects***", Eds. Tyagi and Banerjee, Elsevier (2017), p.533-573.
10. Zouyan Peng Meilin Liu, Ed. Balko, Sensors & Actuators B**72**, 35 (2001).
11. R. H. E. van Doorn, A. J. Burggraaf, *Solid State Ionics* **128**, 65 (2000).
12. R.T. Rajendra Kumar, B. Karunagaran, D. Mangalraj, Sa.K. Narayandass, P. Manoravi, M. Joseph, Vishnu Gopal, *Smart Mater. Struct.* **12** (2003) 188-192; *Sensors and Actuators* ***A 107*** *(2003) 62-67*
13. R.T. Rajendra Kumar, B. Karunagaran, D. Mangalraj, Sa.K. Narayandass, P. Manoravi, M. Joseph, Vishnu Gopal, Proceedings of ISSS-SPIE 2002, International conference on Smart Materials Structures and Systems, Bangalore, India.
14. M.Joseph, H.Tabata , T.Kawai, *Jpn. J. Appl. Phys.* ***38*** *(1999) L1205-1207*
15. M.Joseph, H. Tabata, H.Saeki, K.Ueda, T.Kawai, *Physica* ***B 302-303*** *(2001) 140-148.*
16. M.Joseph, H.Tabata , T.Kawai, Appl. Phys. Lett. **74**, (1999) 2534-36.
17. R. Vasanthi, I. RuthMangani, P. Manoravi, M. Joseph, R. Kesavamoorthy, C.S. Sundar, S. Selladurai, *Scripta Materialia* **50** (2004) 1329–1333
18. P.Manoravi, M.Joseph, N.Sivakumar, *J. Phys. Chem. Solids* ***59*** *(1998) 1271-77.*

	Periasamy Manoravi *has received his PhD for his research work on solid state battery materials in Indian Institute of Technology, Kanpur. He was a lecturer, Physics in Anna University, Chennai where he worked on polymer based Lithium batteries. He is now Scientist in Indira Gandhi Centre for Atomic Research, Kalpakkam. He was a Swiss National Science Fellow during his Post doctoral work in University of Zurich, Switzerland. His area of research is on Solid state ionics, Li batteries, Laser-solid interaction, Pulsed laser deposition, Ion mobility spectrometer, Mass spectrometry and LIBS. He is specialized in designing Mass spectrometer, Laser ablation based sampling technique, Vacuum system and Handling radioactive materials.*
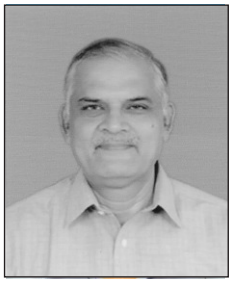	**M. Joseph,** *topper from 26th batch (Chemistry) of BARC training school joined in the Radiochemistry Laboratory, IGCAR, Kalpakkam, in 1983 and since then working in the area of Laser- Mass spectrometry. He worked as a guest researcher at NIST (USA) during 1988-90 and 1997. He was a JSPS post-doctoral fellow at Osaka University during 1998-2000 and worked on pulsed laser deposition of thin films. His notable contribution at IGCAR includes setting up of Laser-induced vaporization mass spectrometer towards the measurement of vapor pressures of nuclear fuels and other refractory materials at ultra high temperatures; Laser-Time-of-flight mass spectrometer for MALDI studies; and development of Ion mobility mass spectrometer for detection of explosives. He served as Group Director, MC & MFCG in IGCAR and superannuated in July 2018. He is presently a Raja Ramanna Fellow at IGCAR.*

Laser Ablated Thin Films of PbS for NH_3 Sensing Under Inert Ambient

Beatriceveena. T.V.[a,b] , E. Prabhu[a], V. Jayaraman[a] and K. I. Gnanasekar[a,*]
[a]*Materials Chemistry Division, Materials Chemistry & Metal Fuel Cycle Group,*
Indira Gandhi Centre for Atomic Research, Kalpakkam-603102, India
[b]*Homi Bhabha National Institute, Training School Complex, Anushakti Nagar, Mumbai-400094, India.*
**Corresponding author E-mail: igsk@igcar.gov.in*

Abstract

Thin films of PbS composed of nanocrystallites were deposited by pulsed KrF laser deposition method with the laser operated at 7 Hz with the fluence of 3 J/cm^2. Grazing incidence X-ray diffraction confirmed the face centred cubic phase of [$Fm\bar{3}m$] PbS thin films. Sensor studies showed that the films were highly selective to ammonia at 473 K even in the presence of hydrogen. Sensors made of PbS operate in the inert ambient with a typical response and recovery times of about 25 s and 120 s respectively. X-ray photoelectron studies on Pb 4f and S 2p levels of PbS reveal that Pb and S are respectively in +2 and -2 valence states. There was no evidence for oxygen contamination implying that the role of adsorbed oxygen is absent. In-situ Hall measurements show an exponential decrease in hole carrier concentration with increasing NH_3 level.

Keywords: Pulsed laser deposition; Lead sulphide; Grazing incidence X-ray diffraction; Ammonia sensor; Hall measurement.

1. Introduction

Development of ammonia sensor which operates in inert ambient is required for monitoring NH_3 generated during hydrolysis of Uranium nitrides (UN). Although the nitride fuel is stored in inert ambient, trace levels of moisture leaks into the fuel storage facilities enforces the hydrolysis of Uranium mononitride resulting in the release of ammonia and hydrogen [1]. Oxide semiconductors such as SnO_2 [2], In_2O_3 [3] can operate only in the presence of oxygen as the later traps the mobile charge carriers around the vicinity of their adsorption site. Hence, they cannot be deployed for monitoring trace levels of NH_3 in the inert ambient. Semiconductors having a direct interaction of the analyte species without the mediation of chemisorbed oxygen are suitable for operations in the inert ambient. Survey of literature yields, semiconducting chalcogenides are promising to be tried as ammonia sensors [4, 5]. PbS, a chemically stable semiconducting chalcogenide used in IR detectors [6], solar cells [7], display devices [8], optical switches [9] is a promising candidate and we report the preparation and gas sensing properties of thin films of PbS.

Gas sensing being the surface phenomenon, not only maximization of surface area is favorable for high probability of the interaction of the trace levels of the analyte gas but also a surface area to volume ratio necessary for fast retrace or recovery of the sensor. These conditions are met in thin film geometry of the sensor. Among the various methods, techniques which provide high quality nanostructured PbS thin films of sensor grade need to be identified. Various methods have been in use for the deposition of PbS thin films namely, electrochemical deposition, chemical bath deposition and successive ionic layer adsorption and reaction. Although these chemical methods are economic and relatively inexpensive, the oxide impurity is inevitable which affects the sensors characteristics adversely. Different physical methods which include sputtering have been known for fabrication of uniform and high-quality thin films but the literature which report preparation of PbS are few. Here, we have employed pulsed (KrF) laser deposition (PLD) which offers greater control over the grain size, thickness, composition, adhesion, and stoichiometry of the multi-component materials for the in-situ growth of PbS thin films.

Gas sensing properties of thin films of PbS for environmental monitoring of trace levels of NH_3 and NO_2 have been reported and the performance in air is relatively poor as the films gradually oxidize [4, 5, 10]. In this work, the ammonia sensing characteristics of thin films of PbS in inert ambient is investigated. In-situ deposition parameters for the growth of PbS thin films are optimized. The influences of working temperature, NH_3 gas concentration and cross-sensitivity in argon and the mechanism of NH_3 sensing probed by in-situ Hall carrier measurements are discussed in the paper.

2. Experimental Details

The PbS powder was prepared by the addition of 0.18 M thiourea (99.5%, M/s Merck) solution to 0.13 M lead acetate (99.9%, M/s Merck) solution under constant stirring at 343 K [11]. The resultant black precipitate was washed thoroughly with water, acetone and finally dried at 373

K in air for 2 h. The resultant powder was made into 12.5 mm diameter discs at a pressure of 20 MPa for a period of 2 hours to be used as targets for PLD. A KrF excimer laser (M/s. Lumonics Inc., Canada) operating at a wavelength of 248 nm under the repetition rate of 7 Hz and a fluence of 3 J/cm^2 was used for deposition. The PbS pellet was mounted in the target holder and the chamber was evacuated to a base pressure of about 3.5×10^{-5} mbar. PbS thin films were deposited on polycrystalline alumina and single crystal $LaAlO_3$ (012) substrates under the in-situ argon pressure of 3×10^{-1} mbar at 553 K for a period of 30 minutes.

The phase purity of the as-deposited films was checked by Grazing incidence X-ray diffraction (GI-XRD, M/s GNR-Explorer, Italy) using Cu K_α radiation (λ=1.5406 Å) with a glancing angle (ω) of 2° with a step size of 0.01°. The topographical features were revealed by atomic force microscopy (M/s NT–MDT, Russia, model SOLVERPRO). The thickness of the films was measured using profilometer (Dektak3 of M/s Veeco, USA). X-ray photoelectron spectroscopy (M/s SPECS, Germany) having Phoibos 150 mm analyzer was used to record the survey and selected area scans. A monochromatic Al K_α (1486.74 eV) source was used and the detection was carried out by the 1D-delay line detector operated in Fixed Analyzer Transmission (FAT) mode with a pass energy of 20 eV throughout the measurements.

The thin film of PbS coated on Al_2O_3 was mounted inside a stainless steel chamber of about 8 mL quantity, provided with an inlet and an outlet for gas flow. The response to different analytes was measured at operating temperature varied from 373 to 523 K. As the intended application of the sensor requires detection of NH_3 in the inert ambient which may contain hydrogen, cross-sensitivitytowards H_2 and NO_x have also been carried out. The carrier gas flowed through the chamber at a rate of 100 mL/min. The flow rates of NH_3, H_2, NO_x, and argon were adjusted using mass flow controllers to yield the desired concentrations in the carrier gas respectively. The response patterns were recorded continuously by measuring the transient changes in electrical resistance of the sensor films using Agilent Bench link data logger (model # 34970A M/s Agilent, Malaysia). Response (R) is defined as

$$R = \frac{(R_g - R_a)}{R_a} \times 100 \qquad (1)$$

where 'R_a' is the resistance of the thin film in argon and 'R_g' is the resistance in the presence of an analyte. The response time is calculated based on the time is taken for 90% change from its initial value and the recovery time is calculated based on the time taken to retrace back to 90% of its initial value after the analyte is withdrawn from the environment.

Temperature dependence of in-situ Hall measurements and four-probe electrical conductivity of PbS thin films were carried out using van der Pauw technique to find the changes in concentration of charge carriers in argon and argon containing trace levels of NH_3.The details of the Hall measurement facility employed for carrying out the carrier measurements were described by Prabhu et al. [12]. PbS thin film deposited on (012) $LaAlO_3$ was mounted on the sample stage and measurements were carried out in the argon and argon containing a specific concentration of NH_3 (100 vppm) flowing at a rate of 50 cc/min. The measurements were carried out in the sensor operating temperature range of 373 to 523 K at a magnetic flux of 3000 Gauss in argon. Hall measurements were also recorded in argon containing 20 – 500 vppm of NH_3 in this temperature interval.

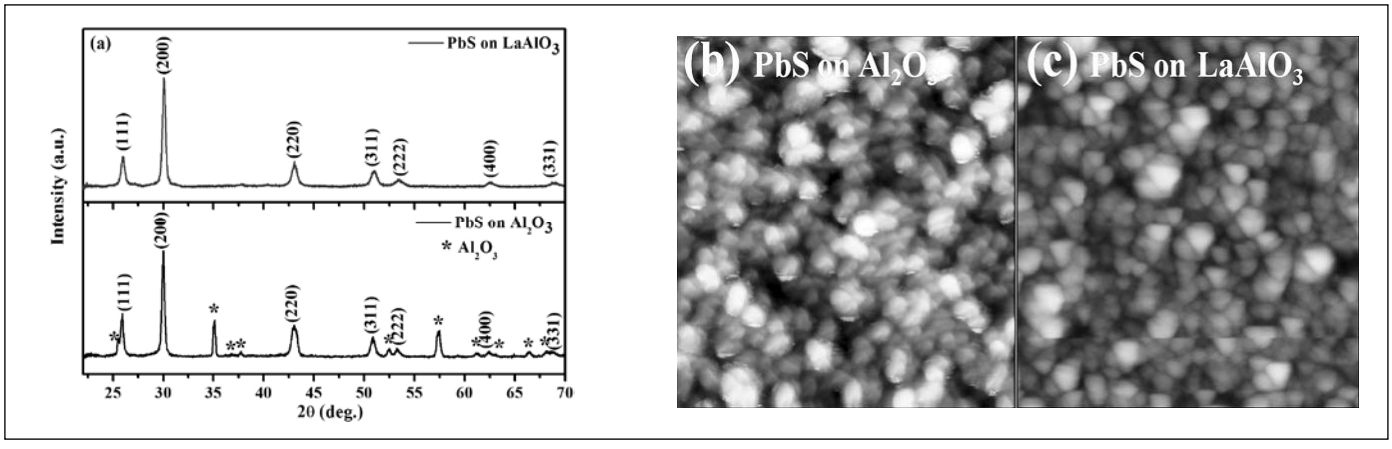

Fig.1 *: (a) GI-XRD patterns and b) & c) AFM images of PbS thin films (2 µm × 2 µm) deposited on Al_2O_3 and $LaAlO_3$ substrates*

3. Results and Discussion

3.1 Structural and morphological studies

The GI-XRD patterns of PbS thin films deposited on single crystal $LaAlO_3$ (0 1 2) and polycrystalline Al_2O_3 substrates are shown in Fig. 1(a). XRD patterns confirm the formation of PbS film on these substrates. The diffraction peaks were indexed in terms of the face-centered cubic structure of PbS with a space group of $Fm\bar{3}m$ (225) (JCPDS Card No. 77-0244). The unit cell length (*a*) was calculated to be 5.9344 Å. The topography of PbS thin films are shown in Figure 1(b) & 1(c) respectively. It reveals that the films are highly granular with grains of uniform size. The average grain size is about 80 nm. The roughness values of films range from 2.5 to 4.2 nm with a mean roughness of about 3.75 nm. The thickness of PbS films under investigation are about 140 nm.

The chemical states of Pb and S in thin film of PbS were examined using core shell XPS. The survey spectrum [Figure 2(a)] illustrates the presence of Pb, S and C and the absence of peak around 530 eV confirms that neither PbO nor SOx species were detected. The high-resolution scan of Pb 4f pattern [Figure 2(b)] was fitted with a curve using the spin-orbit coupling parameter (SOCP) of 4.86 eV and the intensity ratio of 4:3 among the components of $4f_{7/2}$ and $4f_{5/2}$. The fit yields a correlation coefficient of 0.99. The peak positions of $4f_{7/2}$ and $4f_{5/2}$ were found to be 137.98 and 142.84 eV. These values were matching with those reported in the literature for Pb^{2+} [12-14]. Similarly, the S 2p pattern is fitted using a spin-orbit coupling constant of 1.2 eV and the intensity ratio of 2:1 among the components and the overall fit is shown in Figure 2(c). Looking at the position of $2p_{3/2}$ at 161.2 eV peak for sulphur shows an oxidation state of -2 which compares favourably with the value reported in the literature [12-14]. The absence of any extra features in Pb 4f and S 2p patterns confirm that neither PbO nor SO_x were present.

3.2 Gas sensing studies

As the kinetics of the sensing reactions are temperature dependent, sensor studies were carried out for the temperature interval of 373 – 523 K, the usual working range for these type of sensors. A specified concentration of 500 vppm each of NH_3 (reducing gas), H_2 (reducing gas) and NO_x(oxidizing gas) is used to test the response of the PbS thin films. The response for NH_3 increases with the increase in operating temperature and reaches a maximum of 28 % around 473 K and thereafter it decreases giving rise to an optimum temperature of 473 K [Figure 3(a)]. At this temperature the response towards NO_x is about 8 % and that for H_2 is less than 0.5 % which indicates that operating the sensor at this temperature of 473 K provides high selectivity towards ammonia. The response and recovery times for NH_3 were typically around 25 and 125 s respectively at this operating temperature.

After fixing the operating temperature to be 473 K, the concentration of ammonia was varied typically from 20 – 500 vppm and the responses were recorded [Figure 3(b)]. The calibration plot shows that the response is systematic with the increase in NH_3 concentration up to 500 vppmand yields a polynomial fit with the regression coefficient of 0.997. A linear response was observed up to 100 vppm ammonia, thereafter it reaches the saturation. Inset of Figure 3(b) shows typical pattern of transient changes in resistance of PbS thin film towards NH_3 and NO_x. An increase in resistance is observed for NH_3

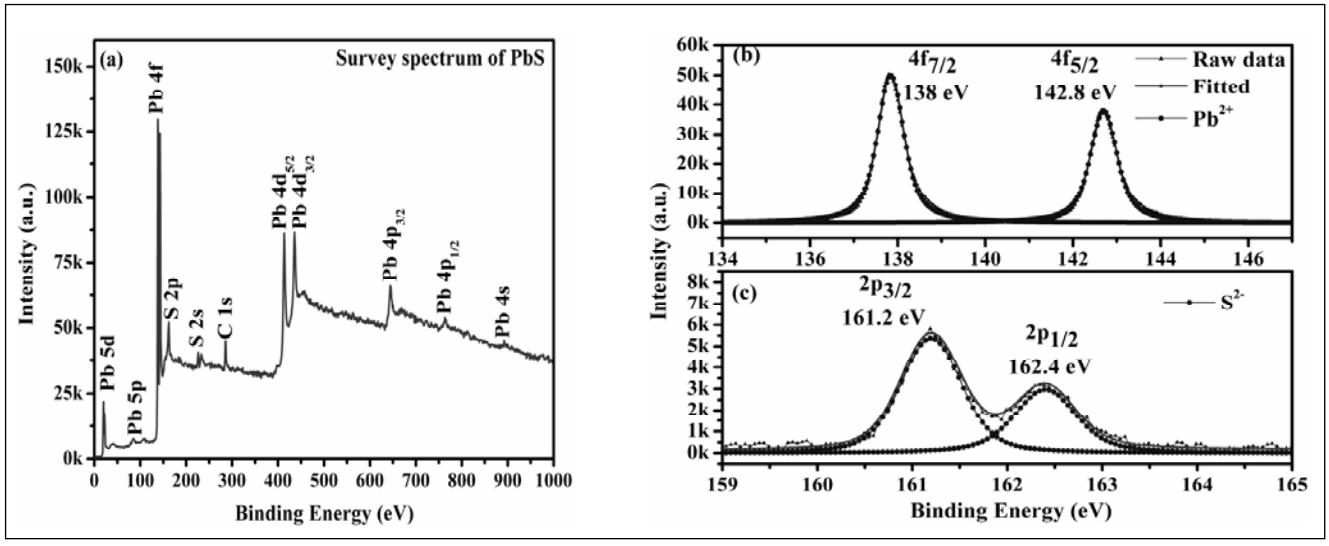

Fig.2: *(a) Survey scan,(b) Pb 4f and (c) S 2p spectra of PbS thin film*

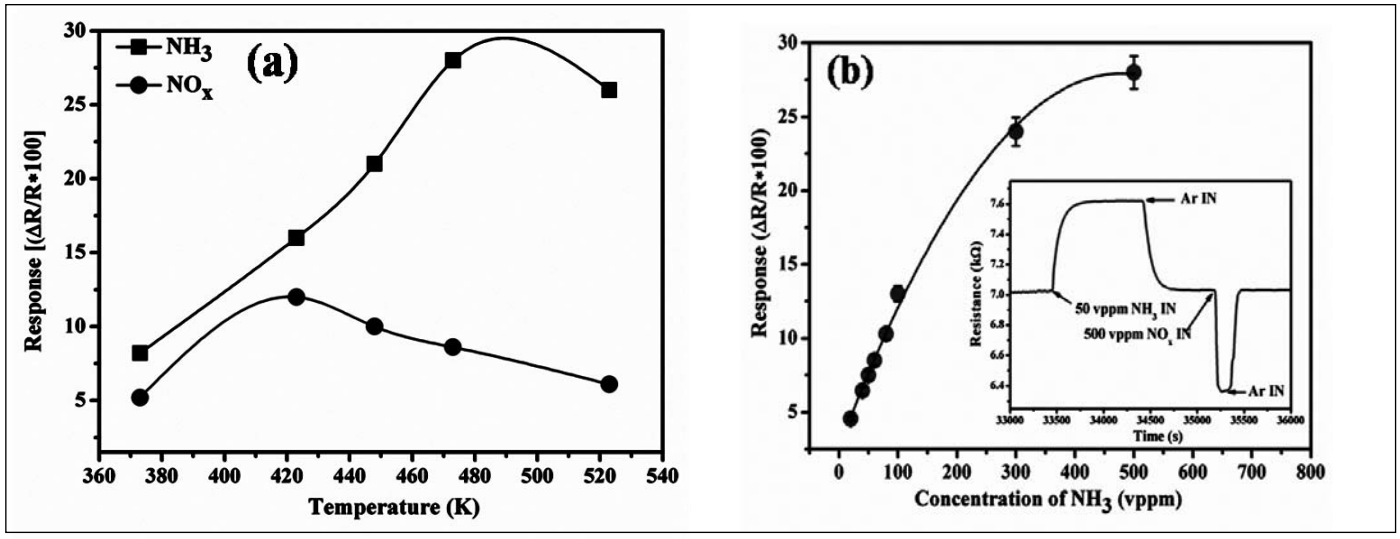

Fig. 3: (a) Response vs temperature plot for 500 vppm of PbS towards two analyte gases and (b) Calibration plot of PbS thin film towards NH_3 at 473 K. Inset: Typical response pattern of PbS thin film towards NH_3 and NO_x at 473 K

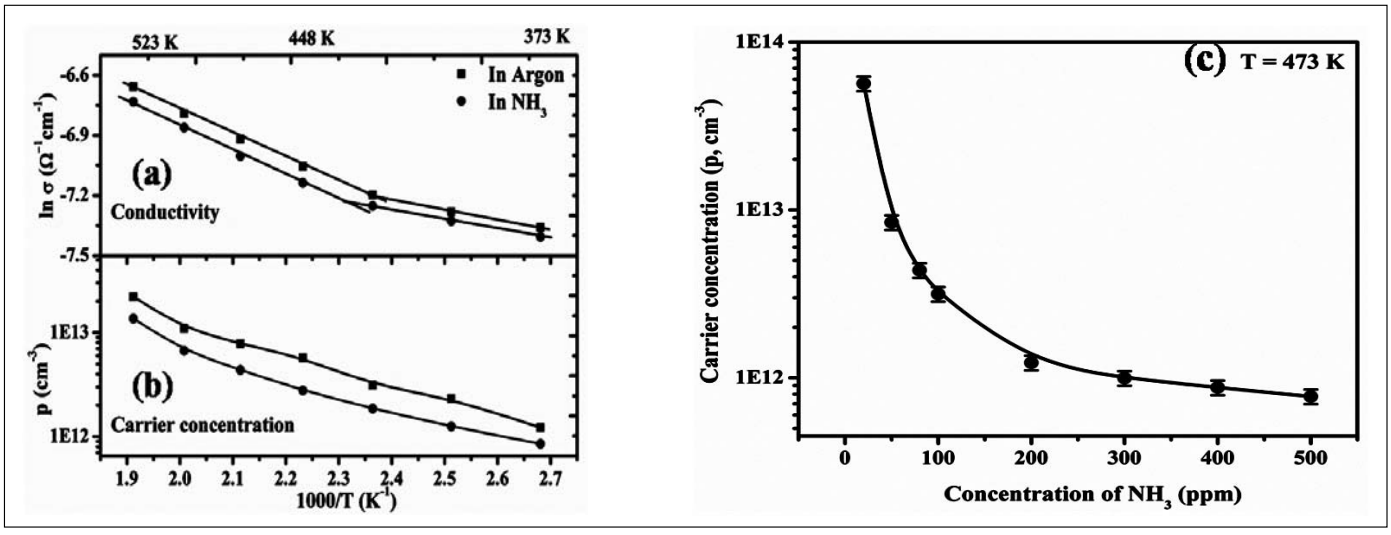

***Fig. 4:** (a) Conductivity (ln σ), (b) Hole carrier concentration (p) vs 1/T of PbS thin film in argon and argon containing 100 vppm of NH_3 and (c) Carrier concentration (p) as a function of NH_3 concentration at 473 K*

whereas a reverse trend is observed for NO_x. NH_3 being a reducing gas, an increase in resistance is reported for p-type semiconductor oxides. On the other hand, a decrease in resistance is reported for an oxidizing gas like NO_x for the p-type oxides. This shows that PbS is behaving like a p-type semiconductor. The sensor retraces to the baseline value on purging with argon.

3.3 Insitu – Hall studies

In order to understand the mechanism of interaction of ammonia with the PbS, Hall coefficients of PbS thin film was measured in the temperature range from 373 to 523 K. The positive Hall voltage indicates that the PbS thin film exhibiting a p-type behavior in this temperature range. The hole carrier concentration (p) is calculated from the Hall coefficient and four probe-conductivity measured at different temperatures.

The logarithmic conductivity (4-probe) versus inverse temperature plot of PbS thin film in argon (■) and argon containing 100 vppm of NH_3 (●) is shown in Figure 4 (a). The plot shows two distinct regions having different slopes observed for both argon and argon containing 100 vppm of ammonia. An activation energy of 0.18 (± 0.04) eV is obtained for the high temperature region (448 – 523 K) and another with an activation energy of 0.03 eV for the low temperature region (323 – 423 K) for PbS in argon. Similar values of activation energy were also observed for argon containing 100 vppm of NH_3. As the band gap

of PbS is found to be 2.25 eV, the high temperature region is dominated by the intrinsic conduction whereas the low temperature region is dominated by the extrinsic conduction. Moreover, the conductivity of PbS thin film in argon containing 100 vppm of NH_3 is lower than that of argon throughout the temperature range of investigation irrespective of nature of conduction.

Figure 4 (b) shows the changes in hole carrier concentration of PbS thin film as a function of inverse temperature in argon containing 100 vppm of NH_3. For comparison, a variation in carrier concentration in argon is also plotted in the same graph. The hole carrier concentration of PbSin argon ambient increased from 10^{11} to 10^{13} cm^{-3}[15, 16] for the entire temperature range of 373 – 523 K. However, a significant reduction in hole carrier concentration is observed even for the presence of 100 vppm of NH_3 in argon. This reduction in carrier concentration is noticed throughout the temperature range of investigation. This implies that ammonia interacts with the PbS through its lone pair of electrons after getting adsorbed on the surface which in turn leads to the localization of holes near its vicinity.

Figure 4(c) shows the plot of variations in hole carrier concentration as a function of ammonia concentration. An exponential dependency is observed with increase in ammonia concentration (20 – 500 vppm) when the sensor is operated at 473 K. It should be noted that the carrier concentration decreases by about two orders even for 200 vppm of ammonia. This may be due to the interaction of the lone pair of electrons with the hole accumulation layer which modulates the total conductivity of PbS thin films.

4. Conclusions

Laser deposited thin films of PbS were highly promising for sensing trace levels of NH_3 in the inert ambient (Ar) and potentially useful for monitoring NH_3 released during the hydrolysis of uranium nitrides stored in inert atmosphere. Films were highly selective and sensitive to NH_3 with a typical response and recovery times of about 26 s and 125 s respectively for 500 vppm of NH_3 at 473 K. XPS results revealed no evidence for oxygen contamination and in-situ Hall studies shows a p-type semiconductivity with the carrier concentration in the range of 10^{11} – 10^{13} cm^{-3} which undergoes a significant change in the presence of trace levels of ammonia (100 vppm). A direct interaction of NH_3 with the valence band is proposed which is responsible for the changes in conductivity.

Acknowledgement

The authors are thankful to HBNI-IGCAR, Kalpakkam for financial support.

References

1. R. Dell, V. Wheeler, N. Bridger, *Transactions of the Faraday Society*, 1967, 63, 1286-1294.
2. J. Rebholz, C. Dee, U. Weimar, N. Barsan, *Procedia Engineering*, 2015, 120, 83-87.
3. S. Wang, B. Xiao, T. Yang, P. Wang, C. Xiao, Z. Li, R. Zhao, M. Zhang, *Journal of Materials Chemistry A*, 2014, 2, 6598-6604.
4. T. Fu, *Sensors and Actuators B: Chemical*, 2009, 140, 116-121.
5. Y. Liu, L. Wang, H. Wang, M. Xiong, T. Yang, G.S. Zakharova, *Sensors and Actuators B: Chemical*, 2016, 236, 529-536.
6. X. Liu, M. Zhang, *International Journal of Infrared and Millimeter Waves*, 2000, 21, 1697-1701.
7. S. Günes, K.P. Fritz, H. Neugebauer, N.S. Sariciftci, S. Kumar, G.D. Scholes, *Solar Energy Materials and Solar Cells*, 2007, 91, 420-423.
8. P. Yang, C.F. Song, M.K. Lü, X. Yin, G.J. Zhou, D. Xu, D.R. Yuan, *Chemical Physics Letters*, 2001, 345, 429-434.
9. A. Martucci, J. Fick, J. Schell, G. Battaglin, M. Guglielmi, *Journal of Applied Physics*, 1999, 86, 79-87.
10. S. Navale, D. Bandgar, M. Chougule, V. Patil, *RSC Advances*, 2015, 5, 6518-6527.
11. L. Koao, F. Dejene, H. Swart, *Int. J. Electrochem. Sci*, 2014, 9, 1747-1757.
12. D.J. Cant, K.L. Syres, P.J. Lunt, H. Radtke, J. Treacy, P.J. Thomas, E.A. Lewis, S.J. Haigh, P. O'Brien, K. Schulte, *Langmuir*, 2015, 31, 1445-1453.
13. K. Laajalehto, I. Kartio, P. Nowak, Applied surface science, 1994, 81, 11-15.
14. B. Touati, A. Gassoumi, I. Dobryden, M.M. Natile, A. Vomiero, N.K. Turki, *Superlattices and Microstructure*s, 2016, 97, 519-528.
15. M.G. Faraj, *American Journal of Condensed Matter Physics*, 2015, 5, 51-55.
16. F. Gode, O. Baglayan, E. Guneri, *Chalcogenide Letters*, 2015, 12, 519-528.

	Beatriceveena. T. V. *received her B.Sc. and M.Sc. degree from Stella Maris College affiliated to University of Madras. At present, she is pursuing Ph.D. under the supervision of Dr. K.I. Gnanasekar in the Materials Chemistry & Metal Fuel Cycle Group, HomiBhabha National Institute, Indira Gandhi Centre for Atomic Research Campus, Kalpakkam. Her research interest is towards the development of chemical sensing devices for applications in process streams as well as hazardous gases detection.In addition, she is also interested in the synthesis and gas sensing studies of 1D nanomaterials.*
	E. Prabhu *received his master degree in chemistry from Annamalai University in 2006 and PhD from HomiBhabha National Institute (HBNI), IGCAR, Kalpakkam during the year 2016. Research areas of his interest are thin film deposition, AC impedance spectroscopy, development of metal oxide chemical sensors for hazardous gases and flammable gases in air.*
	V. Jayaraman *received his master degree in chemistry from Indian Institute of Technology, Madras in 1988 and PhD in 1999 from Indian Institute of Science, Bangalore. He is from 32nd batch of BARC training School and started his research career in Indira Gandhi Centre for Atomic Research (IGCAR) from 1989. Research areas of his interest are solid electrolytes, chemical sensors for ambient monitoring and soft chemical synthesis of multicomponent oxides.*
	K. I. Gnanasekar*received his Masters degree in Chemistry from Indian Institute of Technology, Bombay in 1988 and PhD in 1994. He has been a scientist with Indira Gandhi Centre for Atomic Research since 1996. His main research interests are thin film superconductors, chemical sensors and materials for advanced battery systems.*

Synthesis of highly resistive bismuth titanate ceramics for high temperature piezoelectric applications

P.M. Aiswarya, A.V. Meera, R. Srinidhi, K.I. Gnanasekar, V. Jayaraman, T. Gnanasekaran*
Materials Chemistry Division, Indira Gandhi Centre for Atomic Research, HBNI
Kalpakkam 603 102, INDIA
**Corresponding author E-mail: gnani.home@gmail.com*

Abstract

The structural and electrical properties of bismuth titanates were investigated by preparing them by three different methods such as solid state reaction, co-precipitation and reaction in molten salt medium. Synthesis by reaction in molten salt medium resulted in the formation of highly textured and sufficiently resistive bismuth titanates. Further tuning of electrical conductivity of bismuth titanates was achieved by incorporating Nb and the dopant concentration was optimized to obtain the lowest possible electrical conductivity.

Keywords: Powders, chemical preparation, Electrical conductivity, Piezoelectric properties, Perovskites

1. Introduction

Bismuth titanate ($Bi_4Ti_3O_{12}$), a layered ferroelectric oxide and belonging to the Aurivillius family, has attracted considerable interest for high temperature piezoelectric applications due to its high Curie temperature (948 K), high dielectric constant, large spontaneous polarization (50 μC/cm) and better piezoelectric properties (d_{33} = 8 to 21 pC/N) [1-4]. The layered structure of bismuth titanate is characterized by the perovskite-like $(Bi_2Ti_3O_{10})^{2-}$ layers sandwiched between $(Bi_2O_2)^{2+}$ layers along its crystallographic c-axis [5, 6].

It is well known that the preparation of bismuth titanate at high temperatures is accompanied by the vaporization of Bi_2O_3 along with the generation of bismuth and oxide ion vacancies ($V_{Bi}^{'''}, V_O^{\bullet\bullet}$), which largely affect the electrical properties of bismuth titanate [7]. Upon cooling the product in air, majority of the oxide ion vacancies get compensated by absorption of oxygen and the charge neutrality is acquired by the generation of holes. A detailed structural analysis of bismuth titanate showed that some of the bismuth ions in the perovskite layers are overbonded with a valence state higher than 3+ [8] and the generation of holes in bismuth titanate is associated with the oxidation of Bi^{3+} to Bi^{4+} [7, 9] which would lead to p-type conductivity. The measurements on Seebeck coefficient of bismuth titanate by Kim et al [10] also proved that the conduction to be of p-type. Takahashi et al [11] observed that polycrystalline bismuth titanate ceramics exhibit both ionic and p-type conductions and at high temperatures, the ionic conduction dominates. The dependence of the electrical conductivity of single crystals of bismuth titanate on the oxygen pressure was also studied by Takahashi et al [11]. They observed anisotropic conductivity along the a- and c axes with the maximum value along the c-axis. Along the c-axis, p-type conduction was dominant whereas ionic conduction was dominant along the a-axis of the crystal. They also suggested that the defects responsible for the electrical conduction preferentially existed in the perovskite layer. As the conductivity of bismuth titanate is relatively high, it is very difficult to polarize polycrystalline bismuth titanate ceramics prepared by conventional methods, which has been an obstacle for the piezoelectric applications of bismuth titanate [7]. Conductivity of bismuth titanate along the c-axis can be reduced by restricting the growth of the crystal along the c-axis and allowing its growth along the a-b plane. It is also known from literature that a significant reduction in the conductivity of bismuth titanate can be achieved by the substitution at the Ti^{4+} site by ions such as Nb^{5+}, W^{6+}, Ta^{5+}, etc [12-17].

Different methods have been adopted in the past for the synthesis of highly homogeneous bismuth titanate powder. As mentioned above, synthesis by conventional solid state methods leads to the vaporization of Bi_2O_3 and causes coarsening and agglomeration of particles resulting in poor microstructure and structural/mechanical strength of the ceramic [18, 19]. It is also reported that use of high temperatures for preparing bismuth titanate could result in the formation of an additional pyrochlore phase of $Bi_2Ti_2O_7$ by the vaporization of Bi_2O_3 from the parent $Bi_4Ti_3O_{12}$ phase [11]. Different wet chemical methods such as co-precipitation, hydrothermal synthesis, etc can also be used for the synthesis of bismuth titanate which will allow control over the size and morphology of the particles [20-23]. But the subsequent heat treatment results in loss of Bi_2O_3 by vaporization and the desired reduction in the electrical conductivity of bismuth titanate could not be achieved by these methods.

It is known from literature that highly textured and flake like structures can be prepared by molten salt synthesis [24]. Here, the reactant mixture is heated with a low melting salt at a temperature above the melting point of the salt. At the reaction temperature, the medium melts and acts as a solvent to facilitate the interaction of the reactants. The products formed by this method are found to be highly textured and homogeneous. Also, as the reaction is mediated by the liquid, Bi_2O_3 vaporization losses would be low.

Synthesis of bismuth titanate by molten salt method is reported in literature [25-27]. Zaremba [25] and ChenJie [26] employed molten salt method for the synthesis of bismuth titanates with flake like structures using NaCl-KCl medium and observed that both temperature and duration of heating can affect the shape and size of the crystals. Kimura and Yamaguchi [27] investigated the effect of salt species on the morphology and structure of bismuth titanate using chloride and sulphate fluxes. They reported that the shape of the product particles formed depends upon the flux species.

In the present work, highly textured and sufficiently resistive bismuth titanate ceramics were prepared by molten salt synthesis and further reduction in the electrical conductivity was achieved by doping with Nb^{5+}. The electrical conductivities of the prepared ceramics were compared with those obtained by solid state reaction and co-precipitation.

2. Experimental details

2.1 Synthesis of bismuth titanate

Bismuth titanate was prepared by three different methods: i) solid state reaction, ii) co-precipitation reaction and iii) reaction in molten salt medium.

2.1.1 Solid state reaction

The starting materials used were Bi_2O_3 (99.99% purity on metal basis, M/s Alfa Aesar, USA), TiO_2 (99.99% purity on metal basis, M/s Alfa Aesar, USA). The Bi_2O_3 powder used was calcined at 1023 K in air for about 6 h to remove any carbonate impurities and moisture present in it. The TiO_2 powder was heated at 873 K before its use to remove any moisture present in it. For preparing bismuth titanate, stoichiometric amounts of Bi_2O_3 and TiO_2 were mixed well and pelletized. The pellet was placed in alumina crucible and heated in air at 1073 K for 48 h. At the end of 24 h of heating, the pellet was crushed and uniformly mixed. The powder was repelletized and heated again for another 24 h. The resulting product was quenched to room temperature, powdered and characterized by XRD. The powders were pelletized, sintered in air at 1373 K for 2 h and used for measurement of electrical conductivity.

2.1.2 Co-precipitation reaction

Titanium butoxide ($Ti(C_4H_9O)_4$) (98+% purity on metal basis, M/s Alfa Aesar, USA) and $Bi(NO_3)_3.5H_2O$ (prepared by dissolving high purity Bi metal (99.999 % purity) in concentrated HNO_3) were used as the precursors for Ti^{4+} and Bi^{3+} ions, respectively. The trace impurities in the titanium butoxide were identified by ICP-AES and the total amount of the impurities was determined to be ~140 ppm. The precursors were mixed in the stoichiometric ratio and then dispersed in isopropyl alcohol. The mixture thus obtained was precipitated as oxalate by the drop wise addition of the dispersion in isopropyl alcohol into an excess of 0.3 mol kg^{-1} oxalic acid solution under constant stirring. A small amount of NH_4OH solution was added at the end of the precipitation process. The co-precipitate thus obtained was washed with isopropyl alcohol. The amorphous powder obtained was dried and calcined at 1023 K for 1 h. The calcined powder was thoroughly ground in isopropyl alcohol medium for about 2 h and made into pellets. The compacted pellets were then sintered at 1123 K for 2 h. One of the sintered pellets was crushed, ground well and the ensuing sample was characterized by XRD.

2.1.3 Reaction in molten salt medium

A homogeneous mixture of Bi_2O_3 and TiO_2 in the stoichiometric ratio was prepared. 75 wt% of an eutectic mixture of 44 wt% NaCl (99.9% purity on metal basis, M/s Sarabhai Chemicals, India) and 56 wt% KCl (99.98% purity on metal basis, M/s Sarabhai Chemicals, India) was added to it and thoroughly ground in acetone medium. The well ground mixture was taken in an alumina crucible, covered with an alumina lid and sealed using alumina cement to prevent evaporation of the constituents. The sample was heated at 1323 K for 2 h, which is well above the eutectic temperature of NaCl-KCl (923 K). The crucible was cooled and the product was repeatedly washed with hot distilled water until all the alkali metal chlorides were removed. The effluent was tested for any residual chlorides using silver nitrate solution. Further, the product was repeatedly ultra sonicated under water and washed to remove adsorbed or occluded impurities in it. The product thus obtained was dried in an oven, compacted into pellets and sintered in air at 1373 K for 2 h. The sintered samples were later characterized by XRD.

2.2 Synthesis of Nb-doped bismuth titanates

Niobium-doped bismuth titanates were synthesized both by solid state reaction method and reaction in molten

salt medium. The nominal composition employed was $Bi_4Ti_{3-x/4}Nb_{x/5}O_{12}$ where x = 0.25, 0.5, 0.75, 1 and 1.25, which are designated as BITN-1, BITN-2, BITN-3, BITN-4 and BITN-5, respectively. Preparations were carried out in a similar manner as mentioned in section 2.1.1 and 2.1.3 using Nb_2O_5 (99.9% purity on metal basis, M/s Alfa Aesar, USA) as the precursor. The details of the various compositions chosen are given in Table. 1.

Table 1 Composition of Nb doped bismuth titanates ($Bi_4Ti_{3-x/4}Nb_{x/5}O_{12}$)

Sample	x	Formula
BIT	0	$Bi_4Ti_3O_{12}$
BITN-1	0.25	$Bi_4Ti_{2.9375}Nb_{0.05}O_{12}$
BITN-2	0.5	$Bi_4Ti_{2.875}Nb_{0.1}O_{12}$
BITN-3	0.75	$Bi_4Ti_{2.8125}Nb_{0.15}O_{12}$
BITN-4	1	$Bi_4Ti_{2.75}Nb_{0.2}O_{12}$
BITN-5	1.25	$Bi_4Ti_{2.69}Nb_{0.25}O_{12}$

2.3 Phase identification and morphological characterizations

The powder samples of bismuth titanate prepared were characterized by X-ray diffraction method (XRD) using a powder X-ray Diffractometer (M/s Inel, France) operating with Cu K_α radiation and graphite monochromator. Their surface morphology was investigated by scanning electron microscopy (SEM) imaging using Model XL 30, M/s Philips, Netherlands. The bulk density of the sintered pellets was measured by Archimedes method.

The electrical conductivity of the samples was measured by complex impedance spectroscopy. For these experiments, sintered sample pellets of pristine and doped bismuth titanates were used. The conductivity cell used consisted of two silver electrical leads which were brazed to silver pellets of identical dimension (10 mm diameter). The sample pellet of known diameter (<10 mm) and thickness was mounted between the silver pellets by a spring loading arrangement. A K- type thermocouple was kept close to the sample pellet, so that the sample temperature could be accurately measured. Entire assembly was kept inside a quartz chamber, which in turn was kept in a furnace for heating. The electrical conductivity was measured using a frequency response analyzer (Model SI 1255, Solartron, M/s Schlumberger, UK) coupled with an electrochemical interface (Model 1287, Solartron, M/s Schlumberger, UK). The measurements were carried out in air in the temperature range of 700 to 1050 K in the frequency range of 10 Hz to 1 MHz with an applied perturbation potential of 500 mV. The impedance data obtained at each temperature was fitted using the software Zview® [28]. The bulk resistance of the material was obtained by fitting a semicircle to the experimentally obtained Nyquist plot. By incorporating the dimensions of the sample pellet, the conductivity (σ) of the sample at that temperature (T) was determined. The Arrhenius plot for conductivity was obtained by plotting log σ as a function of 1/T. The activation energy was calculated from the slope of the Arrhenius plot.

2.4 Piezoelectric characterization

Poling of the Nb-doped bismuth titanate samples was performed in silicone oil bath at 448 K at an applied field of 30 kV/cm for 4 h using a dc poling unit (M/s Marine, India). Piezoelectric sensitivity (d_{33}) was measured using the direct piezoelectric effect and for this a piezometer system (M/s Piezotest, UK) was used. Dynamic force was applied through a lead zirconate titanate (PZT) actuator, and a quartz sensor was used as a reference.

3. Results and Discussion

3.1 Structural and morphological characterization of bismuth titanates

The comparison of XRD patterns of bismuth titanate samples synthesized by solid state method and molten salt method is presented in Fig. 1. All the XRD patterns showed the presence of pure orthorhombic phase of $Bi_4Ti_3O_{12}$, which were indexed according to the PCPDF file # 35-0795 as shown in Fig. 1a. There were no additional peaks, suggesting that the compounds formed are phase

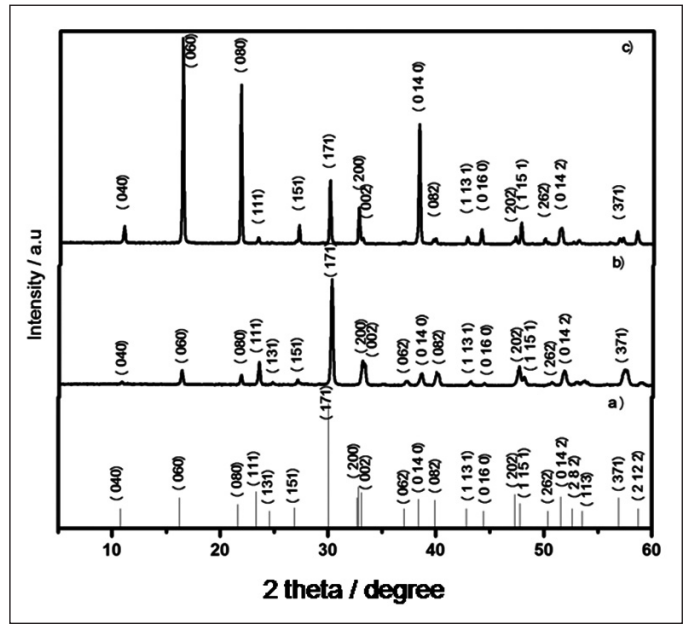

Fig. 1: Graphical comparison of XRD patterns of $Bi_4Ti_3O_{12}$ a) PCPDF pattern, file No# 35-0795, b) prepared by solid state reaction method and c) prepared by reaction in molten salt medium

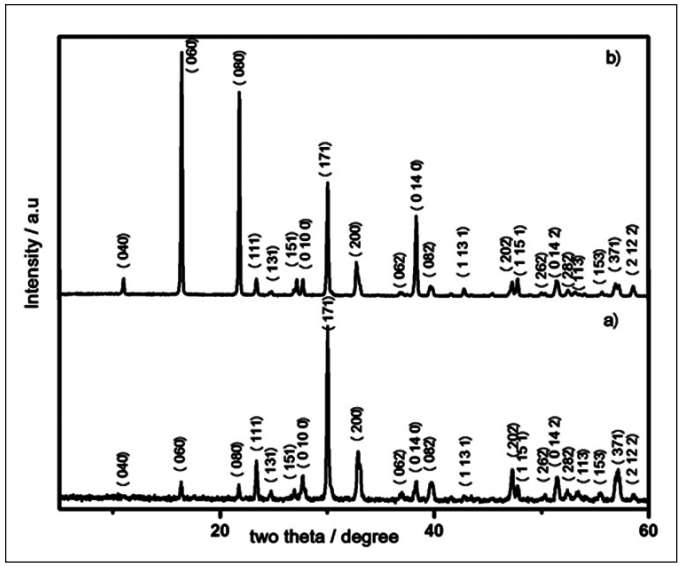

Fig. 2: XRD pattern of $Bi_4Ti_3O_{12}$ prepared by oxalate co-precipitation method a) after calcining at 1023 K and b) after sintering at 1123 K

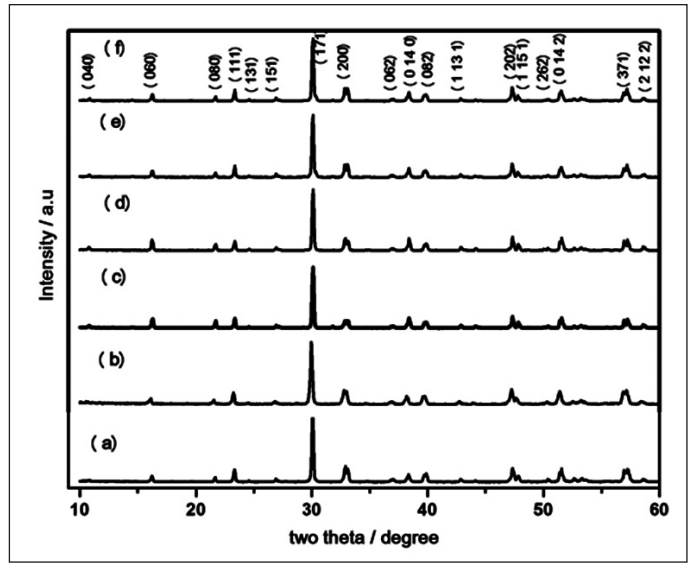

Fig.3: Comparison of XRD patterns of Nb- doped bismuth titanate prepared by solid state reaction; a) BITN- pristine, b) BITN-1, c) BITN-2, d) BITN-3, e) BITN-4 and f) BITN-5

pure. Bismuth titanate prepared by solid state method (Fig. 1b) exhibited the highest intensity peak at 2θ = 30.05°, which is attributed to the diffraction of the (171) plane of $Bi_4Ti_3O_{12}$. The intensities of other diffracted peaks are lower, indicating predominant polycrystalline nature of the sample. In the case of bismuth titanate prepared by molten salt method, the XRD pattern (Fig. 1c) had shown increased intensity along the (0k0) planes, viz., (060), (080) and (0 14 0), indicating the preferential growth of the crystal along the b axis.

Figure 2a shows the XRD patterns obtained for bismuth titanate prepared by oxalate coprecipitation method followed by calcination at 1023 K. The XRD pattern is similar to the one prepared by solid state reaction with the highest intensity peak at 2θ corresponding to 30.05°. However, it is seen from Fig. 2b that after sintering at 1123 K, the intensity of the diffraction peaks along the (0k0) planes increased.

The influence of Nb addition in bismuth titanate was also investigated by XRD. The XRD profiles of bismuth titanate obtained before and after Nb doping by both solid state reaction and by reaction in molten salt medium are shown in Figs. 3 and 4. The XRD patterns of pristine and Nb-doped bismuth titanates are similar. All diffraction data showed the existence of a single orthorhombic phase, without any detectable secondary phase.

The relative densities of the sintered pellets of bismuth titanate synthesized by various routes were determined by Archimedes method and were found that all the specimens had attained 95-98% of theoretical density.

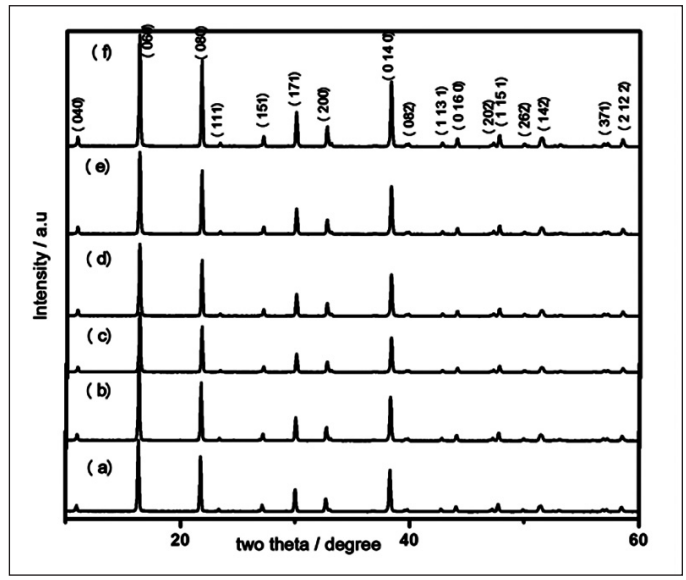

Fig.4: Comparison of XRD patterns of Nb-doped bismuth titanate prepared by the reaction in molten salt medium; a) BITN- pristine, b) BITN-1, c) BITN-2, d) BITN-3, e) BITN-4 and f) BITN-5

The microstructures of pristine bismuth titanate samples prepared by both solid state reaction and reaction in molten salt medium were followed by SEM analysis. The morphological changes that occurred in the bismuth titanate samples upon Nb doping were also studied by SEM imaging of the sintered specimens. Fig. 5 represents SEM images of bismuth titanate prepared by solid state reaction and Fig. 6 shows those of bismuth titanate prepared by reaction in molten salt medium.

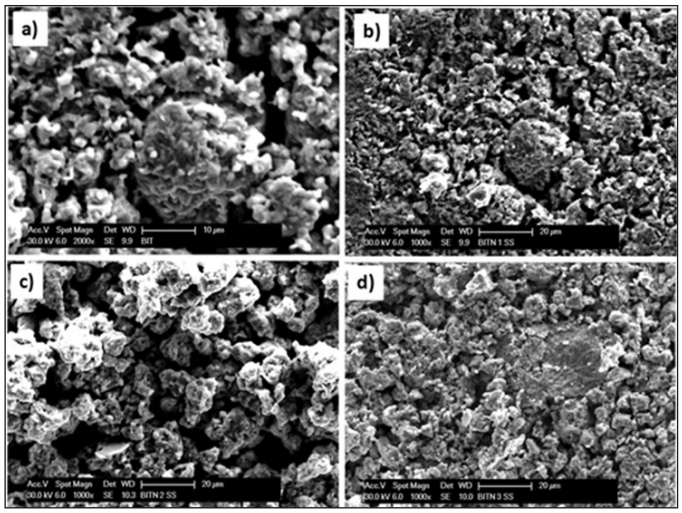

Fig.5: *SEM images of pristine and Nb doped BIT prepared by solid state method a) BITN- pristine, b) BITN-1, c) BITN-2 and d) BITN-3*

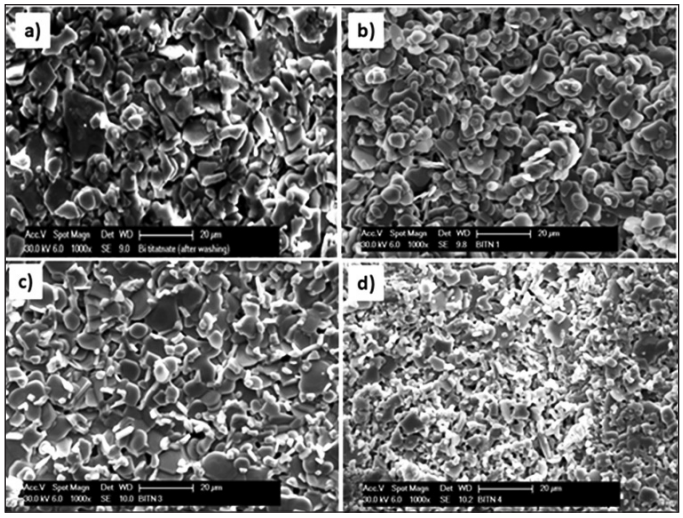

Fig.6: *SEM images of pristine and Nb doped BIT prepared by molten salt method a) BITN- pristine, b) BITN-1, c) BITN-3 and d) BITN-4*

The micrographs of bismuth titanate prepared by solid state reaction shows the presence of small agglomerates of grains. Nb doping has resulted in an increase in the agglomeration of particles. It is seen that the spherical agglomerates are randomly scattered and the average size of the agglomerates ranges from 10-20 µm. The SEM images of the samples prepared by reaction in molten salt medium showed the presence of flake-like microstructures. The flake like structures arises due to the restricted growth of the crystal along the c-axis. Doping with Nb has also modified the appearance of the flakes. Instead of plane flakes as obtained for pristine bismuth titanate, Nb-doped bismuth titanate showed the presence of a globule- like structure within each flake. The incorporation of Nb has led to the evolution of microstructures which is indicated by the increased flowering of the flakes with increase in the Nb content.

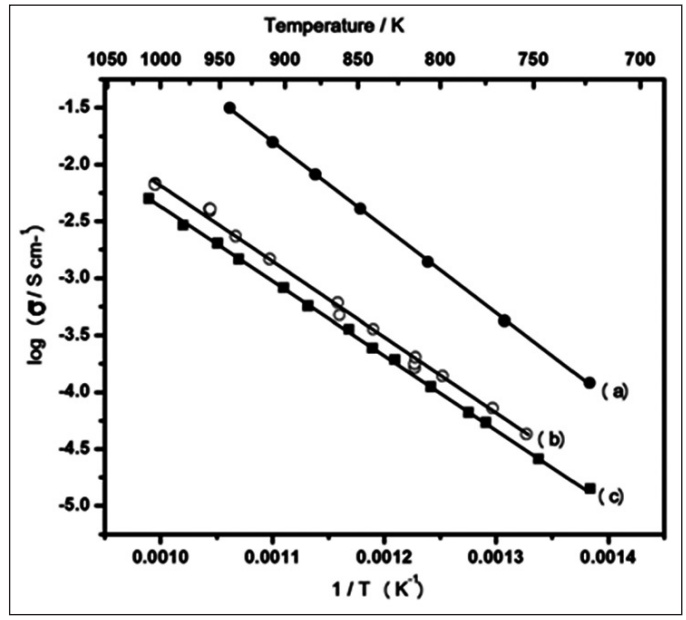

Fig.7: *Arrhenius plot of electrical conductivity of bismuth titanates prepared by different methods a) solid state method, b) oxalate co-precipitation method and c) molten salt method.*

3.2 Electrical characterization of bismuth titanates

Figure 7 shows the variation of electrical conductivity with temperature for pristine bismuth titanates prepared by three different methods.

The conductivity values obtained by three different methods at 873 K are compared and the typical conductivity values (log σ) obtained for bismuth titanate prepared by solid state reaction, co-precipitation reaction and reaction in molten salt medium are -2.1, -3.1 and -3.3, respectively. It is seen that bismuth titanate prepared by the reaction in molten salt medium has shown the lowest conductivity. The observed reduction in electrical conductivity can be attributed to two factors: 1) as the preparation by molten salt method is mediated by the liquid, evaporation losses of Bi_2O_3 would be low. Thus formation of bismuth and oxide ion vacancies is suppressed during the preparation itself. However, Bi_2O_3 losses can occur during the high temperature sintering of the specimen in air. As the compound has already formed, thermodynamic activity of Bi_2O_3 in the compound would be less as it is in the bound state and consequently evaporation losses would be low and hence, conductivity will be low. 2) It is evident from SEM images that the preparation of bismuth titanate by reaction in molten salt medium had resulted in the formation of flake like structures which are indicative of the restricted growth of the crystal along the c-axis (i.e. a-b plane oriented). As bismuth titanate shows maximum conductivity along the c-axis, this component of conductivity would get reduced in the case of a-b

plane oriented crystal. During the preparation as well as sintering of bismuth titanate by solid state reaction, bismuth and oxide ion vacancies will get generated due to the evaporation of Bi_2O_3. Even though majority of the oxide ion vacancies get compensated by absorption of oxygen upon cooling, ionic conductivity can be still there in the compound due to the presence of very low concentration of oxide ion vacancies. In addition to this, for compensating the charge for the presence of bismuth ion vacancies, holes would be generated which results in p-type conductivity. This is the reason for the high conductivity exhibited by bismuth titanates prepared by solid state reaction. It is also to be noted that electrical conductivity of bismuth titanate prepared by oxalate co-precipitation method is lower than that prepared by solid state method and closer to that prepared by molten salt method. The XRD pattern of the sintered specimen of bismuth titanate obtained by oxalate co-precipitation method had also shown increased intensity of the diffracted peaks along the (0k0) planes suggesting the growth of the crystal along the a-b plane. The conductivity observed is lower and is in accordance with the XRD results. The activation energies observed are 1.50, 1.35 and 1.29 eV, respectively for bismuth titanates prepared by solid state method, oxalate co-precipitation method and molten salt method. The reasons for this change in activation energy for the conduction process with samples prepared by using different methods are not known from the present investigations.

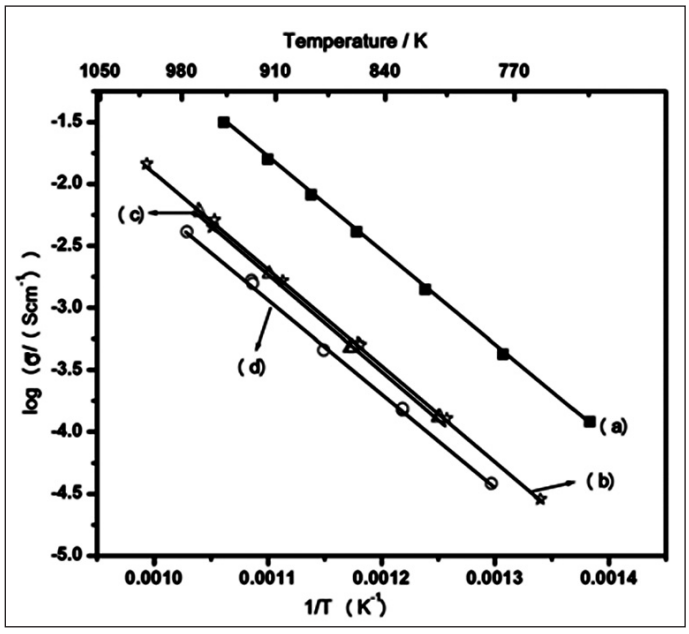

Fig.8: *Comparison of electrical conductivities of pristine and Nb-doped bismuth prepared by solid state method a) BIT-Pristine, b) BITN-2, c) BITN-4 and d) BITN-3.*

The variation of electrical conductivity obtained after doping with Nb^{5+} for bismuth titanates prepared by solid state method is shown in Fig. 8. It is observed that the conductivity of Nb-doped bismuth titanates is lower than that of the pristine bismuth titanate. The conductivity was significantly reduced with a very small Nb content. However, the variation of electrical conductivity with increase in Nb content is not much pronounced. The typical values of electrical conductivity (log σ) obtained at 873 K are -2.2, -3.0, -3.1 and -3.3, respectively for pristine BIT, BITN-2, BITN-4 and BITN-3.

The conductivity measurements on Nb-doped bismuth titanates prepared by molten salt method revealed that the incorporation of Nb has led to the lowering of conductivity by two to three orders of magnitude in comparison with the pristine bismuth titanates synthesized by the same method. The Arrhenius plots of conductivity for all compositions of Nb-doped bismuth titanates are shown in Fig. 9. It is found that all compositions showed similar activation energies. However, there is a drastic change in the conductivity values upon doping with Nb^{5+}. The conductivity values slightly increased for the lowest Nb concentration and it continued to decrease until it reached the composition with x = 0.75 which corresponds to BITN-3. After that, further increase in the Nb concentration has led to an increase in the conductivity. A similar observation in the conductivity of Nb-doped bismuth titanate prepared by solid state reaction method was reported in the studies of Martin et al [29]. The typical values of conductivity (log σ) obtained at 873 K are -4.0, -4.8, -5.6, -5.1, respectively for BITN-1, BITN-2, BITN-3 and BITN-4.

The lowering of conductivity of bismuth titanate with increasing Nb content can be explained on the basis of the defect structure of bismuth titanate. As discussed earlier, bismuth titanate exhibit both ionic and p-type conduction. The introduction of Nb_2O_5 in bismuth titanate results in the substitution of Nb^{5+} at the Ti^{4+} site with the generation of metal vacancy or by accommodating oxygen ion in the already existing vacant oxygen sites. The filling up of vacant oxygen sites causes a reduction in the ionic conductivity as expressed by equation 1.

$$Nb_2O_5 + V_O^{\bullet\bullet} \longrightarrow 2Nb_{Ti}^{\bullet} + 5O_O^X \qquad (1)$$

Once all the oxide ion vacancies are filled up, further substitution of Nb_2O_5 will lead to the generation of electrons. These electrons neutralize the effect of holes, which result in the reduction of conductivity. The conductivity will decrease with Nb_2O_5 doping to a minimum value until the concentration of the electrons equals to the hole concentration. Further introduction

of Nb_2O_5 causes an increase in the conductivity. This is evident from the electrical conductivity behavior of Nb-doped bismuth titanates shown in Fig. 9. The Nb doped bismuth titanate of composition BITN-3 with x = 0.75 has showed the lowest conductivity among the different samples. However, the initial increment in the conductivity for the least concentration of Nb in bismuth titanate could not be explained.

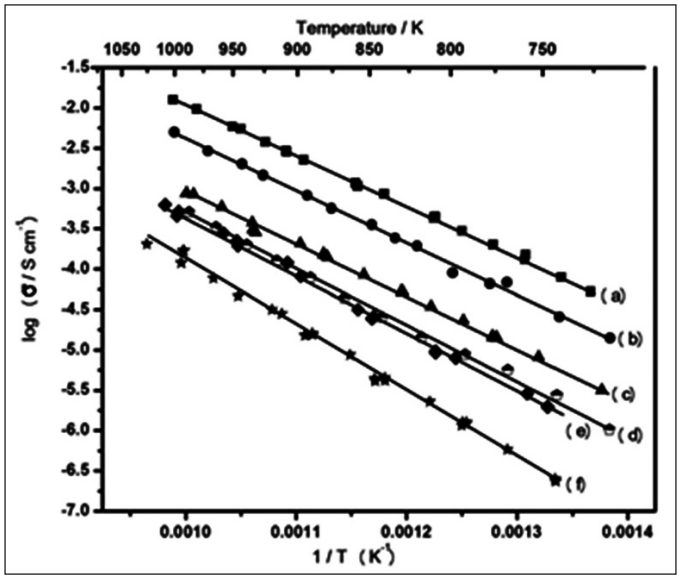

Fig.9: *Comparison of electrical conductivities of pristine and Nb-doped bismuth titanates prepared by molten salt method a) BITN-1, b) BITN-Pristine, c) BITN-2, d) BITN-5, e) BITN-4 and f) BITN-3*

The variation of electrical conductivity as a function of Nb concentration has been plotted and shown in Fig. 10. This shows that the behavior of samples is same for all temperatures.

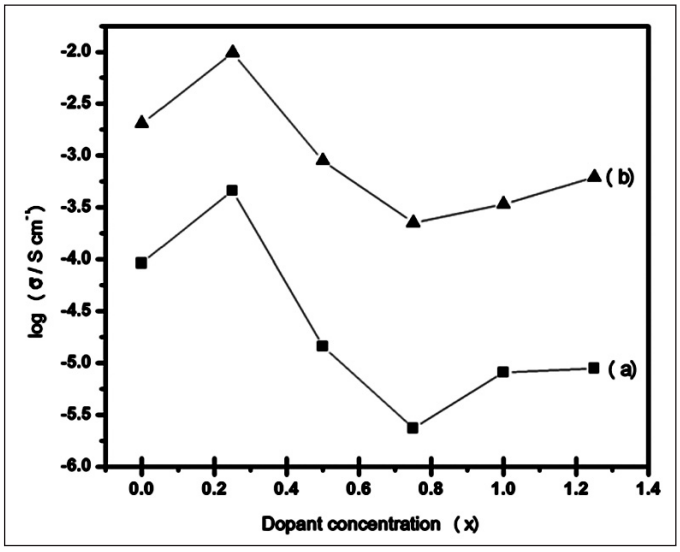

Fig.10: *Variation of electrical conductivity as a function of Nb concentration in $Bi_4Ti_{3-x/4}Nb_{x/5}O_{12}$ at two different temperatures; a) 823 K and b) 923 K*

Based on the experimental studies described so far, it is clear that a reduction in electrical conductivity can be achieved by Nb doping by both solid state method and molten salt method. However, compared to solid state method, highly textured and sufficiently resistive bismuth titanates could be prepared by the reaction in molten salt medium. A pronounced effect in conductivity was observed with Nb doping by this method. The lowest electrical conductivity was obtained for the sample BITN-3 with composition $Bi_4Ti_{2.8125}Nb_{0.15}O_{12}$. The high electrical resistivity allows for applying high poling fields, which is beneficial to polarize the ceramics and obtain high piezoelectric properties.

3.3 Piezoelectric characterization of bismuth titanates

The Nb-doped bismuth titanate sample which exhibited the highest electrical resistance, BITN-3 with composition $Bi_4Ti_{2.8125}Nb_{0.15}O_{12}$ was poled. The d_{33} value obtained was found to be ~16 pC/N. This value compares well with ~20 pC/N reported by Hong et al [21] for $Bi_4Ti_{2.96}Nb_{0.04}O_{12}$. Thus, this sample shows promise for its application at high temperatures.

4. Conclusions

Highly textured and sufficiently resistive bismuth titanates were prepared by molten salt synthesis. The electrical conductivity of bismuth titanates were tuned by incorporating Nb and a reduction in electrical conductivity was observed upon doping. The dopant concentration was optimized to obtain the lowest possible electrical conductivity.

Acknowledgements

The authors are thankful to Dr. R. Sudha for the characterization of samples by SEM. One of the authors (PMA) acknowledges Department of Atomic Energy, India, for providing the financial support.

References

1. L.B. Kong, J. Ma, W. Zhu, O.K. Tan, Preparation of $Bi_4Ti_3O_{12}$ ceramics via a high-energy ball milling process, *Mater. Lett.* 51, **2001**, 108-114.
2. Q. Yang, Y. Li, Q. Yin, P. Wang, Y.B. Cheng, $Bi_4Ti_3O_{12}$ nanoparticles prepared by hydrothermal synthesis, *J. Eur. Ceram. Soc.* 23, **2003**, 161-166.
3. P. Pookmanee, P. Uriwilast, S. Phanichpant, Hydrothermal synthesis of fine bismuth titanate powders, *Ceram. Int.* 30, **2004**, 1913-1915.
4. J.S. Patwardhan, M.N. Rahaman, Compositional effects on densification and microstructural evolution of bismuth titanate, *J. Mater. Sci.* 39, **2004**, 133-139.
5. B. Aurivillius, Mixed oxides with layer lattices, *Ark. Kemi.* 1, **1950**, 499-512.

6. C. Jovalekic, S. Stevic, A study of ferroelectric properties of $Bi_4Ti_3O_{12}$ ceramics prepared from chemically derived powders, *Ferroelectrics.* 132, **1992**, 185-196.
7. C. Long, Q. Chang, H. Fan, Differences in nature of electrical conductions among $Bi_4Ti_3O_{12}$-based ferroelectric polycrystalline ceramics, *Scientific Reports*, 7, **2017**, 1-15.
8. R.L. Withers, J.G. Thompson, A.D. Rae, The crystal chemistry underlying ferroelectricity in $Bi_4Ti_3O_{12}$, Bi_3TiNbO_9 and Bi_2WO_6, *J. Solid. State. Chem.* 94, **1991**, 404-417.
9. H.S. Shulman, M. Testorf, D. Damjanovic, N. Setter, Microstructure, electrical conductivity, and piezoelectric properties of bismuth titanate, *J. Am. Ceram. Soc.* 79, **1996**, 3124-3128.
10. S.K. Kim, M. Miyayama, H. Yanagida, Electrical anisotropy and a plausible explanation for dielectric anomaly of $Bi_4Ti_3O_{12}$ single crystal, *Mater. Res. Bull.* 31, **1996,** 121-131.
11. M. Takahashi, Y. Noguchi, M. Miyayama, Electrical conduction mechanism in $Bi_4Ti_3O_{12}$ single crystal, *Jpn. J. Appl. Phys.* 41, **2002**, 7053-7056.
12. J.H. Park, J.S. Bae, H.J. Park, Y.S. Kim, B.E. Jun, B.C. Choi, J. H. Jeong, Electric response as a function of applied voltage of Nb-doped $Bi_4Ti_3O_{12}$ thin films, *Thin Solid Films*, 516, **2008**, 5304-5308.
13. S.H. Hong, S.T. McKinstry, G.L. Messing, Dielectric and electromechanical properties of textured niobium-doped bismuth titanate ceramics, *J. Am. Ceram. Soc.* 83, **2000,** 113-118.
14. J.K. Kim, J. Kim, T.K. Song, S.S. Kim, Effects of niobium doping on microstructures and ferroelectric properties of bismuth titanate ferroelectric thin films, *Thin Solid Films.* 419, **2002,** 225-229.
15. T. Sakai, T. Watanabe, M. Osada, M. Kakihana, Y. Noguchui, M. Miyayama, H. Funakubo, Crystal structure and ferroelectric property of tungsten-substituted $Bi_4Ti_3O_{12}$ thin films prepared by metal-organic chemical vapor deposition, *J. Appl. Phys.* 42, **2003**, 2850-2852.
16. J.K. Kim, T.K. Song, S.S. Kim, J. Kim, Ferroelectric properties of tungsten-doped bismuth titanate thin film prepared by sol–gel route, *Mater. Letter.* 57, **2002**, 964-968.
17. L.N. Zhang, G.R. Li, S.C. Zhao, A.L. Ding, Q.R. Yin, *Integrated Ferroelectrics*. 79, **2006,** 253-263.
18. S.H. Ng, J. Xue, J. Wang, Bismuth titanate from mechanical activation of a chemically coprecipitated precursor, *J. Am. Ceram. Soc.* 85, **2002**, 2660-2665.
19. W.F. Su, J.F. Lee, M.Y. Chen, R.M. Ho, Bismuth titanate nanoparticles dispersed polyacrylates, *J. Mater. Res.* 19, **2004**, 2343-2348.
20. A.Q. Jiang, H.G. Li, L.D. Zhang, Dielectric study in nanocrystalline $Bi_4Ti_3O_{12}$ prepared by chemical coprecipitation, *J. Appl. Phys.* 83, **1998**, 4878-4883.
21. S.H. Hong, J.A. Horn, S.T. McKinstry, G.L. Messing, Dielectric and ferroelectric properties of Ta-doped bismuth titanate, *J. Mater. Sci. Lett.* 19, **2000**, 1661-1664.
22. J.A. Horn, S.C. Zhang, U. Selvaraj, G.L. Messing, S.T. McKinstry, Templated grain growth of textured bismuth titanate, *J. Am. Ceram. Soc.* 82, **1999**, 921-926.
23. G. Tomandl, A. Stiegelschmitt, R. Bohner, *Proceedings in Science of Ceramic Chemical Processing*, John Wiley & Sons, New York, **1986**.
24. T. Kimura, Molten salt synthesis of ceramic powders in *Advances in ceramics-synthesis and characterization, processing and specific applications,* Edited by C. Sikalidis, InTech, **2011**.
25. T. Zaremba, Anisotropic grain growth of bismuth titanate in molten salt fluxes, *X. Kristallogr. Suppl.* 30, **2009**, 477-482.
26. G. ChenJie, Z.C. Song, Molten salt synthesis of anisotropic $Bi_4Ti_3O_{12}$ particles, *Adv. Mater. Res.* 284, **2011**, 1452-1455.
27. T. Kimura, Y. Yamaguchi, Fused salt synthesis of $Bi_4Ti_3O_{12}$, *Ceram. Int.* 9, **1983**, 13-17.
28. *Z view®-Impedance software*, Scribner Associates, Inc. North Carolina, USA.
29. D. Martin, C. Voisard, D. Damjanovic, N. Setter, Study and control of the conductivity of Nb-doped $Bi_4Ti_3O_{12}$ for high temperature piezoelectric applications, *Bol. Soc. Esp. Ceram. Vidrio.* 38, **1999**, 582-586.

Dr. Aiswarya, P. M. *received her B.Sc. degree from Calicut University and M.Sc. degree from Cochin University, Kerala. She has completed her PhD under the supervision of Dr. T. Gnanasekaran, Former Associate Director, Chemistry Group, IGCAR. Her research interest include phase diagram and thermodynamic investigations on M-Mo-O (M: Pb, Bi) systems.and in the synthesis of materials for piezoelectric applications.*

Dr. Meera, A. V. *received her B.Sc. and M.Sc. degree from Mahatma Gandhi University, Kottayam, Kerala. She has completed her PhD under the supervision of Dr. T. Gnanasekaran, Former Associate Director, Chemistry Group, IGCAR. Her research interest is towards the phase diagram and thermodynamic investigations on Bi-M-O (M: Fe, Cr) systems. In addition, she is also interested in the synthesis of materials for piezoelectric applications.*

	Ms. Srinidhi *received her B.E. degree from Indo French Educational Trust Pondichery in the year 2014. She holds M.Tech. degree on Sensor System Technology from Vellore Institute of Technology University.*
	Dr. K.I. Gnanasekar *received M.Sc., Chemistry and Ph.D., degrees from the Indian Institute of Technology, Bombay. He worked in thin films of high* T_c *superconductors by pulsed laser deposition method. Currently he is working on the development of thin film based chemical sensors for nuclear program. His area specialization includes interfacial interactions, mechanism of chemical sensing and tailoring of materials with high selectivity towards a specificity analyte gas.*
	Dr. V. Jayaraman *is from 32nd batch of BARC Training School and started his research career in IGCAR, Kalpakkam from 1989. He was awarded Ph.D. from Indian Institute of Science, Bangalore. His research interests include solid electrolytes, chemical sensors for process monitoring and soft chemical synthesis of multicomponent oxides.*
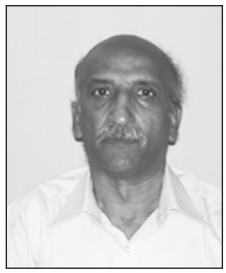	**Dr. T. Gnanasekaran** *obtained his M.Sc and Ph.D from University of Madras. After graduating from the 17th batch of BARC Training School, he joined IGCAR in 1974. He was a postdoctoral fellow at the University of Vienna, Austria and was a visiting scientist at the Nuclear Research Centre, Karlsruhe in Germany. His main themes of studies are high temperature thermodynamics, electrochemistry and development of chemical sensors for use in liquid metals and gaseous ambients. He is recipient of Homi Bhabha Award for Science and Technology for his work in sodium chemistry and former Associate Director of Chemistry Group, IGCAR.*

SOCIETY FOR MATERIALS CHEMISTRY (SMC)
(Reg. No. - Maharashtra, Mumbai/1229/2008/GBBSD)
c/o Chemistry Division
Bhabha Atomic Research Centre, Mumbai 400 085

APPLICATION FOR MEMBERSHIP

Please enroll me as a Life member of the *Society for Materials Chemistry* (**SMC**). My particulars are as follows:

Name :_____

Educational Qualifications :_____

Field of Specialization :_____

_____

Official Address :_____

_____

Telephone No. (Off.) :_____

Residential Address :_____

_____

Telephone No. (Res.) :_____

Address for Correspondence : Home/Office (Please tick one of the options)

E-mail Address :_____

Subscription Details

Mode of Payment : Cheque/DD/Cash
(Cheque/DD should be drawn in favor of "*Society for Materials Chemistry*" for Rs. 1000/- payable at Mumbai. For out-station *non-multi-city* cheques, please include Rs.50/- as additional charge for bank clearance.

Number :
Dated :
Drawn on Bank & Branch :
Amount :
Place:
Date: Signature

_____

Registration Number: _____ (To be allotted by SMC office)